Structural controls on volcanism and degassing in the Main Ethiopian Rift

Jonathan Hunt
University College

Department of Earth Sciences,
University of Oxford

Thesis submitted in July 2019 for the degree of Doctor of Philosophy (Environmental Research NERC DTP)

Supervisors:
Prof. Tamsin A. Mather
Prof. David M. Pyle

Abstract

The interactions between magmatism and crustal structure in continental rifts are manifold, and affect both rift dynamics and the populations that live within them. This thesis explores these interactions, focussing on structural controls on volcanism and degassing in the Main Ethiopian Rift, an archetypal continental rift. The rift hosts up to 10 large silicic volcanoes that have been active in the Quaternary, along with extensive basaltic volcanic fields and widespread geothermal activity. Using a range of geological, geochemical and remote sensing techniques, I examine past volcanism and present degassing with conclusions relevant for the local, regional and global scale.

I use new diffuse CO_2 surveys to show the variability of fault-controlled degassing in the rift, and combine the results with a new compilation of geothermal sites to extrapolate for a rift-scale estimate of emissions. Whilst rift-related diffuse CO_2 flux is clearly important for the global carbon budget, the new estimate for degassing in East Africa is lower than previously suggested.

High-resolution digital elevation models produced for 3 silicic volcanoes in the Main Ethiopian Rift and 1 volcano in Afar show vent and crater alignments along both rift-parallel and cross-rift structures. I have mapped previously unidentified deposits, and compared the relative frequency, type, and magnitude of eruptions at each volcano. Morphological constraints suggest emplacement viscosities for peralkaline lavas of ~10^8–10^{10} Pa s, similar to or lower than calc-alkaline rhyolites.

I compare the morphology of basaltic volcanic fields using digital elevation models, and calculate average volumes. Isolated cones adjacent to faults in East Ziway suggests dike capture, and morphometric analysis (e.g., height to width ratios and rim curvature) suggests an older age than cones in the Butajira field on the rift flank. Superimposed cones and maars at Butajira were likely emplaced by fissure eruptions and phreatomagmatic activity fed by deflected dikes.

Extended abstract

The interactions between magmatism and crustal structure in continental rifts are manifold, and affect both rift dynamics and the populations that live within them. This thesis explores these interactions, focussing on structural controls on volcanism and degassing in the Main Ethiopian Rift (MER), an archetypal continental rift. The rift hosts up to 10 large silicic volcanoes that have been active in the Quaternary, along with extensive basaltic volcanic fields and widespread geothermal activity. Volcanism presents a largely-unconstrained hazard in the rift, whilst geothermal fields provides a promising energy source and opportunity for development. Using a range of geological, geochemical and remote sensing techniques, I examine past volcanism and present degassing with conclusions relevant for the local, regional and global scale.

Deep carbon emissions from historically inactive volcanoes, hydrothermal and tectonic structures are among the greatest unknowns in the long-term (~Myr) carbon cycle. Recent estimates of diffuse CO_2 flux from the Eastern Rift of the East African Rift System (EARS) suggest this could equal emissions from the entire mid-ocean ridge system. I report new CO_2 surveys from the MER, and reassess the rift-related CO_2 flux. Since degassing in the MER is concentrated in discrete areas of volcanic and off-edifice activity, characterisation of such areas is important for extrapolation to a rift-scale budget. Locations of hot springs and fumaroles along the rift show numerous geothermal areas away from volcanic edifices. With these

new data we estimate total CO_2 emissions from the central and northern MER as 0.52—4.36 Mt yr^{-1}. Our extrapolated flux from the Eastern Rift is 3.9—32.7 Mt yr^{-1} CO_2, overlapping with the lower end of the range presented in recent estimates. By scaling, I suggest that 6—18 Mt yr^{-1} CO_2 flux can be accounted for by magmatic extension, which implies an important role for volatile-enriched lithosphere, crustal assimilation and/or additional magmatic intrusion to account for the upper range of flux estimates.

High-resolution digital elevation models (DEMs) generated from remote sensing data enable comparison of the geomorphology and structure of large and inaccessible volcanoes. I present new topographic data for three peralkaline volcanoes in the MER (Fentale, Corbetti and Gedemsa) and one volcano in the Afar Rift (Dabbahu), combined with field observations, reveal previously unidentified post-caldera deposits and craters. Vent and crater locations are aligned with rift-parallel faults and also with rift-cutting structures in a variety of orientations. Caldera shape is controlled by interaction with these structures. The relative frequency and type of eruption varies greatly between these volcanoes over the past 150 kyr. Gedemsa is now largely inactive; Fentale hosts deposits from many small volume eruptions (< 0.1 km^3) while Corbetti has produced several large eruptions (~0.4–0.5 km^3). Morphometry of peralkaline rhyolite deposits at Corbetti and Fentale, including ogives and levees, provides constraints on rheology. Emplacement viscosities of ~10^8–10^{11} Pa s at Fentale are similar to or lower than calc-alkaline rhyolites and consistent with experimental and theoretical studies.

Distributed volcanic fields of scoria cones, maars, tuff cones and lava flows represent a crucial expression of the interplay between magmatism, tectonics and surface processes in continental rifts. I compare two such fields (Butajira and East Ziway) in the MER using high-resolution DEMs, linking the morphology of cones and maars to processes and age of emplacement. Volumes of individual cones are similar in both fields (mean ~ 4×10^6 m^3) and lower than other distributed volcanic fields found in extensional environments. Volcanism at Butajira has created linear clusters of superimposed cones, suggesting a small number of larger (10^7–10^8 m^3) fissure eruptions compared to the isolated events at East Ziway and lower confining stresses during emplacement. Dikes at Butajira may have been deflected by topographic unloading, whilst at East Ziway close proximity of cones and faults suggests dike capture. The presence of maars and deep craters within cones at Butajira indicates phreatomagmatic activity, not seen at East Ziway where cones may have been emplaced during a dry climate phase. Shape parameters, including curvature of cone rims and ratios of cone height, width and crater depth, suggest younger eruption ages at Butajira compared to East Ziway and the possibility of ongoing activity in this area. A broader survey of cone fields across the MER using the ASTER global digital elevation model fails to identify such systematic variation in cone morphology, limited by low-resolution.

The results from CO_2 surveys, geological fieldwork and DEM analysis presented in this thesis have significant implications for hazard assessment in the Ethiopian rift, and highlight the importance of structural features in controlling the location, magnitude and style of both degassing and volcanic activity in the MER.

Acknowledgements

There are many people I would like to thank for their help and support over the last four years. I am grateful for my supervisors, Tamsin Mather and David Pyle, particularly for their rapid reading, editing and commenting on manuscripts, and their warm encouragement along the way, which was a real help. Helpful feedback on papers and presentations, and discussions about ongoing work, were much appreciated from colleagues and collaborators, including Karen Fontijn, Will Hutchison, Tyrone Rooney, Peter Barry, Seifu Kebede, Juliet Biggs, and Alison Rust. Karen deserves much thanks for fieldwork logistics, as does Gezahegn Yirgu. Thank you to my companions across my three field campaigns, particularly Kathy Whaler, Julianne Hübert and Derek Keir who were very patient and generous with their time on my first trip to Ethiopia. Working with Ethiopian students and academics was a highlight of the DPhil; particular thanks go to Amde Zafu Tadesse and Abbate Assen. I am thankful for friendships with other Riftvolc PhD students: Ben Clarke and Fiona Iddon among others.

Outside of work, I am very thankful for some key friendships that have helped me through the good and bad of postgrad life. The love and prayers of Daniel Timms and Jonny Payne have been so valuable. Regular breakfasts, coffee breaks and lunches with Tim Crothers, Jonathan Mannouch, Ollie Bartlett and Jon Chan helped me run the race. St Ebbe's Church has been a wonderful family over many years, and I remain so thankful to them all, especially the Thesis community.

The love and support of Alice Fox has been a great blessing and I look forward to many years ahead with her. I am indebted to my family, as ever, for their love and wisdom. Particular thanks go to my Mum, who is a constant inspiration and I am glad to have shared this experience with her. Ultimately, my greatest thanks and praise goes to the Lord Jesus Christ, who is my rock and refuge, my shepherd and king: for his glorious creation, and his gracious re-creation.

> May the glory of the LORD endure forever;
> may the LORD rejoice in his works –
> he who looks at the earth, and it trembles,
> who touches the mountains, and they smoke.
>
> Psalm 104:31-32

Funding

Funding for this works was provided by a studentship grant from the NERC Doctoral Training Programme (DTP) in Environmental Research (NE/L002612/1). Funding for Pleiades imagery was provided by a grant from COMET (NERC Centre for the Observation and Modelling of Earthquakes, Volcanoes and Tectonics). Additional funding for field work was provided by the NERC-funded RiftVolc project (NE/L013932/1, Rift volcanism: past, present, and future) to which this thesis is a contribution, and by Hotspur Geothermal in a collaboration with industry.

For the work in Chapter 3, airborne lidar data for Corbetti were collected during the NERC Airborne Research and Survey Facility (ARSF) campaign ET12-17, and initial processing was carried out by NERC ARSF Data Analysis Node. Airborne lidar data for Dabbahu were also acquired by the NERC ARSF and processed at the University of Leeds as part of the Afar Rift Consortium (NE/E007414/1).

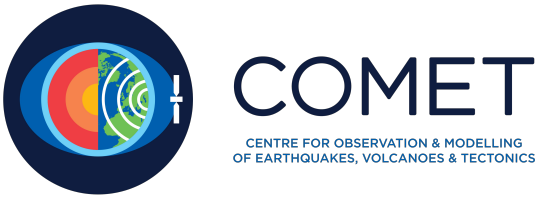

Contents

List of tables and figures

1 Introduction and aims

1.1 Continental rifts

Understanding continental rifting is a key piece of the puzzle in the plate tectonic jigsaw, creating new tectonic boundaries and forming a variety of structures and volcanic features in the process. The architecture of continental rift systems varies widely, from broad zones of extension up to 900 km across (e.g., Basin and Range, USA), to narrow rifts less than 70 km wide (e.g., the East African Rift System and the Baikal Rift). In narrow rifts, crustal deformation forms basins bounded by large border faults above a restricted zone of ductile extension in the lithospheric mantle (**Figure 1.1**).

Continental rifting may promote adiabatic decompression and melting of the underlying mantle, augmented in some settings by contributions from elevated mantle potential temperatures and/or elevated mantle volatile contents [e.g., due to mantle plumes, *White and McKenzie*, 1989; *Furman et al.*, 2006; *Rooney et al.*, 2012; *Ferguson et al.*, 2013], and melting of fusible sub-continental lithospheric mantle [e.g., *Rooney et al.*, 2005]. Magmatic intrusion promotes extension in continental rifts by accommodating strain at low yield stresses, and by thermally weakening the thinning lithosphere [e.g., *Buck et al.*, 2004; *Bialas et al.*, 2010; *Daniels et al.*, 2014].

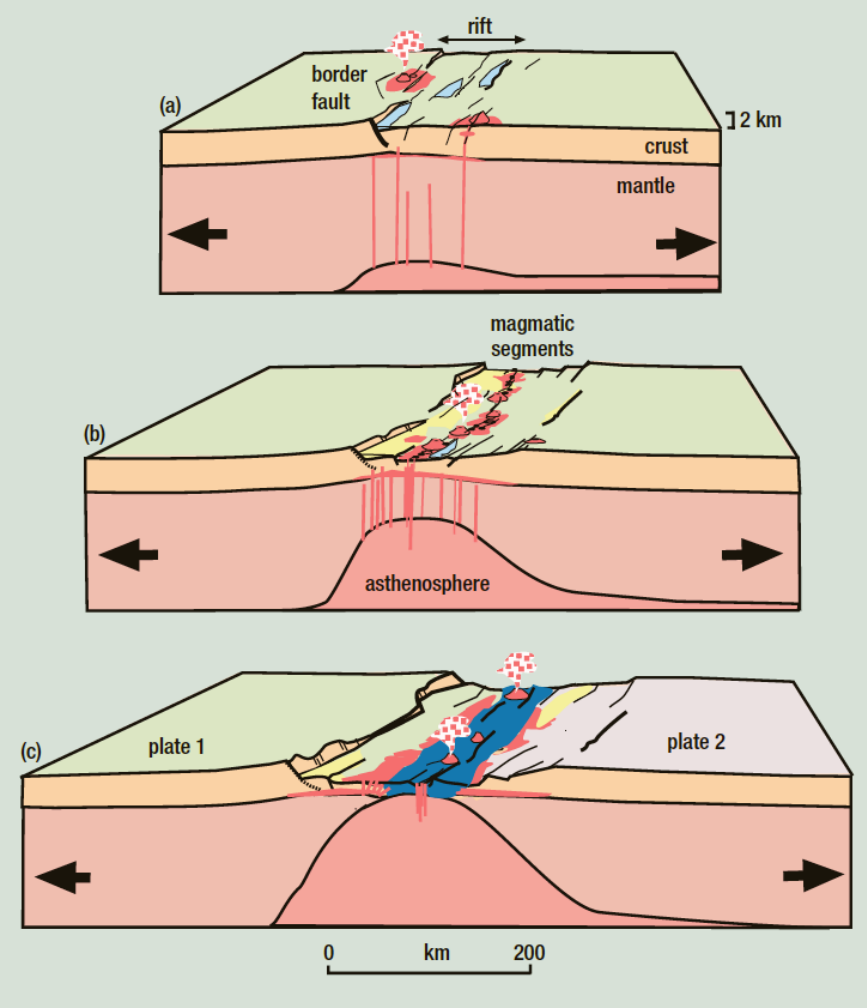

Figure 1.1. Three-stage rifting process, from Ebinger (2005). (a) Brittle deformation in the crust by slip along large border faults forming asymmetric basins. (b) Lithospheric thinning leads to decompression melting, and melt rises through heated and weakened lithosphere. Strain localisation creates a narrow zone of intrusions and extension. (c) Lithospheric rupture as rift proceeds into seafloor spreading.

As rifting progresses, the concentration of strain towards the centre of the rift is enabled by the locations of intrusions, with magma accommodating an increasing proportion of extension [e.g., *Keir et al.*, 2006; *Rooney et al.*, 2011]. Geophysical

observations of rifting events at mature rifts suggest that the majority of extension is accommodated by dike intrusion [e.g., *Wright et al.*, 2012]. The co-location of magmatism and faulting is also associated with the release of volatiles [*Muirhead et al.*, 2016a] – magmatism supports extension and faulting which is assisted by volatile release, and the increased faulting opens pathways for volatile transport.

Further weakening of the lithosphere by repeated intrusions leads to a final stage of lithospheric stretching before the onset of sea-floor spreading [*Bastow and Keir*, 2011]. There is much interest in the development of characteristic structures of sea-floor spreading and rifted margins during continental rifting, such as segmentation [e.g., *Haywood and Ebinger*, 1996; *Ebinger and Casey*, 2001] and seaward dipping reflectors [SDRs; e.g., *Corti et al.*, 2015].

1.2 The Main Ethiopian Rift (MER)

The East African Rift System (EARS) is the clearest example of continental rifting in the present day. The EARS is formed by a series of discrete and diachronous sections running from the Red Sea Rift (RSR) and Gulf of Aden Rift (GoAR) in the north, on the coastline of Eritrea and Djibouti, to the Malawi Rift in the south. The EARS splits into the Eastern Branch and the Western Branch south of Ethiopia, either side of the Tanzanian craton [**Figure 1.2, inset**; e.g., *Saria et al.*, 2014].

The northernmost branch of the EARS is the Main Ethiopian Rift (MER), which extends from the Afar triple junction, where it meets the RSR and GoAR, to the Turkana depression in northern Kenya [e.g., *Wolfenden et al.*, 2004]. The rifting of Arabia away from Africa and the opening of the RSR and GoAR began at ~31–30

Ma, accompanied by flood basaltic magmatism across the uplifted Ethiopian-Yemen plateau as a result of the Afar mantle plume [*Wolfenden et al.*, 2005].

Tectonic extension in the southern MER towards Lake Turkana may have commenced as early as ~18 Ma [*WoldeGabriel et al.*, 1990], whilst the northern MER (~8.5–9.5°) did not begin rifting until ~11 Ma [*Wolfenden et al.*, 2004]. Extension in the central MER (~7.5–8.5°) followed, and was established by ~6–9 Ma [*WoldeGabriel et al.*, 1990].

1.2.1 Rift structures and tectonics

Continental rifting in the MER developed in two phases. Initial mechanical extension in the MER was accommodated by displacement along large border faults, which formed asymmetric basins and diffuse magmatism [e.g., *WoldeGabriel et al.*, 1990; *Corti*, 2009]. The second phase of extension started at ~ 2 Ma with the formation of en echelon magmatic segments and a series of oblique normal faults trending NNE-SSW [e.g., *Ebinger and Casey*, 2001].

In the central MER (CMER), there are two parallel fault zones (Figure 1.2); the Silti-Debre Zeyit Fault Zone (SDFZ) on the western margin of the rift has a lower fault density than the Wonji Fault Belt (WFB) on the eastern margin. The WFB in the northern MER (NMER) acts as an axial spreading centre and the SDFZ is not present in what is deemed a more mature rift structure [*Agostini et al.*, 2011; *WoldeGabriel et al.*, 1990]. Present-day seismic activity is mostly located within the Quaternary fault zones, except for the Ankober border fault at the transition between the MER and the Afar region [*Keir et al.*, 2006].

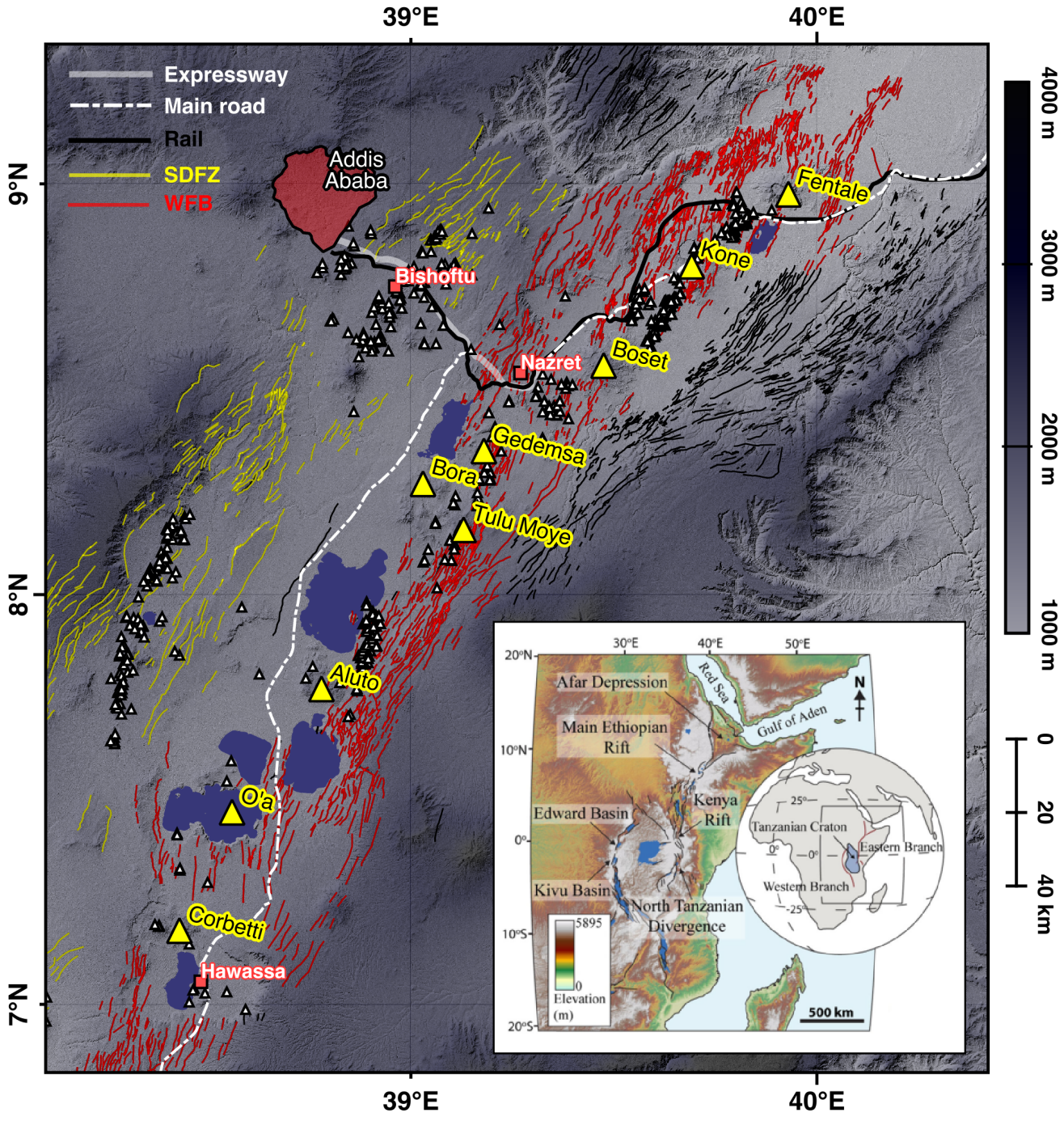

Figure 1.2. Map of the Main Ethiopian Rift with key features labelled – yellow triangles = silicic volcanoes; white triangles = scoria cones; red squares = towns/cities with population > 100,000. SDFZ = Silti-Debre Zeyit Fault Zone; WFB = Wonji Fault Belt. Inset – map of the East African Rift System from *Muirhead et al.* [2015].

The magmatic segments are underlain by elongated areas of high seismic velocities in the mid-crust, interpreted as cooled mafic intrusions [*Keranen et al.*, 2004; *Daly et al.*, 2008]. Low shear wave velocities are found beneath both the SDFZ and WFB, indicative of partial melt [*Kim et al.*, 2012].

Cross-rift structures are prevalent in the MER [e.g., *Korme et al.*, 2004]. E-W structures particularly visible on the rift flanks were likely formed by early tectonics relating to the RSR and GoAR in the Miocene [e.g., *Acocella et al.*, 2002; *Abebe et al.*, 2007]. Two major fault systems trending approximately E-W impinge on the MER – the Yerer-Tullu Wellel Volcano Tectonic Lineament (YTVL) at ~8.5–9.0° and the Goba-Bonga Volcano Tectonic Lineament (GBVL) at ~7.0–7.5° [e.g., *Abebe et al.*, 1998; *Corti et al.*, 2018a].

1.2.2 Rift volcanism and degassing

Surface magmatism in the MER takes two distinct forms – that of large silicic volcanoes and that of distributed mafic cones [**Figure 1.2**; e.g. *Abebe et al.*, 2007]. Each silicic centre has produced a combination of peralkaline rhyolites and alkali basalts with little intermediate magma in between [the so-called "Daly Gap"; **Figure 1.3**; *Peccerillo et al.*, 2003, 2007; *Giordano et al.*, 2014]. Peralkaline rhyolites are mainly pantelleritic [**Figure 1.3**; Hutchison *et al.*, 2018].

Many of the silicic volcanoes have undergone caldera collapse, producing calderas of 5–15 km in diameter [e.g., *Acocella et al.*, 2002; *Fontijn et al.*, 2018]. Several caldera-forming eruptions occurred in a flare-up between 320 and 170 ka [*Mohr et al.*, 1980; *Hutchison et al.*, 2016a]. Most volcanoes are now considered to be in a

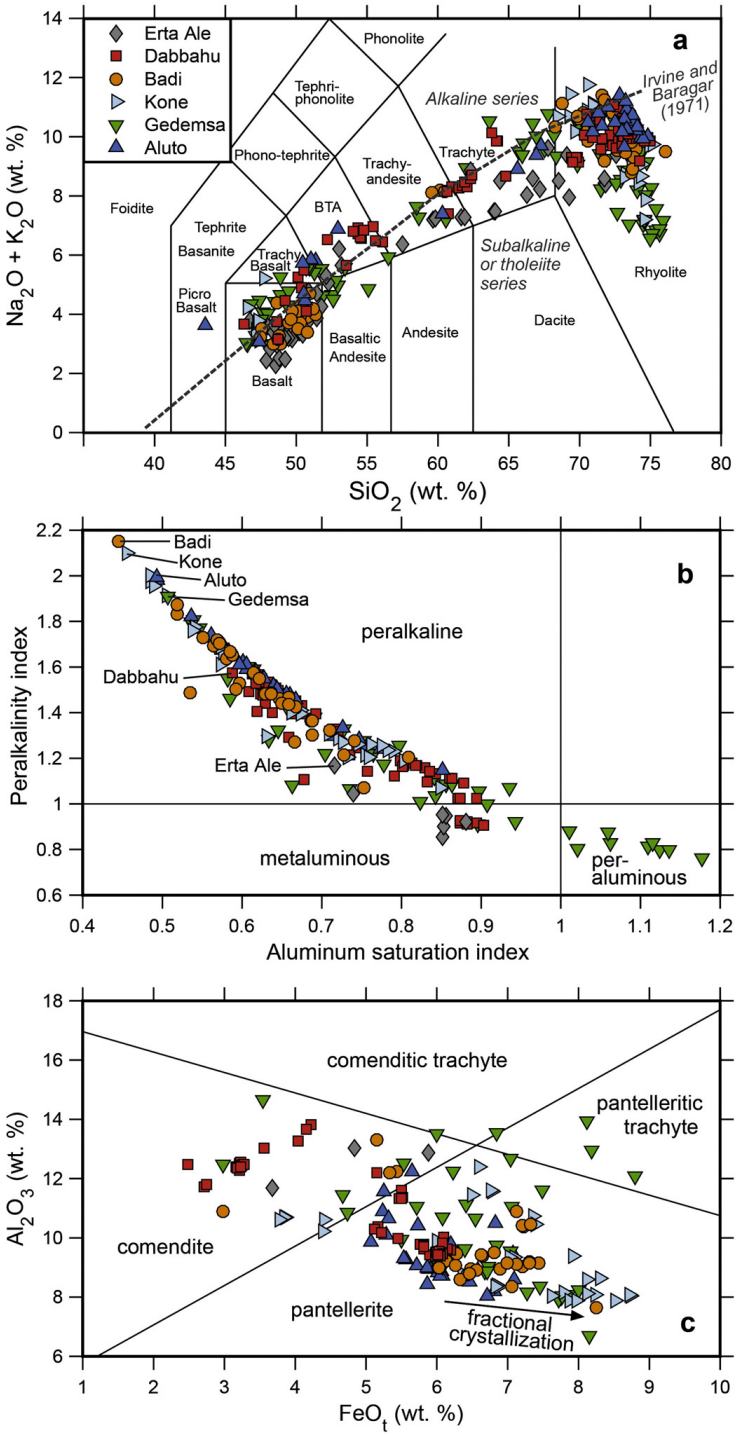

Figure 1.3. (a) Total Alkali–Silica (TAS) plot, (b) Peralkalinity Index (PI) vs Aluminium Saturation Index (ASI) plot, and (c) Al_2O_3 vs FeO_t classification grid for volcanic rocks from various Ethiopian volcanoes, from Hutchison *et al*. (2018). PI is defined as molar (Na_2O + K_2O)/Al_2O_3; ASI is defined as molar Al_2O_3/(CaO + K_2O + Na_2O).

post-caldera phase [Figure 1.4; Hutchison *et al.*, 2016a], a stage in which many centres have erupted obsidian flows, domes and pumice cones [e.g., *Fontijn et al.*, 2018]. There is a range of frequency and magnitude of events at each volcano [*Fontijn et al.*, 2018]. Evidence for multiple, large explosive eruptions has been found for a number of the centres, most notably Corbetti, Aluto and Bora [*Hutchison et al.*, 2016b; *Martin-Jones et al.*, 2017; *McNamara et al.*, 2018; *Fontijn et al.*, 2018].

Distributed mafic cone fields occur within the WFB and SDFZ all the way along the rift (Figure 1.2). Cone locations show a close relationship with faults, such that a genetic link has been posited [*Mazzarini et al.*, 2013a]. Studies using spatial statistics and geochemistry suggest that SDFZ cones are fed by dikes originating from deeper in the crust than WFB cones, from a fractionating magma system spread widely throughout the mid-lower crust [*Mazzarini et al.*, 2013b; *Rooney et al.*, 2011].

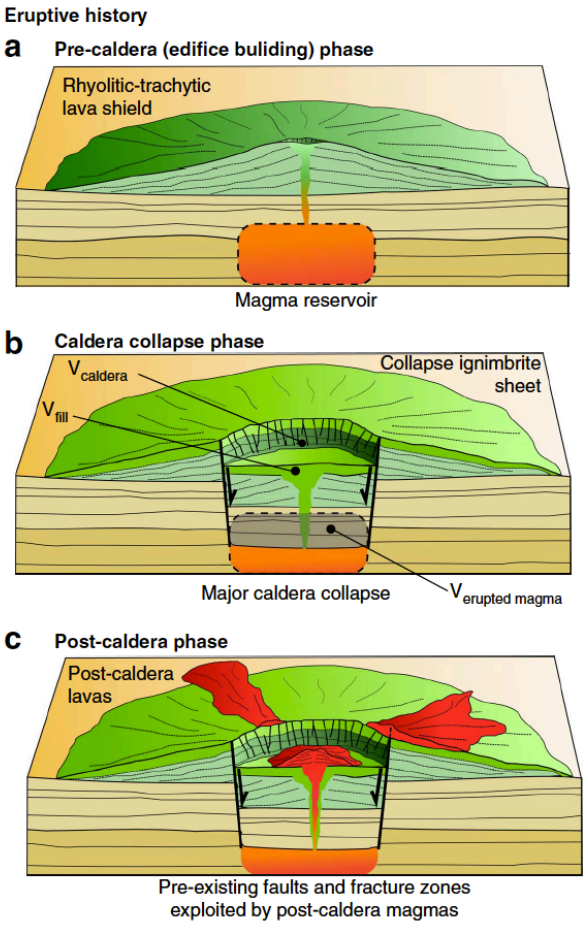

Figure 1.4. Simplified evolutionary history of MER volcanoes, from *Hutchison et al*. [2016a].

Volcanism in the MER is accompanied by prevalent geothermal activity [e.g., *Purschel et al.*, 2013]. Fault-controlled degassing at Aluto volcano, historically inactive but in a present state of unrest, emits ~90–180 kt yr^{-1} diffuse CO_2 [*Hutchison et al.*, 2015]. A review of the long-term carbon cycle highlighted historically inactive volcanoes and tectonic structures as a largely-unconstrained but significant category [*Burton et al.*, 2013], and studies of diffuse CO_2 degassing in the Kenya Rift Valley indicate a potentially vast contribution from continental rifts [*Lee et al.*, 2016].

1.2.3 Human geography

The volcanic record is particularly poorly known in Ethiopia, which leads to considerable uncertainty over the current levels of volcanic risk in the region. A recent survey suggests that more than 9 million people live within 30 km of a volcano in Ethiopia, with 40 out of 65 volcanoes classed within the highest uncertainty level (in terms of known eruption history) and 0 volcanoes monitored at time of writing [**Figure 1.5**, *Aspinall et al.*, 2011]. Within the past decade, four volcanoes have shown unrest as detected by InSAR [Aluto, Corbetti, Bora, Haledebi; *Biggs et al.*, 2011], and many are associated with ongoing geothermal activity [e.g., *Hutchison et al*., 2015].

Eruptions from three MER volcanoes are thought to have occurred in historical times: Fentale and Kone (ca. 1810), and Tulu Moye (ca. 1900) [*Wadge et al.*, 2016; *Fontijn et al.*, 2018]. Volcanoes in the Afar region have been more active – the 2011 eruption of Nabro volcano caused 32 deaths, displaced >5000 people, disrupted regional aviation and provided the largest injection of sulphur into the atmosphere since the eruption of Mount Pinatubo in 1991 [e.g., *Donovan et al.*, 2018]. A similar eruption in the Main Ethiopian Rift could have devastating impacts.

A number of geothermal areas are present in the rift, providing benefits to the local population (e.g., hot spring resorts) in addition to a variety of hazards. Dental fluorosis is common in the rift due to high fluoride concentrations in drinking water, attributed to high rates of degassing from acid volcanic geothermal systems [*Gizaw*, 1996].

Geothermal energy is an effective and clean resource, successfully exploited by volcanically-active countries such as Iceland and New Zealand. Despite the potential for great benefit, many of the geothermal resources in East Africa, most notably Kenya, have not been developed until recently [*Younger*, 2014]. Successive surveys along the Main Ethiopian Rift, spanning several decades, have consistently shown the rift's capacity to generate geothermal energy [e.g., *United Nations Development Programme*, 1973; *Haile Selassie*, 1984; *Purschel et al.*, 2013]. The geothermal industry is beginning to grow in Ethiopia: plans are in place to expand the power station at Aluto-Langano, a station at Corbetti is in development and prospecting is ongoing at Tulu Moye.

In addition to these power stations, there are a number of major infrastructure

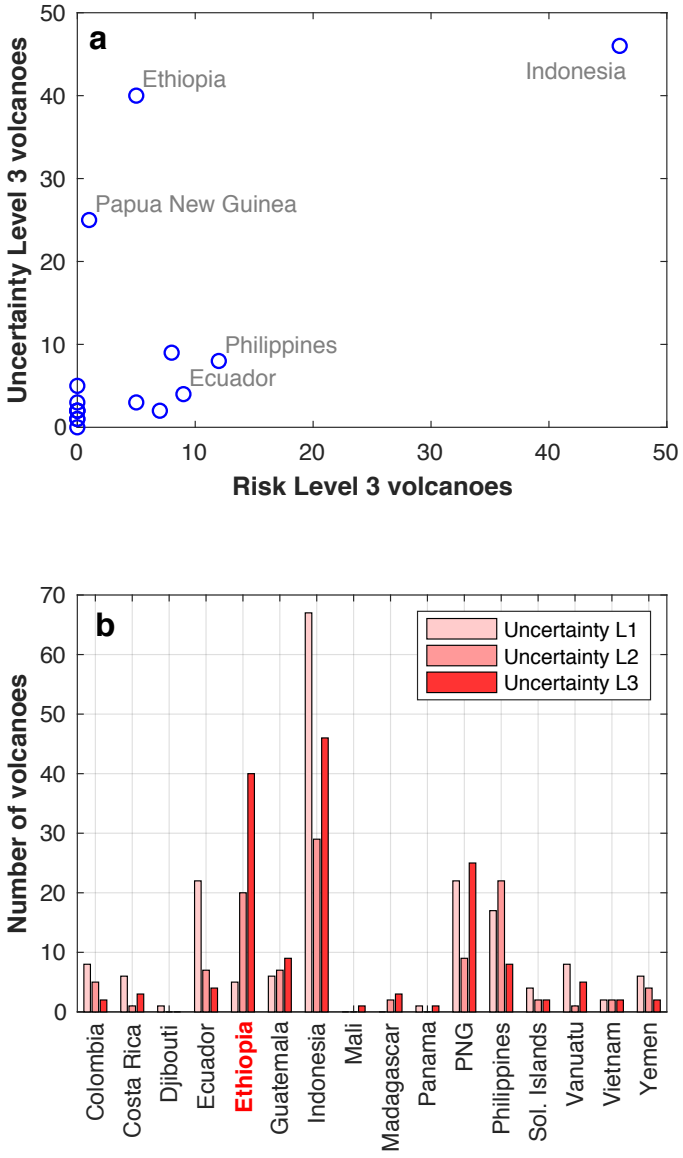

Figure 1.5. Numbers of volcanoes from GFDRR-priority countries in the Risk Level 3 and Uncertainty Level 3 categories, reproduced after Aspinall *et al.* (2011). Risk level is a combination of hazard level and probability exposure index (PEI) – hazard level is low for many Ethiopian volcanoes despite level of uncertainty. PNG = Papua New Guinea.

projects within the rift that are vulnerable to natural hazards. The city of Awassa (syn Hawassa), adjacent to Corbetti volcano (**Figure 1.2**) and the site of the 2016 Hawassa earthquake [*Wilks et al.*, 2017a], is rapidly developing into a tourist resort, with a new airport recently opened. Sections of the main road connecting Addis Ababa to Awassa are under reconstruction to create a new expressway, also connecting the Kenyan, Djiboutian and Eritrean borders. The new railway line from Addis Ababa to Djibouti, opened in 2018, runs along the flanks of Fentale volcano and round the shoreline of Lake Beseka, the lake levels of which have rapidly fluctuated in recent years (**Figure 1.2**).

1.2.4 Recent research projects

A number of large-scale research projects have been conducted on the Main Ethiopian Rift (MER) and the Afar triple-junction in recent years [*Vye-Brown et al.*, 2016]. The success of these projects has formed lasting collaborative partnerships between researchers in the UK, USA and Ethiopia.

The EAGLE project (Ethiopian Afar Geoscientific Lithospheric Experiment; 2003–2007) was a multi-phase geophysical survey of the northern MER and southern Afar region [*Maguire et al.*, 2003], encompassing seismic profiles of crustal structure [*Maguire et al.*, 2006], seismic tomography of upper mantle structure [*Bastow et al.*, 2005], seismicity [*Keir et al.*, 2006] and magnetotellurics [*Whaler and Hautot*, 2006].

The Afar Rift Consortium (ARC; 2007–2012) focussed on the Afar region, using a variety of geochemical [e.g., *Field et al.*, 2012; *Ferguson et al.*, 2013a], geophysical

[e.g., *Bastow et al.*, 2008; *Keir et al.*, 2009a, 2009b, 2011a, 2011b; *Rychert et al.*, 2012], geodetic [e.g., *Ferguson et al.*, 2010; *Wright et al.*, 2012] and geochronological techniques [e.g., *Ferguson et al.*, 2013b; *Field et al.*, 2013] in combination to investigate the mechanisms of magmatic rifting.

Building on these projects, the Riftvolc project started in September 2014 with the aim to investigate the unstudied volcanism and volcanic hazards of the central MER. The project includes researchers from the Universities of Edinburgh, Oxford, Bristol, Cambridge, Southampton, and Leeds, the British Geological Survey (BGS), Addis Ababa University and the Geological Society of Ethiopia (GSE). Project partners include Reykjavik Geothermal (and newly created Corbetti Geothermal) and Hotspur Geothermal (formerly Cluff Geothermal).

The researchers are from a range of disciplines, including geochemistry, petrology, geophysics, seismology and hazard analysis. Three work packages are designed to focus on the behaviour of volcanoes and their plumbing systems in the *past*, current activity and volcanic unrest in the *present*, and potential threats from volcanic activity in the *future*. This thesis represents a contribution towards all three work packages within the Riftvolc project.

1.3 Overview and aims of the thesis

The overarching goal of this thesis is to explore the interactions that volcanism and degassing have with crustal structure in the Main Ethiopian Rift. To do this, we have applied a range of methods including diffuse CO_2 surveys, field campaigns, remote sensing techniques, and morphometry, which all provide geospatial

information on the surface expression of volcanism and degassing, and its relationships with rift structure. We have focussed in depth on particular sites within the rift, making comparisons between sites both across and along the rift, and drawn out implications for our broader understanding of rift dynamics and rift volcanism.

The main themes of the thesis can therefore be categorised within three spatial scales as follows:

- **Local scale – specific sites of volcanism and degassing**

  How do crustal structures affect the location, magnitude and styles of degassing and volcanism at specific sites along the rift?

  What is the past/present behaviour of these specific geothermal/volcanic areas? What is the significance of this for hazard and geothermal energy?

- **Regional scale – across and along the Main Ethiopian Rift**

  What are the similarities and differences between study sites?

  What are the large scale patterns in the locations and sizes of geothermal and volcanic sites in the rift?

  How do degassing and volcanic activity, and their interactions with structure, change systematically along/across the rift, and with time?

- **Global scale – continental rifts worldwide**

  What lessons can be learnt from the Main Ethiopian Rift that can be applied to continental rifts in general?

  How significant is rift degassing and volcanism for the global system?

What are the key characteristics of rift volcanism, and how does it compare to volcanism in other tectonic environments?

These spatial scales are considered in each chapter of the thesis, which is structured as follows:

Chapter 2: Spatially variable CO_2 degassing and its implications. In this chapter, we present results from new surveys of diffuse CO_2 flux in four study sites across the Main Ethiopian Rift, and compile a database of hot springs and fumaroles from industry, government and academic reports. We discuss the variability of fault-controlled degassing on a range of scales, including the influence of rift structure, before scaling up for a rift-scale estimate of diffuse CO_2 emissions.

Chapter 3: Geomorphology and structure of peralkaline rift volcanoes. In this chapter, we use high-resolution digital elevation models (DEMs) in combination with a targeted field campaign to assess the structure and associated deposits of three volcanoes in the Main Ethiopian Rift. One volcano from Afar, Dabbahu, is included for comparison. A number of newly identified deposits are presented, and morphometry is used to estimate the emplacement rheology of peralkaline lava. We discuss similarities and differences between volcanic centres, including their relative eruption frequencies and the varying influences that rift-parallel and cross-rift structures have on eruption locations and caldera formation.

Chapter 4: Morphological comparison of distributed volcanic fields. In this chapter, we compare the morphology of two volcanic fields in the Main Ethiopian Rift using high-resolution DEMs, and use a global, low-resolution DEM to compare fields across the rift. For the two study areas, we identify and categorise

cones and maars in each field, and calculate their average volumes. Using morphometric analysis of regular cones, we investigate the relative ages of the two fields and the influence of hydrology and rift structure on cone/maar formation.

Chapter 5: Summary and conclusions. In this final chapter, I summarise the main findings of the thesis using the three spatial scales outlined above as a framework. I also provide suggestions for the directions of future work on continental rifts and the complex interactions between structure and the surface expression of magmatism.

2 Spatially variable CO_2 degassing and its implications

Abstract

Deep carbon emissions from historically inactive volcanoes, hydrothermal and tectonic structures are among the greatest unknowns in the long-term (~Myr) carbon cycle. Recent estimates of diffuse CO_2 flux from the Eastern Rift of the East African Rift System (EARS) suggest this could equal emissions from the entire mid-ocean ridge system. We report new CO_2 surveys from the Main Ethiopian Rift (MER, northernmost EARS), and reassess the rift-related CO_2 flux. Since degassing in the MER is concentrated in discrete areas of volcanic and off-edifice activity, characterisation of such areas is important for extrapolation to a rift-scale budget. Locations of hot springs and fumaroles along the rift show numerous geothermal areas away from volcanic edifices. With these new data we estimate total CO_2 emissions from the central and northern MER as 0.52—4.36 Mt yr^{-1}. Our extrapolated flux from the Eastern Rift is 3.9—32.7 Mt yr^{-1} CO_2, overlapping with lower end of the range presented in recent estimates. By scaling, we suggest that 6—18 Mt yr^{-1} CO_2 flux can be accounted for by magmatic extension, which implies an important role for volatile-enriched lithosphere, crustal assimilation and/or additional magmatic intrusion to account for the upper range of flux estimates. Our results also have implications for the nature of volcanism in the MER. Many geothermal areas are found >10 km from the nearest volcanic centre, suggesting ongoing hazards associated with regional volcanism.

A version of this chapter has been published as:

Hunt, J. A., A. Z. Tadesse, T. A. Mather, D. M. Pyle, and P. H. Barry (2017), Spatially Variable CO_2 Degassing in the Main Ethiopian Rift: Implications for Magma Storage, Volatile Transport, and Rift-Related Emissions. *Geochemistry, Geophysics, Geosystems*, *18*, 1–24, doi:10.1002/2017GC006975.

2.1. Introduction

Volcanic systems make a substantial contribution to the long-term release of volatile species from the mantle. There is significant interest in understanding the nature of the 'deep carbon' cycle, particularly that associated with the fluxes of magma out of the mantle [*Dasgupta*, 2013; *Kelemen and Manning*, 2015]; on long timescales (~Myr), carbon fluxes from the mantle have a major influence on the global carbon cycle and are an important mechanism in natural climate variability [*Dasgupta*, 2013]. However, there remain significant gaps in our knowledge of the deep carbon fluxes associated with magmatism, especially from magmas that end up stored within the lithosphere, rather than being erupted. In recent reviews of deep carbon emissions, *Burton et al.* [2013] and *Mörner and Etiope* [2002] highlight the dominance of long-term continuous, passive CO_2 degassing over that from short-lived eruptions. It is clearly important to quantify passive emissions if we are to better understand the global carbon cycle.

There is growing recognition that diffuse degassing represents a significant proportion of the total passive CO_2 flux at a number of volcanoes [e.g., Etna, *Allard et al.*, 1997; *D'Alessandro et al.,* 1997; Pantelleria, *Favara et al.*, 2001; Campi Flegrei, *Chiodini et al.*, 2001; Long Valley Caldera, *Lucic et al.*, 2015]. This is in part due to the low solubility of CO_2 in magmas, which means that it can degas at great depths within the Earth's crust and percolate out over a wider area than shallower emissions. CO_2 emissions from historically inactive volcanoes, hydrothermal and tectonic structures are a poorly constrained component of the global deep CO_2 budget [*Burton et al.*, 2013].

Diffuse carbon degassing from volcanic fields is challenging to quantify given their large areal extent, heterogeneous nature, and complex fluid flow regimes. The few existing surveys focus on a small number of restless calderas in Italy and Yellowstone, which may not be representative of calderas worldwide [*Chiodini et*

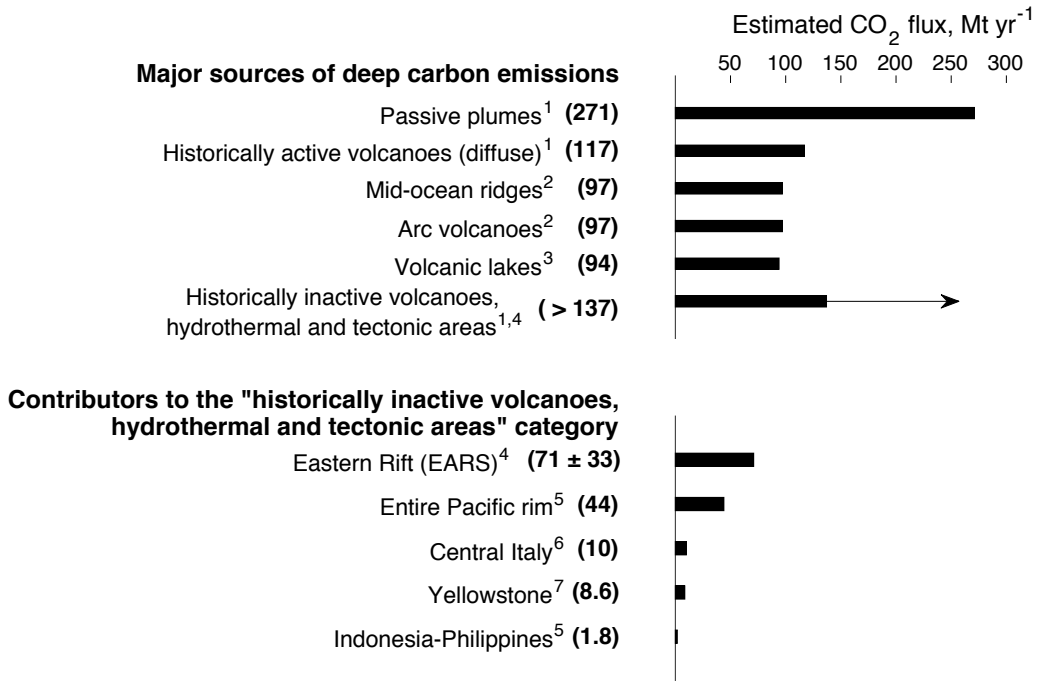

Figure 2.1. Deep CO_2 flux estimates compiled by *Burton et al.* [2013] and developed by *Lee et al.* [2016]. *Top:* Major contributors to the deep carbon budget. The lack of observations of emissions from historically inactive volcanoes, hydrothermal and tectonic areas prevents an estimate of an upper bound. *Bottom:* Major contributors from the 'historically inactive volcanoes, hydrothermal and tectonic structures' group, including the East African Rift [*Lee et al.* 2016]. The current EARS flux estimate exceeds early estimates for the entire Pacific rim (18,000 km of arc volcanoes). References: [1]*Burton et al.* [2013], [2]*Marty and Tolstikhin* [1998], [3]*Pérez et al.* [2011], [4]*Lee et al.* [2016], [5]*Seward and Kerrick* [1996], [6]*Chiodini et al.* [2004], [7]*Werner and Brantley* [2003].

al., 1999; *Chiodini and Frondini*, 2001; *Chiodini et al.*, 2004; *Chiodini et al.*, 2007; *Chiodini et al.*, 2010; *Etiope et al.*, 1999; *Giammanco et al.*, 2007; *Italiano et al.*, 2000; *Mörner and Etiope*, 2002; *Rogie et al.*, 2000; *Werner and Brantley*, 2003]. *Burton et al.* [2013] provide an estimate of global emissions from historically inactive volcanoes, hydrothermal and tectonic structures of > 66 Mt yr^{-1} CO_2; the current estimate rises to > 137 Mt yr^{-1} CO_2 when accounting for recent work on degassing from tectonic structures in East Africa [*Lee et al.*, 2016]. This estimate is largely derived from just four study areas [Central Italy, *Chiodini et al.*, 2004; Taupo Volcanic Zone, *Seward and Kerrick*, 1996; Yellowstone, *Werner and Brantley*, 2003; Kenya Rift Valley, *Lee et al.*, 2016] and depends heavily on extrapolation from emissions associated with the Taupo Volcanic Zone to the entire Pacific Rim [44 Mt yr^{-1}; *Seward and Kerrick*, 1996]. These estimates are compiled in **Figure 2.1**. The lack of representative surveys hinders our ability to determine an upper bound for global, deep degassing from tectonic structures, particularly given the occurrence of very high flux but spatially restricted areas [e.g., Mefite, Italy; *Chiodini et al.*, 2010]. It is likely that the contribution from Pacific Rim settings is larger than current estimates suggest, given the proportionately higher fluxes recorded in smaller regions.

Continental rifts may be an important contributor to deep, diffuse carbon fluxes. Elevated magmatic fluxes, and an abundance of faults and fractures along which CO_2 can migrate, provide both a source of carbon and mechanisms for release [**Figure 2.2**; *Hutchison et al.*, 2015; *Lee et al.*, 2016; *Muirhead et al.*, 2016a]. Melts generated in continental rift settings may be alkaline with elevated CO_2 contents,

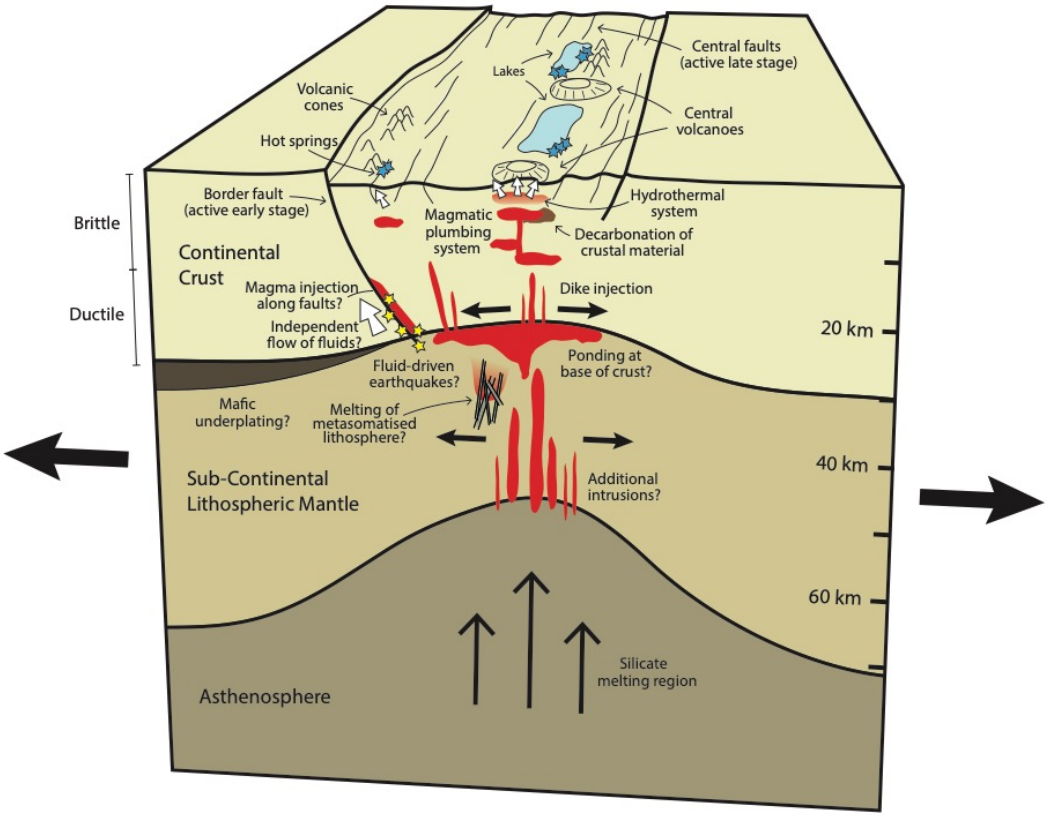

Figure 2.2. Paths for CO_2 degassing out of a continental rift. White arrows denote CO_2 fluid flow; blue stars, hot springs; yellow stars, deep earthquakes. CO_2 travels with the melt and independently along low permeability pathways.

whether due to an enriched and/or metasomatized source region, or conditions of partial of melting [e.g. *Ferguson et al.*, 2013a; *Hudgins et al.*, 2015]. CO_2 and other volatiles are carried into the lithosphere as the melt is intruded, enabling and accommodating extension. Intrusion and melting of metasomatised, volatile-enriched lithosphere may be an important process in rift development, transporting heat and fluids which weaken the surrounding material [*Rooney et al.*, 2005; 2014a; 2017]. Magma may pool and underplate or intrude the crust [e.g. *Plasman et al.*, 2017], and fluids may move independently to the surface if the permeability of the

local rocks is low. Permeability decreases with pressure and increases in fault damage zones; CO_2 therefore flows freely in the fractured, shallow crust [*Etiope and Martinelli*, 2002; *Faulkner et al.*, 2010]. The extent to which large faults may facilitate CO_2 flow in the deep crust is unclear, although some deep earthquakes have been interpreted as fluid-driven [e.g., *Reyners et al.*, 2007; *Keir et al.*, 2009a; *Albaric et al.*, 2014]. Magma may also intrude along these large faults, bringing CO_2 towards the surface [e.g., *Italiano et al.*, 2000].

Continental rifts vary in maturity, from large, fault-bounded basins [e.g. North Tanzanian Divergence; *Ebinger,* 2005] to incipient sea-floor spreading [e.g., Red Sea Rift; *Keranen and Klemperer*, 2008; *Wright et al.*, 2006]. Studying CO_2 emissions from continental rifts may help to constrain degassing from their potential successors, mid-ocean ridges (MORs), and refine estimates for modern-day and past geological CO_2 fluxes to the atmosphere. Quantifying the long-term carbon budget from the solid-earth is important for our understanding of long-term geological feedbacks, environmental change and mass extinction events [e.g., *Berner et al.*, 1983; *Wignall* 2001; *Self et al.*, 2006]. The location and magnitude of degassing from continental rifts may also prove useful for identifying areas of magma storage, assessing the relative activity of volcanic systems [e.g., *Evans et al.*, 2009] and investigating rift architecture with respect to fault activity [*Muirhead et al.*, 2016a]. The extent to which CO_2-rich fluids flow through faults is a key area of research, with implications for trapping and sealing CO_2 for storage [e.g., *Dockrill and Shipton*, 2010]. In extreme cases, CO_2 leakage from the subsurface

may result in the accumulation of lethal concentrations, presenting a hazard to life [*Hernandez Perez et al.*, 2003; *Chiodini et al.*, 2010; *Smets et al.*, 2010].

The largest continental rift on Earth is the East African Rift System (EARS), which cuts through the African continent and separates the Nubian and Somali plates. The system is sub-divided into a number of rifts, including the Main Ethiopian Rift (MER; from southern Afar to Lake Turkana) and the Kenya Rift Valley (KRV; from Lake Turkana to the North Tanzanian Divergence). A recent diffuse CO_2 survey in the southernmost KRV found that faults in the Natron and Magadi basins were responsible for ~4 Mt yr^{-1} CO_2 release, implying that large carbon emissions may be associated with deep degassing from tectonic structures [*Lee et al.*, 2016]. The estimate of mantle-derived, diffuse soil flux from the Natron region [1.09—3.83 Mt yr^{-1}; *Lee et al.*, 2016] is an order of magnitude higher than CO_2 flux estimates due to springs in the Natron region, based on carbon concentrations in fluids and discharge rates [0.022 Mt yr^{-1}; *Barry et al.*, 2013; 0.23 Mt yr^{-1}; *Lee et al.*, 2017]. This result suggests a strong partitioning of CO_2 transport towards diffuse degassing rather than via fluid advection.

By scaling up their results, *Lee et al.* [2016] suggested that the diffuse CO_2 contribution from the Eastern Rift of the EARS (comprising the MER and KRV) could be as much as 38—104 Mt yr^{-1}, comparable to the entire MOR system (**Figure 2.1**). As acknowledged by the authors, more work is required to investigate whether these findings apply to the rift system as a whole, or whether the basins are themselves anomalous. The crust in the KRV is considered to be thicker and older than elsewhere in the rift, with accordingly more potential for reworking and

assimilation of crustal carbon [*Lee et al.*, 2017]. Elevated CO_2 emissions have been recorded from the nearby carbonatite volcano of Oldoinyo Lengai [*Koepenick et al.* 1996; *Oppenheimer et al*., 2002]. Although this style of volcanism may reflect unusually high concentrations of mantle carbon, the volatile composition of Oldoinyo Lengai is indistinguishable from mid-ocean ridge volatiles [*Fischer et al.* 2009]. Consequently, high concentrations of carbon in Lengai lavas may be the result of immiscibility rather than compositional differences in the crust or mantle [e.g. *Dawson et al.*, 1996].

The isotopic composition of the sampled CO_2 from the Magadi and Natron basins (–3.8 to –11.7‰) overlaps with the composition of both air (–8‰), and mantle sources (–3 to –8‰). *Lee et al.* [2016] interpret these data as requiring a significant mantle contribution, however an alternative interpretation of the isotope data would suggest an admixture between air-derived, biogenic, and mantle contributions and thus a potentially smaller mantle-derived CO_2 contribution. Extrapolation of the elevated CO_2 fluxes from the Magadi and Natron basins to the entire Eastern Rift suggests that the rift-scale deep carbon flux may be significantly higher than previously thought [*Lee et al.*, 2016]. Their conclusions imply an elevated flux of mantle-derived CO_2 per unit length of rift compared to MORs (3000 km versus 60,000 km). This hypothesis has important implications for both the magmatic flux to the rift, and the mantle carbon contents required to sustain degassing.

Surveys elsewhere in the EARS suggest that the nature of carbon degassing varies substantially between localities and between volcanoes, and that point source fluxes may vary widely. For example, the CO_2 flux from individual rift volcanoes varies

by more than two orders of magnitude [Aluto, 90—180 kt yr^{-1}; *Hutchison et al.*, 2015; Longonot, 0.1 kt yr^{-1}; *Robertson et al.*, 2016]. The challenge in a rift system that exhibits diverse degassing styles and fluxes across a range of length-scales is to integrate the available data to estimate the deep carbon flux to the surface.

Here, we report new observations from field surveys, compile areas of geothermal manifestations and characterise the distribution of areas of high carbon flux in the Main Ethiopian Rift (MER). We develop an alternative estimate for rift-scale, diffuse CO_2 flux, based on localised areas of strong degassing.

2.1.1. Regional context

The MER started to develop in the Oligocene with the emplacement of continental flood basalts [*WoldeGabriel et al.*, 1990] and progressed from initial mechanical extension on large border faults to focussed strain accommodation within central magmatic segments [*Abebe et al.*, 2007; *Ebinger and Casey*, 2001]. Magmatic intrusion promotes extension in continental rifts, weakening the lithosphere [e.g., *Buck et al.*, 2004]. As rifting progresses, the concentration of strain to the centre of the rift is enabled by the location of magmatism, with magmatic intrusion accommodating an increasing proportion of extension [e.g., *Keir et al.*, 2006; *Rooney et al.*, 2011]. This leads to co-location of magmatism and faulting on the surface and associated gas release [*Muirhead et al.*, 2016a] – magmatism supports extension and faulting which is assisted by volatile release, and the increased faulting enables an increase in volatile transport.

Surface magmatism in the MER takes two distinct forms: large silicic volcanoes and distributed mafic cones [e.g., *Abebe et al.*, 2007]. In the central MER, two parallel zones with high fault and cone density run approximately NNE-SSW; the Silti-Debre Zeyit Fault Zone (SDFZ) on the western margin of the rift has a lower fault density than the Wonji Fault Belt (WFB) on the eastern margin. In the more-mature northern MER, the WFB acts as an axial spreading centre and the SDFZ is absent [*Agostini et al.*, 2011; *WoldeGabriel et al.*, 1990].

The present-day locations of magma storage within the MER is the subject of active research. Previous magmatic intrusion along segments of the rift is indicated by seismic imaging [e.g. *Keranen et al.*, 2004; *Keir et al.*, 2015], and upper mantle seismic structure indicates the presence of partial melt beneath the MER [*Bastow et al.*, 2008; *Gallacher et al.*, 2016]. Several of the volcanoes of the MER are deforming [*Biggs et al.*, 2011]; deformation is in some cases associated with geothermal activity [e.g., Aluto, *Hutchison et al.*, 2015]. Seismicity beneath Aluto volcano is consistent with the presence of a deep (> 9 km) magmatic mush zone [*Wilks et al.*, 2017b], though a magnetotelluric study suggests that deep magma may be stored 40 km to the west, beneath the Silti-Debre Zeyit Fault Zone and related monogenetic cone field [*Samrock et al.*, 2015].

Hutchison et al. [2015] found a strong structural control on CO_2 degassing on Aluto, with elevated fluxes associated both with a cross-cutting regional fault (>>100 g m^{-2} d^{-1}) and the buried caldera rim. CO_2 isotopic values ($\delta^{13}C$ up to -2.5‰ in high flux locations) and their distribution when plotted against the reciprocal of CO_2 concentration that defines a triangular array between magmatic (–3 to –8‰),

atmospheric (–8‰) and biogenic (–20 to –25‰) end members suggest that these strong degassing signals likely contain a significant contribution from mantle sources [*Hutchison et al.*, 2016c and references therein]. To date, no other CO_2 flux measurements from the MER have been published.

2.2. Methodology

2.2.1. Target areas for soil CO_2 surveys

We targeted localities along the MER for new soil CO_2 surveys, on the basis of proximity to known geothermal sites, to extend our understanding of the links between geothermal activity and diffuse CO_2 flux. An area between the towns of Adama and Sodere (**Figure 2.3f**) was surveyed with a sparse (1 km) grid designed to determine the background flux in the centre of the rift. The region typifies the central rift, with normal faults (~50 m throw) and an old, buried caldera rim.

The Butajira fault zone (**Figure 2.3b**) lies to the east of the towns of Butajira and Silte and encompasses those of Koshe and Tora. Monogenetic cones form a line along the western side of the fault zone and extend further south than most of the faults. The largest faults (80—150 m throw) form a graben west of the Tora-Koshe-Dugda ridge, which reportedly contains a number of hot springs [*MOWR*, 2008].

The Aluto-Langano geothermal field (**Figure 2.3c**) is an established resource with active drilling sites. *Hutchison et al.* [2015, 2016c] showed that the diffuse CO_2 flux here is both substantial and fault-concentrated. We extend this survey to the nearby Aluto-Wonji rift flank, which forms part of the Wonji Fault Belt (WFB).

The faults form a cascading series of scarps with average trends of ~NNE, commonly segmented and offset by ~NNW trending features. An area of high cone density lies to the northeast of Aluto volcano and to the north of our study area. The Aluto edifice itself is a low-relief, pre-caldera shield volcano with post-caldera

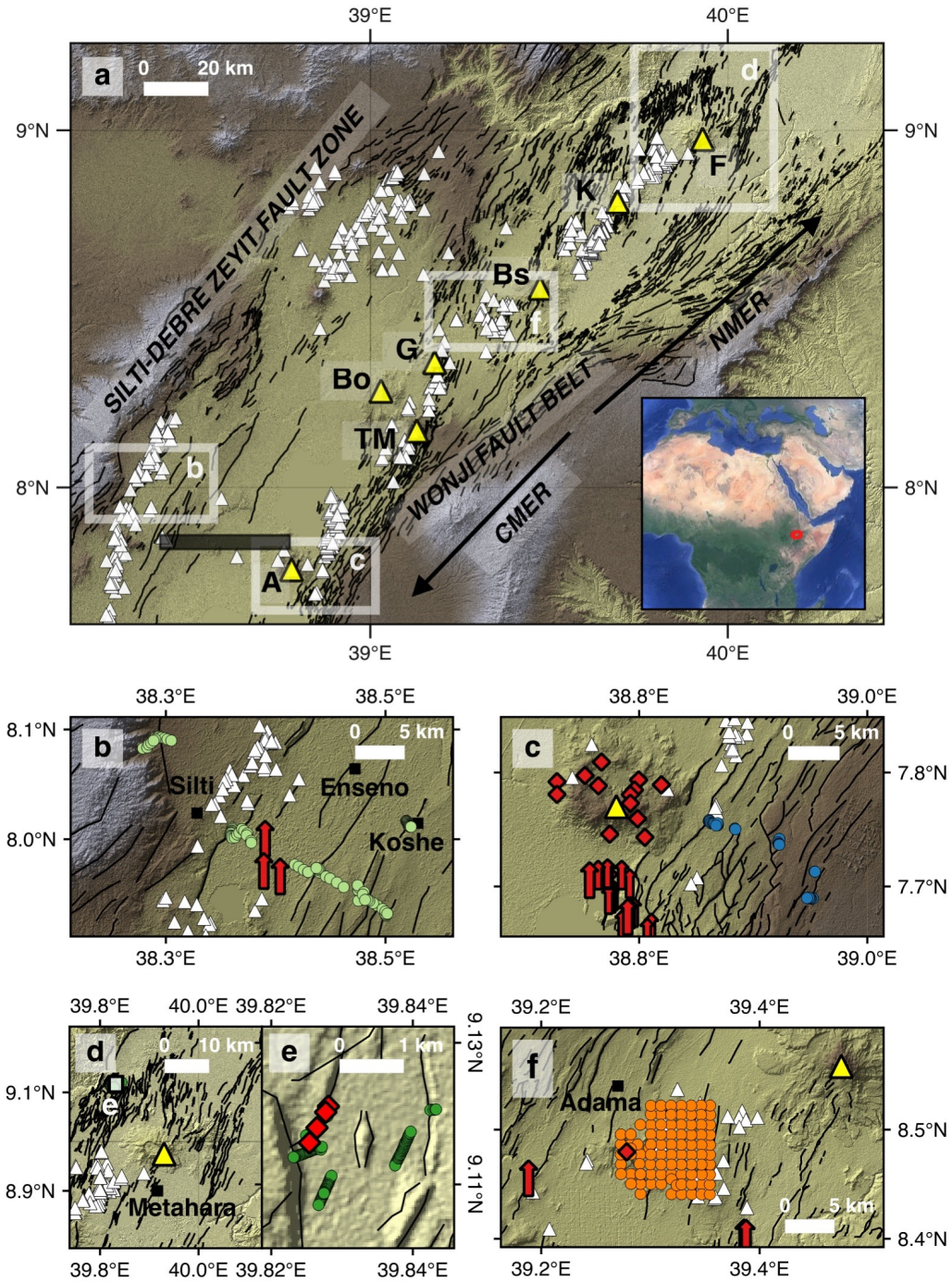

deposits located around the caldera rim and along fault zones [*Hutchison et al.*, 2015, 2016a]. Large volume ignimbrites, possibly from the caldera-forming event(s), have been dated at 306—316 ka, with post-caldera activity (obsidian, pumice and pyroclastic deposits) occurring between 0 and 60 ka [*Hutchison et al.*, 2016a].

Fentale volcano (alternative spellings: Fantale, Fanta 'Ale) sits at the northernmost end of the rift valley (**Figure 2.3d**), as it broadens out into the Afar depression. There are numerous geothermal manifestations both inside the summit caldera and ~15 km to the north [*Bekele et al.*, 2007] – our targeted survey covers Habilo to the NW of the edifice (**Figure 2.3e**). Fentale's most recent eruption, in the 19th century, resulted in a basaltic lava flow on its southern flank [*Gibson*, 1974]. The vents of the basaltic eruptions align with a trend of ~NNE, possibly suggesting regional,

Figure 2.3. (a) Map of the central and northern Main Ethiopian Rift (CMER and NMER respectively): volcanic cones, white triangles; silicic volcanoes, yellow triangles (A - Aluto, Bo - Bora, Bs - Boset, C - Corbetti, D - Dofen, F - Fentale, G - Gedemsa, K - Kone, TM - Tulu Moye); black lines delineate faults from the *Agostini et al.* [2011] database maintained by Giacomo Corti (http://ethiopianrift.igg.cnr.it/corti.htm); elevation from the ASTER GDEM (product of METI and NASA). Semi-transparent black bar shows 40 km west of Aluto volcano; approximate location of the conductor identified by *Samrock et al.* [2015]. Inset: location within East Africa from Google Earth image. (b)-(f) More detailed location maps as indicated in (a) of the four survey areas: (b) Butajira, (c) Wonji Fault Belt (WFB) east of Aluto (hereafter Aluto-Wonji), (d)-(e) Fentale and Habilo maps – (e) which is a detail of (d) as indicated, (f) Sodere. Measurement points, filled circles; known hot spring and fumarole locations, red arrows and diamonds respectively [sources: *Braddock et al.*, 2017; *MOWR*, 2008; *GSE and UN*, 1976; *Purschel et al.*, 2013; see Tables A1.1 and A1.2].

rather than edifice-related, volcanism also indicated by cones to the southwest and north of the edifice.

2.2.2. Measurement strategy and accumulation chamber method

Measurements were made by the accumulation chamber method [*Chiodini et al.*, 1998], with a PP Systems EGM-4 Environmental Gas Analyzer for CO_2 and an SRC-1 Soil Respiration Chamber and soil collar (see Supplementary Information). Three campaigns were conducted, each designed with a different aim: (1) the goal of the Sodere campaign was to quantify background flux in the central rift (**Figure 2.3f**); (2) the cross-rift, central MER campaign was designed to find and assess areas of elevated CO_2 flux in the regions of Butajira (**Figure 2.3b**) and Aluto-Wonji (**Figure 2.3c**); and (3) the Habilo campaign was designed as a more focused study on one degassing area (**Figure 2.3d-e**). In the latter two surveys, profiles were taken across faults to test the hypothesis that high permeability enhances CO_2 flow in such locations. The Habilo campaign afforded the opportunity to decrease the spacing between measurement points, yielding information about the width and flux of degassing at active sites. The influence of seasonal variability on soil gas is untested but expected to be significant due to changes in hydrology and biogenic activity [e.g. *Chiodini et al.*, 2007]. In the MER, the main rainy season is from July to September with a minor rainy season from April to May. The campaigns were conducted within the dry seasons. **Table 2.1** outlines the survey type, number of measurements and average spacing for each campaign.

Table 2.1. Overview of the three campaigns by survey strategy; Sodere (Figure 2.3f), CMER (Central Main Ethiopian Rift, Figure 2.3b-c), Habilo (Figure 2.3d-e).

Campaign	Date	Type	Approx. spacing	Number of measurements
Sodere	Jan–Feb 2016	Grid	800–1000 m	90
CMER (Butajira, Aluto-Wonji)	Jan–Feb 2016	Fault profiles†	20–1000 m	132
Habilo	June 2016	Fault profiles‡	10–20 m	247

†Reconnaissance fault profiles across the rift (see text).

‡Targeted fault profiles (see text).

Table 2.2. Results from the three campaigns. For breakdown by fault see Table A1.3. High flux values in Habilo and Butajira create a large positive skew in the data; standard deviation is therefore higher than the mean.

Area	Number of measurements	Mean flux, g m^{-2} d^{-1}	Standard deviation
Sodere	90	21.9	9.3
Butajira	88	28.7	34.7
Aluto-Wonji	44	10.6	6.4
Habilo	247	157.3†	401.3†

†Represents an underestimate – some values exceed measurement limit (2400 g m^{-2} d^{-1}).

2.2.3. Compilation of hot spring and fumarole locations

To constrain the frequency and distribution of degassing areas along the rift, and investigate the structures controlling CO_2 emission, we reviewed the locations of hot springs and fumaroles in the MER (Table A1.1).

A number of surveys have attempted to catalogue geothermally-active regions in the MER. The first of these was conducted by the United Nations Development Programme [*UNDP*, 1973], combining field work and a helicopter-borne infra-red survey across an area from Lake Abaya in the south to the Danakil Depression in the far north. Subsequent studies confirmed and extended this regional directory [e.g., *Haile Selassie*, 1984], whilst others have focussed on smaller areas of interest [e.g., *Bekele et al.* 2007]. Many of these reports represent research conducted by industry (e.g., Reykjavik Geothermal) or government departments (e.g., Geological Survey of Ethiopia/Ministry of Water and Resources, often in partnership with UNDP), and remain in the grey literature (see **Table A1.1**). Also included are two Master's reports, focussing on the Tulu Moye area [*Bahiru*, 2007; *Mengistu*, 2016].

Many reports do not publish grid references, so locations were obtained by map comparison and/or from field descriptions. Errors up to 5 km are common, however this does not prevent an appraisal of known geothermal areas in most cases.

2.3. Results

2.3.1. Soil CO_2 surveys

CO_2 survey results from each of the four areas are summarised in **Table 2.2** and **Figures 2.4–2.5**. The measurement limit of the instrument is 2400 g m^{-2} d^{-1}; only the Habilo area exhibited sites that exceeded this limit. Habilo shows the greatest average flux over all sites, and greatest variation as shown by standard deviation. The Aluto-Wonji measurements are the lowest and most consistent, with the

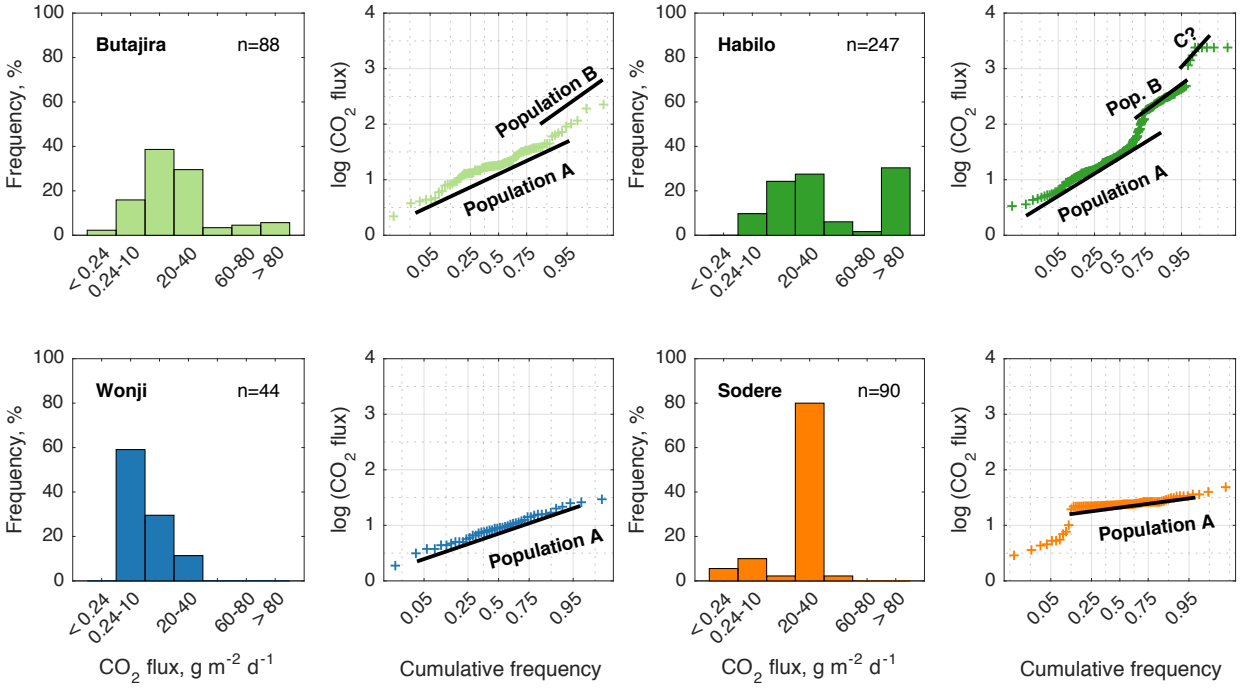

Figure 2.4. Histograms and cumulative frequency plots of each target area. The Wonji measurements exhibit only one population (A) representing background flux, whereas Butajira and Sodere show probable contributions from areas of elevated diffuse degassing (B). Habilo exhibits concentrated degassing along faults (B) and possibly a distinct population provided by fumaroles and their immediate vicinities (C).

majority of flux values < 10 g m^{-2} d^{-1}. Butajira and Sodere areas share a similar mean flux (20–30 g m^{-2} d^{-}

[1]) but the variation in flux from Butajira greatly exceed those from Sodere (**Figure 2.4**). Frequency analysis of the data depends significantly on the measurement strategy – our hypothesis is that CO_2 degassing is closely restricted to near faults, so it is unsurprising that the sparse grid employed for the Sodere area fails to resolve the higher flux values, limiting its variability. The Butajira survey targeted faults using sampling transects and smaller spacing – and is therefore more likely to

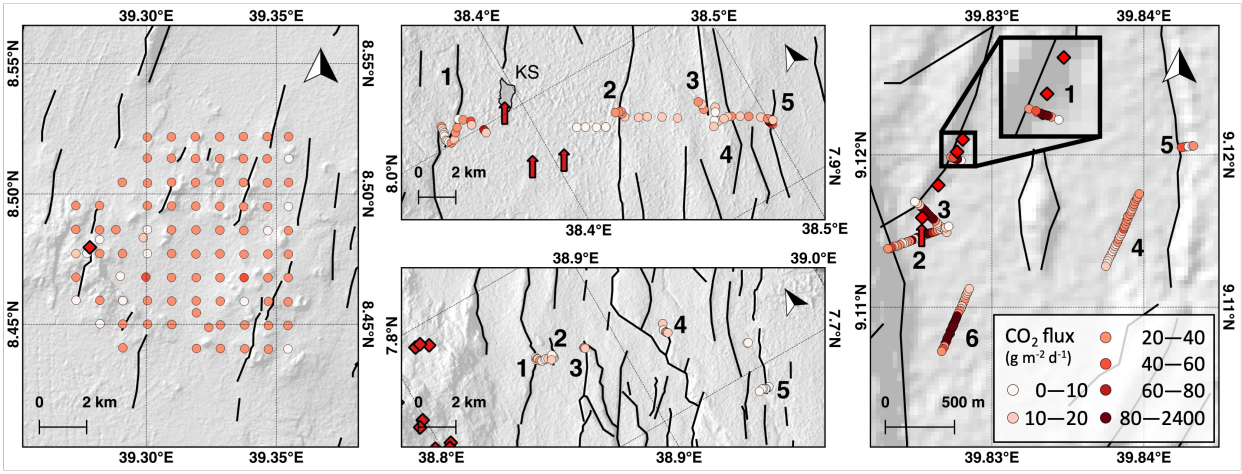

Figure 2.5. Maps showing flux results across four campaigns. *Left*: Sodere, *top*: Butajira, *bottom*: Aluto-Wonji, *right*: Habilo. Red arrows and diamonds represent hot springs and fumaroles respectively. Profile lines have been numbered. KS = Kuntane swamp. Faults from the *Agostini et al.* [2011] database (http://ethiopianrift.igg.cnr.it/ corti.htm).

encapsulate a higher variability. One implication of this interpretation is that the Sodere region could be analogous to Butajira, but a more targeted survey is needed to test this hypothesis.

The relative contribution of different CO_2 sources can be distinguished at least to some extent using cumulative frequency plots [e.g., *Cardellini et al.*, 2003]. An inflection in the plot implies different frequency behaviour in a set of measurements, and therefore two overlapping populations – a single population would appear as a straight line. The example of Habilo is clearest, with an inflection at a flux of around $10^{1.5} \approx 30$ g m^{-2} d^{-1}. We suggest that, for these campaigns, a value of >30 g m^{-2} d^{-1} represents an "elevated" value, associated with a significant contribution from an additional/different source. The background contribution to the soil CO_2 flux is biogenic carbon, with a typical flux of 0.2–50 g m^{-2} d^{-1}, rising

to 100 g m^{-2} d^{-1} in some areas, depending on the type and density of local vegetation and soil [e.g., *Chiodini et al.*, 2008; *Hernández Perez et al.*, 2003; *Hernández et al.*, 2012]. Our choice of cut-off value, on the basis of frequency analysis of our data, is higher than previous studies in similar locations [e.g. 6 g m^{-2} d^{-1} for Aluto; *Hutchison et al.*, 2015] but is consistent with soils in less arid climates [e.g. *Cardellini et al.*, 2003; *Chiodini et al.*, 2008]. We use this cut-off value to argue for the presence (or lack) of deep CO_2 flux only; our estimate of total CO_2 flux is independent of this value (see **section 2.4.3.1**).

The close association between fumaroles and elevated soil gas fluxes (10^3–10^4 g m^{-2} d^{-1}) points to a common volcanic/hydrothermal origin (see **Figure 2.4**), and on this basis we propose a deep origin for the majority of elevated values across the four areas. Carbon-isotopic analysis would be useful to confirm this conclusion, as shown in Aluto and the Magadi and Natron basins [*Hutchison et al.*, 2016c; *Lee et al.*, 2016].

The Aluto-Wonji survey found no elevated values, whilst the Habilo survey has a strong signal assumed to be of magmatic origin. The use of high resolution profiles across faults enables further consideration of the nature of CO_2 flux in the areas surveyed, discussed in **section A1.3** in the Appendices.

2.3.2. Map of hot springs and fumaroles

Figure 2.6 is a map of known hot springs and fumaroles, based on our literature survey, including error estimates on the location (**section 2.2.3**, **Tables A1.1 and A1.2**). Active areas are aligned NE-SW along a straight line, seemingly

independent of the change in rift trend from NNE-SSW in the south to NE-SW further north. Butajira and the Bodicho Springs are located off-axis to this general trend (**Figure 2.6**, **Table A1.2**). The southernmost region of the study area is anomalous (**Figure 2.6**), with isolated hot springs distributed along the Bilate River with possible structural associations with old volcanic centres [e.g., Data and Ashire volcanoes; *UNDP*, 1973]. Rift architecture changes south of Lake Awassa; the southern MER represents an early stage of rift evolution in which border faults still accommodate strain [*Agostini et al.*, 2011], possibly influencing the distribution of magmatism and associated geothermal areas [*Bastow et al.*, 2005; *Muirhead et al.*, 2016a].

Most active regions can be separated into two categories: volcanic, fumarole-dominated systems (e.g., Aluto, Corbetti, Fentale); and regional, hot spring-dominated systems (e.g., Habilo, Filoa, Hippo Pool, Sodere and others). Hot springs are common near some lakes (e.g., Abaya, Shalla, Langano) but absent near others (e.g., Abijata, Awassa, Koka). Many regional systems are possibly related to volcanic centres, e.g. Habilo, Filoa and Hubicha near Fentale and Doredimtu, Wondo Genet and Graha Quhe near Corbetti. The relationships between Hippo Pool (and Gargadi Spring), Boku and Sodere Springs is unclear, as are the influences of the Gedemsa and (older) Boku/Sodere caldera on these features.

Most studies do not systematically record spring geochemistry, and further work is recommended. Hot springs vary in temperature with values commonly around 40—60°C, higher temperatures reach 80—100°C [e.g., 81.5°C, Habilo; *Bekele et al.*, 2007; 82°C, Langano; *Purschel et al.*, 2013; 95°C, Chokore; *UNDP*, 1973].

2.4. Discussion

2.4.1. Diffuse degassing in the Main Ethiopian Rift

The irregular spacing and scarcity of data from the CMER and Sodere campaigns suggest that these results cannot be used to quantify the CO_2 flux from the elevated flux areas, however they do help to constrain the distribution of areas with elevated flux, and therefore the nature of degassing across the MER. In both the Habilo and Butajira areas, some faults concentrate CO_2 release and others do not. There is no evidence for elevated CO_2 release along Wonji faults observed to the east of Aluto, though the number of measurements is low and along-strike variation in degassing cannot be discounted.

The results of the soil CO_2 surveys in Habilo, Butajira and Aluto-Wonji are in concordance with the distribution of hot springs, fumaroles and other geothermal manifestations in each area (**Figure 2.6**). The results have implications for our understanding of degassing through rift structures. The magnitude of CO_2 flux varies on three spatial scales, which we consider in turn. Firstly, variability within degassing profiles (**section 2.4.1.1**). Secondly, variability within areas of high CO_2 flux, since only certain faults concentrate gas flow (**section 2.4.1.2**). Finally, we assess variability along the MER, and discuss implications for magma storage regimes and rift-scale CO_2 emissions estimates (**section 2.4.1.3**). Notably, we have not attempted to constrain the temporal variability in diffuse degassing, which remains a high priority for future work.

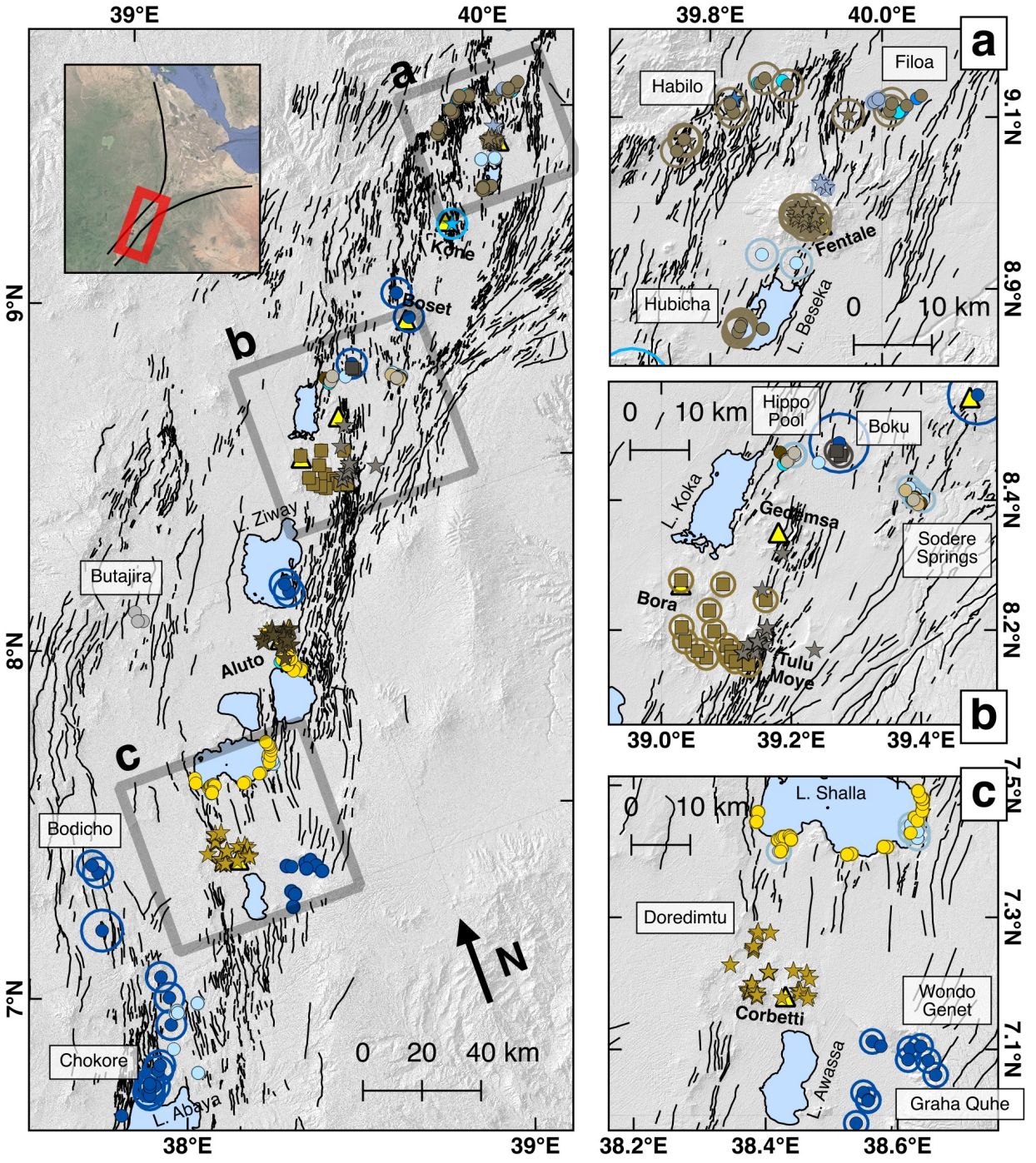

F	HS	
	●	*Alula et al.* [1992]
	■	*Abiye and Haile* [2008]
	●	*Ayenew et al.* [2008]
★		*Bahiru* [2007]
★	●	*Bekele et al.* [2007]
	●	*Beyene* [2000]
★		*Braddock et al.* [in review]

F	HS	
★	●	*GSE and UN* [1976]
★		*Gislason et al.* [2015]
	●	*Kebede* [pers. comm.]
	■	*Mengistu* [2016]
	●	*MOWR* [2008]
	●	*Purschel et al.* [2013]
★		*Rampey et al.* [2010]

F	HS	
	●	*Stadler et al.* [2007]
	●	*Teclu* [2002]
★		This study
	●	*UNDP* [1973]
★	●	*Williams et al.* [2004]

Figure 2.6. Map of fumaroles (stars), hot springs (circles) and reports of fumarolic areas/warm ground (squares) compiled from various data sources (see Table A1.1). Estimates of error in location are shown by hollow circles. Notable sites of off-edifice activity are labelled, shown in more detail in insets (a), (b) and (c). Inset: location within MER from Google Earth image.

2.4.1.1 Profile-scale variability

Soil gas surveys in the MER show that CO_2 flux varies significantly over a length-scale of tens of metres, as observed in many other areas worldwide [e.g. *Chiodini et al.*, 1998; *Lee et al.*, 2016]. The width of the area through which gas flow is concentrated, and the variability of the flux within this area, dictates the appropriate spacing between measurements in surveys of this kind. Since the width of degassing signals can be as little as 50 m (HF1, **Figure 2.7**), the spacing between measurements must be less than 50 m in order to not miss such signals. In the cross-rift campaign (Butajira and Aluto-Wonji), measurement spacing was reduced to 20–50 m near faults. In the targeted Habilo campaign, measurement spacing was reduced further to 10–20 m, in an attempt to capture the shape of the degassing signal and within profile variability (see **Table 2.1**; **section A1.3**).

Within areas of high CO_2 flux, high flux variability is observed on short (< 20 m) spatial scales (e.g., HF6; **Figure 2.7, right panel**), and order of magnitude variations in CO_2 flux have been reported on a scale < 1 m in highly altered environments elsewhere [e.g., *Chiodini et al.*, 1998]. The profiles from the Habilo graben show multiple variations away from a first-order smooth curve, with flux varying by a factor of two within 10–20 m. Quantification of the magnitude of the

flux from these sites requires multiple measurements at a high spatial density (at least 5–10 m) to ensure surveys capture the first order variability. This high spatial density of measurements precludes the use of popular techniques such as Sequential Gaussian Simulation [SGS; e.g. *Cardellini et al.*, 2003] for rift-scale estimates. SGS provides a smooth-varying probability of exceedance from which diffuse degassing structures may be identified and total fluxes estimated, but it requires a regular measurement grid for interpolation. In the absence of such techniques, we fit Gaussian curves to the profiles from the Habilo graben to estimate the total flux from this area (**section 2.4.3.1**). More advanced statistical techniques would be a profitable area for future research.

Point source fluxes from fumaroles/hot springs that exceed the measurement limit are difficult to include in total estimates (see Population C from Habilo, **Figure 2.4**). On Etna, *Giammanco et al.* [2007] sampled both focused and diffuse degassing manifestations from mud volcanoes and showed that the net flux from focused sites were 2–3 orders of magnitude lower than sites of significant diffuse degassing.

The difference in scales between gas flux variation and the area of interest (the width of the rift, ~50 km) presents the central difficulty in constraining rift-scale CO_2 degassing. Surveys of high spatial resolution necessarily focus on degassing areas, and the proportions of degassing to non-degassing areas is left uncertain.

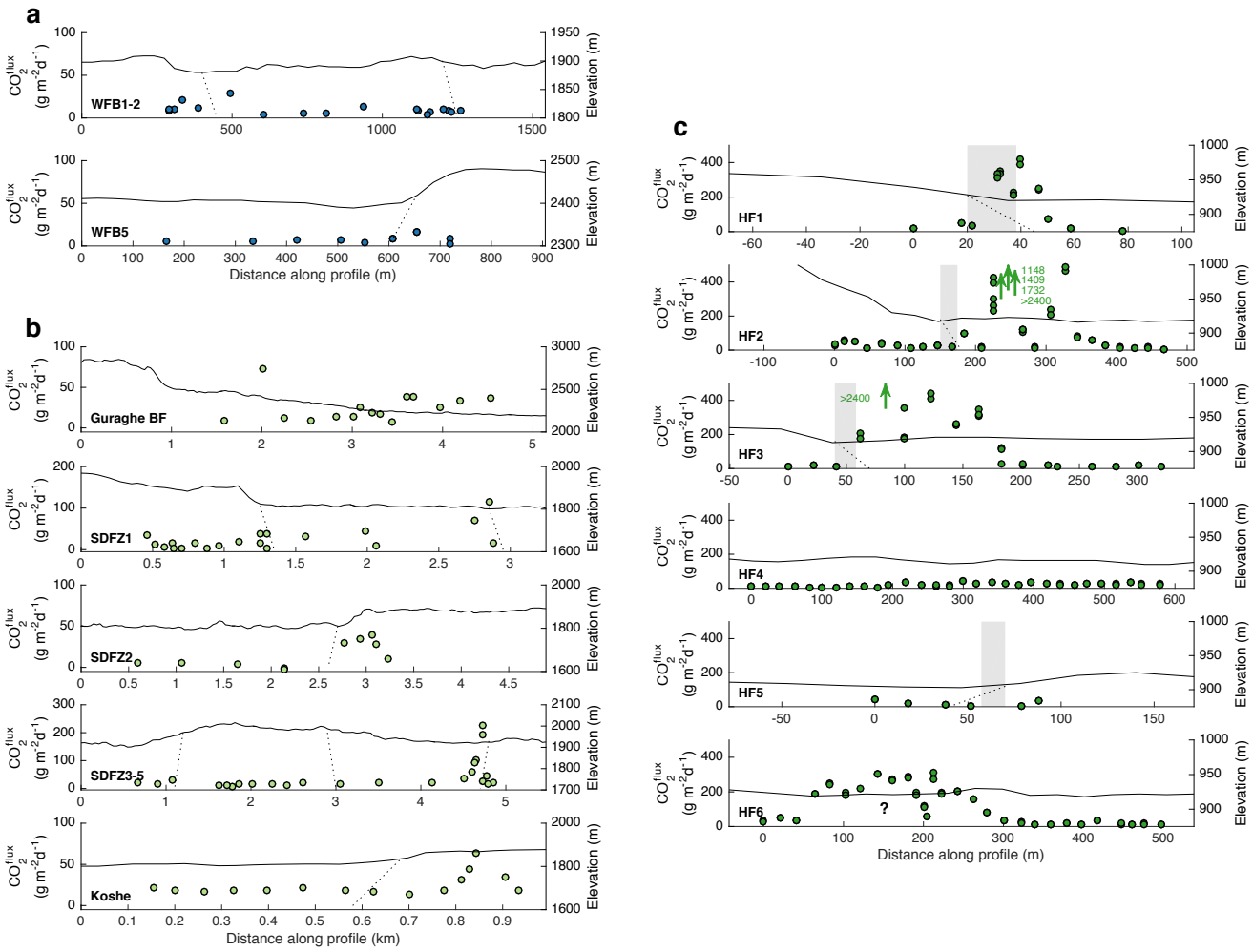

Figure 2.7. Selected profiles across faults. Fault/profile numbers are shown on Figure 2.5, names are derived from appending a regional code (SDFZ – Silti-Debre Zeyit Fault Zone, WFB – Wonji Fault Belt, HF – Habilo-Fentale). Shaded grey areas represent a fault zone based on the faults maximum throw. The throw is calculated using the fault-throw relationship in the same manner as *Lee et al.* [2016]. *Top left*: No elevated flux is observed across Wonji faults. *Bottom left*: SDFZ2 and SDFZ5 show elevated flux, whilst others do not. SDFZ1 represents a large offset fault with no significant carbon release. Further work is needed to investigate the Guraghe border fault (top panel); any elevated flux must be spatially restricted. *Right*: Very high flux is observed along the western side of the Habilo graben (HF1-3); none is observed on the eastern side. An elevated profile is recorded across HF6, with little/no topographic expression of faulting. Elevated flux bears little correlation to fault zones.

2.4.1.2 Basin-scale variability

The Habilo and Butajira areas both exhibit elevated flux, however some faults concentrate degassing whereas others do not. The extent to which a fault will act as a conduit for gas release depends not only on size but also on its permeability and geometry.

Fault permeability represents a major control on fluid transport, and is a function of many parameters including lithology, mean stress and recent activity [e.g. *Sibson*, 2000; *Faulkner et al.*, 2010]. In the Butajira region, the Guraghe border fault did not exhibit a wide degassing signal (**Figure 2.7a**). One single elevated value was measured, ~1.5 km west of the expected fault trace. While the maximum throw of the Guraghe border fault is > 1 km, there is no evidence for degassing from the fault zone across a similar length scale. Whilst large faults may create wider damage zones of increased permeability, and fluid transport, the

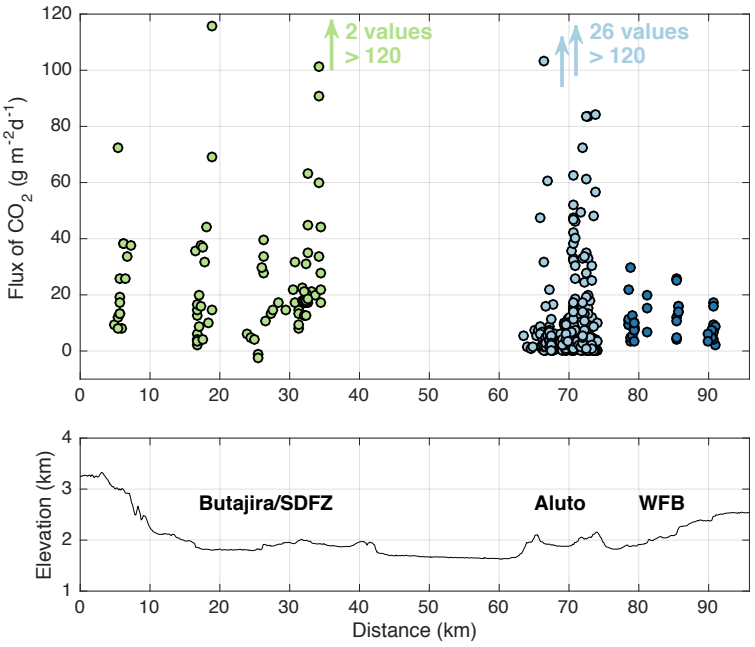

Figure 2.8. Cross-rift profile showing asymmetric degassing in the central MER, through Butajira/Silte Debre Zeyit Fault Zone (SDFZ; pale green), Aluto (pale blue; data from *Hutchison et al.,* 2015) and the Wonji Fault Belt (WFB; dark blue). Diffuse degassing is evident on the western side of the rift as well as focussed on Aluto volcano. The Wonji Fault Belt immediately east of Aluto shows no evidence of elevated flux, suggesting a restricted flow field.

ability of a fault to enhance the CO_2 flux will also depend on recent activity. Studies in Italy and the KRV suggest a close relationship between strain rate and fluid flow [*Camarda et al.*, 2016; *Muirhead et al.*, 2016a]. The time since rupture influences the degree of fault resealing, and is a significant control on porosity. Border faults like the Guraghe fault are large but inactive, and their permeability may therefore be low. The smaller faults that appear to concentrate degassing in the Butajira region may be more recent and active, creating efficient conduits through which CO_2 may flow. In contrast to the Natron basin (3 Ma), the older Magadi basin (7 Ma) is analogous to the MER in this respect: it has reduced border fault activity and increased activity towards the rift centre, leading to enhanced degassing in this location [*Muirhead et al.*, 2016a].

Fault geometry with respect to the source may also control fluid transport. In the Habilo region, we found elevated degassing along the eastward-dipping faults on the western side of the basin, associated with a line of fumaroles. The westward-dipping fault, on the other hand, displays no elevated flux. The eastward-dipping faults of the Habilo graben may therefore exploit a source to the east more effectively, the location of which is the subject of surveys conducted by Hotspur Geothermal. This observation has important implications for which faults we expect to concentrate CO_2 flux – those actively concentrating CO_2 flux can be separated from those that do not by only 1–2 km. The detailed structural associations of degassing are therefore important to account for in estimating a net flux from an active basin. The presence of hot springs and fumaroles provide a first-order assessment of emission along structures.

2.4.1.3 Rift-scale variability

Our surveys also shed light on the distribution and limits on areas of CO_2 emission along the rift. Despite their proximity to the actively degassing Aluto-Langano geothermal field, the Wonji faults to the east of Aluto show no evidence of elevated CO_2 flux (**Figure 2.8**). Although the number of measurements is smaller than other areas (n=44), and degassing along-strike or on different faults cannot be discounted, a lack of high CO_2 flux (i.e., $>40 gm^{-2}d^{-1}$) in the WFB zone close to Aluto volcano and the distribution of hydrothermal manifestations (**Figure 2.6**) suggests that the CO_2 source is spatially restricted. Fumaroles are found almost exclusively on the Aluto edifice itself and associated hot springs are located to the south (**Figure 2.6**). This may reflect local hydrology: Lake Ziway is not connected to Aluto's hydrothermal circulation, or to groundwater flowing into Lake Langano in the south [*Darling et al.*, 1996]. Areas to the north and east are therefore not able to access the restricted CO_2 source beneath the volcanic edifice, whereas the flow of water southwards extends the geothermal field in this direction [*Hochstein et al.*, 2017].

In contrast to these results on the eastern side of the CMER, the Butajira survey suggests fault-controlled degassing along certain faults. Elevated flux is observed in the central graben near the fault-aligned Kuntane swamp and associated hot springs, whilst the highest flux is recorded along a fault trace difficult to identify in the field (**Figure 2.5, top panel**). There is evidently a source of CO_2 available to these faults. The deep conductor predicted from magnetotellurics ~40 km west of Aluto [*Samrock et al.*, 2015] would lie approximately beneath the Tora-Koshe ridge (**Figure 2.8**). Magma storage offset from the main rift axis (along which the

majority of geothermal, volcanic and seismic activity lie) is therefore a likely CO_2 source for the Butajira area.

The storage of magma away from volcanic edifices may be an important feature of the rift. Monogenetic volcanic fields are distributed throughout the MER, with notable cones around the towns of Butajira and Silte (**Figure 2.3**). Field stratigraphy suggests that many of these cones are young, which implies an ongoing risk of eruption from locations away from the main volcanic centres.

The prevalence of off-edifice degassing in continental rifts could be considered evidence towards the widespread potential for regional volcanism. While mantle-derived magmas may be arrested at depth, repeated intrusion into extending crust may be accompanied by occasional surface volcanism. The new observations of CO_2 degassing from the Butajira and Habilo sites, along with that from the Magadi and Natron basins [*Lee et al.*, 2016] and the magnetotellurics study west of Aluto [*Samrock et al.*, 2015], suggest that further investigation of magma storage and volcanic risk in areas which have already shown signs of magmatic intrusion would be worthwhile [c.f. *Biggs et al.*, 2009; *Ibs-von Seht et al.*, 2001; *Keranen et al.*, 2004; *Roecker et al.*, 2017].

2.4.1.4 Summary of diffuse degassing in the Main Ethiopian Rift (MER)

Degassing in the MER is not continuous throughout the rift, but is instead spatially restricted to degassing sites that include both historically inactive volcanoes and off-edifice sites. Extrapolation of fluxes to the rift-scale must account for the patchy nature of degassing within continental rifts. Within each measured site, some faults

concentrate CO_2 flow and others do not. The identification of active structures that act as efficient fluid pathways is therefore important. The magnitude of emissions varies within zones of elevated CO_2 flux. The inherent variability on all scales and the small footprint of diffuse degassing measurements relative to potential degassing structures create difficulties when estimating a rift-scale CO_2 flux.

2.2.3. Areas of geothermal activity in the MER

Having discussed the variability in diffuse CO_2 degassing along the rift, we turn now to the broader identification of geothermal areas throughout the MER as manifested by hot springs and fumaroles. Firstly, the new database must be appraised, before the distribution of active areas is discussed and compared to the KRV.

2.4.2.1 Appraisal of database

Given the scope and frequency of large studies such as that of the *United Nations Development Programme* [1973], in addition to the socio-economic interest shown in areas of geothermal activity and high population density, it is unlikely that there are large areas yet to be explored. However, isolated hot springs and/or fumaroles in remote areas may be unreported. Though we expect most general areas to be in some way documented, the number of specific locations for each area varies greatly and is strongly affected by the number of existing studies. For example, though a number of reports mention fumarolic activity in the Boset Volcanic Complex [e.g., *UNDP*, 1973; *Haile Selassie*, 1984], we do not find any confirmed locations of geothermal manifestations in the literature beyond field descriptions. It is

nevertheless likely that Boset is a geothermally active volcanic system [*Siegburg*, pers. comm.] and it is included in the following discussion accordingly. In contrast, Gedemsa volcano is within the study area of several reports and has been noted as absent of current geothermal manifestations [*Thrall*, 1973; *Alula et al.*, 1992; *Bahiru*, 2007; *Abera et al.*, 2014]. Fumaroles may be under-reported compared to hot springs as they are often smaller, more remote and not targeted for hydrogeochemical analysis, although they may be focused in and around volcanic centers unlike hot springs that may be more widespread.

A number of caveats must be stated for using hot spring/geothermal feature locations as a proxy for geothermal activity, and by extension CO_2 emissions. Incidences of large CO_2 flux apart from associated geothermal features (cold, dry vents) have been reported in many regions globally, though not in the MER [e.g., Hokkaido, Japan; *Hernandez Perez et al.*, 2003; Lake Kivu, DRC; *Smets et al.*, 2010; Mammouth Mountain, USA; *Sorey et al.*, 1998; Rungwe Volcanic Province, Southern Tanzania; *Barry et al.*, 2013; *de Moor et al.*, 2013]. Hot springs are also intimately tied to local hydrology. Their locations are therefore biased towards lakes, rivers and areas of shallow groundwater. This may explain the relative abundance of features in the central MER (Lakes District) compared to the northern MER (Awash basin, Boset-Fentale).

Well-known sites of geothermal interest are included in many datasets (e.g., Hippo Pool, Sodere Springs), leading to a duplication of these locations within the combined catalogue. The errors in location prevent us from identifying these duplicates beyond doubt. Geospatial analysis concerning the density and alignment

of features is therefore precluded by the presence of duplicate features, the errors in location and the uncertainty in the completeness of the final database. The value of the database is in the identification of geothermally active areas and their relationship with tectonic and volcanic features. A comprehensive record of temperatures and geochemistry of springs and fumaroles across the Main Ethiopian Rift would help to assess the geothermal activity of each area. The compilation presented here represents the first step towards this goal.

2.4.2.2 Characterizing CO_2 source areas

As noted in **section 2.3.2**, the majority of geothermal areas in the MER are found along a NE-SW line and can be divided into two categories: edifice-based, fumarole-dominated systems relating to Holocene volcanic centres and off-edifice, hot spring-dominated systems which may or may not be interconnected at depth (**Figure 2.6**). The distance from Butajira and the Bodicho Springs to the nearest Holocene volcanic centres implies separate heat sources for these features, and therefore the possibility of magma storage offset from the main rift axis. Most manifestations are co-incident with structural features (see **Table A1.2**), underlining the role of fault networks in heat and fluid flow.

The MER is an area of high geothermal activity and, whilst the local population benefit from hot spring resorts (e.g., Sodere Springs, Wondo Genet, etc.) and the country benefits from energy production (e.g., Aluto, Corbetti, etc.), hazards must also be assessed. Fluoride concentrations in drinking water are often above guidelines presented by the World Health Organisation, and are attributed to the high rate of CO_2 outgassing [e.g., *Gizaw*, 1996]. The Fentale area in particular hosts

several manifestations of hydrothermal activity both on- and off-edifice, and is one of the most seismically active regions in the rift [*Keir et al.*, 2006], warning of the potential for seismic and volcanic hazards. Similarly, the abundance of hot springs around the O'a caldera coupled with seismic activity and the unknown present state of volcanic unrest suggest a high priority for future work on Lake Shalla and the underlying volcanic complex [*Mohr et al.*, 1980].

Though the magnitude of degassing likely varies substantially between active geothermal areas, the compilation map (**Figure 2.6**) provides a first-order view on the distribution and frequency of such areas. By assuming a range of CO_2 fluxes from each type of area (on- or off-edifice) and extrapolating along the rift, an estimate for rift-scale degassing can be found (**section 2.4.3.1**).

2.4.3. Estimating rift-scale carbon flux

In scaling up from their measurements of the Magadi and Natron basins, *Lee et al*. [2016] categorised their survey area into three structural zones (hanging wall, footwall and fault zone) using aerial and satellite imagery, supplemented by field mapping. They defined the fault zone as an area of width equal to the maximum fault throw (see **Figure 2.7**), and estimated the flux from the total zone area in each basin (Magadi and Natron) multiplied by the mean CO_2 flux for each zone. *Lee et al*. [2016] noted the sparse sampling used in regional surveys, and the errors associated with assuming a fair distribution of sampling within these structural zones. In their extrapolation to the entire Eastern Rift they calculate a mean flux per area for the segment of the rift in which the basins are located (from Oldoinyo Lengai to Suswa volcano). The segment area is 9,200 km^2 (184 km long × 50 km

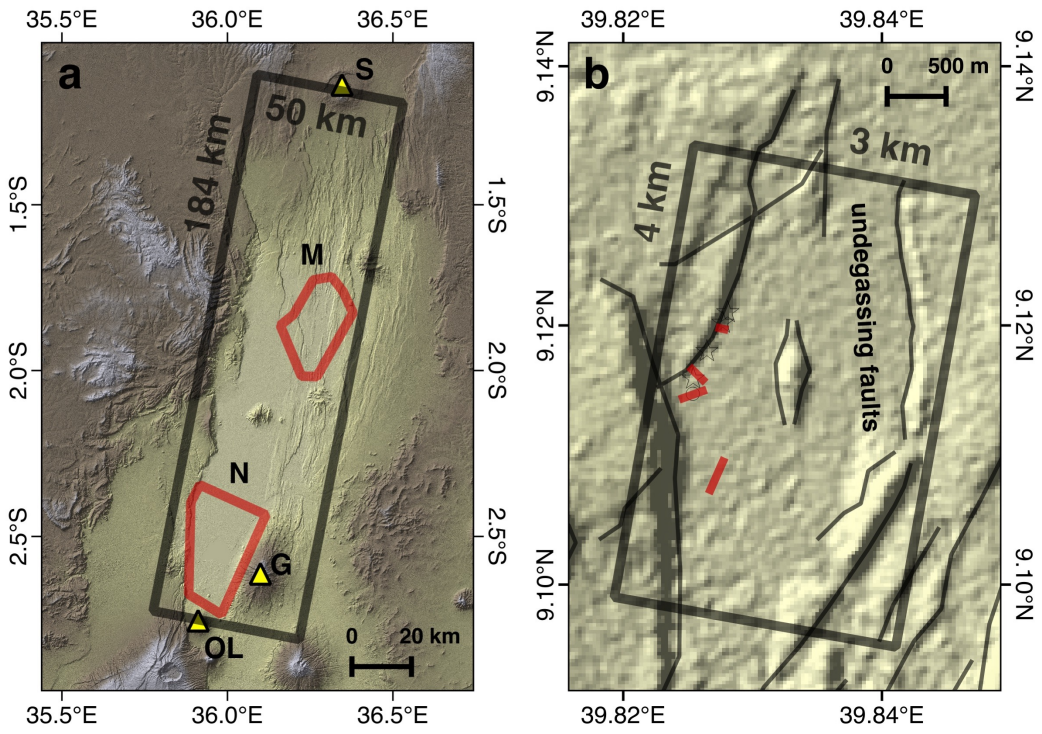

Figure 2.9. (a) Scaling argument from *Lee et al.* [2016]. Emissions from the Natron (N) and Magadi (M) basins are averaged over a segment of the rift (taken to be 50 km wide), the along-rift length of which is limited by Oldoinyo Lengai (OL) and Suswa volcano (S). (b) Simple estimate for CO_2 emissions from the Habilo graben. The faults on the western side are degassing, whereas our data provides no evidence of elevated flux elsewhere. Assuming a mean width and magnitude of elevated flux, a total degassing figure can be estimated (see section 2.4.3.1, Table 2.3).

wide), ten times the combined areas of the basins surveyed (982 km^2, see **Figure 2.9**). The flux per unit area within the Magadi and Natron basins is 3,900 and 4,300 t km^{-2} yr^{-1} respectively. Assuming emissions within the segment are solely from the Magadi and Natron basins, the mean flux per area drops to 440 ± 206 t km^{-2} yr^{-1} across the entire segment. Assessment of the spatial frequency of areas such as the

Magadi and Natron basins would help to constrain this estimate. Extrapolation of a mean flux of 440 ± 206 t km^{-2} yr^{-1} along the entire Eastern Rift (comprising KRV and MER; 3,240 × 50 km) yields an estimate for a total flux of 71 ± 33 Mt yr^{-1}. *Lee et al.* [2016] called for further surveys along the Eastern Rift to better constrain this extrapolation. Here, we use our observations from the MER (**section 2.4.3.1**) to evaluate the outgassing flux, and explore possible CO_2 sources that might account for this flux (**section 2.4.3.2**).

2.4.3.1 CO_2 emissions from the Main Ethiopian Rift

We estimate the rift-scale degassing by combining our new surveys (**section 2.4.1**) with the distribution of geothermal areas in the MER (**section 2.4.2**). The CO_2 flux from a degassing area is estimated, and the total flux from the Main Ethiopian Rift is extrapolated on the basis of the spatial frequency of geothermal areas following our observation that CO_2 flux correlates with geothermal activity (**section 2.4.1**). This remains a hypothesis to test in future surveys. Extrapolation to the entire Eastern Rift is provided for comparison with previous estimates.

The total load from Habilo can be estimated by considering the flux of CO_2 from the western side of the graben (**Figure 2.9b**). We find no evidence for degassing on the eastern side, though along-strike variation cannot be ruled out. The major, CO_2-concentrating fault exhibits fumaroles and hot springs, and elevated degassing across a width of 25—275 m (**Figure 2.7c**). The elevated signal is here modelled as a Gaussian curve for profiles HF1, HF2, HF3 and HF6 (see **Figure 2.10**). Profiles HF1, HF3 and HF6 provide close fits despite small-scale variability (likely due to permeability variations in the near subsurface, see **section 2.4.1.1**). HF2 requires

two Gaussian curves, although it is unclear whether this signal represents two elevated regions or one with higher variability. Owing to this uncertainty, confidence bounds are too broad for a useful estimate and are not used in further calculations.

The curves do not include values recorded in the immediate vicinity of fumaroles and hot springs (often beyond the measurement limit of the instrument). The relative contribution of these point sources compared to that from the faults is unclear (see section 2.4.1.1). The following discussion therefore deals only with diffuse degassing. The integrated area beneath the Gaussian curves, resolved perpendicular to the local fault strike, represents diffuse CO_2 flux per unit length of the CO_2-concentrating fault. We do not account for the biogenic carbon flux on the basis of a cut-off value, but assume all degassing is magmatic. The approximate error associated with this assumption is

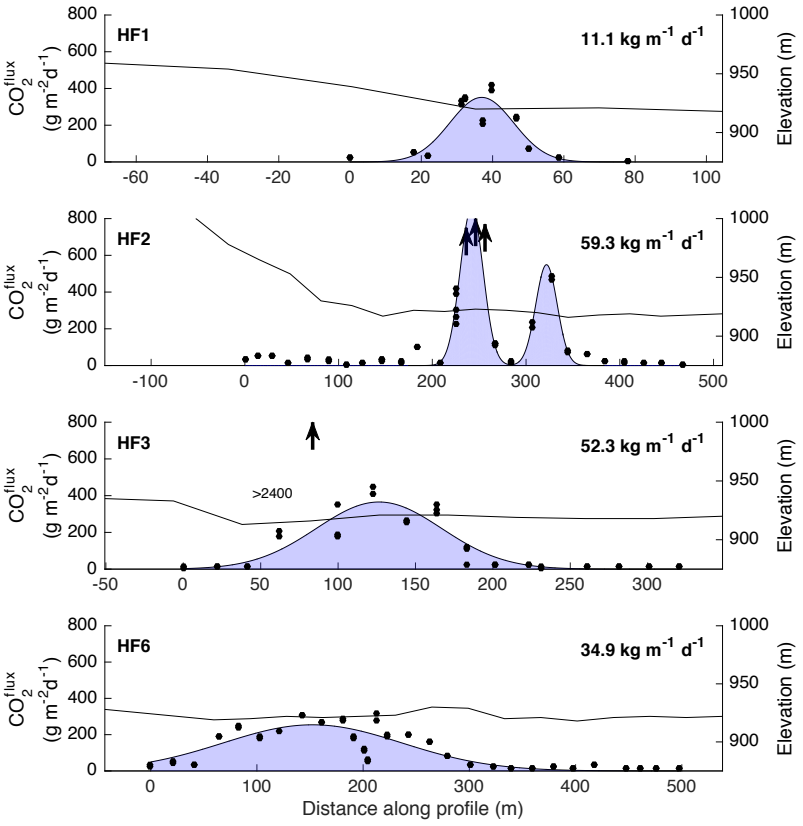

Figure 2.10. Degassing profiles from the Habilo survey, along the western boundary of the graben. Best-fit Gaussian curves are shown – the area under the curves represents the estimates of CO_2 flux per unit length along the degassing fault from each profile (see Table 3).

< 10 kg m^{-1} d^{-1}, given the maximum observed width of the signal (275 m) and the biogenic cut-off value from frequency analysis (30 g m^{-2} d^{-1}). If we assume a degassing fault length of 4 ± 2 km (see **Figure 2.9b**), the total load is estimated as 5—155 kt yr^{-1} (see **Table 2.3**).

Scaling up to quantify the rift-scale CO_2 degassing flux requires an estimate of the number of degassing fields. We separate geothermal degassing sites (**section 2.4.2**), into on- and off-edifice. Most geothermal energy prospects in Ethiopia are centred on volcanic edifices [*Kebede et al.*, 2012], and we obtain an upper estimate of the flux from these sources by assuming that the 5—7 volcanic areas (Fentale, Boset, Tulu Moye, Aluto, and Corbetti) each release a diffuse CO_2 flux similar to that measured for Aluto volcano [90—180 kt yr^{-1}; *Hutchison et al.*, 2015]. O'a caldera feeds multiple hot springs, and is clearly degassing; the status of Kone Volcanic Complex is uncertain. This yields a total volcanic flux of 0.45—1.26 Mt yr^{-1}.

We use Habilo (5-155 kt yr^{-1}) as a representative of the off-edifice areas along the rift. Further surveys of off-edifice sites are required to assess how robust this assumption is. Habilo contains a single hot spring [81.5°C; *Bekele et al.*, 2007] and numerous fumaroles and dried mud pools, suggesting greater geothermal activity than elsewhere [e.g., Hippo Pool, 35—47°C; *UNDP*, 1973]. From our compilation of geothermal locations, we estimate that there may be 14—20 off-edifice geothermal areas (see **Table 2.4**), yielding an estimate for off-edifice degassing of 0.07—3.10 Mt yr^{-1}.

Table 2.3. Estimates for the along-strike CO_2 flux from the CO_2-concentrating faults of the Habilo basin, extrapolated from profiles HF1, HF3 and HF6 assuming a degassing fault length of 4 ± 2 km. HF2 is not included in analysis owing to uncertainty in fitting a Gaussian curve.

Fault	CO_2 flux per length of degassing fault, kg m^{-1} d^{-1} (95% confidence bounds)	Total estimated load from Habilo, kt yr^{-1}
HF1	11.1 (7.4—15.5)	16.2 (5.4—33.9)
HF3	52.3 (36.6—70.8)	76.4 (26.7—155.0)
HF6	34.9 (25.8—45.3)	51.0 (18.9—99.3)

Table 2.4. Estimating the total CO_2 flux from the Main Ethiopian Rift.

Type	Flux per site, kt yr^{-1}	Number of sites	Total flux, kt yr^{-1}
On-edifice degassing	90—180 Aluto; *Hutchison et al.*, [2015]	6 ± 1*	450—1,260
Off-edifice degassing	5—155 Habilo; this study	17 ± 3**	70—3,100
Total			**520—4,360**

*Fentale, Boset, Tulu Moye, Aluto, Corbetti, Oa/Shalla? Kone?

**Chokore, Bilate, Bodicho, Wondo Genet, Graha Quhe, Doredimtu, Butajira, Hippo Pool/Gargadi, Boku, Sodere Springs, Filoa, Hubicha, Habilo, Kessem River, Data volcano? Ashire volcano? Lake Chitu? Debre Tseyon? Gecha island? Western Fentale? (Figure 6; Supplementary Table 2)

Combining edifice and off-edifice areas, the total diffuse CO_2 flux along the central and northern MER (from the north coast of Lake Abaya to Fentale volcano) is estimated at 0.52—4.36 Mt yr^{-1}. Scaling up from the central and northern MER (~400 km) to the Eastern Rift (~3000 km), we might expect the Eastern Rift to produce ~3.9—32.7 Mt yr^{-1}. Whilst the top of this estimate range is the same order

of magnitude as the previous estimate (71 ± 33 Mt yr^{-1}) from *Lee et al.* [2016], it suggests that the diffuse CO_2 flux per length of rift from the central and northern MER is lower than that from the Magadi and Natron basins (1.3—10.9 kt yr^{-1} km^{-1} compared to 11.7—32.3 kt yr^{-1} km^{-1}). This may reflect differences in degassing behaviour, for example in spatial frequency, size or type (edifice or off-edifice) of high-flux areas, between the MER and KRV.

Our data suggest that CO_2 degassing varies substantially along the Eastern Rift and re-enforces that more surveys will be required to further constrain rift-scale emissions. With more data, more sophisticated statistical techniques could be applied to this problem [e.g., Bayesian approaches: *De Angelis et al.*, 2014]. Further profiles across degassing faults could be used to build models of CO_2 flux with distance from fault traces, given fault parameters such as throw and age. Identifying the abundance and distribution of faults concentrating CO_2 degassing remains a central obstacle in constraining rift-scale emissions.

2.4.3.2 Sources of CO_2 emissions

The sources and modes of transport of magma and CO_2 in a rift are summarised in **Figure 2.2**. The flux of magma into the lithosphere is largely unknown and may be affected by multiple intrusions and melt pooling. As an instructive exercise the minimum crustal magma flux into a rift assuming that extension is accommodated exclusively through dike intrusion ["magmatic extension" hereafter; *Ebinger and Casey*, 2001; *Agostini et al.*, 2011; *Keir et al.*, 2006; *Keranen et al.*, 2004] can be estimated from the extension rate and crustal thickness. For given values of initial

CO_2-content, and assuming complete degassing of intruded magma, CO_2 emissions can be estimated.

The extension rate along the EARS varies from 0.7—5.2 mm yr^{-1} from the south to the north [*Saria et al.*, 2014]. Highest rates are located in Afar and along the MER (4.7—5.2 mm yr^{-1}). South of Lake Turkana the EARS splits into the magma-rich Eastern Rift and magma-poor Western Rift with extension rates varying north-south from 3.1—0.9 and 1.1—2.9 mm yr^{-1} respectively. We consider the

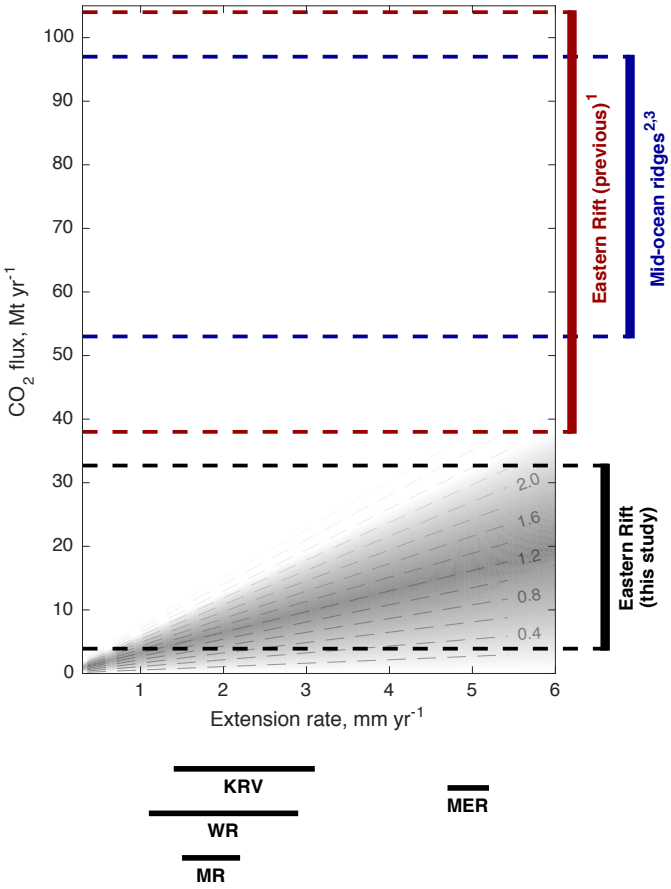

Figure 2.11. Estimating total CO_2 flux from magmatic extension of the Eastern Rift for a range of extension rates and initial carbon contents in magma [dashed lines show contours of equal initial carbon concentration in wt% in the range 0.02—2.4 wt%, *Le Voyer et al.*, 2017]. For comparison, estimated CO_2 flux from mid-ocean ridges (53—97 Mt yr^{-1}) is shown along with the existing estimate for the Eastern Rift (38—104 Mt yr^{-1}) and the Eastern Rift estimate from this study (3.9—32.7 Mt yr^{-1}). Complete degassing of highly enriched melt and intrusion of magma required to accommodate ≤ 5 mm yr^{-1} extension accounts for ≤ 32 Mt yr^{-1} CO_2 flux. Results assume magmatic extension along the 3000 km Eastern Rift over a crustal thickness of 30 km, with an approximate magma density of 3000 kg m^{-3}. Extension rates from *Saria et al.* [2014] shown by horizontal bars (MER = Main Ethiopian Rift, KRV = Kenyan Rift Valley, MR = Malawi Rift, WR = Western Rift). References: [1]*Lee et al.* [2016], [2]*Marty and Tolstikhin* [1998], [3]*Kagoshima et al.* [2015].

case that the Eastern Rift (MER and KRV, ~3000 km) is entirely accommodated by magmatic intrusion. For an average crustal thickness of ~30 km and a fast extension rate of ~5 mm yr^{-1}, approximately 0.45 km^3 yr^{-1} of magma is required to accommodate crustal extension in the Eastern Rift.

Initial carbon contents in primary magmas may vary considerably [*Helo et al.*, 2011; *Le Voyer et al.*, 2017]. The CO_2 concentration in melt inclusions provides a lower limit to the initial melt content, but a substantial proportion of CO_2 may be lost prior to melt inclusion formation. This shortcoming may be addressed by using ratios of CO_2 to a trace element on the basis of their similarly incompatible behaviour during melting [most commonly Nd; *Saal et al.*, 2002]. *Le Voyer et al.* [2017] use CO_2 ratios and trace element compositions from the literature to provide a global range of upper mantle CO_2 content of 20—1,200 ppm, spanning the published estimates from many previous studies on depleted and enriched sources [e.g., *Cartigny et al.*, 2008; *Helo et al.*, 2011; *Chavrit et al.*, 2014; *Barry et al.*, 2014]. Assuming an average melt fraction of 5—10%, this implies an initial CO_2 content of the melt before intrusion of 0.02—2.4 wt%.

Estimates of total emissions from magmatic extension for a range of initial CO_2 contents and extensions rates are shown in **Figure 2.11**. A maximum CO_2 concentration of 2.4 wt%, assuming total degassing of intruded magma, suggests that magmatic extension in the Eastern Rift contributes a maximum flux of ~32 Mt yr^{-1}, with lower initial CO_2 contents suggesting a contribution of approximately 6—18 Mt yr^{-1}. Our new estimate of 3.9—32.7 Mt yr^{-1} (**section 2.4.3.1**) is broadly

consistent with degassing of a volume of magma equivalent to that accommodating extension.

This analysis is not intended to imply that extension related magmatism is the only possible source of deep CO_2 to the EAR. The flux of magma into the crust may exceed that accommodated by magmatic extension alone. Sills are observed in many volcanic rifted margins [*Magee et al.*, 2016] and magma or mush reservoirs are inferred along the rift [e.g. *Biggs et al.*, 2011; *Desissa et al.*, 2013; *Johnson et al.*, 2016; *Roecker et al.*, 2017]; these may represent additional sources of magmatic CO_2. Melting of easily-fusible metasomes in the sub-continental lithospheric mantle (SCLM) has been posited as a key process in melt generation and strain localisation within rifts [e.g., *Rooney et al.*, 2014a; 2017]. Recent studies suggest abundant re-fertilization of the SCLM in southern and central Ethiopia by carbonate-rich, hydrous metasomatic agents [*Casagli et al.*, 2017; *Rooney et al.*, 2017; *Trestrail et al.*, 2017]. Carbon stored in metasomatised mantle could represent a significant additional source for CO_2 degassing. Similarly, decarbonation of crustal material (e.g., limestone) could contribute to the CO_2 flux [e.g., *Parks et al.*, 2013; *Sano and Marty*, 1995]. In fact, analysis of thermal springs in the Magadi and Natron basins suggests that a large proportion of dissolved CO_2 could be derived from a limestone end-member [up to 90.9% for individual samples; *Lee et al.*, 2017].

In addition to CO_2 carried and/or released by magma intruded into the crust, CO_2 may also be supplied from deeper sources, including magmas intruded into, and pooled within, the lithosphere [*Plasman et al.*, 2017]. The sizes of these reservoirs

are unknown. Earthquakes have been observed in the lower crust of the MER and KRV, interpreted as driven by fluids [*Albaric et al.*, 2014; *Keir et al.*, 2009a]. Through-going faults are hypothesised to concentrate CO_2 flow directly from the lithosphere [*Lee et al.*, 2016], but the decreased permeability due to lithostatic pressure at these depths may prohibit significant fluid flow [*Manning and Ingebritsen*, 1999]. The behaviour of faults and their permeability, and the behaviour of CO_2-rich fluids, at lower crustal depths is poorly constrained and further experimental studies would be valuable.

These additional sources of CO_2 may also vary along the Eastern Rift and constraining the provenance of diffuse CO_2 is challenging. As previously discussed (**section 2.1**), the mantle carbon flux out of the Eastern Rift inferred from the Magadi and Natron basins [*Lee et al.*, 2016] may be an overestimate depending on how representative these basins are, the scaling methodologies employed, and the interpretation of isotopic analysis. *Lee et al.* [2016] interpret the carbon isotopic compositions of soil gases to suggest a dominantly mantle contribution to the observed CO_2 flux in the KRV. However, there is uncertainty in assigning a provenance to soil gases, due to overlapping $\delta^{13}C$ compositions between air (–8‰) and mantle-derived gases (–3 to –8‰). The soil gas collected for isotopic analysis included an unquantified contribution from the air, complicated by the addition of isotopically-light biogenic carbon, which reduced the isotopic value of some samples to significantly below the mantle-air mixing line (–11.7‰). *Lee et al.* [2016] account for this uncertainty by supposing an average mantle contribution of 10%, however the true value may be lower. The CO_2 concentrations in the *Lee et*

al. [2016] measurements ranged from 500—2,000 ppm, and can be used alongside isotopic ratios to estimate the relative proportions of the air and mantle sources in the samples. For example, if we take 400 ppm and 11.9wt% as the CO_2 concentration in air and mantle-derived gases respectively [*Fischer and Chiodini*, 2015], not accounting for biogenic input, we find a mantle contribution of just 1%. Air contamination is therefore difficult to account for accurately and could be substantial. A proportion of the diffuse CO_2 flux in this region could also be due to heating and fracturing of carbonate rocks, which would provide a similar isotopic signature to mantle [*Lee et al.*, 2017].

If the high estimates for deep CO_2 flux in these areas are real, they may represent a large proportion of the total Eastern Rift contribution, in which case scaling up from these regions would overestimate the total flux. Understanding the factors controlling the spatial variability of rift CO_2 emissions must remain a research priority. The time-dependence of CO_2 emissions from rift sites also remains unknown, and repeated measurements to provide a temporal dimension to our understanding of diffuse CO_2 degassing remains a key research priority.

In summary, our new estimate suggests that, although CO_2 emissions from the Eastern Rift of the EARS are likely lower than emissions from the global mid-ocean ridge system, they are still substantial. The mechanisms resulting in such large fluxes are likely to be significant for our understanding of rift dynamics, relating volatile movement and melt generation to lithospheric deformation.

2.5. Conclusions

Understanding diffuse CO_2 degassing in volcanically active areas is important in terms of global CO_2 budgets and hazards. A series of diffuse soil surveys in the Main Ethiopian Rift (MER) have shown that CO_2 flux varies greatly on three spatial scales: within concentrated zones of emission, between faults in the same basin and between adjacent terrains. CO_2 degassing is not merely restricted to volcanic edifices, however off-edifice degassing is not distributed evenly along the MER. The areas of Butajira and Habilo emit a significant flux of CO_2, suggesting magma storage some lateral distance from the nearest volcanic centre. The patchiness of degassing presents difficulties in scaling up to estimations of rift-related diffuse CO_2 emissions. A compilation of hot spring and fumarole locations elucidates the distribution of geothermal areas along the rift; numerous, small sites of activity are found, similar to Habilo and Butajira.

Extrapolation from our surveys using the distribution of geothermal areas suggests a total CO_2 flux from the Main Ethiopian Rift of 0.52—4.36 Mt yr^{-1}. In the case that the MER is representative of the entire Eastern Rift, we predict a flux of 3.9—32.7 Mt yr^{-1} over this region. Although the maximum and minimum of the ranges are consistent, this result is significantly lower than the total CO_2 flux estimated by extrapolation from the Kenya Rift Valley (38—104 Mt yr^{-1}), possibly implying a fundamental difference in the deep carbon cycle between the two areas of the rift. Additional surveys along the Eastern Rift are required to further test these extrapolated estimates, given the uncertainty over how representative either test case is for the Eastern Rift as a whole.

The results of this study suggest that, whilst diffuse degassing of deep CO_2 within continental rifts is a large contributor to the long-term global carbon budget, its total flux may have been previously overestimated. Nevertheless, the magnitude of emissions raises questions over the CO_2 sources and mechanisms associated with rifting. We estimate that a range of 6—18 Mt yr^{-1} (with an absolute maximum of 32 Mt yr^{-1}) CO_2 along the Eastern Rift can be accounted for by magmatic intrusion into the crust as it accommodates extension. Additional magmatic intrusions in the form of sills and magma mush zones in addition to melting a lithosphere enriched in volatiles and assimilation of crustal material may play an important role. Further work towards estimating total magma flux into rifts is required.

The release of deep CO_2 through large faults has been posited as a mechanism for transporting high fluxes through the lithosphere. Investigation into the permeability structures as well as the decoupling of CO_2-rich fluid and melt at lower crustal depths are valuable next steps. The high flux of volatiles through the East African Rift System has important implications for rift development, the global carbon cycle and regimes of magma storage within the lithosphere and crust.

3 Geomorphology and structure of peralkaline rift volcanoes

Abstract

Detailed topographic data from volcanoes can yield key insights into the controls on volcanic activity as well as hazards. High-resolution digital elevation models generated from remote sensing data enable comparison of the geomorphology and structure of large and inaccessible volcanoes. We present new topographic data for three peralkaline volcanoes in the Main Ethiopian Rift (MER; Fentale, Corbetti and Gedemsa) and one volcano in the Afar Rift (Dabbahu), combined with field observations, reveal previously unidentified post-caldera deposits and craters. Vent and crater locations are aligned with rift-parallel faults and also with rift-cutting structures in a variety of orientations. Caldera shape is controlled by interaction with these structures. The relative frequency and type of eruption varies greatly between these volcanoes over the past 150 kyr. Gedemsa is now largely inactive; Fentale hosts deposits from many small volume eruptions (< 0.1 km^3) while Corbetti has produced several large eruptions (~0.4–0.5 km^3). Morphometry of peralkaline rhyolite deposits at Corbetti and Fentale, including ogives and levees, provides constraints on rheology. Emplacement viscosities of ~10^8–10^{11} Pa s at Fentale are similar to or lower than calc-alkaline rhyolites and consistent with experimental and theoretical studies. The observations presented here have significant implications for hazard assessment in the Ethiopian rift, and highlight the importance of structural features in controlling the location, magnitude and style of volcanic activity in the MER.

A version of this chapter has been published as:

Hunt, J. A., D. M. Pyle, and T. A. Mather (2019), The geomorphology, structure, and lava flow dynamics of peralkaline rift volcanoes from high-resolution digital elevation models. *Geochemistry, Geophysics, Geosystems*, *20*, 1508–1538, doi:10.1029/2018GC008085.

3.1. Introduction

The geomorphology of volcanoes has long been used to investigate volcanic development and activity [*Thouret*, 1999]. Digital topography has been used to classify volcano morphology [e.g., *Favalli et al.*, 1999; *Prima and Yoshida*, 2010; *Euillades et al.*, 2013; *Grosse et al.*, 2014; *Pedersen and Grosse*, 2014], identify and assess eruptive deposits and structures [e.g., *Hofton et al.*, 2006; *Csatho et al.*, 2008; *Zouzias et al.*, 2011; *Hutchison et al.*, 2015], and evaluate on-going volcanic hazards [e.g., *Favalli et al.*, 2005; *Stefanescu et al.*, 2012; *Cordoba et al.*, 2015]. Many studies have used the morphometry of lava flow deposits [e.g., *Pyle and Elliott*, 2006; *Ventura and Vilardo*, 2007; *Tarquini et al.*, 2012; *Nomikou et al.*, 2014], cones [e.g., *Fornaciai et al.*, 2012; *Kervyn et al.*, 2012], and other deposits [e.g., *Jessop et al.*, 2012] to investigate their rheology and dynamics of emplacement. The spatial distribution of vents, and orientations of craters and faults, can be used to investigate the influence of stress regimes and pre-existing structures on eruptive locations [e.g., *Hutchison et al.*, 2015], and inform hazard assessment on the basis of likely event location. As satellite capabilities continue to develop, high-resolution remote sensing data is becoming increasingly important in studying large, inaccessible and/or remote volcanoes across the world [e.g., *Kervyn et al.*, 2007; *Ernst et al.*, 2008; *Favalli and Fornaciai*, 2017].

Here, we demonstrate the use of high quality topographic data to develop and test hypotheses fundamental to rift volcanism and its dynamics. We use high-resolution digital elevation models to study the morphology of three volcanoes from the Main Ethiopian Rift (MER; Fentale, Gedemsa and Corbetti) and one from Afar

(Dabbahu, Figure 3.1). Using this data and complementary fieldwork, we (i) assess volcanic features, including observation of previously unidentified deposits, (ii) evaluate and compare caldera architecture, (iii) identify alignments of volcanic vents and craters, (iv) estimate eruptive volumes and frequencies along the rift, and (v) assess morphometry of peralkaline lava deposits. Peralkaline lavas (molar $[Na_2O + K_2O] / Al_2O_3 > 1$) with high alkali, halogen and water content are common in rift settings [e.g., at Fentale; *Webster et al.*, 1993]. Experimental and theoretical studies suggest that such magmas have anomalously low viscosity due to depolymerisation [e.g., *Hess et al.*, 1995; *Dingwell et al.*, 1998]. No silicic peralkaline eruption has yet been observed, so the rheological constraints provided by morphology of peralkaline lava flow deposits are of significant interest and we further use our new data to assess the rheological properties of such flows.

3.1.1. Introduction to volcanism in Ethiopia

Rifting in Ethiopia began in the Oligocene along the Red Sea Rift in Afar [~28 Ma; *Wolfenden et al.*, 2005] and in the Miocene along the MER [~15–18 Ma; *Wolfenden et al*., 2004]. Extension began along border faults, before migrating closer to the rift axis. The Red Sea Rift is more evolved than the MER, representing incipient seafloor spreading [e.g., *Hayward and Ebinger*, 1996; *Keir et al.*, 2013]. Continental rifting in the MER is more evolved in the north than in the south [e.g., *Corti*, 2009; *Keir et al.*, 2015]. The differences in maturity between and along rifts may lead to differences in present-day volcanic activity at within each rift.

Volcanic activity in the MER has formed both silicic peralkaline 'central' volcanoes, and distributed mafic cones and lavas [e.g., *Gibson*, 1969; *Abebe et al.*,

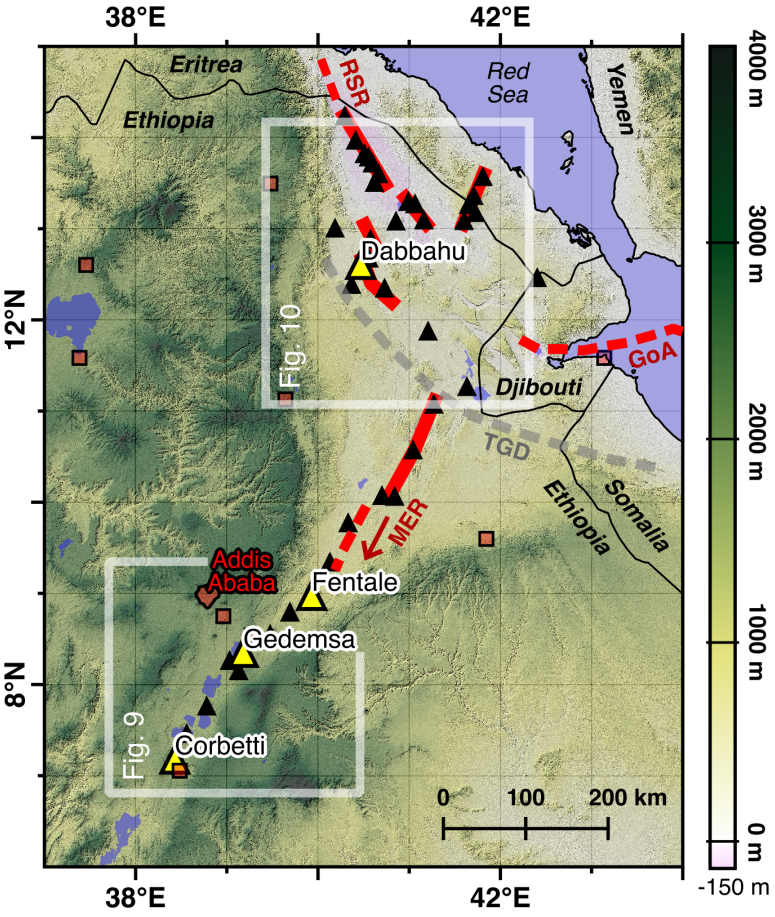

Figure 3.1. Location map for the volcanoes in this study (yellow triangles: Dabbahu, Fentale, Gedemsa, Corbetti). Elevation and hillshade provided by Aster GDEM (product of METI and NASA). Shown in red dashed lines are the approximate locations of the three rifts that meet at the Afar triple junction: the Red Sea Rift (RSR), Gulf of Aden (GoA) and Main Ethiopian Rift (MER). Full red lines show rift segments in Afar [after *Donovan et al.*, 2018; *Wright et al.*, 2012]. Grey dotted line delineates the Tendaho-Goba Discontinuity (TGD). Black triangles: other volcanoes; red squares, towns of population > 100,000; black lines, country borders (Ethiopia, Eritrea, Djibouti, Somalia).

2007]. The poorly-known volcanoes of the MER have become the focus of much recent work [*Aspinall et al.*, 2011; *Vye-Brown et al.*, 2016; *Hutchison et al.*, 2015, 2016a, 2016b, 2016c, 2018; *Rapprich et al.*, 2016; *Martin-Jones et al.*, 2017; *Siegburg et al.*, 2017; *Lloyd et al.*, 2018a, 2018b; *Fontijn et al.*, 2018; *McNamara et al.*, 2018; *Tadesse et al.*, 2018].

Previous work on the volcanoes in this study is summarized in **Table 3.1**. The central volcanoes commonly host elliptical calderas [*Acocella et al.*, 2002], possibly influenced by structures cross-cutting the rift [e.g., *Abebe et al.*, 2007].

Re-activation of pre-rift structures is inferred to have influenced the development of both the caldera and post-caldera products, notably at Fentale, Gedemsa and Corbetti [*Acocella et al.*, 2002; *Lloyd et al.*, 2018]. At Corbetti, surface deformation, internal structures and post-caldera vents and craters are all thought to be controlled by cross-cutting structures, associated with a major crustal lineament [e.g., *Gislason et al.*, 2015; *Lloyd et al.*, 2018a; *Corti et al.*, 2018a].

The silicic MER volcanoes are in a post-caldera stage of evolution [*Hutchison et al.*, 2016a]. Four volcanoes have shown recent geodetic unrest (Aluto, Corbetti, Bora and Haledebi), with some deformation associated with ongoing geothermal activity [*Biggs et al.*, 2011; *Hutchison et al.*, 2015, 2016c; *Lloyd et al.*, 2018a, b]. Corbetti and Aluto are considered the most active volcanic centers in the rift, with deposits from explosive eruptions implying an eruptive flux of 0.01–0.1 km^3 (magma)/kyr over the past 12 kyr [*Fontijn et al.*, 2018]. This flux has declined significantly since the mid-Pleistocene peak of caldera-forming activity, when eruptive rates at Aluto and Corbetti may have been as high as 0.5–0.75 km^3/kyr [*Hutchison et al.*, 2016a].

The Afar region hosts a series of en-echelon magmatic segments analogous to sea-floor spreading segments [e.g., Dabbahu/Manda Hararo, Alayta, Tat ‘Ale, Erta ‘Ale; *Hayward and Ebinger*, 1996; *Wright et al.*, 2006; *Keir et al.*, 2009b; *Wright et al.*, 2012; **Figure 3.1**]. In comparison to the MER, volcanoes in Afar have been more active, with four eruptions in the period 2002–2015 [*Wadge* et al., 2016]: Nabro, Alu-Dalafilla, Erta Ale, Dabbahu-Manda Hararo. See **Table 3.1** for further details of previous activity at Dabbahu.

Table 3.1. Summary of relevant previous work on each volcano in this study.

Volcano	Geology	Caldera	Post-caldera activity	Notable features	Dates
Fentale[1-4]	Major locations of eruptive activity: W, SE, & E of caldera. Edifice comprises trachytes and water-rich pantellerites with rare intercalated tuffs[4,5].	Simple, regular ellipse with steep cliff. Long axis 273º [6].	Several obsidian lava flows, within caldera & on NE flank[3]. Vents lie along fracture zone across caldera parallel to long axis. Historical basaltic volcanism, prior to ~1808–1810 CE[7,8], following rift-parallel trend associated with tensional fissures[1,9].	Fentale ignimbrite: associated with caldera-formation. Forms thick deposit of welded ignimbrite on plain around edifice. Deposit is absent from much of the upper edifice[3]. Enigmatic blisters S of edifice, may have formed by release of volatiles after emplacement[3].	Fentale ignimbrite: 168 ± 38 ka (fission track dating on glass[9]).
Gedemsa[10]	Oldest products: pantelleritic lavas, followed by layers of pumice and dilute PDC deposits[8]. 2 ignimbrites followed by further pumice deposits[8,10].	Broad (~7×9 km) & low (max. topography ~ 100—150 m)[6].	Intra-caldera deposits follow a 280º trend. 3 coalesced domes (Kelo, Dima and Kore) of lapilli and bomb breccias, interbedded with welded facies & obsidian lavas[8]. Kore hosts summit crater of ca. 600 m diameter. Ash-rich scoria cone & basaltic lava (NE rim of caldera)[10], related to regional faults[11].	Pantellerite lava domes & pumice deposits outside caldera wall lie along extension of post-caldera trend[6], as well as along rift-parallel faults[10]. Age of these deposits is unknown.	Caldera: mid-Pleistocene, pre- and post- caldera deposits dated at 319 ± 2 ka and 265 ± 2 ka respectively (K/Ar dates[11]).
Corbetti[12-13]	3 post-caldera edifices: Artu (oldest, partially buried[14]), Urji (syn. Wendo Koshe), Chabbi. Early post-caldera rocks are comenditic, shifting to pantelleritic in later stages[14].	Old, large ignimbrites (0.9 & 0.67 Ma), suggest multiple caldera-forming eruptions[14,15,16].	Urji comprises predominantly pyroclastic deposits, Chabbi predominantly obsidian lavas. Numerous craters on both Urji & Chabbi edifices, as well as a pumice flow on the N flank of Urji & six aphyric obsidian coulees on Chabbi[14,17]. Tephrostratigraphy suggests large explosive eruption every 900 years for the past 10 kyr[18].	Most recent eruption from Urji emplaced Wendo Koshe Younger Pumice (WKYP), with 4 Chabbi lava coulees post-dating that event[14]. Post-caldera vents & craters are preferentially aligned to a cross-cutting structure[19]. Seismicity suggests the structure extends outside the caldera.	Ignimbrite: 182 ± 28 ka; post-caldera lava (E Chabbi): 19 ± 15 ka (both Ar-Ar) after hiatus[20]. WKYP: 2.3 ka (^{14}C, palaeosol[14])
Dabbahu[21-22]	Basaltic trachy-andesites are common. Rhyolites divided into comendites, (summit & satellite centers), and pantellerites (series of N-S fissures).	Pit craters and/or small calderas at summit, elliptical structures to W.	Satellite centers of Alcoma, Gab'ho & Da'Ure. 3He dating of basalt surfaces indicates cyclic behavior (20-40 kyr periodicity)[23]. The rifting episode of 2005-6 resulted in a small eruption to S of Da 'Ure (N-S trending vent & fault system deposited pumice[24]), followed by basaltic eruptions further south[25].	Elliptical structures associated with fumaroles identified[21]. Summit craters smaller than MER calderas. Larger structures may have been buried. Extensive suite of lavas from basalt to peralkaline rhyolite, in contrast to MER where intermediate compositions largely absent.	

References: [1]*Gibson* [1967], [2]*Gibson* [1969], [3]*Gibson* [1970], [4]*Gibson* [1974], [5]*Webster et al.* [1993], [6]*Acocella et al.* [2002], [7]*Harris* [1844], [8]*Fontijn et al.* [2018], [9]*Williams et al.* [2004], [10]*Thrall* [1973], [11]*Peccerillo et al.* [2003], [12]*Mohr* [1966], [13]*Di Paola* [1972], [14]*Rapprich et al.* [2016], [15]*Žáček et al.* [2014], [16]*Žáček et al.* [2015], [17]*Macdonald and Gibson* [1969], [18]*Martin-Jones et al.* [2017], [19]*Lloyd et al.* [2018a], [20]*Hutchison et al.* [2016b], [21]*Field et al.* [2013], [22]*Field et al.* [2012], [23]*Medynski et al.* [2013], [24]*Wright et al.* [2006], [25]*Ferguson et al.* [2010]

3.2. Methodology

Very-high-resolution panchromatic (50 cm) and multispectral (2 m) orthoimages from the Pléiades-HR 1A satellite were obtained in stereo for three areas: Fentale, Gedemsa and Urji (western half of Corbetti Caldera). In addition to the satellite-derived DEMs, lidar-derived DEMs of Chabbi (eastern half of Corbetti Caldera) and Dabbahu (Afar) are used in this study. The Urji and Chabbi DEMs were combined to create a merged DEM of Corbetti Caldera.

The satellite data were processed using the Leica Photogrammetry Suite (**Figure A2.1**); the full methodology is detailed by *Zhou et al.* [2015]. The use of stereo images to create a digital elevation model (DEM) works on the principle of parallax. Two images from different perspectives can be joined together with tie-points – the same feature identifiable in both orthoimages. Initial creation of a DEM using tie-points results in a point cloud with a variable spatial density. Pleiades-derived DEMs have an average horizontal resolution of 1–2 m, varying with point cloud density due to lack/abundance of features and cloud cover. For analysis, it is convenient to regrid points using a block mean filter and an interpolation algorithm using continuous curvature splines, creating a regular grid of elevation values at 0.5-m spacing. Dense cloud cover must be removed from the point cloud. Cloud cover affects < 8% of the stereo images for Fentale and is negligible for Gedemsa and Urji. Gaps in the final DEMs have been replaced by a low resolution model (30-m Aster GDEM). Once a final point cloud is generated, raster images of elevation are created and images of hillshade and slope can be calculated. The lower

resolution multispectral images were pansharpened using the 50-cm resolution panchromatic images and used for feature identification and mapping.

Lidar data were acquired by the UK Natural Environmental Research Council's Airborne Research and Survey Facility in October 2009 (Dabbahu) and November 2012 (Chabbi). A DEM of 0.5-m pixel resolution was generated for Dabbahu by *Barnie et al.* [2016]; full details of processing are provided in *Hofmann* [2013]. A DEM of 2-m resolution was generated for Chabbi using GRASS (Geographic Resources Analysis Support System; http://grass.osgeo.org/) as described in *Hutchison et al.* [2015].

From these models and using QGIS (http://www.qgis.org), we manually mapped vents, craters, faults, cones, flow deposits and other features at each volcano. We used a scale of 1:5000 in identifying features and a scale of 1:2500 in drawing contacts. Rose diagrams were then produced for craters, faults and other linear features observed from the DEMs, weighted by length. Vent/crater alignments were manually identified on the basis three or more features and/or elongation of craters/cones.

Due to the lack of recent studies at Fentale and its complex geomorphology, we conducted a one-week field campaign in November 2017 to complement DEM observations and ground truth results relating to flow deposits and relations between units. Access to the north and east of the edifice is restricted, whilst the steep slopes of the volcano prevent detailed exploration of many other areas. The high-resolution DEM provided an invaluable base map for making field observations and enables us to apply these observations more generally. The

campaign was in part targeted, prioritizing geomorphological features such as levees identified from the DEM, and in part exploratory, surveying the accessible southern flank of the volcano.

Volumes of features such as lava flow deposits and cones were estimated using a DEM-differencing technique (**Figure A2.2**): a feature is masked and the resultant gap in the data is interpolated using the same surface gridding algorithm (continuous curvature splines) used in the original DEM construction. A similar method was used to estimate lava flow deposit volumes on the Kameni islands, Santorini, by *Nomikou et al.* [2014]. A variable tension factor (between 0 and 1) is used during interpolation to find the pre-eruptive surface – we found that a factor of 0.7 produced geologically reasonable surfaces, with little dependence on tension above a factor of 0.3. For the Kameni islands, minimum and maximum volumes were calculated for lava flow deposits, varying by < 25% [*Nomikou et al.*, 2014] – we follow *Hutchison et al.* [2016a] in using this value as an approximation of error using this method.

A number of studies have used morphometry to estimate the rheology of lava flow deposits [e.g., *Hulme*, 1974; *Moore et al.*, 1978; *Fink and Griffiths*, 1990; *Wadge and Lopes*, 1991; *Gregg and Fink*, 2000; *Pyle and Elliott*, 2006; *Wilson and Mouginis-Mark*, 2014; *Nomikou et al.*, 2014; *Gregg*, 2017]. Assuming a constant Bingham rheology, the apparent yield strength of a fluid can be estimated from the dimensions of the deposit [*Hulme*, 1974; *Gregg*, 2017]. For a deposit of thickness, h, bulk density, ρ, emplaced on a slope of angle, α, the yield strength, Y, is:

Eq. 3.1: $$Y = hg\rho \sin \alpha$$

Coulees on both Corbetti and Fentale exhibit surface wrinkles, or ogives. Frequency analysis of elevation data along profiles down the length of the coulee can provide a quantitative assessment of the wavelengths of these features [*Pyle and Elliott*, 2006; *Lescinsky et al.*, 2007], which depends on the viscosity of the lava and the thickness of the solidifying crust [*Fink and Fletcher*, 1978; *Warner and Gregg*, 2003]. Using custom scripts in MATLAB, data from the profiles were filtered with a bandpass filter (5–100 m) and Fast Fourier Transform (FFT) analysis was performed along each profile within windows of length 200 m, with an overlap of 150 m.

Studies of rheology from levees/channelized flows have largely focused on basaltic lava [e.g., *Mazzarini et al.*, 2005; *Wantim et al.*, 2013; *Cashman et al.*, 2013]. *Kerr et al.* [2006] considered the channelized flow of lava on an unconfined slope. They suggest an initial phase of both down-slope and across-slope flow before a later phase of constant width. Lateral spreading is limited by the growth of a cooling crust on the surface of the flow [*Kerr et al.*, 2006; *Deardorff and Cashman*, 2012 – who consider a range in composition from basaltic andesite to dacite]. The width of the flow channel, W, limited in this way depends on the angle of the slope, θ, according to

Eq. 3.2 $$W = 2\left[\frac{(g\Delta\rho)^2 Q^7 \mu^4 \cos^9\theta}{\sigma^6 \kappa^3 \sin^7\theta}\right]^{1/13}$$

which can also be written

Eq. 3.3 $$W = \Phi\left[\frac{\cos^9\theta}{\sin^7\theta}\right]^{1/13}$$

where

Eq. 3.4 $$\Phi = 2\left[\frac{(g\Delta\rho)^2 Q^7 \mu^4}{\sigma^6 \kappa^3}\right]^{1/13}$$

in which g is gravity (m/s^2), $\Delta\rho$ is the density difference between lava and air (kg/m^3), Q is the volumetric flow rate (m^3/s), μ is the viscosity of the lava (Pa s), σ is the effective yield strength of the crust (Pa), and κ is the thermal diffusivity of the lava (m^2/s). We present measurements of channel width versus angle of slope for coulees at Fentale to provide reasonable bounds for volumetric flow rate and emplacement viscosity.

3.3. Results

An overview of the main features of each volcano is presented in **Table 3.2**. Satellite imagery and digital elevation models (DEMs) of Fentale, Gedemsa and Corbetti enable an assessment of geomorphology and geological units, some of which have been mapped previously. Here we compare these DEMs with previously observed features and make new observations of volcanic structures and deposits. In **sections 3.3.1–3.3.4** we present results from each of the volcanoes in this study, including a longer section for Fentale owing to more newly identified features and additional detail from field observations. In **section 3.3.5** we present results from flow morphometry.

In the absence of field observations for most of the study areas, we are unable to distinguish between some deposits formed by lava flows, pyroclastic density currents (PDCs) and other types of flows – we use the term "flow deposit" to describe these. For deposits identifiable as formed by silicic lava flows, we use the term "lava flow" during deposition and "coulee" after deposition.

3.3.1. Fentale

3.3.1.1 Large-scale observations

Fentale is a tall edifice with a narrow and deep caldera (**Figure 3.2**, **Table 3.2**). The edifice footprint is comparable to other MER volcanoes, although burial of the lowest flanks obscures the full extent of Fentale's structure. In places, the low relief outlines of the buried edifice are exposed.

The edifice flanks consist of shallow-sloped (~3–15°) lobate features bounded by steep slopes (**Figure 3.2d**). There are notable flat-topped ridges in the west (oriented E-W) and north (oriented N-S). The higher flanks are steeper, more variable in slope (~10–40°, **Figure 3.2d**) and host a much greater complexity of geomorphological features.

Table 3.2. Attributes of each volcano edifice and caldera in this study.

Volcano	Peak elevation, m	Height*, m	Area*, km^2	Caldera width, km		Caldera long-axis orientation	Caldera relief, m**
				Short axis	Long axis		
Fentale	1940	980	140–200	2.9	4.4	112ºN	150–400
Gedemsa	1940	390	100–130	7.3	9.6	75ºN	0–270
Corbetti	2300	560	220–260	10.9	15.6	104ºN	0–150
Dabbahu	1360	940	180–450	-	-	-	-

*Height and area were estimated by drawing two polygons (minimum and maximum) around the edifice bounding the topographical footprint of each volcano. The area of the edifice was calculated, and the peak elevation minus the lowest elevation at the polygon limits provided an estimation of height.

**An estimate of caldera relief was calculated by subtracting the elevation of the caldera floor near the rim from the elevation at the top of the rim nearby. Minima and maxima are presented for each caldera.

The lobate features with shallow/flat tops are interpreted as flow deposits of the Fentale ignimbrite and other pyroclastic material. The lack of burial by later deposits preserves the geomorphology of older overlapping deposits on the higher flanks.

Fentale's caldera is regular and elliptical, as observed by *Acocella et al.* [2002], although the northern rim of the caldera is straight and forms a linear feature trending ~291º (~WNW-ESE). This trend is in the same direction as the caldera long axis. The elevation of the caldera rim varies between 1600 m and 1850 m (above sea level), with the highest cliffs to the west, to the north and to the south-east. The elevation of the caldera infill ranges from ~1450 m in the west to ~1650 m in the east. The sharp edge of the crater bisects several pre-existing morphological features. Along segments of the crater rim lacking these topographical highs, the rim is lower and more uniform in elevation (north, south-west, north-east). Field mapping shows that variably welded ignimbrite has been deposited in smaller valleys around the caldera (**Figure 3.3**, **3.4B**).

The areas of uniform rim elevation correspond to the major eruption pathways suggested by *Gibson* [1970]. Our observations show that the deposits from the caldera-forming eruption are thickest in pre-existing topographic lows. In the broad valleys between ridges on the south-western side of the edifice, ignimbrite deposition was particularly significant and is associated with distinctive, level topography and relatively even slopes. Surficial deposits at higher elevations may have been lost in later erosion.

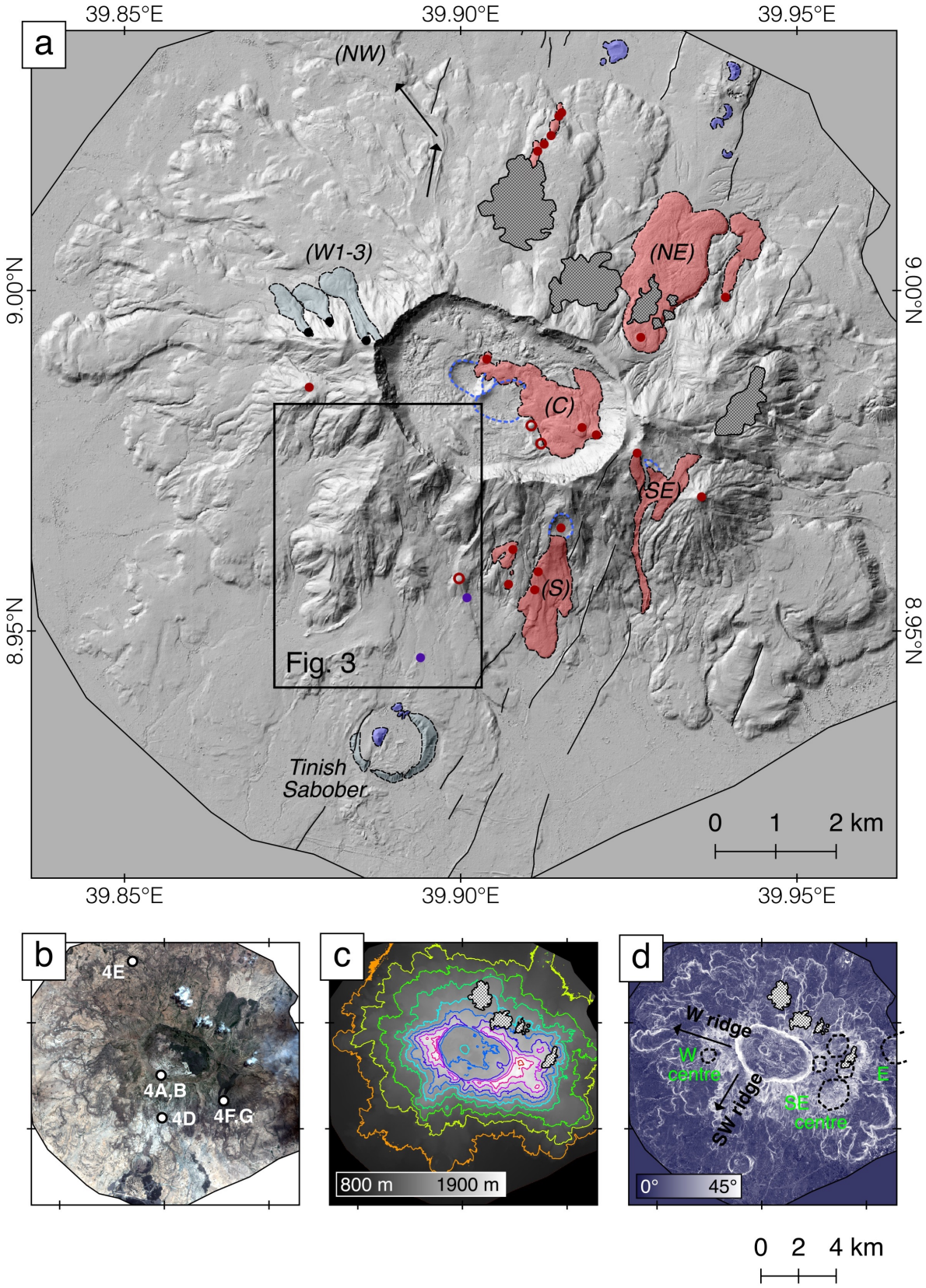
a
39.85°E
39.90°E
39.95°E
9.00°N
8.95°N
(NW)
(W1-3)
(NE)
(C)
(SE)
(S)
Fig. 3
Tinish
Sabober
0 1 2 km
b
4E
4A,B
4D
4F,G
c
800 m
1900 m
d
W ridge
W
centre
SW ridge
SE
centre
E
0°
45°
0 2 4 km

Figure 3.2. Maps derived from the digital elevation model (DEM) of Fentale, clouds are masked in grey. (a) Hillshade map, illuminated from 300ºN. Key features discussed in the text are highlighted, including post-caldera coulees (red), basaltic scoria cones (blue), other notable deposits (grey), craters (blue dashed line), faults (black line) and vents (post-caldera silicic, red; pre-caldera silicic, black). (b) Pansharpened multispectral image of Fentale, locations of photographs in Figure 3.3 are labelled. (c) Elevation map, with contour lines every 100 m. (d) Slope map, with key ridges and domes labelled.

Two ridges, aligned W and SSW, project from the caldera on the western side of the edifice (**Figure 3.2c-3.2d**). A number of dome-shaped structures are clustered on the eastern side of the edifice, oriented approximately NNE-SSW, including the south-east center of *Gibson* [1967]. The east and west centers are also apparent, in addition to minor domes at the bottom of the upper flank to the south. The tallest point on the edifice is the peak of a dome close to the eastern rim of the caldera.

3.3.1.2 Coulees

Young post-caldera obsidian coulees are observable from the topography and were mapped by *Gibson* [1967, 1974]. The morphology of the coulees is strongly controlled by pre-existing topography, forming narrow channels down steep valleys (e.g., south-eastern and south-western flanks; **Figures 3.2a**, **3.3**). Field observations from the coulee on the south-eastern flank (SE, **Figure 3.2a**) show a crystallinity of ~10% and reveal the presence of crystal cumulates (**Figure 3.4F-3.4G**). Coulees along the western ridge (W1-3, **Figure 3.2a**) are onlapped by the Fentale ignimbrite and are therefore pre-caldera.

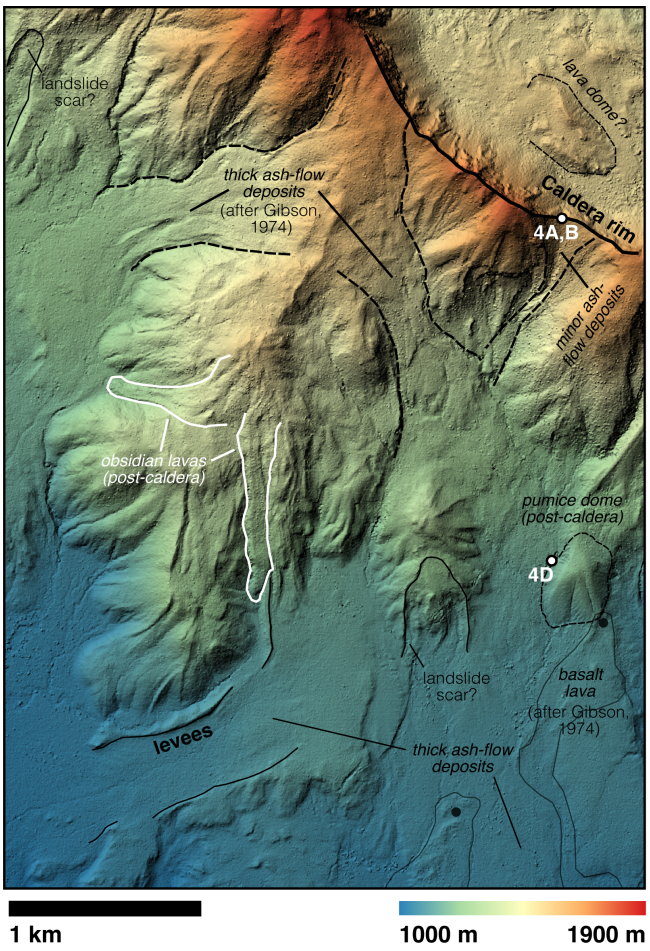

Figure 3.3. Combined hillshade and elevation map of the south-west ridge of Fentale, with features labelled. The limits of the basalt lava and thick ash deposits are after *Gibson* [1974], the rest of the features are newly identified in this study using a combination of field and DEM observations (section 3.3.1.3).

The coulee on the north-eastern flank (NE, Figure 3.2a) exhibits flow wrinkles, or ogives, that form double chevrons due to the extended flow in two neighboring valleys. Levees are common in both pre- and post-caldera coulees, across the lower flanks of the edifice, and around the dome-shaped structures on the eastern flank. They range in width between 30 and 400 m. An obsidian coulee on the north west side of the edifice (NW, Figure 3.2a) displays well-formed levees accompanied by a break-out structure as the channel is deflected by ~60º. The coulee fans out on the horizontal plain which surrounds the edifice, forming enigmatic ripple structures. Much of this coulee is covered by variably welded ignimbrite, as observed in the field (Figure 3.4E). The partial burial of pre-caldera lava coulees with ignimbrite is a common observation across the lower flanks of Fentale.

Table 3.3. Volumes of features on each volcano (see figures for locations: Fig 3.2a, Fentale; Fig 3.5a, Gedemsa; Fig 3.6a, Corbetti; and Fig A2.5 for summary), with an approximate error of 25% [see methodology; *Nomikou et al.*, 2014; *Hutchison et al.*, 2016a].

Volcano	Feature	Volume, km^3	Area, km^2	Vol/Area, m
Fentale	**Total silicic post-caldera**[†]	**< 1.0**		
Individual features	Dome* (W)	**0.061**	6.08	10
	Lava coulee (S)	**0.015**	3.84	3.8
	Lava coulee (NE)	**0.091**	9.72	9.4
	Lava coulee (C)	**0.034**	12.0	2.8
	Lava coulee (W1)	**0.0038**	1.84	2.1
	Lava coulee (W2)	**0.0029**	1.31	2.2
	Pumice cone	**0.0036**	1.33	2.7
	Tuff ring	**0.0054**	2.88	1.9
Gedemsa	**Total silicic post-caldera**[†]	**< 1.0**		
Individual features	Intra-caldera deposits	**0.57**	51.9	11
	Dome (E)	**0.11**	9.96	11
	Dome (SW)	**0.11**	7.37	15
	Dome (NW)	**0.021**	4.32	4.9
	Scoria cone (NE)	**0.013**	3.32	3.9
	Scoria cone (SE)	**0.0061**	2.49	2.4
	Scoria cone (SW)	**0.0043**	2.33	1.9
	Scoria cone (W)	**0.0039**	1.48	2.6
Corbetti	**Total silicic post-caldera**[†]	**14.5**		
Individual features	Artu	**0.61**	48.7	12
	Urji	**6.36**	133	48
	Chabbi	**7.53**	169	45
	WKYP flow deposit	**0.26**	16.8	15
	Lava coulee (CO6)	**0.47**	40.5	12
	Tuff ring	**0.038**	9.72	3.9

*Domes may be composite structures, formed of multiple events.
[†]Estimated by summing individual features for Fentale and Gedemsa, and summing the Artu, Urji and Chabbi for Corbetti. Additional post-caldera features may be unaccounted for at Fentale and Gedemsa.

Table 3.4. Attributes of lava coulees on Fentale, including aspect ratios at successive points away from the vent. Location labels refer to Figure 3.2a.

Location	UTM of vent(s) (easting, northing)	Length, m	Aspect ratio			Width of levees, m	Average slope (channel), °
			Width, m	Height, m	W/H		
Western ridge (W1)	4439129, 1005311	1040	85 135 328 240	17 17 44 28	5.0 7.9 7.5 8.6	-	-
Western ridge (W2)	4439483, 1005474	970	113 278 395 448	17 28 38 30	6.6 9.9 10.4 14.9	-	-
Western ridge (W3)	4440089, 1005138 4440338, 1005122?	1350	90 142 510 533	15 18 40 32	6.0 7.9 12.8 16.7	20–50	25.5
North-west	4441137, 1006918?	~5000	287 1313 2174	16* 35* 44*	17.9* 37.5* 49.4*	60–140	5.4–7.0
SW ridge (see Fig 3.3)	4439917, 1002394?	>1090	85 85 121 113	10 12 12 18	8.5 7.1 10.1 6.3	-	-
S slope (S)	4443244, 1001995 4442924, 1001366 4442885, 1001080	2110	520 563	58** 24	9.0** 23.5	-	-
SE dome	4444570, 1003332 4445276, 1002800	2520	134 148	11 5	12.2 29.6	30-70	11.9
Caldera (C)	4443637, 1003769 4443903, 1003637 4442444, 1004767? 4442090, 1004891?	2340	717 335	30 27	23.9 12.4	-	-
NE slope (NE)	4444656, 1005290	2510	738 1200 1139 1219	49 53 33 47	15.1 22.6 34.5 25.9	-	-

*Affected by later deposition of ignimbrite.
**Height affected by uncertainties over pre-eruptive topography.

Several small volume features accompany the coulee on the southern flank (400×400 m), mapped as post-caldera obsidian lavas by *Gibson* [1967, 1974]. Further features are identified on the northern flank which we propose as additional small lava coulees (150×300 m), though field observations are required for validation. Vent spacing ranges from 200 m up to 2,000 m for the larger flows.

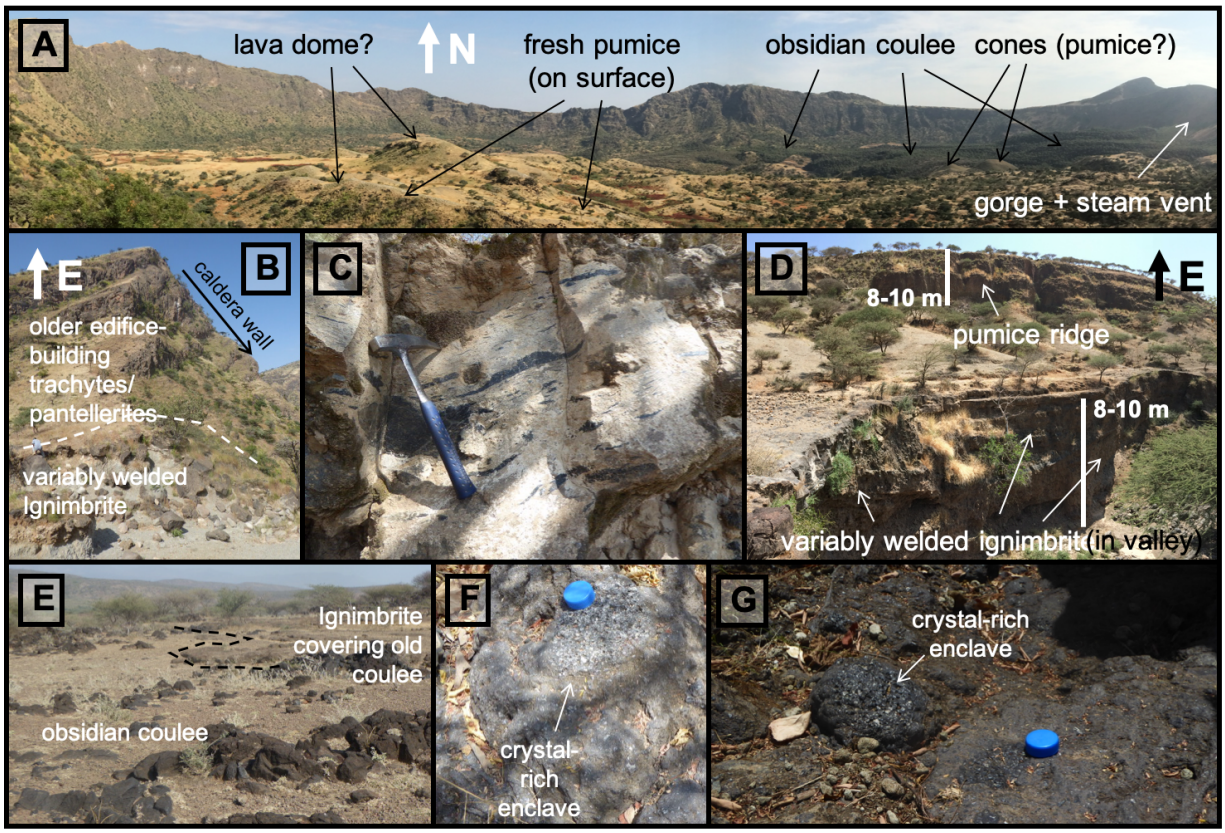

Figure 3.4. Field photographs from Fentale; locations are labelled in Figures 3.2-3.3. (A) Panorama of caldera, including evidence of post-caldera eruptions. (B) Ignimbrite in small valley near the caldera rim (photograph taken from same location as A). (C) Example of fiamme within welded section of ignimbrite. (D) Pumice ridge and ignimbrite within a valley, southern flank of Fentale. (E) Example of ignimbrite partially covering the pre-caldera obsidian coulee, north-west Fentale. (F)-(G) Crystal-rich enclave in post-caldera obsidian coulee, south-east flank of Fentale.

Volumes have been calculated for the lava coulee within the caldera (C, 0.034 km^3) and for the coulees on the north-eastern (NE, 0.091 km^3) and southern flanks (S, 0.015 km^3; **Table 3.3**). Pre-caldera coulees on the western ridge are much smaller in volume (0.003-0.004 km^3).

The coulees on the western ridge have lengths of ~1 km compared to 2–2.5 km for post-caldera coulees (**Table 3.4**, **Figure 3.2a**). The larger pre-caldera coulees, evidenced by relict flow morphology now partially buried, have lengths up to and exceeding 5 km. The coulees on the western ridge (W1-3) have variable aspect ratios, starting low (~5–8) and increasing away from the vent as the pre-eruptive slope shallows (ending ~10-14; **Table 3.4**). Coulees on the south-west ridge and the north-east slope end with a lower aspect ratio – we interpret this as the flow stopping prior to build up at the flow nose (**Figures 3.2a**, **3.3**).

3.3.1.3 Additional observations

A broad crater to the south of the edifice named Tinish Sabober was mapped as a tuff ring by *Gibson* [1967] and *Williams et al.* [2004; **Figure 3.2a**]. The ring is buried in places by deposits including the Fentale ignimbrite, suggesting that it pre-dates the caldera-forming eruption. The surviving topography of the tuff ring provides a minimum volume estimate of 0.0054 km^3 (**Table 3.3**).

Two craters are nested in the center of the caldera, with areas of 0.2 and 0.05 km^2. The larger crater is elongated in the WNW-ESE direction, similar to the caldera, whereas the smaller crater is elongated in the NNE-SSW direction, along the rim of the larger crater (**Figure 3.2a**). The craters precede the emplacement of the

obsidian coulee. The presence of additional craters, cones and domes, together with observations of surficial pumice, suggests multiple intra-caldera explosive and effusive eruptions (**Figure 3.3**; **section A2.2**).

There is a steep gorge down the caldera rim on its eastern side; we observed a column of steam rising from the base of this gorge, suggesting the presence of a hot spring or fumarole. We interpret the alignment of vents, a geothermal manifestation and a steep gorge as evidence of a fault striking ~ESE.

Additional post-caldera deposits have also been observed on the flanks of the edifice. A pumice cone is located at the base of the southern upper flanks (**Figure 3.3**), and is associated with a fresh pumice deposit distributed across the nearby slopes. A new obsidian coulee was also observed along the south-west ridge, overlying the variably welded ignimbrite (**Figure 3.3**). Further post-caldera deposits may yet be unmapped on Fentale given the size and inaccessibility of the volcano – this remains a priority for further study. Concave structures have been identified as possible landslide scars in a number of locations (**Figure 3.3**), indicating the potential for collapse of unstable slopes on the flanks of the edifice.

The recent basaltic volcanism is visible on the satellite imagery (**Figure 3.2b**) but produces negligible topography. The vents are not easily identifiable but seem to have a strong association with rift-related faults/fissures and NNE-SSW trend, encroaching onto the edifice [*Williams et al.*, 2004]. The most northerly basaltic vent is located close to the pumice cone on the southern flank of the volcano (**Figure 3.3**).

Regional normal faults, striking ~NNE, intersect the edifice creating offsets of up to 10–15 m. Faults are particularly prevalent on the western side of the edifice, along with the majority of post-caldera eruptive vents (**Figure 3.2a**). Associated with regional normal faults, basaltic cones have been emplaced to the north and south of the edifice (**Figure 3.2a**, **section A2.2**).

Blister structures hosted by the ignimbrite are particularly prevalent on the flat plain to the south, close to the present-day Lake Metehara. We mapped blisters across an area of 1.5 km^2 and found no systematic variation of size or orientation (**section A2.2**, **Figures A2.3-A2.5**). The low-lying ground could have been a source of groundwater which boiled after burial by ignimbrite, providing steam which expanded to form the blisters, in a manner analogous to the formation of rootless cones [*Baloga et al.*, 2007; *Fagents and Thordarson*, 2007].

3.3.2. Gedemsa

The edifice of Gedemsa is broad and shallow, and has been largely evacuated by caldera forming eruptions (**Figure 3.5**, **Table 3.2**). The remaining edifice forms a broken, arcuate structure with its highest elevations to the east (1900 m) and south (1950 m; **Figure 3.5c**). The pre-caldera edifice is the most extensive in the north-east, in the form of broad, fault-cut lobes, and in the south, with a ridge projecting southwards (**Figure 3.5b-3.5c**).

A ridge to the west forms the limit of the edifice and the eastern limit of Lake Koka, striking NNE along a regional normal fault (**Figure 3.5b**). Two or three pantellerite domes/coulees with volumes of ~0.02–0.1 km^3 form satellite centers up to 9 km

from the center of the Gedemsa caldera. The significant fault which delineates the ridge also dissects a dome in the NW suggesting continuation of fault activity after dome emplacement (**Figure 3.5b**).

Numerous normal faults cut through the eastern side of the caldera with variable offsets both on the old edifice and on the caldera floor (**Figure 3.5**). Within the caldera the faults appear to splay into multiple fractures of smaller offset – we suggest that this is the result of lower cohesive strength of lake sediments in the shallow subsurface. These faults are not co-located with volcanic products but are apparently independent from the activity of Gedemsa volcano.

The caldera wall is heavily and variably eroded, and partially covered by later deposition of lake sediments. It hosts several embayments and arcuate features on its eastern end related to rift-related normal faults (**Figure 3.5a**). The northern and southern sections of the caldera are straight and parallel; we suggest this indicates a possible influence of cross-cutting structures striking ~ENE-WSW.

The elevation of the caldera floor ranges from ~1570 m in the north to nearly 1700 m in the south, immediately to the west of the regional normal faults (**Figure 3.5c**). The center of the Kore crater has an average elevation of ~1620 m. The crater predates the dome that partially covers its north-east rim. The central domes vary in morphology from smooth and gentle topography to incised (**Figure 3.5a**). The westernmost of the three coalesced domes, Kelo, hosts a ridge striking NE-SW in line with a portion of the caldera wall to the NE. The ridge is highly incised by valleys in comparison to the two domes at each end of the ridge, perhaps suggesting an older age or softer material.

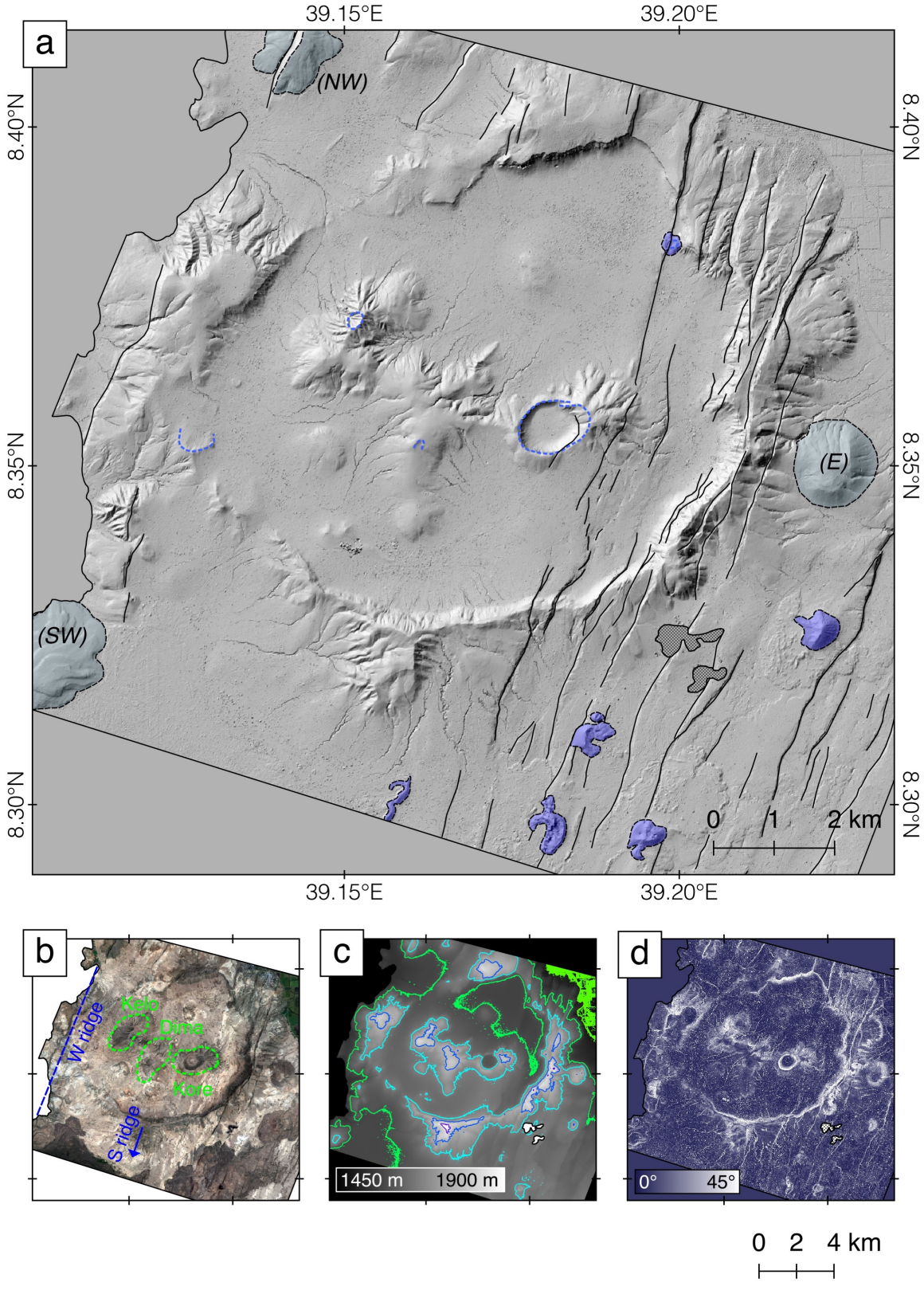
a
39.15°E
39.20°E
8.40°N
8.35°N
8.30°N
(NW)
(E)
(SW)
0 1 2 km
b
W ridge
Kelo
Dima
Kore
S ridge
c
1450 m
1900 m
d
0°
45°
0 2 4 km

Figure 3.5. Maps derived from the digital elevation model (DEM) of Gedemsa, clouds are masked in grey. (a) Hillshade map, illuminated from 300ºN. Key features discussed in the text are highlighted, including basaltic scoria cones (blue), other notable deposits (grey), craters (blue dashed line) and faults (black line). (b) Pansharpened multispectral image of Gedemsa, with key ridges and domes labelled. (c) Elevation map, with contours every 100 m. (d) Slope map.

Additional areas of elevated relief are also observed within the caldera: a broad prominence is located in the northern half of the caldera, with three or four steeper hills in the south (**Figures 3.5a**, **3.5c**). These may be related to activity post-dating caldera formation but older than the formation of the Kore crater and related domes.

Basaltic cones and lava flow deposits have been erupted along faults to the south-east of the caldera, and are themselves cut by later activity along the same faults (**Figure 3.5a-3.5b**). Cones and lavas are closely attributed with each other, suggesting single events for emplacement of both cone and lava flows as is observed elsewhere in the rift (e.g., west of Fentale, east of Tulu Moje).

A feature inside the NE caldera wall is identified as the scoria cone associated with an ash-rich deposit (**Figure 3.5a**). This cone is cut by later activity on a fault, and is located at the intersection between a fault and a sharp change in strike of the caldera wall.

3.3.3. Corbetti

The high-resolution DEM produced in this study (**Figure 3.6**) allows the identification of 30 craters across the Corbetti Volcanic Complex, an additional 14 to those mapped previously [**Figure 3.6a**; *Lloyd et al.*, 2018a]. Craters are

Figure 3.6. Maps derived from the digital elevation model (DEM) of Corbetti. (a) Hillshade map, illuminated from 300ºN. Key features discussed in the text are highlighted, including post-caldera coulees (red), pumice flow deposit (purple), other notable deposits (grey), craters (blue dashed line), faults (black line) and coulee vents (red circles). The speckled effect is produced by vegetation which is largely below the resolution of the DEM. (b) Pansharpened multispectral image of Urji and the limits of the Chabbi lidar dataset. (c) Elevation map, with contours every 100 m. (d) Slope map, with Artu, Urji and Chabbi edifices labelled.

distributed WNW-ESE across the complex in two broad swaths. The craters range in diameter from 150 to >1,500 m and are commonly highly elliptical, with long axes trending WNW-ENE and N-S. In several cases, multiple small craters are coalesced forming a longer depression (**Figure 3.7a**).

Urji (2230 m) forms a lower and broader edifice than Chabbi (2300 m) as shown on the elevation and slope DEMs (**Figure 3.6c-3.6d**). This is in part due to Urji's predominately explosive history, creating an edifice mainly of ash, pumice and other fall deposits. On the other hand, Chabbi's numerous effusive eruptions have created a steeper edifice mainly comprising obsidian lava coulees. Despite the greater flux from Chabbi over the last 2300 years, the edifices of Urji (6.4 km^3) and Chabbi (7.5 km^3) are similar in volume (**Table 3.3**).

The highly incised surface morphology of Urji suggests an older age than Chabbi on average, as well as the softer material with which it is formed (**Figure 3.6a**). Two main domes form the bulk of Urji's edifice (**Figure 3.6c-3.6d**), aligned along with the southern swath of craters WNW-ENE. A large cone creates the highest

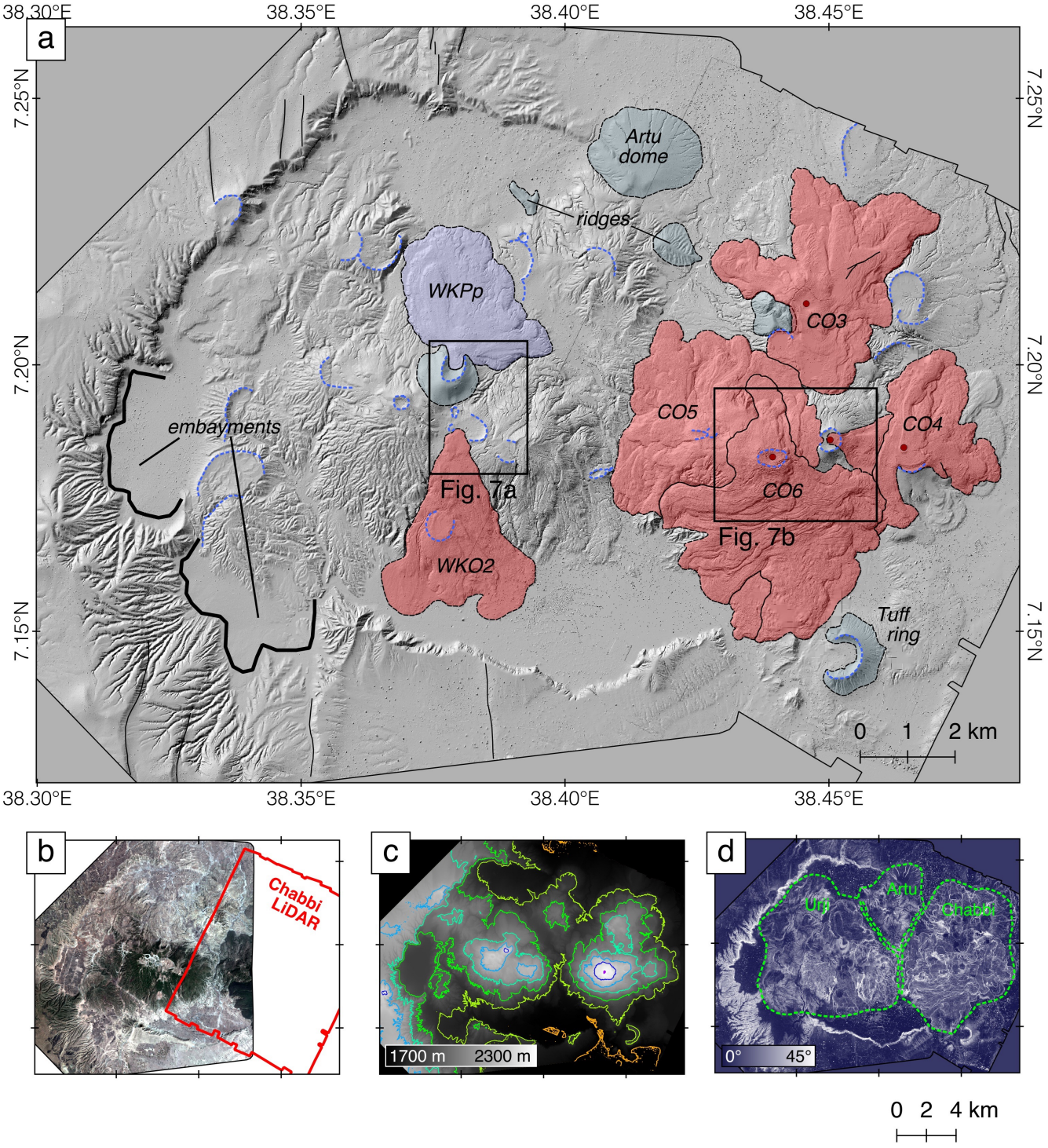

point on the edifice, mapped by *Rapprich et al.* [2016] as the Wendo Koshe young cone. Two flow deposits are apparent on Urji. A high-relief, lobate deposit originates from northern rim of the summit cone and crater, mapped by *Rapprich*

et al. [2016] as a pumice deposit associated with the WKYP emplaced predominantly by flow (WKPp, **Figure 3.6a**). To the south of the summit cone and emanating from between the two main domes, a lower relief obsidian coulee covers the flank of Urji, including a crater part way down the slope (WKO2, **Figure 3.6a**).

The large obsidian coulees on Chabbi are clearly recognizable on the hillshade DEM (**Figure 3.6a**) as are their ogives, which reveal the direction of flow in some places (**Figure 3.7b**). The coulees have originated from single vents, many of which are large, elongated craters that may be the product of preceding explosive activity. The source regions of other coulees have been fully buried, however the topography is depressed possibly indicating the presence of a crater (**Figure 3.7b**). Coulees partially cover pre-existing, incised deposits which form steep cones at the sides of the coulee edge, e.g., on the NW and SW flanks of Chabbi.

The obsidian coulees form large lobes in multiple directions as they radiate out from the source, with typical widths of 300–500 m. Typical runout distances are 2–3 km. The most recent obsidian coulee (CO6) is of similar magnitude (0.47 km^3; **Table 3.3**) to the DRE (Dense Rock Equivalent) of WKYP [0.4 km^3; *Rapprich et al.*, 2016]. There are six mapped lava coulees associated with Chabbi – assuming a similar magnitude for each coulee, ~2.4 km^3 of lava is accounted for. The total volume of the Chabbi edifice is 7.5 km^3, implying a number of completely buried coulees and/or extensive explosive deposits to account for the remaining erupted volume.

The older edifice of Artu is smaller (0.6 km^3) but hosts several large craters and two ridges running ~WNW-ESE (**Figure 3.6a**). A broad dome (diameter ~ 2 km,

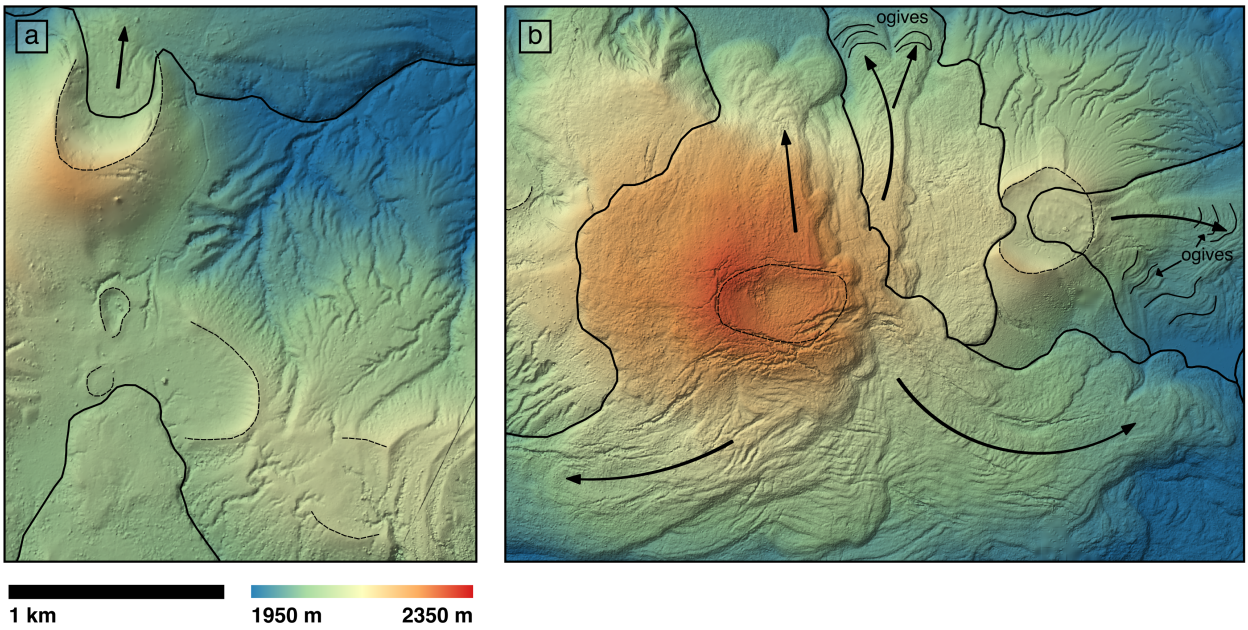

Figure 3.7. Combined hillshade and elevation map of craters (dotted lines) and flow deposits (solid lines) mapped in this study from (a) Urji, and (b) Chabbi.

height ~ 100 m) to the north is located along the extension of the northern rim of the caldera. Much of the original Artu edifice may now be buried by sediment filling the caldera.

The Corbetti caldera is irregular and segmented, delineated by a steep cliff along its northern and southern rim and a broad, incised slope on the western side (**Figures 3.6a**, **3.6d**). The overall shape is governed by linear features, including a NE-SW trending wall on the western side and a WNW-ESE trending walls on the north and south. As noted by previous authors, the eastern side of the caldera is covered by the Chabbi edifice [e.g., *Di Paola*, 1971]; the presence or absence of an original caldera rim on this side cannot be confirmed.

The elevation of the caldera floor ranges from 1700–1850 m, lowest in the area south of Urji and Chabbi and highest to the west of Urji (**Figure 3.6c**). The area

outside of the caldera on the west is also elevated with respect to the area to the south of the caldera. The activity of rift-related faults may have caused the central section of the complex to subside with respect to the areas to the west. Later deposition may also have been greater in the western side of the caldera.

The western side of the complex is cut by numerous normal faults visible to the north and south of the volcano but no offsets visible within the caldera. Faults have not disrupted volcanic products and sedimentary deposits, implying either recent deposition, a lack of recent fault activity, or the discontinuation of faults at the volcanic margins. There is a notable embayment in the south-western corner of the caldera, forming a highly eroded, broad slope adjacent to a steep cliff (**Figure 3.6a**).

The intersection of normal faults with the caldera rim is coincident with areas of caldera rim deflection. This is most clearly seen in the NW and SW of the caldera, where small offsets in the caldera rim are aligned with regional faults and the northern corner of the caldera is coincident with intersection of a fault (**Figure 3.6a**).

Basaltic volcanism is less prevalent in the Corbetti area than around Fentale or Gedemsa – no basaltic volcanism has been identified within the caldera limits. Scoria cones can be found to the south east near the town of Awassa, and to the north towards O'a caldera along regional faults (see **Figure 3.9**).

3.3.4. Dabbahu

The edifice of Dabbahu is tall and steep (**Table 3.2**), with two main summits aligned NW-SE (1320 m and 1370 m; **Figure 3.8**). The summits are linked by

ridges trending E-W and N-S, with a lower, parallel N-S ridge to the east. The northern flank of the edifice is much steeper on average than the south (**Figure 3.8c**). An area to the east of the highest summit has a relatively shallow slope surrounded by a steep cliff (**Figure 3.8b-3.8c**) – this is an area of proposed caldera in-fill [*Field et al.*, 2013]. A number of satellite centers are located to the northeast of the main edifice, each of which is elongated in the N-S direction.

The DEM shows curved faults in the southwest of the study area that form rims of proposed caldera structures. Offsets of ~10 m cut through the ~E-W ridge protruding from the main summit, suggesting movement on the curved fault more recently than formation of the ridge. In the case that the curved faults in the southwest form an elliptical caldera with the buried caldera rim to the northeast (dashed line, **Figure 3.8a**), the proposed caldera would have a long-axis width of 6–8 km. This caldera would be comparable in size to many of those in the Main Ethiopian Rift. The ellipticity of this caldera would trend at 45/225–60/240°, oblique to local fault trends.

Many of the vents, craters and scoria cones are closely associated in N-S fissure swarms. Craters and coulee vents are co-located, e.g., on the western N-S ridge (**Figure 3.8a**), suggesting a combination of explosive and effusive eruptions within the same event. Separate coulees are difficult to identify along the ridge, although a difference in color observed from freely available satellite imagery (via Google Earth) is able to distinguish between a set of recent coulees and the pre-existing ridge. The ridge therefore comprises of more than one episode of activity from N-S trending fissures. The coulees form narrow (300–500 m) channels with runouts

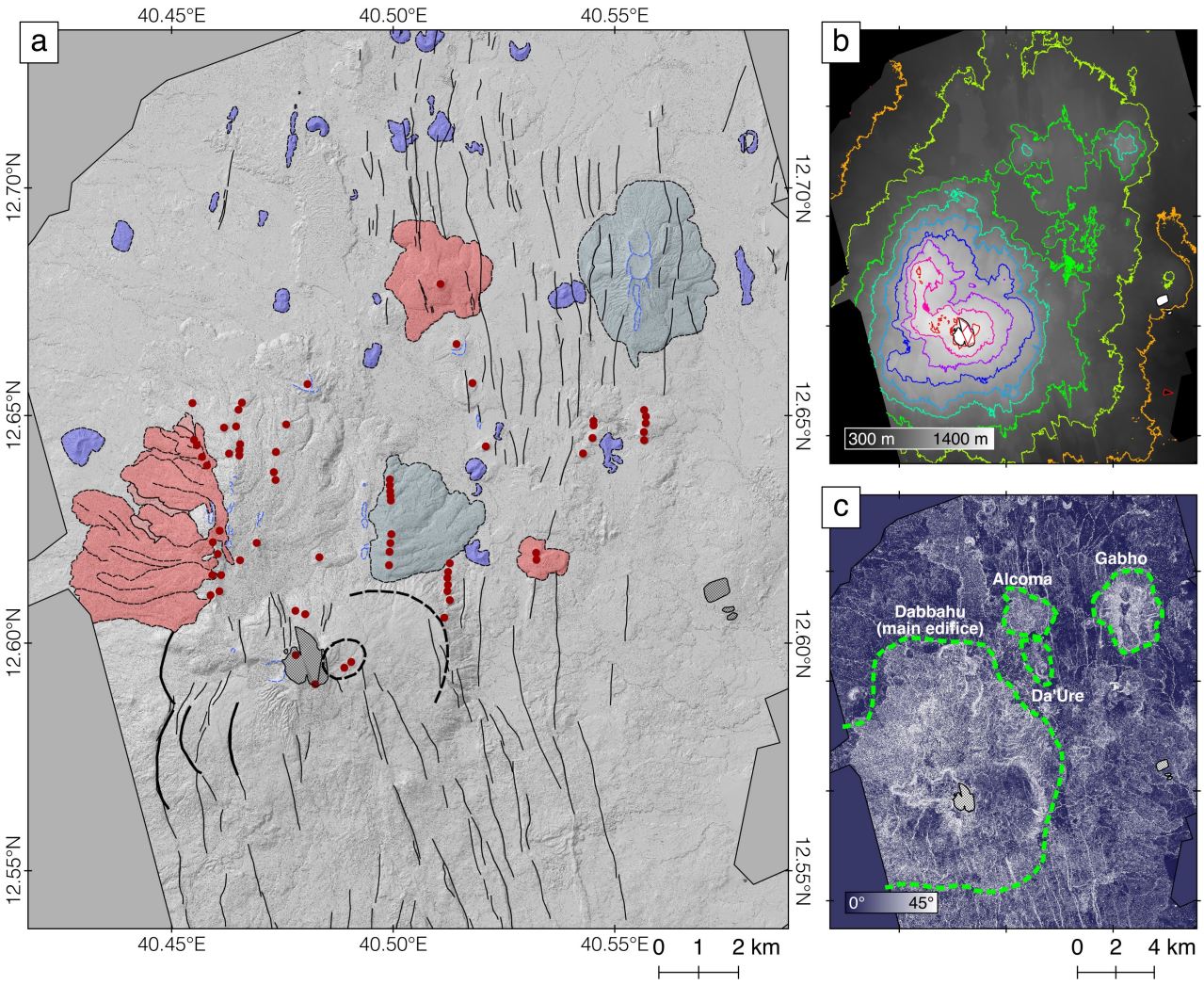

Figure 3.8. Maps derived from the lidar digital elevation model (DEM) of Dabbahu, data gaps are masked in grey. (a) Hillshade map, illuminated from 300ºN. Key features discussed in the text are highlighted, including post-caldera coulees (red), basaltic scoria cones (blue), other flow deposits (grey), craters (blue dashed line), faults (thin black line), possible caldera faults (thick black line), proposed caldera limits (dashed black line) and silicic vents (red circles). (b) Elevation map, with contours every 100 m. (c) Slope map, with the central Dabbahu edifice and Alcoma, Da'Ure and Gab'ho satellite centers labelled.

of ~3.5 km and host ogives and lobes similar to those on Fentale and Corbetti. The satellite center of Alcoma also hosts a broad coulee, which radiates in many

directions, forming several lobes (**Figure 3.8a**).

A line of craters aligned N-S are parallel to more rhyolite vents forming a N-S ridge in the north east of the main edifice and feeding a series of flow deposits (**Figure 3.8a**). Another line of nested craters runs through the center of the Gab'ho edifice to the north east, which is also cut by numerous faults (**Figure 3.8a**).

The majority of identifiable silicic vents and craters are to the north of the main summit of Dabbahu. Older deposits of trachyte/trachyandesites and rhyolites to the southwest [*Field et al.*, 2013] may suggest a progression of silicic activity from the southwest to the northeast over time. This remains a hypothesis to test by field work, dating and further mapping.

Extensive basaltic trachyandesites are found across the area in the form of scoria cones and associated lavas. The cones are commonly aligned along faults and/or in N-S fissures (**Figure 3.8a**). The cones are larger than the basaltic scoria cones observed near Gedemsa. Whilst scoria cones are not identified on the silicic edifices, *Field et al.* [2013] mapped deposits of basaltic trachandesite across a large area on the eastern flank of the main edifice and suggested that the bulk of the main edifice was basaltic on the basis of exposure in river beds.

Faults are concentrated to the south of the main Dabbahu edifice and to the northeast among the satellite centers. To the south they trend approximately NNW-SSE whereas to the northeast they trend ~N-S with some examples of NNE-SSW (**Figure 3.8a**). Whilst faults cause large offsets on the southern flank of the edifice, they do not cut the more recent deposits on the northern flank. Concentration of

faults in localized areas, each with a characteristic orientation, is common across the Afar region (see Figure 3.12).

Table 3.5. Apparent yield strengths, from measurements of thickness and slope using Eq. 3.1 (assuming a bulk density of 2300 kg/m^3), of 3 lava coulees from Fentale identified in the field. Thickness was estimated from the difference in elevation between the coulee and an estimated pre-eruptive surface.

Location	UTM of vent(s) (easting, northing)	Thickness, m	Slope, °	Apparent yield strength, kPa
Western ridge	4440089, 1005138 4440338, 1005122?	15–40	26	150–400
North west	4441137, 1006918?	15–40	5–7	30–110
SE dome	4444570, 1003332 4445276, 1002800	5–10	12	23–47

3.3.5. Flow morphometry

The lava coulees on Fentale and Corbetti display distinctive morphology which provides insight into the eruptive dynamics of each system. Table 3.5 shows the estimates for apparent yield strengths on the basis of deposit thickness and slope for three of the coulees on Fentale (using Eq. 3.1 from section 3.2). Yield strengths are not estimated for the larger coulees on Corbetti due to uncertainties over pre-eruptive surface and variable slope/thickness. The estimates from Fentale range from 20–390 kPa; the lower estimates are in the approximate range for dacites [e.g., 30–70 kPa; *Pyle and Elliott*, 2006] and the upper estimates are in the range for

rhyolites and trachytes [e.g., 80–400 kPa; *Moore et al.*, 1978, *Wadge and Lopes*, 1991].

Figure 3.9 shows profiles along coulees hosting ogives, and results of analysis for two coulees on Corbetti and one on Fentale. Contoured periodograms show the FFT (see **section 3.2**) results by relative power (arbitrary scale) of fold wavelengths at each window location along the length of the flows. Ogives of wavelength 20–100 m are observed. Multiple generations of folds are visible for each coulee. The Corbetti coulees exhibit folds at the scale of 80–100 m, 30–50 m and 22–28 m, with a faint signal from small-scale folds of wavelength ~17–20 m. The folds in the first panel progress to longer wavelengths down-slope. In contrast, the longer wavelengths are more dominant up-slope in the second panel, where the shorter

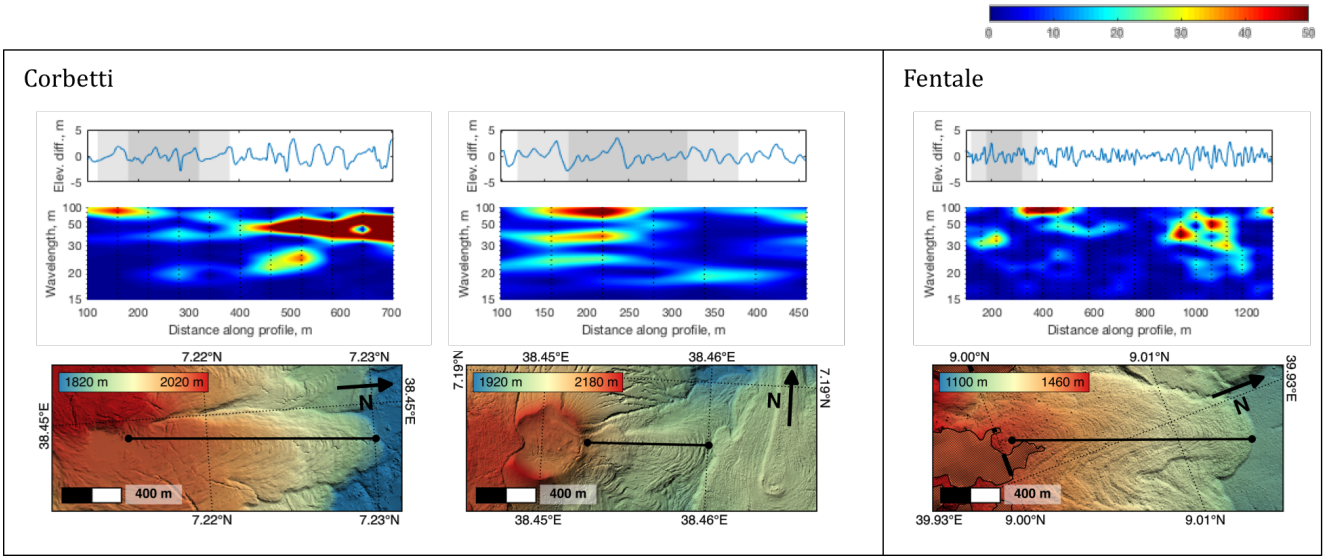

Figure 3.9. *Top:* Profiles along lava coulees from Corbetti and Fentale exhibiting wrinkles/ogives. *Middle:* Contoured periodograms showing the dominant wavelength of ogives with distance along profile, with two example windows for each profile shaded grey. *Bottom:* Combined hillshade and elevation maps of coulees showing ogives and profile lines.

wavelength folds are clearer down slope. This may indicate differences in flow thickness along the flow, and therefore thickness of the cooling surface.

The wavelengths of folds on the Fentale lava coulee are less consistent, however there exist folds of similar wavelengths to those observed on Corbetti. Folds of wavelength 30–50 m and 80–100 m are observed early in the profile and reappear towards the end of the coulee, along with shorter wavelengths of 18–25 m.

The abundant levees at Fentale enable further constraints on lava rheology. The widths of leveed channels on Fentale are plotted against the average slope of the channel in **Figure 3.10**. The average slope of the channel is a proxy for the

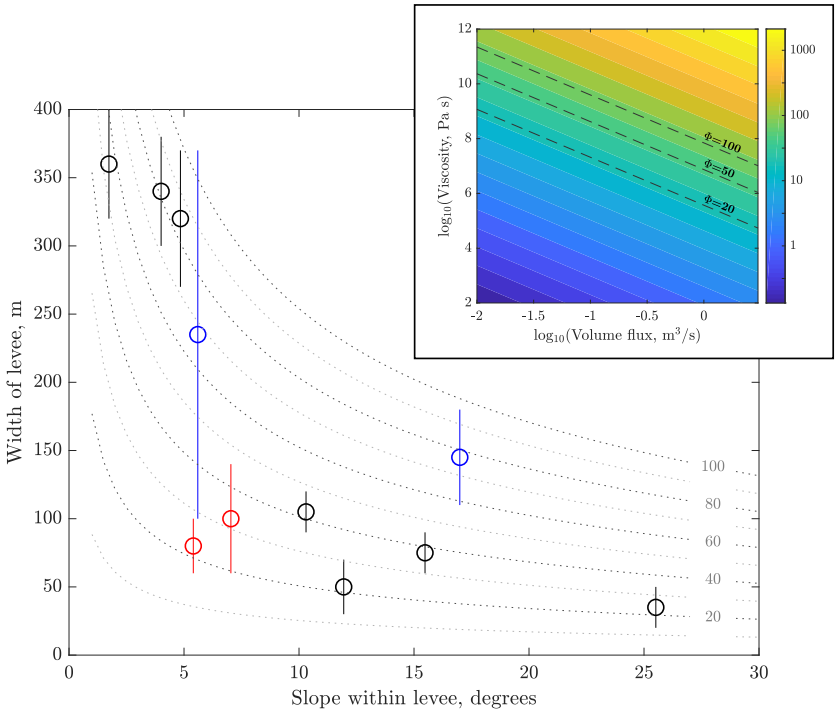

Figure 3.10. Relationship between levee width and slope within levees for 11 sets of levees on Fentale, including pre- and post-caldera coulees. In two coulees, two sets of levees are found at different distances from the vent – these are identified in red and blue. Dotted lines show the relationship predicted by equations 2–4 for Φ = 10–100 defined in equation 3.4 (section 3.2), a coefficient combining material properties of the lava and the volume flux of the eruption. *Panel:* Dependency of Φ on volume flux and viscosity according to equation 3.4, assuming values of density (2300 kg m^{-3}), yield strength (3×10^5 Pa) and thermal diffusivity (5.5×10^{-7} m^2/s).

slope of the pre-eruptive surface, assuming an approximately constant thickness. Narrow channels form on steeper slopes, whilst broader channels form on shallow slopes.

The predicted relationship between channel width and angle of slope from the *Kerr et al.* [2006] model is shown in **Figure 3.10** for a range of Φ values (see **Eqs. 3.2–3.4** in **section 3.2**). The data are consistent with the general shape of the relationship, for Φ values of ~20–100 m. The panel in **Figure 3.10** presents Φ values for a range of viscosities and flow rates, assuming a density difference of 2300 kg/m^3, an effective yield strength of the cooled crust of 3×10^5 Pa [*Fink and Griffiths*, 1998; *Castruccio et al.*, 2013] and a thermal diffusivity of 5.5×10^{-7} m^2/s [*Romine et al.*, 2012]. For maximum Φ values of 100 m, the maximum viscosity is ~10^{11} Pa s for a flow rate of 0.02 m^3/s and ~10^8 Pa s for a flow rate of 2 m^3/s.

3.4. Discussion

Having assessed volcanic features and observed previously unidentified deposits, we use the DEMs to compare centers along the length of the Main Ethiopian Rift (MER), and between the MER volcanoes and Dabbahu. We compare caldera architecture (**section 3.4.1**), identify vent and crater alignments (**section 3.4.2**), estimate eruptive volumes and frequencies along the rift (**section 3.4.3**) and assess the morphometry of peralkaline lava deposits (**section 3.4.4**).

Figure 3.11 shows structural observations of the three MER volcanoes in this study, alongside two volcanoes previously studied using remote sensing. Aluto volcano has been the subject of a number of recent studies [e.g., *Hutchison et al.*,

2016b; 2016c; *Samrock et al.*, 2015; *Gleeson et al.*, 2017; *Wilks et al.*, 2017b], including the use of a lidar DEM to identify structural features [*Hutchison et al.*, 2015]. The geological evolution of Boset volcano has been studied by *Siegburg et al.* [2017] using a lidar DEM in addition to field work, geochemistry and geochronology. **Figure 3.12** shows structural observations of Dabbahu within the context of the Afar region, with faults across the region redrawn using the Aster Global Digital Elevation Model (GDEM) and previously published maps [*Barberi and Varet*, 1977; *Donovan et al.*, 2018].

3.4.1. Caldera architecture

The overall structures of Gedemsa, Corbetti and Fentale vary widely. The edifice of Fentale is taller than that of Gedemsa and Corbetti, and whilst Fentale's footprint is similar to that of Gedemsa, the footprint of Corbetti is notably larger (**Table 3.2**). The difference in edifice structure is largely due to the difference in caldera architecture – the caldera of Fentale is deep and narrow, whereas the formation of the broad calderas of Corbetti and Gedemsa were presumably accompanied by the subsidence of a larger proportion of their ancestral edifices. The regular and elliptical shape of Fentale's caldera is also in contrast to the calderas of Gedemsa and Corbetti, which are heavily and variably eroded, and partially covered by later deposition of lake sediments. This may be related to the influence of faults, erosion rates and age of the calderas.

Only short segments of the calderas at Aluto and Boset are unburied. *Hutchison et al.* [2015] proposed the approximate location of a caldera fault at Aluto on the basis of vent and crater locations. The proposed caldera is larger than that of Fentale and

the low and broad edifice of Aluto may suggest a broad and shallow underlying caldera similar to those of Gedemsa and Corbetti.

Several arced structures on Dabbahu suggest the presence of multiple calderas in addition to summit pit craters. *Field et al.* [2013] proposed three overlapping calderas, similar to the nested calderas mapped at Kone Volcanic Complex in the MER [*Rampey et al.*, 2010]. The size of the nested calderas at Dabbahu (~3–8 km wide) is similar to those in the MER. Subsequent burial of the structures by post-caldera activity has produced an overall structure analogous to Boset, with fissure eruptions of both silicic and basaltic material.

Gedemsa and Corbetti host several embayments and offsets leading to highly irregular shapes. These embayments and offsets are partly influenced by rift-related normal faults which cut the calderas to differing degrees (**Figure 3.11**). The normal faults form limits to the depression, causing the caldera rim to be locally deflected. The faults impinge on the caldera rim at points of greatest curvature, indicating a possible control on the extent of subsidence.

In addition to faults offsetting caldera rims at various points, all three MER volcanoes from this study display linear sections of caldera rim controlled by underlying structures (highlighted in blue, **Figure 3.11**). At Fentale and Corbetti, these proposed fault-controlled sections are parallel to other structural alignments. In controlling the large-scale shape of the caldera, these fault-controlled sections effect the long-axis orientation of the calderas.

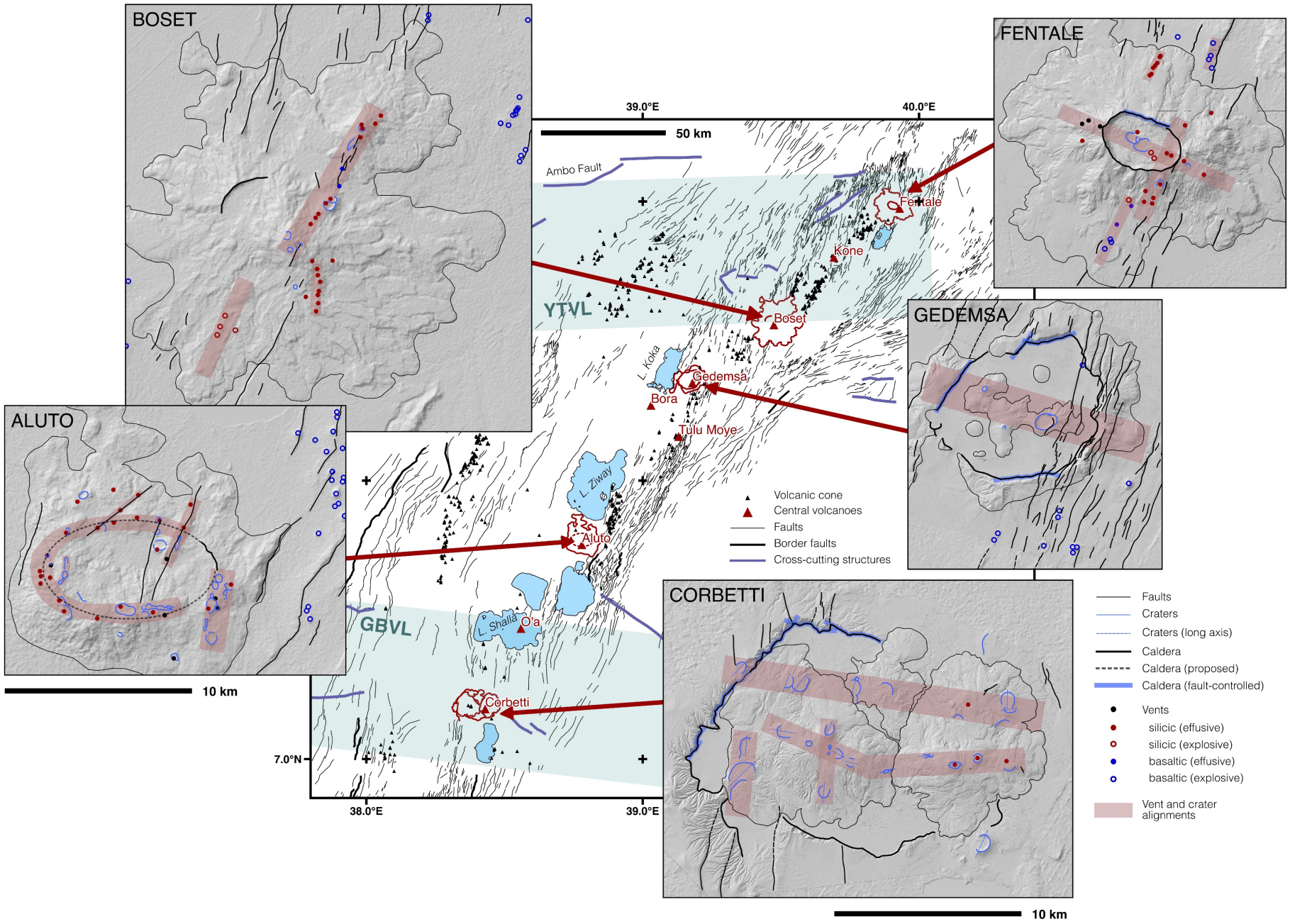
BOSET
FENTALE
GEDEMSA
ALUTO
CORBETTI
39.0°E
40.0°E
50 km
Ambo Fault
Fentale
Kone
YTVL
Boset
L. Koka
Gedemsa
Bora
Tulu Moye
L. Ziway
Aluto
GBVL
L. Shalla
O'a
Corbetti
7.0°N
38.0°E
39.0°E
10 km
10 km
Volcanic cone
Central volcanoes
Faults
Border faults
Cross-cutting structures
Faults
Craters
Craters (long axis)
Caldera
Caldera (proposed)
Caldera (fault-controlled)
Vents
silicic (effusive)
silicic (explosive)
basaltic (effusive)
basaltic (explosive)
Vent and crater alignments

Figure 3.11. Map of the Main Ethiopian Rift, including volcanoes, faults and border faults [*Agostini et al.*, 2011; updated version available from http://ethiopianrift.igg.cnr.it/]. Panels display structural associations, vents and craters for the volcanoes in this study (right) and two other volcanoes for comparison (right). Hillshade products from the Aster GDEM (product of METI and NASA) are used to display the topography of Boset and Aluto.

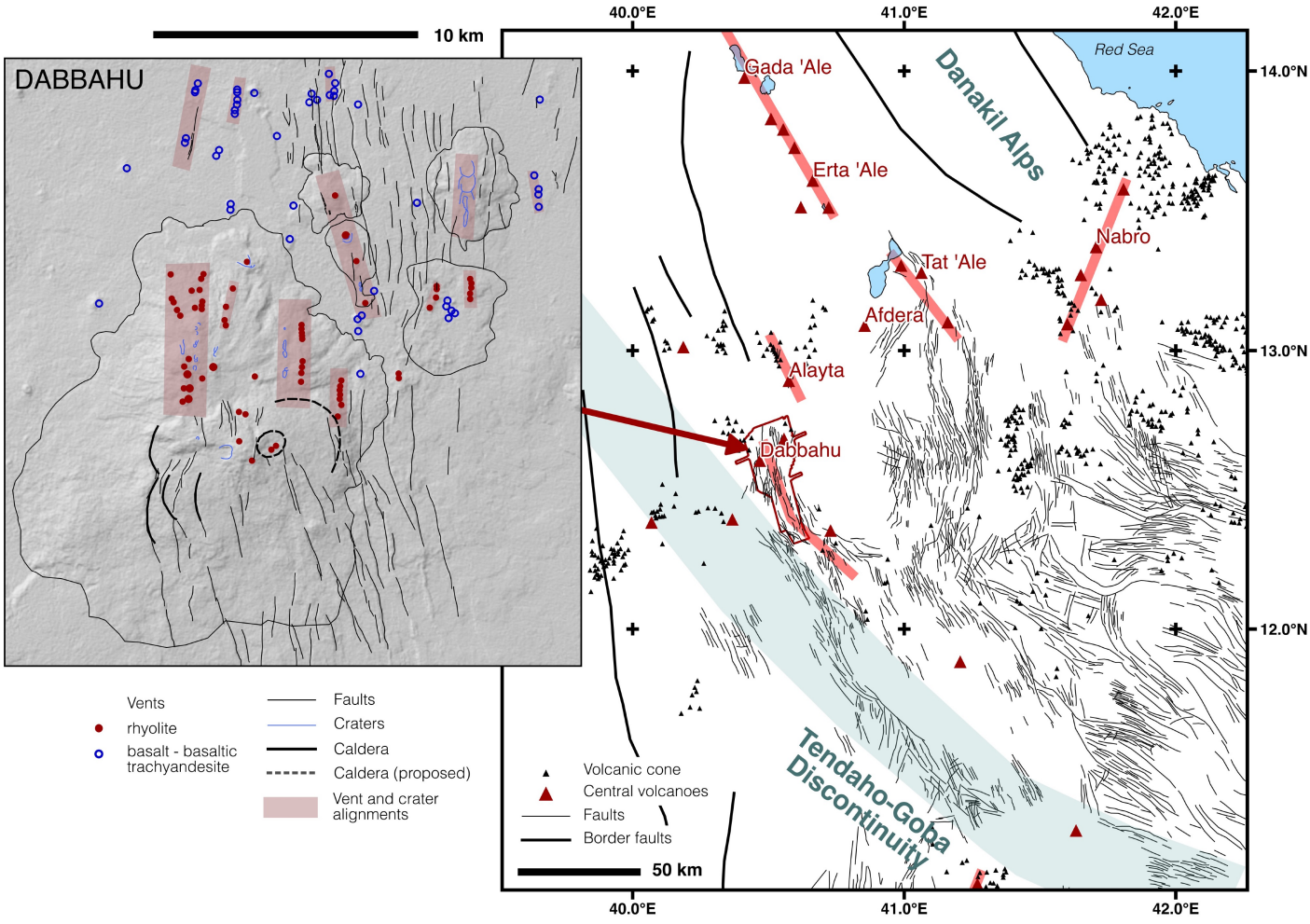

Figure 3.12. Map of the Afar, including volcanoes and faults [redrawn from *Barberi and Varet*, 1977; *Donovan et al.*, 2018; using the Aster GDEM product from METI and NASA]. Panel: Dabbahu volcano, displaying structural associations, vents and craters on a hillshade map derived from the Aster GDEM.

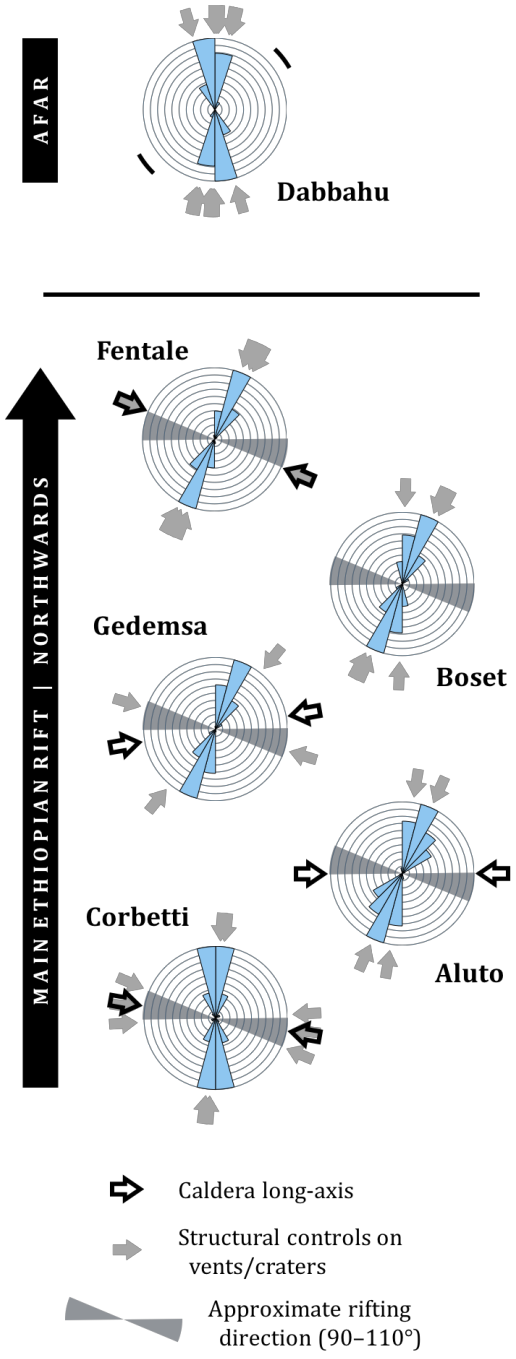

Figure 3.13. Rose diagrams of fault orientations (blue) around each volcanic center, orientations of structural alignments and caldera long-axis shown by arrows. The long-axis of the postulated caldera at Dabbahu is shown by a black line. Approximate spreading direction in the Main Ethiopian Rift is shown in grey [*Saria et al.*, 2014].

Figure 3.13 displays rose diagrams which show the changing strike of regional faults as well as the long-axis direction for each caldera. The orientation of the main proposed caldera for Dabbahu is also indicated. In every case except for Fentale, the caldera long-axis is cross-cutting but not orthogonal to the local normal faults. At Fentale, the long-axis is orthogonal to the faults but parallel to an alignment of vents and the linear northern rim of the caldera.

Ellipticity of calderas is influenced by the local stress regime, pre-existing structures, multiple collapses and post-caldera processes [*Holohan et al.*, 2005; *Roberton et al.*, 2015]. Caldera ellipticity in the MER was related to natural extension-related strain by *Casey et al.* [2006]. Examples of faults controlling the geometry of calderas are found in Indonesia [Ranau and Toba; *Bellier and Sébrier*, 1994], New Zealand [*Spinks et al.*, 2005] and Kenya [*Robertson et al.*, 2015].

The phenomenon was reproduced in analogue experiments by *Holohan et al.* [2005] in which a number of key observations were made. Pre-existing faults commonly became caldera-bounding faults, truncating or distorting the otherwise preferred elliptical structure of the caldera. The nearest regional faults accommodated some of the subsidence from caldera collapse, and faults pervading the caldera center caused piecemeal collapse as subsidence was accommodated variably between fault blocks. Our observations are consistent with similar impacts of pervasive faulting on the formation of calderas in the Main Ethiopian Rift, with rift-related normal faults truncating and distorting caldera geometry and cross-cutting structures becoming caldera-bounding faults.

For cross-cutting structures to influence the formation of calderas and location of eruptions, they must be long-term structures and have shallow manifestations. A number of known cross-cutting structures exist around the MER (**Figure 3.11**), including the Yerer-Tulu Wellel volcano-tectonic lineament [YTVL; *Abebe et al.*, 1995; 1998] and the Goba-Bonga volcano-tectonic lineament [GBVL; *Abbate and Sagri*, 1980; *Corti et al.*, 2018a]. *Acocella et al.* [2002] mapped many left-lateral, E-W trending structures on the rift flanks and associated them with the ellipticity of calderas within the rift. These structures may have been reactivated during rifting, and could have formed pull-apart structures encouraging the formation of elliptical magma reservoirs in specific locations [*Acocella et al.*, 2002].

Along axis variations in rifting stage may affect caldera architecture and the extent to which cross-cutting structures influence their formation. The influence of such pre-existing structures is likely larger in early stages of rifting than late stages [e.g.,

Corti et al., 2018b]. This is arguably supported by the simpler geometry of Fentale's caldera in the northern MER (late stage rifting) compared to the geometry of Corbetti in the southern MER (earlier stage). The mode of caldera formation may also be influenced by rifting stage, with simple piston collapse forming Fentale's regular caldera and possibly Dabbahu's pit craters, compared to complex piecemeal collapse of Gedemsa and Corbetti's larger, irregular calderas.

Variable erosion of the caldera rims and large irregularities in caldera shape may suggest the presence of more than one collapse event. This hypothesis is supported at Gedemsa by the existence of multiple ignimbrites and extensive pumice deposits [*Thrall*, 1973; *Fontijn et al.*, 2018]. The abundance of incision along the western rim of the Corbetti caldera compared to the north and south may be due to hydrology or local geology (i.e., weaker substrate), or possibly an older age. In this case, multiple collapse events may be responsible.

Slope failure during the post-caldera phases of each volcano could also account for the observations the influence of faults and irregularities in shape – in this case, caldera geometry is modified by erosion with slope failure likely to be bounded by faults as planes of weakness. Given the age of the MER calderas [~170–320 ka; *Hutchison et al.*, 2016a], post-caldera modification is likely an important factor in caldera morphology. Further work is required to constrain the number of collapse events, the relative importance of faults in controlling subsidence, and the extent of post-caldera modification at each volcano.

3.4.2. Locations of eruptions

The volcanoes each show structural controls on the locations of eruption, as identified by vents, domes and craters. Post-caldera activity at Fentale, Gedemsa and Corbetti is frequently aligned along cross-rift structures (**Figure 3.11**). At Fentale, several craters and silicic vents, post- and pre-caldera, align parallel to the caldera long-axis (WNW-ESE) and in line with an observed steam vent. At Gedemsa, post-caldera domes delineate a WNW-ESE alignment, and at Corbetti there exist two or three swaths of craters aligned from WNW-ESE to ~E-W (**Figure 3.11**).

Contrastingly, vents and craters on Aluto follow a proposed caldera rim, which is now buried under subsequent deposition from eruptions [*Hutchison et al.*, 2015; **Figure 3.11**]. Caldera-aligned activity is not observed at other volcanoes, except for the basaltic scoria cone along the north-east rim of Gedemsa (**Figure 3.5a**; **Figure 3.11**). The majority of vents and craters on Boset are aligned along the same axis, running parallel to rift-related faults. Vents are not identified along the buried caldera rim, nor are they found aligned with cross-rift structures. Studies of seismic anisotropy at Corbetti and Aluto show fast shear-wave polarisations parallel to cross-cutting structures – in the case of Corbetti, parallel to the Wendo Genet fault scarp [~NW-SE; *Lloyd et al.*, 2018], and in the case of Aluto, parallel to NE-SW alignments of vents [**Figure 3.11**; *Nowacki et al.*, 2018].

Rift-parallel trends in activity are observed at each volcano, commonly in line with regional faults to the north and/or south of the edifice. A number of silicic vents at Fentale are aligned NNE-SSW along a rift-parallel trend on the eastern side of the

edifice (Figure 3.2a; Figure 3.11), along with a newly reported cluster of domes aligned in the same direction (Figure 3.2c). Basaltic vents to the south of the edifice are also aligned parallel to the rift, along with a pumice deposit.

At Gedemsa, the westernmost intra-caldera dome (Kelo) strikes NE-SW in line with a regional fault which offsets the caldera rim (Figure 3.9). At Corbetti, a number of craters have a long-axis trending N-S and are aligned in the same direction, parallel to local, rift-related faults. These are common on the western side of the edifice, where the regional faults are most abundant (Figure 3.11). The vents of Dabbahu are dominantly aligned parallel to local faults, similar to Boset (Figure 3.12).

The rose diagrams in Figure 3.13 compile these observations and compare orientations of the rift-related faults, caldera long-axes, structural alignments of vents and craters, and the spreading direction in the Main Ethiopian Rift [MER; *Saria et al.*, 2014]. Fault orientation is N-S at Corbetti but consistently NNE-SSW to the north. Most structural alignments are parallel to the rift-related faults. Cross-cutting structural controls, where they exist, are mainly parallel to the long-axis of each caldera except at Gedemsa, which combines several structural orientations.

While caldera ellipticity may suggest an important role for cross-cutting structures in forming elliptical magma reservoirs, the absence of cross-cutting alignments at Boset suggests that they are not solely responsible for the location of major volcanoes along the rift. In addition, there are many cross-cutting structures observed on the rift flanks that apparently do not enable the formation of a magma reservoir along their strike.

Whether magma reservoirs are themselves influenced by cross-cutting structures or not, vent and crater locations are clearly influenced by these structures. Elsewhere in the rift, scoria cones and other erupted products are closely related to rift-related faults [e.g., *Casey et al.*, 2006; *Corti et al.*, 2013], as is the case at these volcanoes (**Figures 3.11**, **3.13**).

The propensity for vents and craters to follow faults and other structures in the Main Ethiopian Rift indicates that structural control on eruption locations is greater than the influence of the local stress fields. The regional stress field encourages dike formation orthogonal to the rift-direction [*Anderson*, 1951; *Nakamura*, 1977; *Guðmundsson*, 1995]. For most of the rift, this is difficult to distinguish from the trend of rift-related normal faults – vents and craters influenced by these faults are therefore also likely influenced by the regional stress field.

However, stress fields associated with edifice loading, pressurized magma reservoirs and/or cylindrical conduits lead to radial dikes and therefore alignments of cones and craters [e.g., *Muirhead et al.*, 2015, *Wadge et al.*, 2016). The absence of these alignments, and the presence of cross-cutting alignments, suggests a strong structural control rather than influences of stress fields influenced by crustal loading or magma pressure, as found elsewhere in the rift [*Wadge et al.*, 2016]. Edifice loading is a significant feature for volcanoes with heights ~1–2 km [*Wadge et al.*, 2016] – a combination of evacuation by caldera formation, ubiquitous normal faulting and low eruptive rates lead to low heights of most MER volcanoes.

3.4.3. Volumes and frequency of eruptions

Figure 3.14 presents the number of vents and craters of various types for each MER center, estimates of the total volume erupted in the post-caldera phase, and published estimates for the ages of each caldera [*Hutchison et al.*, 2016a; *Bigazzi et al.*, 1993; *Peccerillo et al.*, 2003; *Siegburg et al.*, 2017; *Williams et al.*, 2004]. Caldera ages are associated with large uncertainties, particularly at Gedemsa, Boset and Fentale – more dates are needed to constrain these ages further.

Hutchison et al. [2016a] estimated the total post-caldera volume of Corbetti (15 km^3), Aluto (27 km^3) and Gedemsa (1 km^3) using an SRTM 30m-resolution DEM. These estimates agree with the volumes calculated in this study to the nearest 1 km^3 (Table 3.3). *Siegburg et al.* [2017] published volumes for each eruptive phase at Boset. These volumes have been combined to give an estimate of the total volume for the post-caldera phase, allowing for uncertainty concerning the age of the caldera and therefore the identification of which phases post-date caldera formation.

The number of vents and craters observed at each center provides an insight into the frequency of eruptions at each volcano. Other factors affect the identification of vents and craters, including the burial of vents and craters by subsequent eruptions, and eruptions that retain no discernable vent or crater. Burial of vents and craters has occurred at Boset, Corbetti and Dabbahu, a consequence of large eruptive volumes and high eruption frequencies. Gedemsa has produced post-caldera erupted deposits with very few observable vents and craters – this may be

a consequence of post-emplacement erosion or immediate burial at time of emplacement.

Aluto hosts the most identifiable craters and vents of the five MER volcanoes in question. Corbetti, Fentale and Boset host a similar number of craters and vents. Craters are common on Corbetti and Aluto, and less common on Boset and Fentale. Dabbahu hosts a large number of scoria cones and rhyolite vents, many of which feed coulees (**Figure 3.12**). The scoria cones at Dabbahu are basaltic trachyandesite in composition [*Field et al.*, 2013] – more silicic than the basaltic scoria in the MER.

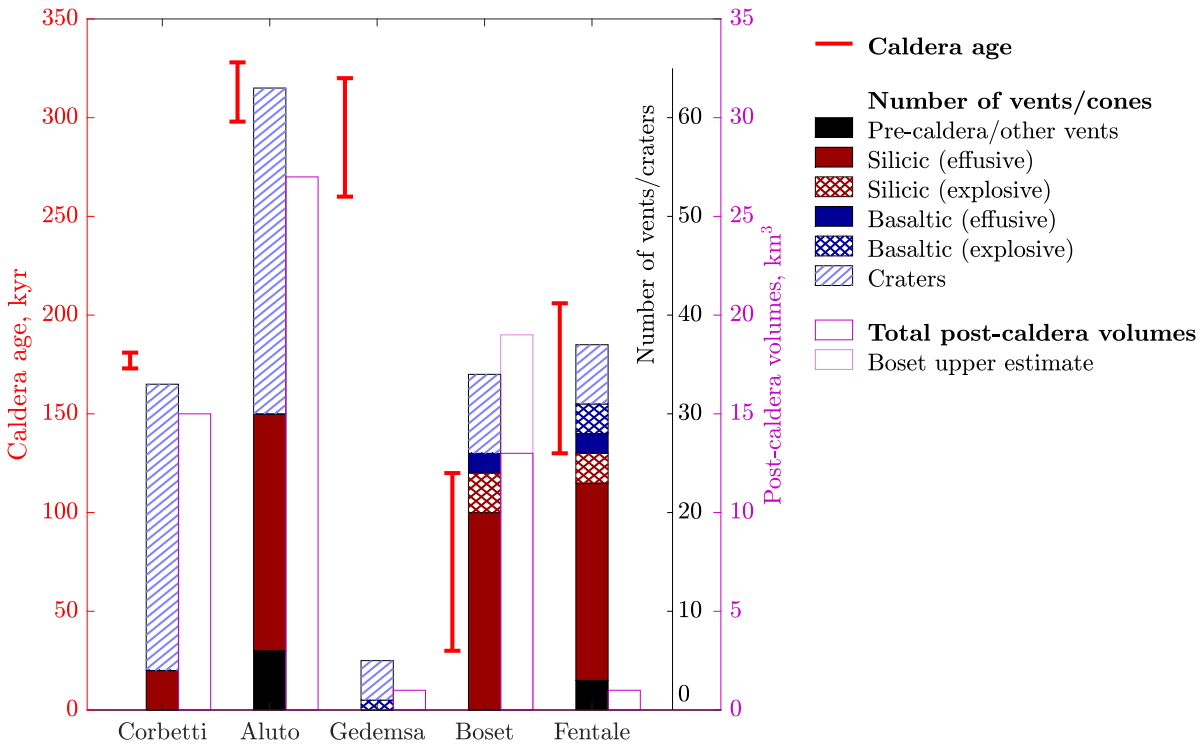

Figure 3.14. Bar graph displaying the number of vents, cones and craters for each volcanic center alongside total post-caldera volumes and the age of each caldera.

The closest basaltic cones or lava flow vents to Corbetti and Aluto are 2-3 km from the edifice, whereas basaltic eruptions have occurred on the edifice at both Boset and Fentale (**Figure 3.11**). At Boset, basaltic flows have been erupted from the central fissure between the two peaks, along which silicic flows have also been erupted. At Fentale, a basaltic eruption also led to the formation of fissures [*Williams et al.*, 2004]. The vents for this lava deposit are meters away from the newly observed pumice cone. Basaltic and silicic vents are also found close together at Dabbahu, where the main silicic vents are spread out between several satellite centers (**Figure 3.12**).

A scoria cone has been emplaced within the north east caldera rim at Gedemsa (**Figure 3.5a**; **Figure 3.11**), and an historical basaltic eruption at Kone, in the north of the rift, occurred within the caldera. The lack of basaltic volcanism in the south at Corbetti and Aluto may suggest a shielding effect by the active peralkaline magma reservoirs [*Fontijn et al.*, 2018; *Mahood and Hildreth*, 1986; *Mahood*, 1984; *Jeffrey et al.*, 2016], whereas the less active volcanoes to the north may have only small or temporarily active magma reservoirs.

The ages of the calderas at Fentale and Gedemsa are similar to those at Corbetti and Aluto respectively, but the volcanoes have much lower post-caldera erupted volumes. This suggests a much lower eruptive flux on average over the past 300 kyr. Despite the age of Gedemsa's caldera, the volcano has deposited little in its post-caldera phase and features few vents/calderas, suggesting a paucity of activity. Fentale hosts a high number of vents and craters relative to its post-caldera erupted volume, suggesting high-frequency, low-volume eruptions.

Lava coulee volumes at Corbetti are as much as ten times greater than those at Fentale (**Table 3.3**), a relationship which is reflected in the total post-caldera erupted volume (**Figure 3.14**). The six lava coulees observed on Chabbi account for less than half of the volume of the edifice, suggesting a number of vents and craters lay buried beneath subsequent deposits. The total post-caldera erupted volume is also likely to be much higher than indicated at Corbetti and Aluto, as explosive eruptions and large craters are common. Such eruptions deposit material over a wide area, and only thick, proximal deposits are accounted for using the DEMs.

The volume of the CO6 lava coulee on Chabbi (0.47 km^3) is similar to the volume of the pyroclastic deposit of the Wendo Koshe Younger Pumice [WKYP; 0.4 km^3 DRE, dense rock equivalent; *Rapprich et al.*, 2016]. WKYP was deposited at 2.3 ka and has been followed by four lava flows on Chabbi. An estimated combined volume from these eruptions is ~2 km^3, giving an eruptive flux of 8.7×10^5 m^3/yr. The long-term volume flux is 8.3×10^4 m^3/yr (15 km^3 over 180 kyr), an order of magnitude lower. This implies a greater flux in the volcano's recent history.

3.4.4. Morphology of peralkaline lava flow deposits

The impact of the proposed rheological difference of peralkaline magmas [due to the abundance of halogens and excess alkali resultsing in depolymerization and lower viscosities compared to metaluminous silicic melts, e.g. *Hess et al.*, 1995; *Dingwell et al,* 1998] on eruption dynamics and lava emplacement is poorly understood. The lava coulees on Fentale and Corbetti display distinctive morphology which provides insight into the eruptive dynamics of each system.

Several large-volume coulees at Corbetti are erupted from single, large, elliptical craters, perhaps suggesting a prior explosive phase of eruption. The resulting flows spread in multiple directions and form large lobes. Craters and effusive vents are also collocated at Aluto and Dabbahu, (**Figure 3.11**, **Figure 3.12**), where lava flow deposits are smaller than at Corbetti. The Alcoma satellite center at Dabbahu is a larger coulee emplaced on a shallow slope, which forms large lobes similar to those at Corbetti (**Figure 3.8**).

Small-volume coulees are erupted at Fentale from multiple vents, the spacing of which varies from 200 – 2,000 m. Short spacing of vents is also observed on Boset (**Figure 3.11**) and Dabbahu (**Figure 3.12**). Post-caldera coulees commonly cease before reaching the flat plain surrounding Fentale's edifice. Considering both post- and pre-caldera coulees, downflow slope appears to be a dominant factor controlling flow width. Crossflow slope and confining topography are also expected to influence flow width [*Rogers et al.* 1996; *Peitersen and Crown*, 1999], however apart from isolated examples (e.g. narrow flow to the west of the SE dome) these factors are less important.

Ogives/folds form on the surface of a lava flow whose viscosity decreases with depth, as the product of compression within the solidifying crust of a flow as it progresses down slope [*Fink and Fletcher*, 1978; *Fink*, 1980]. Ogives on coulees at Corbetti and Fentale have wavelengths of 20–100 m, similar to those previously noted on lava flow deposits of andesitic, dacitic, trachytic and rhyolitic composition [e.g., *Warner and Gregg*, 2003; *Pyle and Elliott*, 2006; *Latutrie et al.*, 2017]. Shorter wavelength folds have been observed on dacite deposits [*Lescinsky et al.*,

2007]; post-emplacement erosion and weathering may have altered small-scale morphological features on the Corbetti and Fentale lava coulees.

Multiple generations of folds form as the solidifying crust thickens, lengthening the optimum wavelength for folds to form [*Gregg et al.*, 1998]. The ratio between successive generations of folds depends on the relative importance of crust thickening by cooling and by shortening, which itself depends on composition [*Gregg et al.*,1998]. Crusts on rhyolite flows grow largely due to cooling; basaltic crusts grow largely due to shortening because of higher strain rates [*Gregg et al.*, 1998]. Ratios between successive fold wavelengths are therefore lower in rhyolites (1.4–2.2) compared to basalts (4.0–6.2). The folds on Corbetti and Fentale have ratios of 1.4–3.3, similar to those observed in rhyolite and dacite deposits elsewhere [*Gregg et al.*, 1998; *Pyle and Elliott*, 2006].

Though the relationship between measured channel width and angle of slope at Fentale agrees with the *Kerr et al.* [2006] model, there is a range of possible Φ values (defined in **Eq. 3.4**, **section 3.2**; **Figure 3.10**). Values of Φ depend on material properties (density, yield strength, thermal diffusivity) as well as volumetric flow rate and viscosity. We have assumed that the rheology of every coulee forming a levee is similar. Narrow channels are more likely to be affected by confining topography, which presents an additional factor controlling the width of the flow – for this reason, narrower channels may be more narrow than expected from the theoretical relationship. In addition to a simple, planar pre-eruptive surface, the model assumes constant viscosity and flow rate and therefore does not account for pulses, blockages and other complicating factors [e.g., *Bailey et al.*,

2006]. The model assumes that levees are formed due to yield stress, but other models of levee formation may apply, including the build-up of rubble [e.g., *Sparks et al.*, 1976; *Bailey et al.*, 2006]. This may be particularly relevant for low yield stress lavas, including acrystalline lavas similar to those found in the MER. Experimental studies on the rheology of peralkaline rhyolites, similar to those at Fentale [*Gibson*, 1974; *Webster et al.*, 1993] and elsewhere in the rift [*Gibson*, 1972; *Peccerillo et al.*, 2007; *Giordano et al.*, 2014], suggest that their viscosities are relatively low – ~$10^{5.5}$ Pa s for a volatile-free peralkaline rhyolite magma at 1223°C compared to ~10^{8} Pa s for a calc-alkaline rhyolite [*Giordano et al.*, 2008; *Di Genova et al.*, 2013; *Hughes et al.*, 2017]. Viscosities of lava at time of emplacement are higher due to lower temperatures as well as crystal and bubble content, whilst high water content [present at Fentale; *Webster et al.*, 1993] reduces viscosity especially for peralkaline melts.

Our observations, combined with the *Kerr et al.* [2006] model, suggest maximum emplacement viscosities of 10^{8}–10^{11} Pa s for peralkaline rhyolite lavas on Fentale (**Figure 3.10**), similar to those estimated for calc-alkaline rhyolites [10^{10}–10^{11} Pa s; e.g., *Stevenson et al.*, 1994; *Bagdassarov and Dingwell*, 1992]. For volumetric flow rates of 1 m^3/s or greater, maximum viscosity of the peralkaline rhyolites in this study is ~10^{8}–10^{9} Pa s, consistent with experimental and theoretical approaches in being lower than their calc-alkaline counterparts.

Analysis of the morphology of lava flow deposits using remote sensing data provides valuable constraints on eruptive dynamics. Further investigation of the development of morphological features, in combination with experimental and

rheological analyses, may provide important developments in modelling the dynamics of peralkaline lavas.

3.5. Conclusions

This study provides an abundance of new geomorphological data which, together with geological observations, presents a wealth of information concerning the behavior of several volcanoes in the Main Ethiopian Rift (MER) and Afar. Several previously unidentified post-caldera deposits have been observed on Fentale volcano, as well as a number of newly observed craters on Corbetti volcano.

The shapes of calderas in the MER are largely controlled by both rift-parallel and rift-cutting structures. Variations in caldera architecture exist, the caldera at Fentale having a deeper and simpler definition to those at Corbetti and Gedemsa. The more complex caldera shapes may be the result of multiple collapses.

Post-caldera activity at each volcano is aligned with rift-cutting structures in various orientations. Alignment with the rift-parallel faults is also observed, similar to nearby Boset. The influence of the caldera structure on vent location seems less important, in contrast to nearby Aluto. The dominance of faults and other structures controlling the location of vents and craters in the MER and in Afar suggests that the regional stress field, edifice loading and pressurized reservoirs/conduits play minor roles in determining the location of eruptions.

The relative frequency of eruptions, as discerned from the number of deposits, vents and craters since caldera formation, varies greatly between volcanoes. Gedemsa has been largely inactive whereas Fentale and Corbetti have produced a number of

eruptions in the past 300 kyr. Fentale has produced many small-volume eruptions (< 0.1 km^3), whereas events at Corbetti are usually much larger (~0.4–0.5 km^3). Basaltic eruptions at large volcanic centers are infrequent in the south of the rift, increasing in frequency to the north.

Typical lava volumes, lengths and number of vents are reported, providing indicative characteristics for use in hazard planning. Peralkaline rhyolite coulees at Corbetti and Fentale exhibit levees and ogives formed during emplacement. The morphometry of these deposits suggests emplacement viscosities of 10^8–10^{11} Pa s compared to 10^{10}–10^{11} Pa s for calc-alkaline rhyolites – the lower end of our estimates are in agreement with experimental and theoretical studies suggesting a reduced viscosity for peralkaline melts. Further observations of morphometry and dynamics are required to test this hypothesis, which remains unverified in nature.

Satellite data and remote sensing tools are invaluable resources in rapidly comparing the previous activity of large, inaccessible volcanoes. The observations reported here highlight fundamental questions concerning the dynamics of rift volcanoes, and its variability along rift. Further work regarding the influence of rift structure and peralkaline composition on magma dynamics is needed to progress our understanding of these systems.

4 Morphological comparison of distributed volcanic fields

Abstract

Distributed volcanic fields of scoria cones, maars, tuff cones and lava flows represent a crucial expression of the interplay between magmatism, tectonics and surface processes in continental rifts. We compare two such fields (Butajira and East Ziway) in the Main Ethiopian Rift (MER) using high-resolution digital elevation models (DEMs), linking the morphology of cones and maars to processes and age of emplacement. Volumes of individual cones are similar in both fields (mean ~ 4×10^6 m^3) and lower than other distributed volcanic fields found in extensional environments. Volcanism at Butajira has created linear clusters of superimposed cones, suggesting a small number of larger (10^7–10^8 m^3) fissure eruptions compared to the isolated events at East Ziway and lower confining stresses during emplacement. Dikes at Butajira may have been deflected by topographic unloading, whilst at East Ziway close proximity of cones and faults suggests dike capture. The presence of maars and deep craters within cones at Butajira indicates phreatomagmatic activity, not seen at East Ziway where cones may have been emplaced during a dry climate phase. Shape parameters, including curvature of cone rims and ratios of cone height, width and crater depth, suggest younger eruption ages at Butajira compared to East Ziway and the possibility of ongoing activity in this area. A broader survey of cone fields across the MER using the ASTER global digital elevation model fails to identify such systematic variation in cone morphology, limited by low-resolution. High-resolution topography provides a useful insight into rift environments at the time of emplacement, and further surveys across the Main Ethiopian Rift may advance our understanding of distributed volcanism in extensional settings and the hazards they present.

A version of this chapter has been submitted for publication in the Journal of Volcanology and Geothermal Research (JVGR) as:

Hunt, J. A., T. A. Mather, and D. M. Pyle (in review), Morphological comparison of distributed volcanic fields in the Main Ethiopian Rift using high-resolution digital elevation models.

4.1. Introduction

The interplay between magmatism and tectonics in continental rifts is a key relationship that governs rift architecture [e.g., *Ebinger and Casey*, 2001; *Corti et al*., 2003], extensional dynamics [e.g., *Wright et al*., 2006; *Keir et al*., 2006; *Daniels et al*., 2014], and the location and style of volcanism [e.g., *Acocella et al*., 2002; *Abebe et al*., 2007]. In continental rifts, extension is driven by a large-scale stress regime interacting with multiple generations of new or inherited crustal structures [e.g., *Corti et al*., 2018]. Melt generation [e.g., *Armitage et al*., 2010; *Ferguson et al*., 2013] and dike intrusion [e.g., *Keir et al*., 2009] provide frequent opportunities for small-volume basaltic volcanism. Distributed volcanic fields are a common expression of this relationship in extensional environments [e.g., *Connor and Conway*, 2000; *Michon and Merle*, 2001; *Hughes et al*., 2002; *Le Corvec et al*., 2013a], comprising spatially dispersed, small-volume and usually mafic scoria deposits with individual vents [e.g., *Smith and Nemeth*, 2017]. Such fields are commonly referred to as "monogenetic" volcanic fields, though formation from single eruptions is often difficult to verify.

The deposits create a range of land forms (scoria cones, maars, tuff cones, and lava domes) with variable sizes, shapes and alignments depending on a number of internal and external factors. Internal factors include the physical and chemical properties of the magma, whilst external factors include the local stress regime, crustal structure, host rock and surface environment [e.g., *Kereszturi et al*., 2011; *Smith and Nemeth*, 2017]. The surface environment of continental rifts is varied, with resurfacing by fresh volcanism and a changing hydrological cycle over time.

Lakes, high surface run-off and high groundwater levels are common in rifts due to topography. All of these processes depend on the stage of rifting, as the continental rift progresses from inception to late stage extension [e.g., *Haywood and Ebinger*, 1996]. The contexts in which monogenetic volcanic fields are formed in rifts are therefore rich and varied, leading to a wide variety in their geography and morphology.

The shape of distributed or monogenetic volcanic fields and the alignment of vents have been used to investigate magma transport [e.g., *Connor et al*., 1992; *Condit and Connor*, 1996]. Poisson Nearest Neighbour analysis applied to 37 monogenetic volcanic fields from a variety of tectonic settings showed that magma transport depends on both deep level influences (e.g., magma source) and the shallow stress field and structures [*Le Corvec et al.*, 2013a]. Fields in extensional environments showed multiple orientations of volcanic alignments [*Le Corvec et al.*, 2013a; *Mazzarini et al*., 2016], probably owing to the multiplicity in rift environments of crustal structures [*Le Corvec et al*, 2013b] and small-scale stress fields [e.g., due to segmentation, obliquity, and/or transfer zones; *Muirhead et al*., 2015; *Corti*, 2008].

Simple vent alignments may imply simple plumbing systems whereby single dikes propagate from depth for each eruptive episode in the field; however, observations of exposed networks of sills and dikes beneath monogenetic volcanic fields suggest complex plumbing systems [*Muirhead et al*., 2016]. Petrology and pre-eruptive seismicity also suggest magma mixing and the possibility of multiple intrusions of melt before eruption [*Albert et al*., 2016].

Cone morphology has been used to investigate both internal and external conditions at time of emplacement, including changes in surface water [*Risso et al.*, 2008; *Kereszturi et al*., 2011], tectonic activity [e.g., *Tibaldi*, 1995; *Corazzato and Tibaldi,* 2006], and physical and chemical properties of erupted material [e.g., *Settle*, 1979; *Riedel et al*., 2003; *Bemis and Ferencz*, 2017]. Morphometry can also provide an indication of age due to degradation of the cones. A common approach is to use the ratio of height to width (H/W), which has been proposed to be approximately constant for fresh scoria cones [0.18; *Porter*, 1972; *Wood*, 1980a]. Erosion of the scoria cone leads to a reduction in height and enlargement of the base, resulting in smaller H/W ratios for older ages [*Settle*, 1979; *Wood*, 1980b; *Inbar et al.*, 2011].

However, H/W ratios depend on a large number of primary processes in addition to age [*Favalli et al*., 2009; *Bemis and Ferencz*, 2017]. The exact method of calculating H/W may also influence the results, particularly if the cones have been emplaced on an inclined substrate and/or have been subsequently buried [*Favalli et al*., 2009]. Further, the resolution of the elevation data used to calculate the H/W may result in bias [*Fornaciai et al*., 2012]. Analysis of a large number of scoria cones from a range of geodynamic settings suggests that cones in extensional settings exhibit lower H/W and higher ratios of crater width to cone width (W_{cr}/W_{co}) compared to those in subduction settings [*Fornaciai et al*., 2012]. The morphology of small-volume, distributed volcanism in a rift environment therefore includes information on their age as well as extensional dynamics, eruption style and surface environment at time of emplacement.

4.1.1. Volcanic fields in the Main Ethiopia Rift

The extension which formed the Main Ethiopian Rift (MER) began in the Late Miocene, first creating large NE-SW faults, a series of asymmetric basins and widespread volcanic activity [*Woldegabriel et al*., 1990; *Corti*, 2009]. In the Late Pliocene, extension migrated from the rift border faults to en echelon, axial magmatic segments [*Ebinger and Casey*, 2001] due to progressive thinning of the lithosphere, weakening associated with magmatism and/or a change in rift kinematics [*Wolfenden et al.*, 2004; *Kendall et al.*, 2005; *Corti*, 2008, 2009]. These two phases of rift development created the two systems of faults in the present-day MER: older NE-SW border faults and currently active NNE-SSW rift-floor faults [*Keir et al*., 2006].

Distributed volcanic fields are found within two fault belts [**Figure 4.1**; *Mazzarini and Isola*, 2010]: on the west, the Silti-Debre Zeyit Fault Zone (SDFZ); on the east, the Wonji Fault Belt (WFB). The SDFZ includes fields near the major town of Bishoftu, and smaller towns of Butajira, Silti and Soddo [e.g., *Rooney et al*., 2011]. While the deposits (mostly scoria cones) are Quaternary to recent in age [< 2 Ma; *Chernet et al*., 1998; *Abebe et al*., 2005], a cluster of cones further offset from the rift axis at Akaki are Pliocene-Quaternary [3–2 Ma; *Mazzarini et* al., 1999; *Abebe et* al., 2005] but are geochemically similar to the rest of the SDFZ [*Rooney et al*., 2014b]. The WFB runs along the eastern side of the central MER (~7.5–8.5°N) and becomes the rift's axial spreading centre in the northern (~8.5–9.5°N) and southern (~6.5–7.5°N) MER. The major silicic centres within the MER are found within or closely associated with the WFB, with cone fields interspersed.

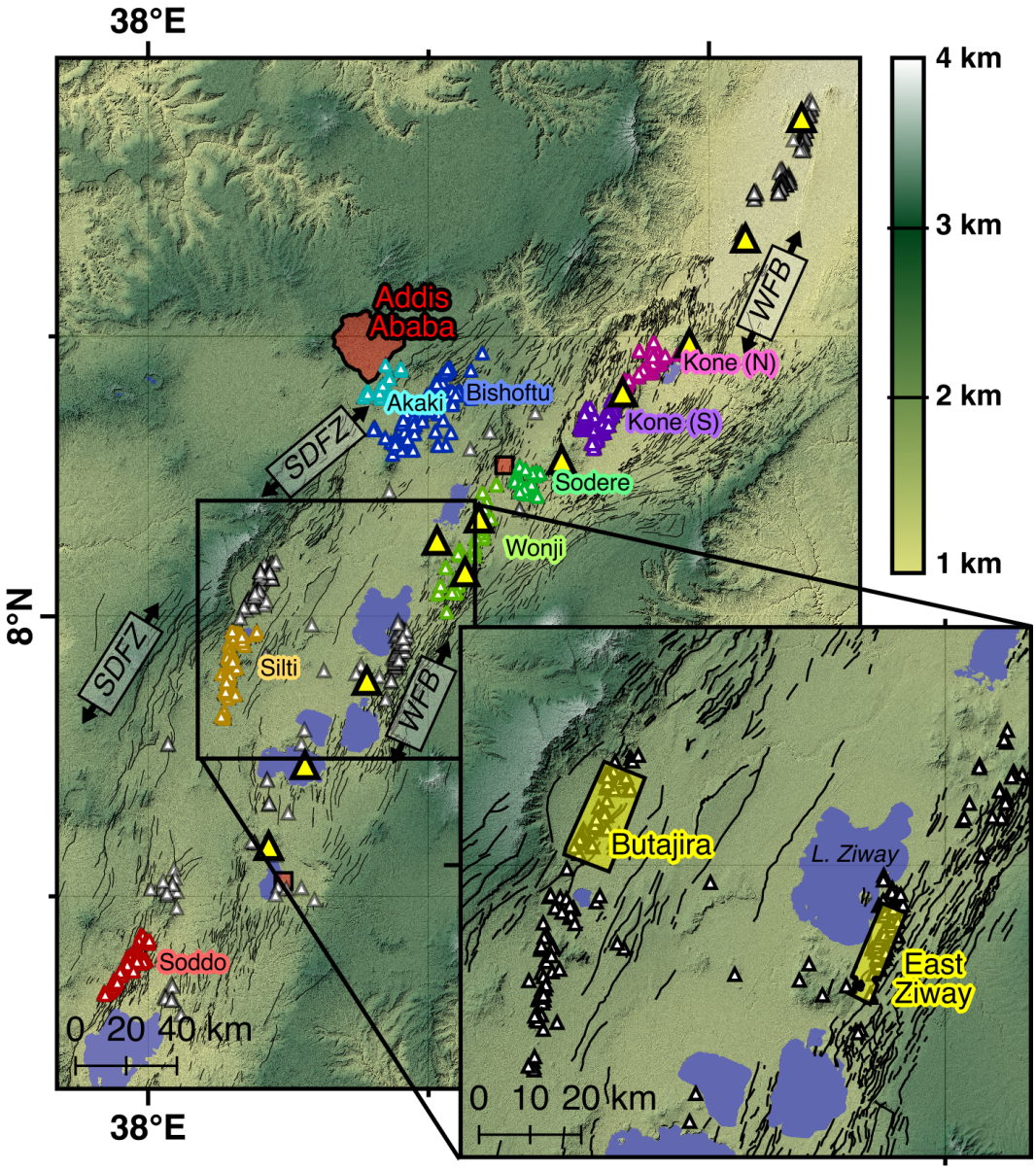

Figure 4.1. Location map for the cone fields in this study. Elevation and hillshade provided by Aster GDEM (product of METI and NASA). Yellow triangles, major silicic centers; small triangles, volcanic cones (colored by field); red-filled squares/settlement outlines, cities of population > 100,000; black lines, faults located in two major fault belts (SDFZ: Silti-Debre Zeyit Fault Zone; WFB: Wonji Fault Belt).

Cones in both the SDFZ and WFB are commonly located near or on top of extensional faults [*Korme et al.*, 1997, 2004; *Casey et al.*, 2006; *Corti et al.*, 2013]. The spatial distribution of both vents and faults in the MER displays self-similar (fractal) clustering, and the length-scales at which this clustering occurs is hypothesised to correlate with the depth from which dikes are fed [e.g., *Mazzarini and Isola*, 2010]. Accordingly, the SDFZ is hypothesised to be fed by dikes from deeper in the crust than the WFB [*Mazzarini and Isola*, 2010; *Mazzarini et al.*, 2013b]. Similarities between the fractal behaviour of earthquakes and that of vents throughout the MER suggest a genetic link between faults and vents [*Mazzarini et al.*, 2013a].

Statistical analysis of the locations of vents within the Bishoftu (syn. Debre Zeyit), Wonji, Kone and Akaki fields suggests that the shape of each field is determined by large crustal structures [*Mazzarini et al.*, 2016]. Within fields closer to the rift axis, vent location is principally controlled by the state of stress and vents are therefore aligned with contemporaneous faults; further from the rift axis (i.e., SDFZ fields, particularly Akaki), vent location is controlled by pre-existing structures and border faults [*Mazzarini et al.*, 2016].

Geochemical analysis of lavas from the distributed volcanic fields suggests that SDFZ magmas are the result of lower degrees of melting and greater depths of differentiation than WFB lavas, with a fractionation system that is spread widely through the mid-lower crust [*Rooney et al.*, 2005; 2007; 2011].

In this study we compare the morphology of distributed volcanism in two fields of the MER (**Figure 4.1**): the Butajira field (within the SDFZ) and the East Ziway

field (within the WFB). Both fields are at the same latitude in the central MER. The Butajira field is on the western flank of the rift, adjacent to the Guraghe border fault [*Woldegabriel et al*., 1990; *Corti et al*., 2018b], and is situated close to a conductor imaged at depth by magnetotellurics [*Hübert et al*., 2018]. The East Ziway field lies to the east of Lake Ziway and Aluto volcano, one of the most active silicic centers in the MER [*Hutchison et al*., 2016b; *McNamara et al*., 2018; *Fontijn et al*., 2018].

We use high-resolution digital elevation models (DEMs) generated from Pleiades imagery to compare the morphology of these two fields, before comparing the morphology of fields across the MER using a low-resolution digital elevation model from ASTER. We then discuss our results concerning the morphology of fields within a continental rift environment.

4.2. Methodology

4.2.1. High-resolution Pleiades digital elevation models (DEMs)

Very-high-resolution panchromatic (50-cm) and multispectral (2-m) orthoimages from the Pléiades-HR 1A satellite were obtained in stereo for the areas of Butajira and East Ziway (**Figure 4.1**). The satellite data were processed using the Leica Photogrammetry Suite; the full methodology is detailed by *Zhou et al.* [2015]. The use of stereo images to create a DEM works on the principle of parallax. Two images from different perspectives can be joined together with tie-points – the same feature identifiable in both orthoimages. Initial creation of a DEM using tie-points results in a point cloud with a variable spatial density.

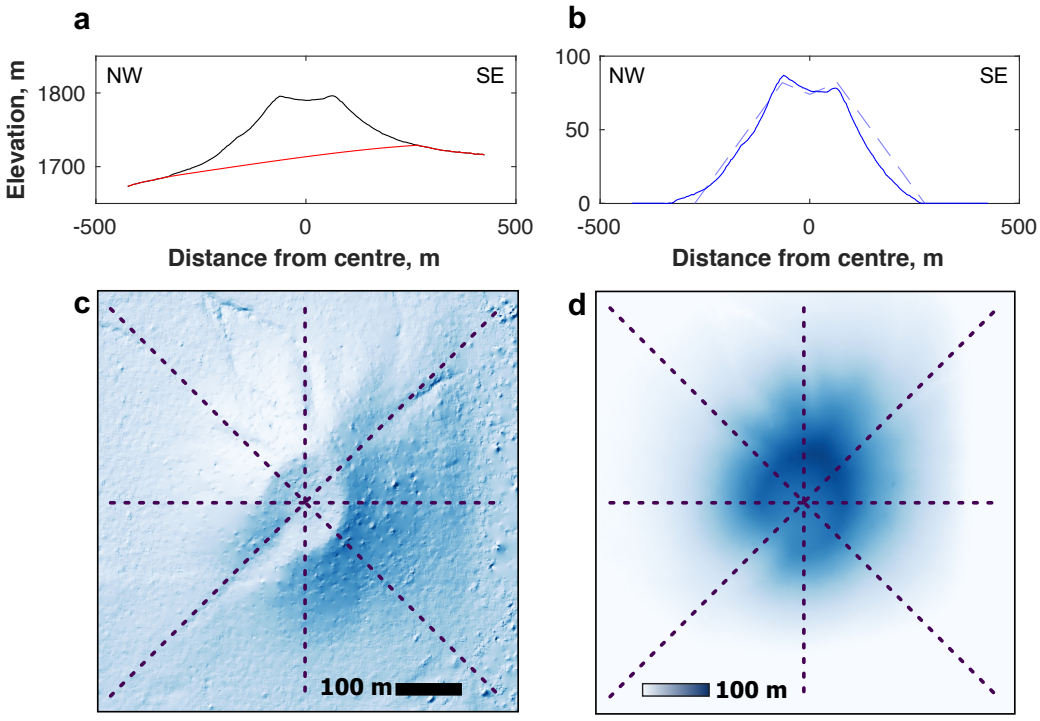

Figure 4.2. Example of cone profiles and removal of interpolated base topography (from EZ28: East Ziway field, 7.8535°N 38.8785°E). (a) Profile from NW-SE of the cone: black = unedited DEM; red = interpolated basal topography. (b) Profile from NW-SE of the cone after removal of the basal topography: solid blue = edited DEM; dashed light blue = constructed visualization of ideal cone for V_{ideal} (using W_{co}, W_{cr}, H_{co} and D_{cr}; see text, Table 4.1, and section A3.2). (c) Hillshade map of the cone from unedited DEM (solar azimuth 315°). (d) Elevation map of the cone after removal of the basal topography.

Pleiades-derived DEMs have an average horizontal resolution of 1–2 m, varying with point cloud density due to lack/abundance of features and cloud cover. For analysis, it is convenient to regrid points using a block mean filter and an interpolation algorithm using continuous curvature splines, creating a regular grid of elevation values at 0.5-m spacing. Dense cloud cover must be removed from the

point cloud. Cloud cover affects 2.1% of the stereo images for Butajira and 7.1% at East Ziway.

From these models and using QGIS (http://www.qgis.org), we manually mapped cones and maars in each volcanic field at a scale of 1:4000. We classified cones according to their regularity, extent of burial/erosion, and local geological context (e.g., nearby faults, associated lava flows, offset craters) in the following categories: partial/buried, dissected/eroded, breached/irregular and regular (see **Figures A3.1-A3.2**). The areal extent of each cone/maar was mapped on the basis of slope (below ~3°).

We generated an estimated basal topography by removing the data within the cone bounds and interpolating across the data gap, using the same surface gridding algorithm (continuous curvature splines) used in original DEM construction (**Figure 4.2a**). By subtracting the basal topography from the unedited DEM, we created a new DEM of cone elevations (**Figure 4.2b**). The new DEM was used to calculate volumes from each separable deposit (i.e., whether clusters or isolated cones). We generated best fitting probability distributions to the volume data using MATLAB's fitdist function, with a non-parametric kernel-smoothing distribution and a normal kernel smoother.

For regular cones, morphometric parameters were calculated (see **Table 4.1**). A sub-circular base was drawn for each cone, on the basis of a change in slope. Irregularities, such as adjacent cones/other features, were excluded from the sub-circular polygon. Craters on regular cones were also mapped as enclosed polygons, in some cases extended across a crevasse breaching a part of the cone. From the

sub-circular base and crater polygons, areas and average diameters were calculated (A_{co}, A_{cr}, W_{co}, W_{cr}; **Table 4.1**).

Using the isolated DEMs of each cone after basal topography was removed, maximum cone height was calculated. Four profiles were constructed across each regular cone and were used to calculate average height of cone rim (H_{co}) and depth of crater (D_{cr}). Idealised volumes were calculated for regular cones using a simple geometry of an ideal cone on the basis of cone height and width, and crater width and depth (**Figure 4.2b**, dashed line; see **section A3.2** and **Figure A3.3** for further details). The curvature of the cone rims was calculated using a MATLAB script in which a 4th-degree polynomial was fit to 150-m sections of each profile (**Figure A3.4**). The second derivatives of the polynomials then provided an estimate of the curvature of the cone rims (**Figure A3.5**). Some cone rims were not accurately captured by the profile sections, and/or did not represent a point of greatest negative curvature – these were discarded.

4.2.2. Low-resolution ASTER GDEM

To extend our survey across the Main Ethiopian Rift, we used the freely downloadable ASTER Global DEM (GDEM; http://www.gdem.aster.ersdac.or.jp), a product of METI (Ministry of Economy, Trade, and Industry of Japan) and NASA (United States National Aeronautics and Space Administration). The ASTER GDEM has a resolution of 1 arc second (~30 m). Using the cone locations published in *Mazzarini and Isola* [2010] as a starting point, we mapped approximate bounds for cones in ten cone fields (**Figure 4.1**): Soddo, Silti, Butajira, Bishoftu, Akaki,

East Ziway, Wonji, Sodere, Kone (South) and Kone (North). Cones were selected on the basis of simple morphology and subcircular bases.

The resolution of the ASTER GDEM is insufficient to resolve crater width and depth. Cone width was calculated from the sub-circular polygons using the same method as the Pleiades analysis, and maximum heights and volumes were calculated using the same interpolation method to estimate basal topography (**Table 4.1**).

Table 4.1. Morphometric parameters calculated from the Pleiades DEMs and ASTER GDEM.

Parameter	Unit	Description
V	m^3	Cone volume calculated by the DEM differencing method between the original DEM and an interpolated pre-eruptive surface.
H_{max}	m	Maximum cone height above interpolated pre-eruptive surface.
H_{co}	m	Average height of cone rim above interpolated pre-eruptive surface, calculated from four profiles across the cone.
A_{co}	m^2	Planimetric area of the cone base (green polygons in Figures A3.1-A3.2).
A_{cr}	m^2	Planimetric area of the cone crater, where applicable (blue polygons in Figures A3.1-A3.2).
W_{co}	m	Average diameter of the cone base, calculated as $2\sqrt{A_{co}/\pi}$.
W_{cr}	m	Average diameter of the cone crater, calculated as $2\sqrt{A_{cr}/\pi}$.
D_{cr}	m	Elevation difference between cone rim and lowest point of crater, averaged for four profiles across the cone.
V_{ideal}	m^3	Idealised cone volume calculated from H_{co}, W_{co}, W_{cr} and D_{cr} (see section A3.2).
H_{max}^{AS}	m	Maximum height of cones within bounds in analysis of the Aster GDEM.
W_{co}^{AS}	m	Average diameter of the cone base in analysis of the Aster GDEM, calculated in the same way as W_{co}.

4.3. Results

4.3.1. Overview of morphology from Pleiades DEMs

Figure 4.3 shows Pleiades-derived slope maps for the two study areas, Butajira and East Ziway, with cone bounds shown in red. Both fields contain ca. 50 cones (Table 4.2), that share a number of similar features. Cloud cover may obscure one or two cones, particularly in the south of the Butajira field.

The Butajira cones are found in clusters. Two linear clusters lie in the center and south of the field, with the northern cones forming a further two or three smaller clusters. In contrast, the most cones in East Ziway are isolated from each other, with the exception of a ridge (Figure 4.3d). Within this ridge, individual cones are indistinguishable, unlike the overlapping but distinct cones which form clusters in the Butajira field.

In central and southern areas of Butajira, the cone clusters lie parallel to a series of east-dipping rift-related normal faults at a distance of 2–3 km to the west (on the upthrown side). Similarly in the East Ziway field, many cones lie immediately to the west (upthrown side) of east-dipping fault scarps, particularly in the north of the field. The distance between faults and cones in the East Ziway field is far shorter

Table 4.2. Number of cones/maars in each category by field.

Cone field	Total cones/ maars	Maars	Regular cones	Breached/ irregular	Dissected/ eroded	Partial/ buried
Butajira	50	6	7	18	7	12
East Ziway	51	0	8	15	14	14

than in Butajira, with many cones within 1 km of faults and a number lying along the fault trace. In these cases, faults have cut through the cones, indicating fault activity post-emplacement.

Profiles across the cone fields (**Figure 4.3**, upper panels) show the broader topographical context of the cones. In the Butajira field, cones are emplaced on a broad high formed by successive lava deposits, possibly related to the same fissure eruptions that formed the cones. A number of lava flow deposits related to cone emplacement can be identified at Butajira, particularly at the clusters in the center and south of the field, and associated with two large maars in the north. Lava flow deposits are less clear in the East Ziway field, where the topography is dominated by lake sediments, normal faults and river-cut channels. There are no clear examples of lava flows emanating from cones in the East Ziway field.

Figure 4.3. Slope maps of the Butajira (left) and East Ziway (right) cone fields derived from Pleiades digital elevation models (DEMs). Cone centers are denoted by black crosses, and red lines mark the outer areas used to generate the basal topography and associated volumes for each mapped cone/cluster. Black dashed line demarks broad high associated with the central cluster. Elevation profiles across the cone fields are shown above (blue = unedited DEM, red = basal topography, dashed red = basal topography including broad high). (a)-(e) Zoom-in panels of particular features: (a) BU34 with associated lava flow and possible rootless cones; (b) Butajira cluster showing lack of clearly overlapping deposits, including regular cone BU19e; (c) and (e) East Ziway examples of dissected cones; (d) East Ziway ridge (multiple rifted cone).

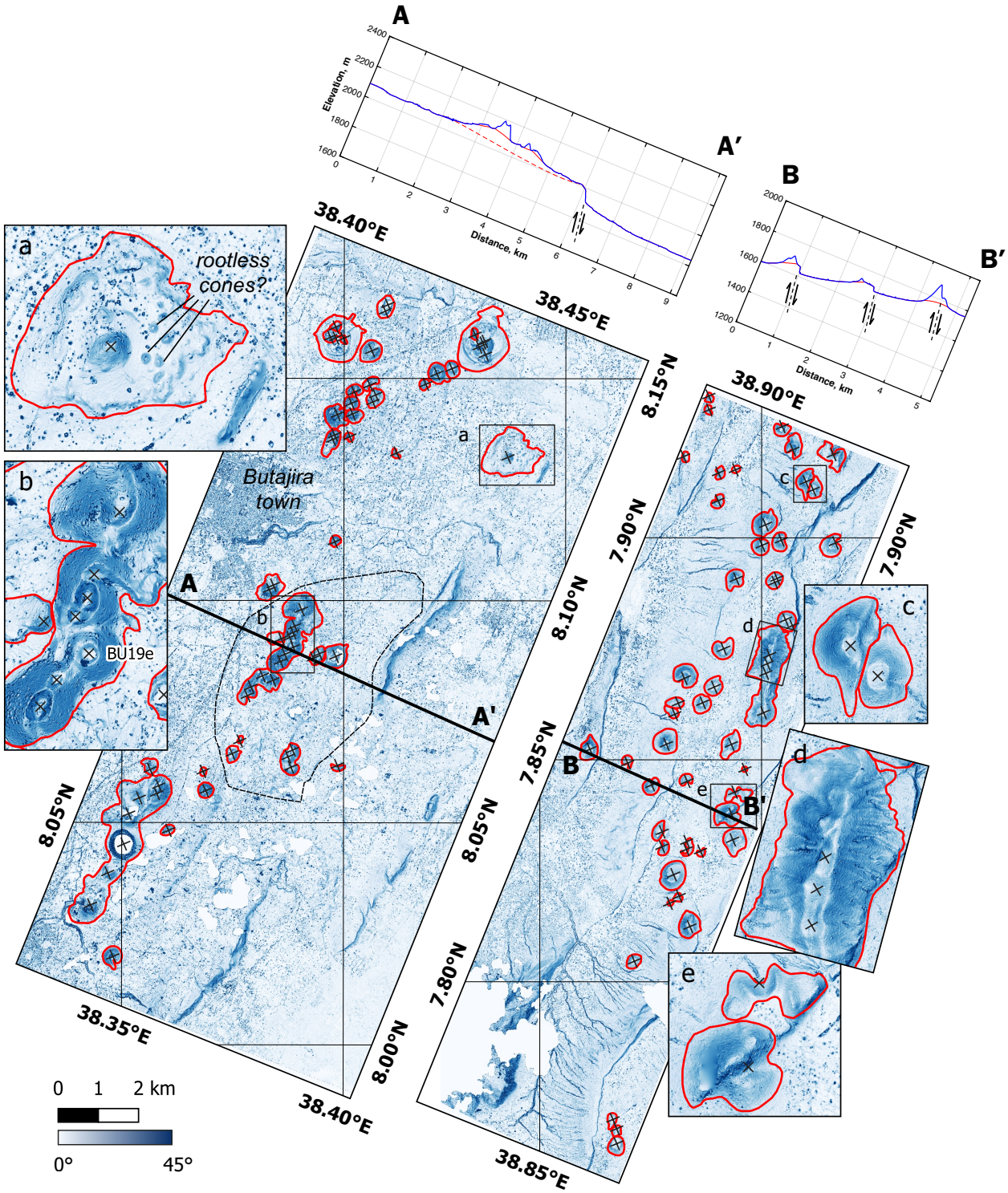
A
A′
Elevation, m
Distance, km
B
B′
Distance, km
38.40°E
38.45°E
38.90°E
8.15°N
8.10°N
7.90°N
8.05°N
7.85°N
8.00°N
7.80°N
38.35°E
38.40°E
38.85°E
a
rootless
cones?
b
BU19e
Butajira
town
A
A'
B
B'
c
d
e
0 1 2 km
0°
45°

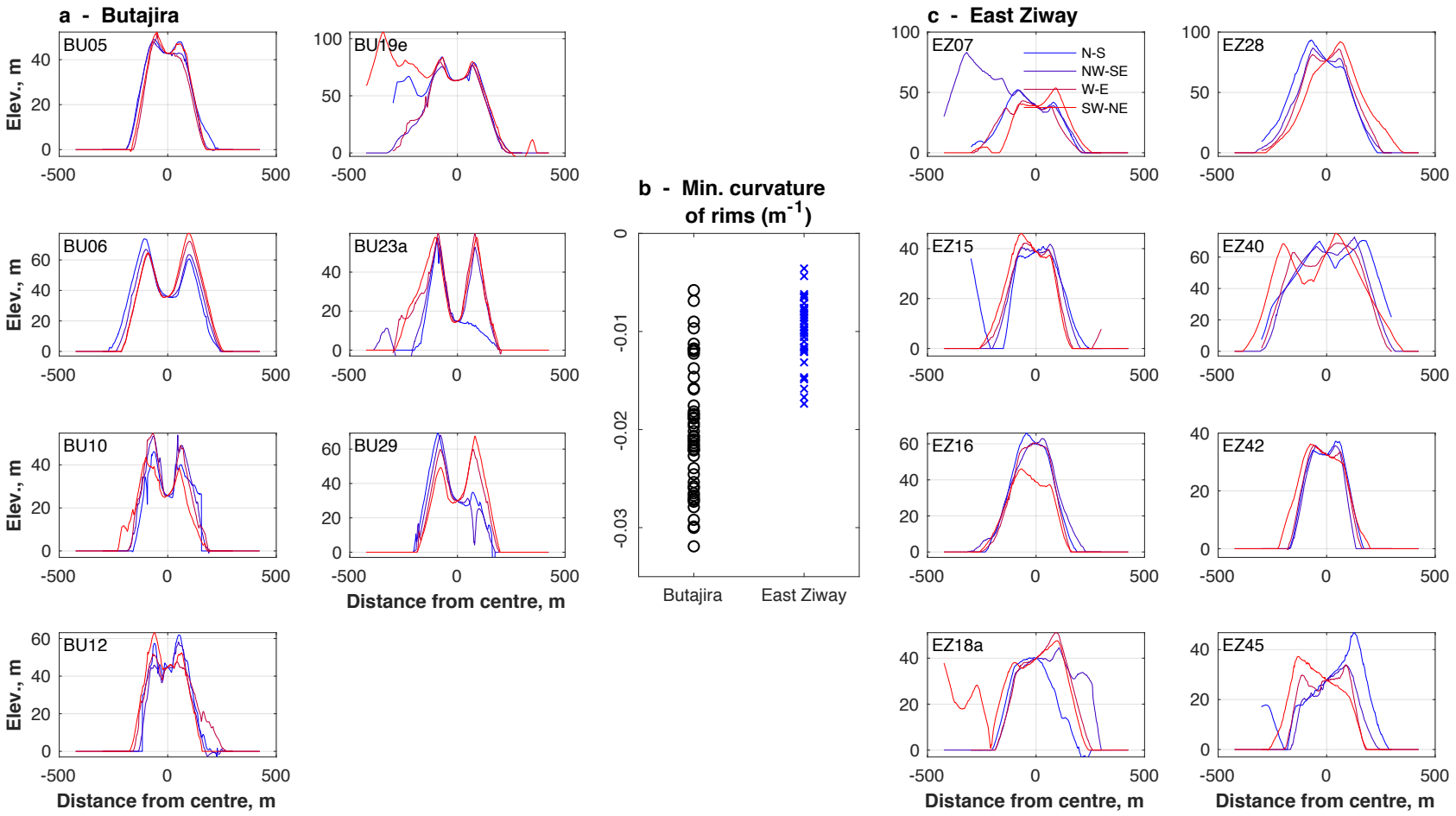

Figure 4.4. (a) and (c) Profiles of regular cones from Butajira and East Ziway. Cone IDs correspond to those in Figure A3.1 and Figure A3.2. (b) Minimum curvature of cone rims at Butajira and East Ziway, see Figure A3.4 for best-fitting polynomials and Figure A3.5 for second derivatives.

Table 4.2 lists the numbers of features recognized in the two cone fields. Cone types are broadly similar across the two fields, but maars have only been identified in Butajira. A number of the Butajira maars host cones emplaced after maar formation, along with associated lava flows. In the case of BU34, small cones distributed across the area may be rootless in origin (Figure 4.3a). More "breached/irregular" cones have been identified at Butajira, whereas more "dissected/eroded" cones have been mapped at East Ziway, partly a function of the more numerous faults at a closer proximity to cones in the East Ziway region (Figure A3.1–A3.2; Figure 4.3c, Figure 4.3e; Table 4.2, noting the similar total cones/maars in each field).

Profiles drawn in four compass directions across regular cones are shown in Figure 4.4. Regular cones in Butajira are more symmetrical than in East Ziway, where profiles commonly vary dependent on orientation. Craters are shallow or absent in East Ziway and are deeper in Butajira, with crater depth as much as 40–70% of cone height in three cases. Cone rims are sharper on regular cones in Butajira than they are in East Ziway, as shown by with a greater negative curvature (Figure 4.4b).

4.3.2. Volumes and morphometric parameters from Pleiades DEMs

The volumes calculated using the DEM differencing technique on the Pleiades-derived DEMs are plotted in Figure 4.5. The clustered cones in the Butajira field are inseparable – the volumes of the clusters are plotted instead of individual cones. Most cones, excluding the "partial/buried" category, are between 10^6–10^7 m^3.

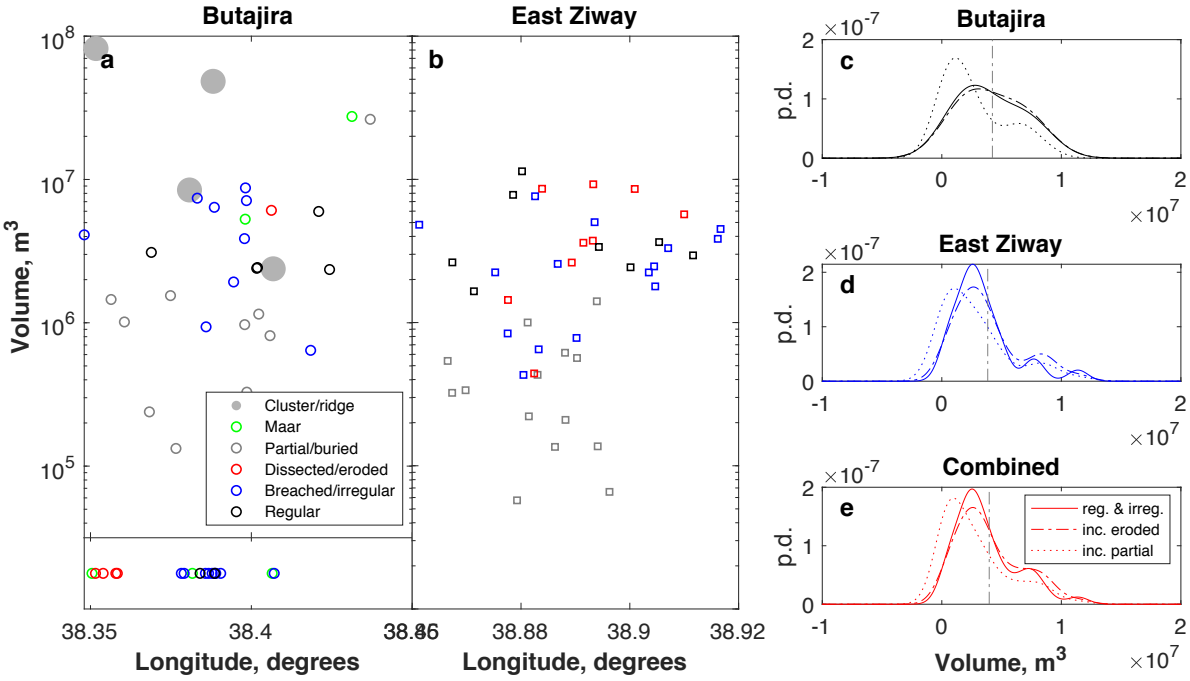

Figure 4.5. (a)-(b) Volumes of maars, cones and associated deposits from Butajira (a, circles) and East Ziway (b, squares). At Butajira, numerous cones and maars form inseparable clusters/ridges – the locations of these are plotted in the box below (a) and combined volumes are plotted as solid grey circles. (c)-(e) Probability distributions of cone/maar volumes for Butajira, East Ziway and the combined dataset (p.d. = probability density) for three sets of data each: (1 – solid line) "regular" and "breached/irregular"; (2 – dot/dashed line) additionally including the "dissected/eroded" category; and (3 – dotted line) additionally including the "partial/buried" category. Vertical grey line shows the mean for set (2).

The probability distributions show positive skew. The averages of the cones in Butajira (median = 4.1×10^6 m^3; mean = 4.2×10^6 m^3) are higher than those in East Ziway (median = 3.2×10^6 m^3; mean = 3.8×10^6 m^3). When "regular", "breached/irregular" and "dissected/eroded" cones are considered (dot/dashed

lines), the cones in East Ziway produce a bimodal distribution. The Butajira cones produce a unimodal distribution except when including "partial/buried" cones. In both cases, inclusion of the "partial/buried" category shifts the distribution significantly to lower values. Analysis of the combined volume data provides a combined probability distribution with a median cone/maar volume of 3.4×10^6 m^3 and a mean of 4.0×10^6 m^3. In Butajira, the volume of the broad topographic high associated with the central cluster and associated lava flows, possibly emplaced alongside/immediately preceding the scoria cones, is estimated as ~4.6×10^8 m^3 (see **Figure 4.3** and **Figure A3.6** for a map and bounds).

Idealized volumes calculated for "regular" cones using cone heights/widths (H_{co}, W_{co}) and crater widths/depths (W_{cr}, D_{cr}) allow the comparison of volumes of isolated cones with those that form part of a cluster (which would otherwise be inseparable; e.g., BU19e, **Figure 4.3b**). The idealized volumes reproduce DEM-calculated volumes within 10% and relative volume differences between isolated cones (**section A3.3**, **Figure A3.7**).

In **Figure 4.6**, the morphometric ratio H_{max}/W_{co} is plotted against V_{ideal}, W_{cr}/W_{co} and D_{cr}/H_{co} (see **Table 4.1** for definitions) for the Butajira and East Ziway fields. The fields are largely separable on the basis of the H_{max}/W_{co} ratio: Butajira cones have larger ratios than East Ziway cones, except for EZ28. There is a large scatter in these ratios which range between 0.1–0.21, either side of the average for fresh cones of 0.18 [*Porter*, 1972; *Wood*, 1980a]. Three Butajira cones have greater ratios than this global average.

There is a large overlap in V_{ideal} except for two outliers in the East Ziway field, EZ28 and EZ40. The values of W_{cr}/W_{co} are also indistinguishable between the two fields, except for EZ28, and are broadly consistent with the average for fresh cones of 0.4 [*Porter*, 1972; *Wood*, 1980a]. The fields are mostly separable on the basis of D_{cr}/H_{co}, with high ratios typifying the deep craters of Butajira cones compared to those of East Ziway. However, a number of Butajira cones overlap with the range of D_{cr}/H_{co} values from East Ziway.

4.3.2. Morphometric parameters from ASTER GDEM

Morphometric parameters H_{max}^{AS} and W_{co}^{AS} (defined in **Table 4.1**) are plotted in **Figure A3.8**, as well as volumes calculated from DEM-differencing using the ASTER GDEM. The average H_{max}^{AS}/W_{co}^{AS} is 0.148 with most cones below the

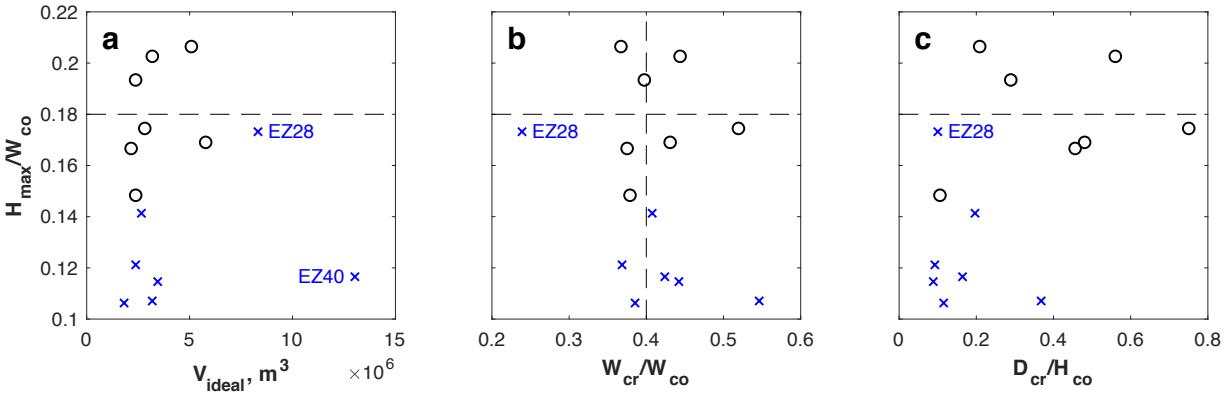

Figure 4.6. H_{max}/W_{co} of "regular" cones against (a) idealized volume, (b) W_{cr}/W_{co}, and (c) D_{cr}/H_{co} (see Table 4.1 for definitions). Cone EZ16 does not have a crater and is therefore not included in the plots. Black circles = Butajira; blue crosses = East Ziway. Dashed lines are shown for average values for fresh scoria cones: H_{max}/W_{co} = 0.18 and W_{cr}/W_{co} = 0.4 [*Porter*, 1972; *Wood*, 1980a].

average for fresh cones of 0.18 [*Porter*, 1972; *Wood*, 1980a]. There is a positive correlation between the ratio H_{max}^{AS}/W_{co}^{AS} and volume.

The results are presented by cone field in **Figure 4.7**. The cone fields of Soddo, Silti, Butajira, East Ziway and Sodere exhibit similar patterns on H_{max}^{AS}–W_{co}^{AS} and H_{max}^{AS}/W_{co}^{AS}–volume plots, broadly scattered across the ranges exhibited by the population as a whole. The Wonji cone field exhibits a larger range of H_{max}^{AS} and W_{co}^{AS} and is responsible for many of the extreme values in the population. The Akaki field has a low sample size.

The cone fields at Bishoftu and north and south of Kone Caldera Complex are distinguishable by lower volumes and a more restricted range of H_{max}^{AS} and W_{co}^{AS}, together responsible for the low volume–high H_{max}^{AS}/W_{co}^{AS} values in the population.

4.4. Discussion

4.4.1. Comparison of the Butajira and East Ziway fields

Our digital elevation models highlight several key differences between the Butajira and East Ziway cone fields. At Butajira, cones are found in linear clusters with associated lava flows, approximately 200 m west of nearby east-dipping faults. At East Ziway, isolated cones are found on or immediately adjacent to pervasive faulting. As a consequence, there are more dissected cones in East Ziway than in Butajira, where maars and breached/irregularly-formed cones are common. Cones in Butajira have sharper rims and larger H_{max}/W_{co} and D_{cr}/H_{co} ratios than those in East Ziway (**Figure 4.4**, **Figure 4.6**, **Table 4.1** for definitions).

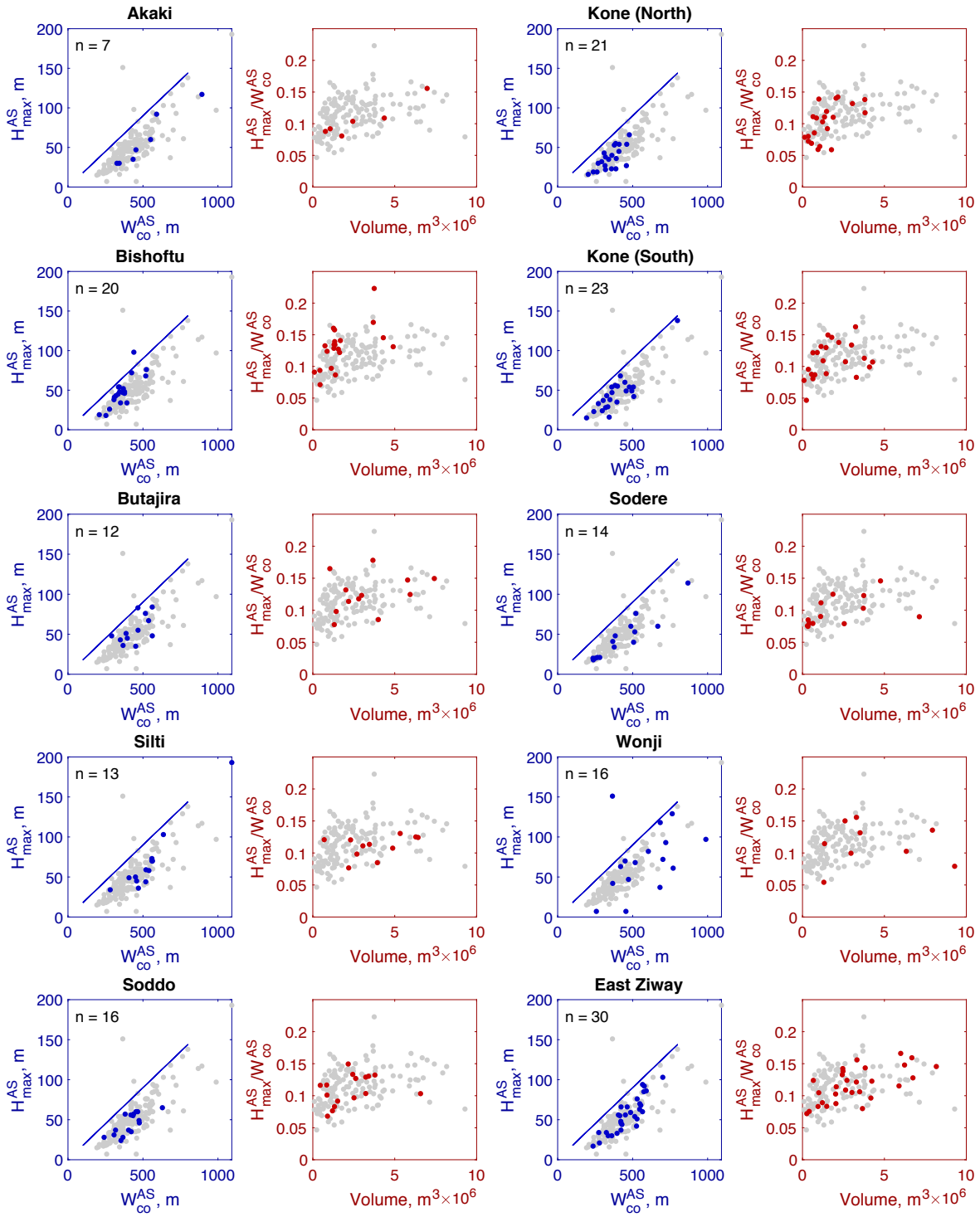

Figure 4.7. Results from the analysis of ten cone fields (Figure 4.1) across the Main Ethiopian Rift using the ASTER GDEM. The total set of results from the analysis are shown in grey (see Figure A3.8).

Multiple factors influence these morphometric and geospatial differences between cone fields (see **section 4.1**). In this section we discuss these differences and the possible influences of dikes, faults and plumbing systems, hydrology and age.

4.4.1.1 Dikes, faults and plumbing systems

The clustered locations of cones at Butajira indicates differing behavior of dikes in the near surface compared to the isolated cones at East Ziway. Clusters can be formed either by dikes repeatedly using similar pathways, or by multiple cones being emplaced by the same dike. The lack of clearly onlapping deposits in cone geomorphology (deposits from each eruption location are inseparable; **Figure 4.3b**) suggests that the cones were emplaced contemporaneously and the clusters were therefore formed by few/single events. This is supported by the consistent linear shape of each cluster. This suggests that the Butajira field has hosted large-volume eruptions, with the larger cone clusters ranging between $10^7 – 10^8$ m^3 (**Figure 4.5a**). These values are a lower bound, with associated lava flows building a broader topographic high as large as 4.6×10^8 m^3 (**Figure A3.6**).

Corazzato and Tibaldi [2006] proposed a morphological classification of cones on the basis of the coeval eruption points along the same magma-feeding fracture. Simple cones are formed from a single eruption point. A multiple superimposed cone (e.g., a cluster from the Butajira field) forms from numerous eruption points along the same fracture. A multiple rifted cone is a large, elongated ridge formed when craters at each eruption point coalesce entirely – an example is found in the east of the East Ziway area (**Figure 4.3d**). Simple cones are fed by a fracture constrained by high stresses and/or low magma pressure [*Corazzato and Tibaldi*,

2006]. With lower confining stresses and/or higher magma pressures, the fracture feeds a great number of eruption points with shorter separations, creating multiple superimposed cones or multiple rifted cones [**Figure 4.8**; *Corazzato and Tibaldi*, 2006].

On this basis, the Butajira field has been fed by fractures with generally lower confining stresses and/or higher magma pressures than the East Ziway field, except for the fracture that fed the multiple rifted cone in East Ziway. The confining stress can be considered as a superposition of the lithostatic pressure, the normal component of topographic stress and the far-field extensional stress [e.g., *Maccaferri et al.*, 2015]. It is possible that the confining stresses are lower on the rift margins due to a smaller normal component of topographic stress, allowing off-rift volcanism at Butajira to create superimposed cones in contrast to higher confining stresses nearer the rift axis at East Ziway. Further work is required to test this hypothesis.

Cones in both fields are preferentially located to the west of the east-dipping normal faults. Modelling studies suggest that topographic unloading during rift formation can lead to the formation of off-rift volcanism, due to dike deflection away from low topography [*Maccaferri et al.*, 2014]. Similarly, differential topographic loads of < 100 m induced by individual normal faults can cause dike deflection and can be responsible for the emplacement of cones on the footwall [*Maccaferri et al.*, 2015]. Dike deflection may therefore explain the location of cones in the Butajira field, offset from the main depression of the Main Ethiopian Rift and ~2 km west of east-dipping normal faults (**Figure 4.8**).

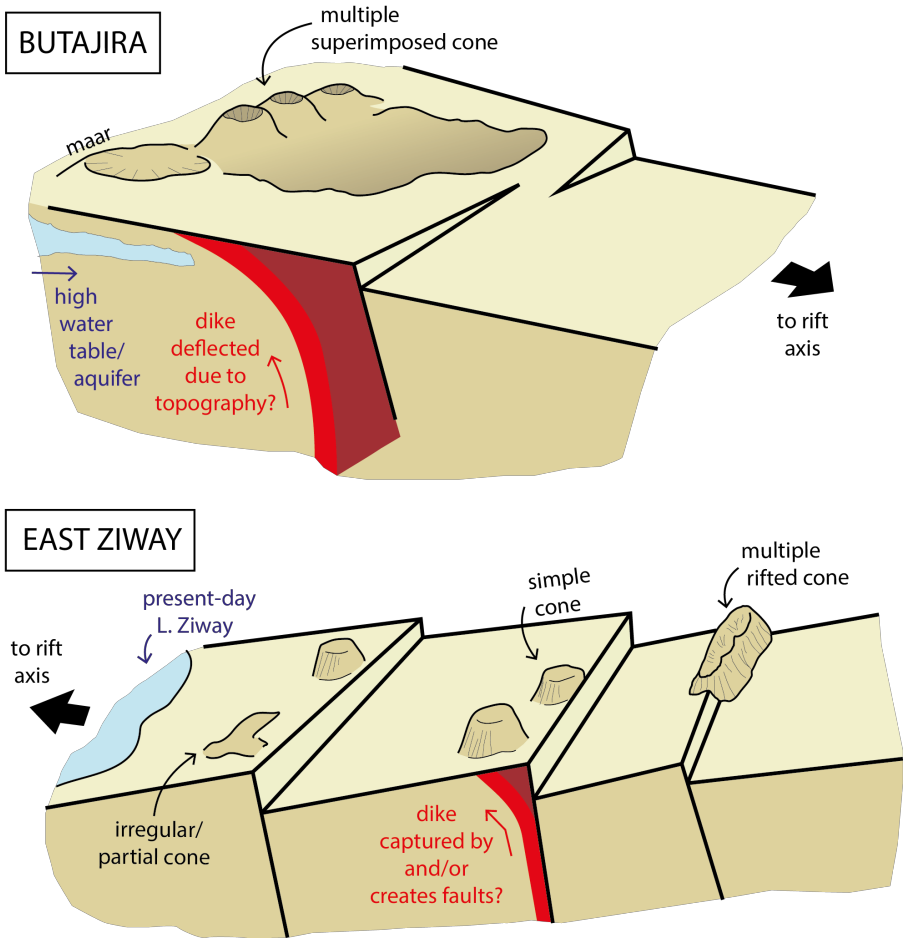

Figure 4.8. Summary of the tectonic and hydrological contexts of the Butajira and East Ziway volcanic fields and their influence on cone/maar formation.

In East Ziway, the main rift depression is to the west and local normal faults have relatively small offsets. The high number of active faults in the area provide several competing pathways for magma ascent. It is possible that dikes are captured by these faults [e.g., *Le Corvec et al.*, 2013b; *Gaffney et al.*, 2007], and are deflected by the differential topographic load of the fault scarps only at shallow depths, creating small offsets to the west (Figure 4.8).

Faults have been active after cone emplacement in East Ziway as shown by highly dissected cones (**Figure 4.3c**, **4.3d**); fault activity may be partially driven by dike events. The presence of east-dipping normal faults on the east side of the rift (profile B-B' in **Figure 4.3**; **Figure 4.8**) requires explanation, since the greatest subsidence is to the west (on the footwall side). This phenomenon can be explained either by fault rotation or by local subsidence caused by dike injection. Further research is required to investigate the relative influences of faults on dikes and dikes on faults in these areas.

4.4.1.2 Lakes, groundwater and local hydrology

The central Main Ethiopian Rift hosts numerous lakes – in the present day these are mostly on the eastern side of the rift although a variable number of small, transient lakes are found within the horst and graben structures of the SDFZ.

The lakes have developed through four stages from the Late Pleistocene onwards [100 ka; *Gasse and Street*, 1978; *Le Turdu et al.*, 1999; *Benvenuti et al.*, 2002]: (i) a megalake phase (Late Pleistocene, 100–22 ka), in which one lake covered much of the rift floor; (ii) a reduced-lake phase (latest Pleistocene, 22–10 ka) coinciding with the Last Glacial Maximum; (iii) a macrolake phase (early-mid Holocene, 10–5 ka), with lake connectivity limited by tectonic changes in topography; and (iv) the separated-lake phase (late Holocene-present, <5 ka). Large fluctuations in lake levels are common in all four phases [*Benvenuti et al.*, 2002], fluctuating by as much as 120 m in the Holocene [*Chalie and Gasse*, 2002; *Benvenuti et al.*, 2002; *Benvenuti et al.*, 2013].

Lacustrine sedimentation in East Ziway was significant during the megalake phase (Late Pleistocene), and restricted to the west of the cone field during the macrolake phase (early-mid Holocene). Sedimentation may have obscured evidence for small maars and other structures. However, the lack of any observable structures attributable to phreatomagmatic activity in East Ziway may indicate a lack of surface water in this area at time of eruption. This suggests that the East Ziway cones may have been emplaced during a dry phase, at a time of low lake level, perhaps prior to 100 ka [when estimates of lake extents are largely uncertain; *Le Turdu et al*., 1999], or during a later lake-level low stand.

In contrast, the presence of maars in the Butajira field indicates phreatomagmatic activity. One cone, BU34, may host a series of rootless cones (**Figure 4.3a**) suggesting the presence of surface water. Phreatomagmatic activity may influence ratios of crater depth to cone height (D_{cr}/H_{co}) and the abundance of breached cones [*Risso et al*., 2008]. Generally, phreatomagmatism results in lower and broader structures [e.g., *Risso et al*., 2008]. Surface water and/or groundwater increases the explosivity of the eruption – the depth at which fragmentation occurs may change depending on the depth of the groundwater/nearby aquifer, which may increase or decrease the depth of the crater and the likelihood of breaching the cone [e.g., *Aranda-Gomez and Luhr*, 1996; *Risso et al*., 2008].

The abundance of water in the Butajira area is evident in the present-day. The higher elevation on the rift flanks provides a wetter climate the rift floor, and the nearby plateau and Guraghe mountains act as a major source of groundwater for the whole rift [*Kebede et al.*, 2008; *Bretzler et al.*, 2011]. Accordingly, there are

numerous small bodies of water, including the crater lake of Har Shetan within a maar structure (BU31e).

The morphology of the Butajira cone field indicates that the cones and maars were emplaced in a similarly wet environment to the present day, or wetter (**Figure 4.8**). The hydrological context of rift-related cone fields is therefore key to morphological characteristics, eruptive process and associated hazards.

4.4.1.3 Relative ages of cones

There are few age constraints on the scoria cones of the Main Ethiopian Rift, and any indication of relative age is of great use in hazard assessment, as well as identifying the environment into which these cones were emplaced [e.g., *Le Corvec et al*., 2013c]. Age is a significant control on cone morphometry, with progressive degradation leading to lower H_{max}/W_{co} values than the average for fresh cones of 0.18 [e.g., *Inbar et al.*, 2011; **Figure 4.6**]. However, several recent studies suggest that other factors may dominate this ratio, including eruption dynamics, baseline topography and the exact method of calculating H_{max}/W_{co} [ratio of maximum height to average width; e.g., *Favalli et al.*, 2009; *Kervyn et al.*, 2012]. The grainsize of the scoria comprising the cone is a key parameter, which is also linked to explosivity and water content [e.g., *Riedel et al*., 2003].

The Butajira cones have higher H_{max}/W_{co} than those in East Ziway. Lake-sediment accumulation around the East Ziway cones may also have influenced their apparent heights and widths, perhaps contributing to low H_{max}/W_{co} ratios [*Favalli et al*., 2009] and an underestimation of cone volumes. The Butajira cones also have higher

D_{cr}/H_{co} (ratio of crater depth to average height) than those in East Ziway. This may be influenced by phreatomagmatism (as discussed in **section 4.4.1.2**). The Butajira cones also have sharper rims, with greater curvature on radial profiles, than those in East Ziway (**Figure 4.4b**).

Higher H_{max}/W_{co}, lower D_{cr}/H_{co} and sharper rims in the Butajira cones are all consistent with a younger apparent age than for cones in East Ziway. The combination of factors provides a greater degree of confidence than any single factor. Differences in erosion processes at each field may contribute to a younger apparent age at Butajira compared to East Ziway, and prevents a quantitative assessment of the difference in age between cone fields. Nonetheless, the cones at each field are separable using the factors outlined above which suggests minimal overlap in ages between these fields. This hypothesis requires corroboration from absolute dating techniques.

Our data suggest that the East Ziway area in this study has not been active since activity began in the Butajira field. Since activity in the Butajira field is more recent, the possibility of ongoing activity cannot be ruled out. A recent magnetotelluric survey found a conductive body along the SDFZ to the east of Butajira [*Hübert et al*., 2018] and a diffuse CO_2 survey found elevated levels of magmatic degassing (**Chapter 2**). The current state of any magmatic reservoir in the area and the potential for future events is largely unknown.

In contrast, no magmatic degassing has been observed to the east of Aluto volcano, south of the East Ziway area in this study (**Chapter 2**). Successive magnetotelluric surveys have found no evidence for a conductor to the north east of Aluto towards

East Ziway [*Samrock et al.*, 2015; *Hübert et al.*, 2018]. This supports our hypothesis that activity at East Ziway precedes that of Butajira, and may have ceased.

4.4.2. Comparison of cone fields across the MER

The comparison of morphometric parameters using the ASTER GDEM showed little systematic variation with cone field (**Figure 4.7**). The ASTER GDEM has insufficient resolution to categorize cones as regular or otherwise. The cones used in the analysis, therefore, include many irregular structures including clustering, maars, breaching and post-emplacement processes.

The low resolution also leads to errors for each parameter, systematically underestimating H_{max}^{AS} and volume. These errors are volume-/size-dependent, with larger cones more accurately estimated [*Fornaciai et al.*, 2012]. Cones in the Main Ethiopian Rift are on average smaller than in many cone fields worldwide [e.g., 10–50 × 10^6 m^3; *Fornaciai et al.*, 2012], leading to larger associated errors.

Despite these shortcomings, a number of observations can be made. The variability of H_{max}^{AS}, W_{co}^{AS}, and volume for the Wonji field is greater than other fields, perhaps suggesting a greater degree of irregularity and variation across the field. The Wonji field encompasses a number of silicic volcanic centers along the rift (Gedemsa, Bora, Tulu Moye), the activity and plumbing systems of which may interact with the emplacement of scoria cones within the field. The field is close to numerous lakes; variable lake sediment deposition may also influence the variability of morphometric parameters.

In contrast, the fields north of Kone, south of Kone, and at Bishoftu exhibit a restricted range of H_{max}^{AS} and W_{co}^{AS}, and are low in volume. The cones surrounding Kone are along the axial spreading center, in the more mature northern rift. It is possible that cones in the north are more regular due to a relative lack of surface water/groundwater, and lake sediment deposition, compared to the south. This remains a hypothesis to test.

Despite the difficulties of using low resolution DEMs, their wide coverage and free availability enables their use in comparing a large number of fields. As new global, free products at higher resolution become available, morphometric comparisons of cones will provide useful insights into each cone field's characteristics.

4.4.3. Comparison with extensional environments worldwide

Our analysis of two rift-related volcanic fields using high-resolution topography is part of a growing literature on extension-related volcanic fields. *Fornaciai et al*. [2012] found that cones in extension-related fields have lower height to width (H/W) ratios and higher crater width to cone width (W_{cr}/W_{co}) ratios than those in subduction-related fields. They speculated that higher water content in magma produced in subduction environments leads to greater explosivity and smaller grainsize, which enables steeper sides to the cones [*Riedel et al*., 2003].

Our results show that cones in East Ziway have low H/W ratios, similar to many cone fields that show significant degradation [*Fornaciai et al.*, 2012]; this is probably the result of degradation rather than phreatomagmatism. The relatively W_{cr}/W_{co} ratios at East Ziway may indicate an erosional trend in which mass eroded

from the top of the cone is not redistributed at its base but removed [e.g., similar to Potrillo volcanic field; *Fornaciai et al.*, 2012].

Cones in Butajira have a range of H/W ratios, including values above those expected for freshly emplaced cones and at the highest end of values observed in either extension- or subduction-related fields [*Fornaciai et al.*, 2012]. The propensity of rift-environments to host an active hydrological cycle, with high groundwater and many lakes, may lead to increased explosivity and higher H/W ratios in some cones (e.g., at Butajira), whilst also leading to maar formation. This may counteract the effects of lower water content in magma proposed by *Fornaciai et al*. [2012].

The cones in our analysis are smaller in volume (~4×10^6 m^3) than a large number of fields from a variety of geodynamic environments [~9–96×10^6 m^3; *Fornaciai et al*., 2012]. Whilst erosion may have reduced the size of some cones, particularly in the East Ziway field, the low volumes calculated here may suggest that small pockets of melt are able to reach the surface with relative ease in the Main Ethiopian Rift compared to other environments.

Le Corvec et al. [2013a] found that cone fields in extensional environments incorporate a greater number of different alignments than other tectonic regimes. The influence of pre-existing structures is dominant in many extensional environments, but is inferred to weaken in mature parts of the East African Rift System and closer to rift axes where the state of stress has a larger impact [*Mazzarini et al*., 2016; *Delcamp et al*.., 2019].

Our observations of eruption locations and isolated/superimposed cones at East Ziway and Butajira suggest that topographic unloading also plays a crucial role in determining where dikes intersect with the surface at various stages and locations of rift evolution. In sum, our analysis shows that the interplay of stress, structures and hydrology strongly influence both the distribution and morphology of cones in extensional environments.

4.5. Conclusions

The morphology of distributed volcanic fields in rift environments is influenced by a range of characteristic factors, including multiple generations of faults, repeated dike intrusions, an active hydrological cycle and rift development through time. In this study, we have presented new digital elevation models and compared the morphology of two distributed volcanic fields in the Main Ethiopian Rift, each hosting ca. 50 cones/maars.

Whilst average cone volumes are similar between the fields (mean ~ 4×10^6 m^3), most other parameters differ significantly. The Butajira field hosts a mixture of maars and cones deposited in linear clusters of superimposed cones, whereas the East Ziway field comprises isolated cones and no maars (**Figure 4.8**). Clusters at Butajira form part of a broader topographic high (volume ~4.6×10^8 m^3), possibly the result of lava flows and other volcanic deposits associated with the distributed cone field. The Butajira field is likely to have been fed by a few large fissure eruptions (cluster volumes ~ 10^7–10^8 m^3), whereas the East Ziway field is the result of a larger number of small eruptions.

The location of cones in distributed volcanic fields provides insight into the geometry of dikes feeding the eruptions. Cones at Butajira are located 2–3 km from faults on the upthrown side, whereas cones at East Ziway are found on or immediately adjacent to fault scarps (**Figure 4.8**). Dikes at Butajira may have been deflected to the west by topographic unloading; dikes at East Ziway may have been captured by faults at depth. Short vent spacing, characteristic of the superimposed cones at Butajira, may be the result of low confining stresses.

Maars and high D_{cr}/H_{co} ratios at Butajira suggest phreatomagmatic activity and the presence of surface water and/or groundwater, implying emplacement at a time when the local climate was at least as wet as the present day. At East Ziway, on the other hand, there is no evidence for phreatomagmatic activity despite the field's proximity to Lake Ziway. The cones were likely emplaced during a dry phase, although later lacustrine deposition may have buried maars and affected estimations of volume and cone height.

High H_{max}/W_{co}, D_{cr}/H_{co} and high negative curvature of cone rims all indicate a younger age of cones at Butajira compared to East Ziway. Despite an active volcanic center nearby in Aluto, the East Ziway field shows no sign of recent activity. A young age for the Butajira field is supported by its association with areas of elevated diffuse CO_2 degassing (**Chapter 2**), and a conductor detected by magnetotellurics [*Hübert et al.*, 2018]. Despite the main magmatic and tectonic activity of the rift migrating to the rift axis, ongoing activity at the Butajira field on the rift shoulder cannot be ruled out.

Cones in Butajira and East Ziway are smaller in volume than in many fields worldwide. Analysis of other distributed volcanic fields across the MER using the ASTER GDEM is complicated by low-resolution which prevents classification of regular and irregular morphologies. The fields have a combined average H_{max}/W_{co} = 0.148, far lower than the average for fresh cones largely due to irregular morphology. Most of the fields are indistinguishable using H_{max}/W_{co} ratios and calculated volumes. The Wonji field in the center of the rift exhibits the greatest range of values, whereas fields on the western flank (Bishoftu) and in the more developed northern section of the rift (north and south of Kone volcano) have restricted ratios and small volumes (**Figure 4.7**).

Further comparison of the morphology of distributed volcanic fields in rift environments is required to assess the competing factors that influence their emplacement and degradation. Higher resolution digital elevation models with large-scale, freely accessible coverage are becoming available. This study demonstrates the use of careful analysis of morphometry to infer process and relative age of cones towards a more developed understanding of distributed volcanic activity within the Main Ethiopian Rift.

5 Summary and conclusions

5.1 Overview

This thesis explores the many and varied interactions between continental rift structure and magmatic activity as exemplified by the Main Ethiopian Rift, with a particular focus on degassing and volcanism. I have taken a regional, comparison-based approach to make a broad evaluation of structural controls on the release of volatiles and the emplacement of volcanic deposits. I have brought together a range of techniques including diffuse CO_2 surveys, field campaigns, satellite-derived digital topography, and morphometry, investigating specific sites in depth before comparing across and along the rift. The thesis therefore advances our understanding of rift processes and their interactions.

The introduction to the thesis (**section 1.3)** set out three spatial scales on which the thesis focuses: local, regional and global. Here I summarise the main findings regarding degassing and geothermal activity, basaltic volcanism and silicic volcanism, using these spatial scales as a framework. The local scale deals with previous and ongoing activity at specific sites within the Main Ethiopian Rift, in the hope of understanding each volcano/volcanic field/geothermal system in depth, including relevant hazards. The regional scale looks at the Main Ethiopian Rift as

a whole, identifying patterns and trends between features both across the rift and along the rift. Finally, the global scale seeks to apply findings from the Main Ethiopian Rift to continental rifts more generally, in the hope of advancing our fundamental understanding of this important tectonic and magmatic phenomenon.

5.2 Local scale – specific sites of volcanism and degassing

5.2.1 Degassing and geothermal activity

In **chapter 2** we presented new diffuse CO_2 surveys across four sites in the Main Ethiopian Rift (MER). Elevated values and inflections on cumulative frequency plots (**Figure 2.4**) were observed for the Butajira and Habilo sites. Targeted profiles (**Figure 2.7**) revealed fault-controlled degassing on the west side of the Habilo graben along east-dipping faults, with a total flux of approximately 5–155 ky yr^{-1}. The main sources of error on this estimate are (1) the length of degassing faults, and (2) the confidence intervals associated with fitting a Gaussian curve to the profiles. The exclusive use of east-dipping faults as permeability pathways in the Habilo graben highlights the importance of fault geometry in the structural control of degassing.

Degassing at Butajira is elevated near the Kuntane swamp and associated hot springs. Magnetotellurics suggest a large conductor in this area [*Samrock et al.*, 2015; *Hübert et al.*, 2018] which may represent the source of heat and gas. In contrast, no elevated diffuse CO_2 measurements were recorded along the Wonji faults to the east of the hydrothermally-active volcano Aluto, suggesting a limited area of degassing perhaps due to local hydrology.

A rift-wide compilation of observed hot springs and fumaroles highlights a number of particularly active areas. The area around Fentale volcano hosts several sites of hydrothermal activity (including Filoa, Habilo, Hubisha; **Figure 2.6**) and is one of the most seismically active regions of the rift [*Keir et al.*, 2006]. Abundant hot springs around the O'a caldera (Lake Shalla) suggests a heat source, but the activity of the underlying volcanic and hydrothermal system remains largely unstudied.

5.2.2 Silicic volcanism

We presented new digital elevation models (DEMs) in **chapter 3** for three silicic volcanoes in the MER – Fentale, Gedemsa and Corbetti. Using these DEMs and a complementary field campaign, we mapped new and previously identified features at each centre. At Fentale, additional post-caldera deposits were identified, specifically small-volume coulees, a pumice cone and multiple intra-caldera features. The morphology of coulees at Fentale are strongly controlled by pre-existing topography, commonly forming levees with slope-dependent widths. Post-caldera coulees have lengths of 2–2.5 km, volumes of 0.01–0.1 km^3, and short vent spacing (200–2,000 m).

At Corbetti, 14 newly identified craters were mapped. The craters are located in two swaths aligned WNW-ESE in the same direction as the two main edifices, Urji (6.4 km^3) and Chabbi (7.5 km^3). We observed large, elliptical depressions in the source regions of large coulees at Corbetti, interpreting them as buried craters from which the silicic lavas emanated. The most recent coulee has a calculated volume of 0.47 km^3. Since the explosive eruption of the Wendo Koshe Younger Pumice (WKYP, 2300 BP), four such coulees have been emplaced, resulting in an average

eruptive flux of ~9×10^5 m^3/yr. The average eruptive flux for the entire post-caldera phase (180 kyr) is 8×10^4 m^3/yr, suggesting that Corbetti has recently been in a state of elevated activity.

5.2.3 Basaltic volcanism

In **chapter 3** we note that basaltic vents are present on the edifices of Fentale and Boset, but are absent in Corbetti. A single scoria cone is located within the caldera of Gedemsa, with several cones and lava flows immediately to the south-east along regional faults. Cones are also found immediately to the north and south of Fentale's edifice.

Regional basaltic volcanism is evident across much of the MER, and in **chapter 4** we present DEMs of two specific fields – Butajira and East Ziway. Each host ca. 50 cones exhibiting great morphological diversity. Butajira hosts linear clusters of cones, probably formed by large, multi-cone eruptions with conservative estimated volumes of ~10^7–10^8 m^3. East Ziway hosts isolated cones with volumes of 10^6–10^7 m^3. Maars and rootless cones at Butajira indicate phreatomagmatic processes at time of eruption, whilst such evidence is lacking in East Ziway. Lower cone height-width and crater depth-cone height ratios, along with smoother cone rims, are consistent with a younger age at East Ziway compared to Butajira. The Butajira field may, therefore, still be active, a hypothesis supported by our diffuse degassing results from Butajira in **chapter 2**.

5.2.4 Further work

This study has done much to progress our knowledge of key sites within the MER, but much work is yet to be done. Whilst numerous recent studies have focussed on the volcanoes in the south of the rift [Aluto, Corbetti; *Hutchison et al.*, 2016a, 2016b, 2016c; *Martin-Jones et al.*, 2017; *McNamara et al.*, 2018; *Lloyd et al.*, 2018a, 2018b, *Nowacki et al.*, 2018; *Wilks et al.*, 2018], less research has been done on the northern volcanoes. In **chapter 3** we show that Fentale has been more active in its post-caldera phase than previously thought, and though the deposits are not voluminous they are numerous. A thorough mapping campaign of the edifice, off the back of this study, would be beneficial.

In addition to Fentale, further research into volcanism in the Main Ethiopian Rift should focus on the Butajira area. Elevated degassing (**chapter 2**) and relatively young deposits (**chapter 4**), along with the presence of a large conductor imaged by magnetotellurics [*Hübert et al.*, 2018], suggest a possibility of ongoing activity. Dating of the maars and scoria cones would test this hypothesis, as well as the hypothesis that each cluster of cones was emplaced contemporaneously. The lifespan of cone fields around the world varies widely, and is totally unknown for the MER.

The compilation of hot springs and fumaroles presented in **chapter 2** is an important guide in the number and distribution of geothermally active areas, but large uncertainties remain concerning the extent of each area and the magnitude of degassing. More surveys are required to adequately constrain the emissions from each site, and assess their importance regarding local geothermal/volcanic activity

as well as rift-scale emissions. This study suggests the extent of degassing along-fault is a key parameter which needs further constraint.

5.3 Regional scale – across and along the Main Ethiopian Rift

5.3.1 Degassing and geothermal activity

According to the locations of hot springs and fumaroles collated in **chapter 2**, geothermally active areas in the Main Ethiopian Rift (MER) align NE-SW, apparently independent of change in rift trend. Off-axis areas include Butajira and Bodicho Springs (**Figure 2.6**). Most manifestations are co-incident with regional faults, with some features associated with cross-cutting structures like the Wondo Genet fault scarp.

The sites can be broadly categorised into (1) fumarole dominated systems located in and around central volcanoes and (2) regional, hot-spring dominated systems. Many of these regional systems are located near lakes, highlighting the importance of hydrology in rift-wide geothermal activity, and a potential bias of the compilation of degassing locations. The abundance of degassing sites which are > 10 km from the nearest volcanic edifice may imply magmatic storage laterally offset from edifices, and/or lateral transport of volatiles before they reach the surface. If magma storage is common away from volcanic edifices, there may be ongoing potential for regional volcanism within the rift.

5.3.2 Silicic volcanism

The DEMs presented in chapter 3 show a diversity of caldera architecture along the MER, ranging from Fentale's regular, elliptical, deep and narrow caldera to the highly irregular, broad and low calderas of Gedemsa and Corbetti (Figure 3.11). We suggest that these differences in architecture are due to different processes of formation, with the former the product of a simple piston collapse and the latter being produced by piecemeal collapse. It is possible that simple piston collapse is more common in late stage rifting (i.e., Fentale in the northern MER), and piecemeal collapse more common in earlier stages (i.e. Corbetti in the southern MER), when larger and more silicic magma reservoirs are allowed to form.

Pervasive faulting has greatly influenced the shapes of the calderas and may have encouraged piecemeal formation. Rift-related normal faults have created offsets, and underlying structures may have acted as caldera faults, leading to linear sections of caldera rim. However, it is unclear whether these geometrical observations were formed during or after eruption, by erosional processes such as slope failure.

For the three MER volcanoes presented in chapter 3, post-caldera activity is frequently aligned along cross-rift structures (Figure 3.11, Figure 3.13). In comparison, activity at Aluto is mostly aligned with the trace of the caldera [*Hutchison et al.*, 2015]. Seismic anisotropy studies show shear-wave polarisations parallel to cross-cutting structures at Corbetti and Aluto [Lloyd et al., 2018; Nowacki et al., 2018]. Trends parallel to rift-related faults are found at every volcano (Figure 3.13), particularly Fentale, Boset and Dabbahu (Afar). These

findings are consistent with the hypothesis that rift-related faults play a more important role in transporting melt to the surface in more mature rifts (i.e., northern MER and Afar), whereas in less mature rifts cross-cutting structures still play a vital role (i.e., southern MER).

5.3.3 Basaltic volcanism

As presented in **chapter 3**, the closest basaltic cones or lava flow vents at Corbetti and Aluto are 2–3 km from their edifices. Basaltic eruptions have occurred on the edifice at both Boset and Fentale. This may imply shielding by large, active, peralkaline magma reservoirs at Aluto and Corbetti, whereas reservoirs in the volcanoes to the north are smaller, less active, or less long-lasting. At Boset, Fentale and Dabbahu, basaltic vents are found in close proximity to silicic vents, suggesting that basaltic volcanism may have a closer association with silicic volcanism in more mature rifts.

In **chapter 4** we suggest that the Butajira cone field may be younger than the East Ziway cone field. This suggests that off-rift volcanism is a key feature of the MER, and the assumption that volcanic deposits are progressively younger towards the rift axis is inaccurate. *Maccaferri et al.* [2013] propose a mechanism for off-rift volcanism by showing that dikes are deflected by topographic unloading.

The East Ziway field host cones that have close associations with regional faults. The normal faults dip to the east despite the majority of rift-related subsidence lying to the west – this could imply that the faults are formed by local subsidence above dike intrusions which might be associated with cone formation. Further work is

needed to investigate potential genetic relationships between cones and dikes in the MER.

5.3.4 Further work

The database of hot springs and fumaroles that has been compiled in this study is the first step towards a systematic compilation of features along the rift. Particular areas require further mapping for geothermal features, particularly the volcanoes of Boset and Kone, and the region to the west and south of Corbetti. Systematic recording of spring geochemistry and temperature would also allow further classification of these features, and enable information on the distribution of CO_2 and heat flux to be gathered.

This study proposes hypotheses regarding the relation between rift maturity and volcanic behaviour. Further work should focus on quantifying the proportion of silicic vs basaltic volcanism at each centre, and robust statistical analysis of vent alignments to test these hypotheses.

In **chapter 4** we conducted a rift-wide survey of cone morphometry using the ASTER Global DEM. Some systematic differences can be observed, including a greater scatter in values of height-width ratio and volume for the Wonji field compared to other fields (**Figure 4.7**). Global DEMs of higher resolution are becoming increasingly available, and further work should focus on using these to assess cone morphometry on a greater scale than presented in this study.

5.4 Global scale – continental rifts worldwide

5.4.1 Degassing and geothermal activity

By extrapolating the results of our diffuse CO_2 surveys, as well as previous surveys on Aluto volcano, we estimate in **chapter 2** that the Main Ethiopian Rift (MER) emits a total of 0.52–4.36 Mt yr^{-1}, of which 0.45–1.26 Mt yr^{-1} is "on-edifice" and 0.07–3.10 Mt yr^{-1} is "off-edifice". This is similar to the diffuse CO_2 degassing proposed for the Natron and Magadi basins in the Kenya Rift Valley [KRV, ~4 Mt yr^{-1}; *Lee et al.*, 2016], but for a larger area. The diffuse CO_2 flux per length of rift is therefore lower for the MER (1.3–10.9 kt yr^{-1} km^{-1}) than the KRV (11.7–32.3 kt yr^{-1} km^{-1}).

The causes of these differences could be due to spatial frequency of degassing sites, the size and type of high-flux areas, or error in the method of extrapolation. Further extrapolation to the whole Eastern Rift provides total emissions of 3.9 – 32.7 Mt yr^{-1} from the survey in this study, lower than the 38 – 104 Mt yr^{-1} estimated from extrapolating the KRV results [*Lee et al.*, 2016]. Continental rifts may therefore contribute a smaller proportion of diffuse CO_2 degassing than previously thought, however the proportion is still very significant. We present scaling analysis (**Figure 2.11**) that suggests approximately 6–18 My yr^{-1} CO_2 can be accounted for by degassing of magma intruded to accommodate crustal extension, indicating that additional sources are significant. These sources may include additional magma intrusions, metasomatised lithosphere and decarbonation of limestone.

5.4.2 Silicic volcanism

The alignments inferred from our DEMs in chapter 3 suggest that structural controls on eruption locations are greater than the influence of the local stress fields (e.g., edifice loading, pressurised magma reservoirs and/or cylindrical conduits). The relative influence of regional stress fields versus structures is difficult to determine – regional stress fields encourage dike formation orthogonal to lowest compressional stress, which in a rift is the spreading direction. Rift-parallel faults are also nearly orthogonal to spreading direction, so alignments in this direction could be due to faults or regional stress. Edifice loading is a significant feature for volcanoes greater than 1–2 km tall [*Wadge et al.*, 2016] – MER volcanoes are short due to a combination of caldera formation, ubiquitous normal faults and low eruptive rates.

This study provides the first estimates of peralkaline rheology from the morphology of deposits. The ranges of yield strengths and ogive wavelength ratios span those estimated for calc-alkaline dacites and rhyolites. Emplacement viscosity inferred from levees (10^8-10^{11} Pa s) is similar to, or lower than, calc-alkaline rhyolites. Further work on the emplacement rheology of peralkaline rhyolites would greatly increase our understanding of rift volcanism.

5.4.3 Basaltic volcanism

In a survey of cone fields across North America, *Fornaciai et al.* [2012] found that cones in extensional environments have lower volumes and lower height-width ratios than cones in compressional environments. The average volume of cones in

Butajira and East Ziway, calculated in **chapter 4**, is ~4.0×10^6 m^3. This value is significantly lower than cones elsewhere [e.g., $10–50 \times 10^6$ m^3; Fornaciai et al., 2012]. This study highlights the interaction of the processes of cone field formation with many features of continental rifts (e.g., changing hydrology, relief, multiple generations of structures, extensional stress regimes). Cone fields are key indicators of these environmental and architectural features of rifts [e.g., *Kereszturi et al.*, 2011], and so our study should encourage further work into the emplacement of cones within rift environments.

5.4.4 Further work

More surveys are required to adequately constrain the globally significant emissions of diffuse CO_2 from continental rifts. In particular, temporal variability of diffuse CO_2 degassing is poorly understood, and unstudied in a continental rift setting. Repeat measurements should be made at key sites at a number of temporal scales to address this issue. Estimating rift-scale emissions is hindered by the scale of measurement – this study and other similar studies use a portable monitor that practically provides a point-source measurement. New techniques are being developed to overcome these issues, as are novel proxies for diffuse CO_2 flux including measuring responses in vegetation. In addition to more surveys and better measurement techniques, more robust statistical methods (e.g., Bayesian inversion) for extrapolation need to be developed.

This study acts as the first step towards a broader morphological survey of peralkaline deposits. This should be the focus of future work and could greatly advance our understanding of eruption dynamics and emplacement mechanisms.

Further studies of cone fields in extensional environments, with a particular focus on dating and linking emplacement to environmental conditions, would also greatly develop our understanding of continental rift volcanism, and its many and varied interactions with rift structures.

References

Abbate, E., and M. Sagri (1980), *Volcanites of the Ethiopian and Somali Plateaus and Major Tectonic Lines*. Accademia Nazionale dei Lincei: Geodynamic Evolution of the Afro- Arabian Rift System: Meeting Vol. 47 pp. 219–227.

Abebe, T., F. Mazzarini, F. Innocenti, and P. Manetti (1995), The Yerer-Tullu Wellel Extensional Structure (Central Ethiopia): Evidences from Remote Sensing, Petrologic and Geochronologic Data. In IEEE (Ed.), *Geoscience and Remote Sensing Symposium, IGARSS '95: "Quantitative Remote Sensing for Science and Applications"* (Vol. 1, pp. 374–376), doi:10.1109/IGARSS.1995.520285.

Abebe, T., F. Mazzarini, F. Innocenti, and P. Manetti (1998), The Yerer-Tullu Wellel volcanotectonic lineament: a transtensional structure in central Ethiopia and the associated magmatic activity. *Journal of African Earth Sciences*, *26*(1), 135–150, doi:10.1016/S0899-5362(97)00141-3.

Abebe, T., P. Manetti, M. Bonini, G. Corti, F. Innocenti, F. Mazzarini, and Z. Pècksay (2005), Geological map (scale 1:200,000) of the northern Main Ethiopian Rift and its implications for the volcano-tectonic evolution of the rift. *Geological Society of America Map and Chart Series MCH094*, 20 pp., doi:110 .1130 /205GMOTNMERTXT.

Abebe, B., V. Acocella, T. Korme, and D. Ayalew (2007), Quaternary faulting and volcanism in the Main Ethiopian Rift. *Journal of African Earth Sciences*, *48*(2–3), 115–124, doi:10.1016/j.jafrearsci.2006.10.005.

Abera, F., K. Dander, A. Mengste, G. Burusa, and T. Beyene (2014), Magnetic and Gravity Survey of Gedemsa Geothermal Prospect Area-Main Ethiopian Rift, *ARGEO-C5 Conf.*, (October), 29–31.

Abiye, T. A., and Tigistu Haile (2008), Geophysical exploration of the Boku geothermal area, Central Ethiopian Rift, *Geothermics*, *37*(6), 586–596, doi:10.1016/j.geothermics.2008.06.004.

Acocella, V., T. Korme, F. Salvini, and R. Funiciello (2002), Elliptic calderas in the Ethiopian Rift: Control of pre-existing structures. *Journal of Volcanology and Geothermal Research*, *119*(1–4), 189–203, doi:10.1016/S0377-0273(02)00342-6.

Agostini, A., M. Bonini, G. Corti, F. Sani, and F. Mazzarini (2011), Fault architecture in the Main Ethiopian Rift and comparison with experimental models: Implications for rift evolution and Nubia-Somalia kinematics. *Earth and Planetary Science Letters*, *301*(3–4), 479–492, doi:10.1016/j.epsl.2010.11.024.

Albaric, J., J. Déverchère, J. Perrot, A. Jakovlev, and A. Deschamps (2014), Deep crustal earthquakes in North Tanzania, East Africa: Interplay between tectonic and magmatic processes in an incipient rift, *Geochemistry, Geophysics, Geosystems*, *15*(2), 374–394, doi:10.1002/2013GC005027.

Albert, H., F. Costa, and J. Martí (2016), Years to weeks of seismic unrest and magmatic intrusions precede monogenetic eruptions. *Geology, 44*(3), 211–214, doi:10.1130/G37239.1.

Allard, P., P. Jean-Baptiste, W. D. Alessandro, F. Pare, B. Parisi, and C. Flehoc (1997), Mantle-derived helium and carbon in groundwaters and gases of Mount Etna, Italy, *Earth*

and Planetary Science Letters, *148*(97), 501–516, doi:10.1016/S0012-821X(97)00052-6.

Alula, D., Boccaletti, M., Getaneh, A., Mazzuoli, R., Tortorici, L., Trua, T., (1992). Geological Map of the Nazret-Dera Region (Main Ethiopian Rift). *Consiglio Nazionale delle Ricerche. Scale 1:50 000.*

Anderson, E. M. (1951), *The Dynamics of Faulting and Dyke Formation with Applications in Britain* (2nd ed.). London: Oliver and Boyd.

Armitage, J. J., J. S. Collier, and T. A. Minshull (2010), The importance of rift history for volcanic margin formation. *Nature*, *465*, 913–917, doi:10.1038/nature09063.

Aspinall, W., M. Auker, T. Hincks, S. Mahony, F. Nadim, J. Pooley, S. Sparks, and E. Syre (2011), *Volcano hazard and exposure in GFDRR priority countries and risk mitigation measures - GFDRR, Volcano Risk Study*. Oslo: Bristol University Cabot Institute and Norwegian Geotechnical Institute (NGI) for the World Bank: NGI Report 20100806.

Ayele, A., M. Teklemariam, and S. Kebede (2002), Geothermal Resource Exploration in the Abaya and Tulu Moye-Gedemsa Geothermal Prospects, Main Ethiopian Rift, *[Internal Report:] Geological Survey of Ethiopia, Addis Ababa, Ethiopia,* 172 pp.

Ayenew, T., S. Kebede, and T. Alemyahu (2008), Environmental isotopes and hydrochemical study applied to surface water and groundwater interaction in the Awash River basin, *Hydrological Processes*, *22*, 1548–1563, doi:10.1002/hyp.6716.

Bagdassarov, N. S., and D. B. Dingwell (1992), A rheological investigation of vesicular rhyolite. *Journal of Volcanology and Geothermal Research*, *50*(3), 307–322, doi:10.1016/0377-0273(92)90099-Y.

Bahiru, E. A. (2007), Structural Study and Its Effect on Thermal activities of Tulu Moye-Gedemsa Area, *[M.Sc. thesis]: Addis Ababa, Ethiopia, Addis Ababa University*, 88 pp.

Bailey, J. E., A. J. L. Harris, J. Dehn, S. Calvari, and S. K. Rowland (2006), The changing morphology of an open lava channel on Mt. Etna. *Bulletin of Volcanology*, *68*(6), 497–515, doi:10.1007/s00445-005-0025-6.

Baloga, S. M., L. S. Glaze, and B. C. Bruno (2007), Nearest-neighbor analysis of small features on Mars: Applications to tumuli and rootless cones. *Journal of Geophysical Research E: Planets*, *112*(3), 1–17, doi:10.1029/2005JE002652.

Barberi, F., and J. Varet (1977), Volcanism of Afar: Small-scale plate tectonics implications. *Geological Society of America Bulletin*, *88*(9), 1251–1266, doi:10.1130/0016-7606(1977)88<1251:VOASPT>2.0.CO;2.

Barnie, T. D., D. Keir, I. Hamling, B. Hofmann, M. Belachew, S. Carn, D. Eastwell, J. O. S. Hammond, A. Ayele, C. Oppenheimer, and T. Wright (2016), A multidisciplinary study of the final episode of the Manda Hararo dyke sequence, Ethiopia, and implications for trends in volcanism during the rifting cycle. *Geological Society, London, Special Publications*, *420*(1), 149–163, doi:10.1144/SP420.6.

Barry, P. H., Hilton, D. R., Fischer, T. P., De Moor, J. M., Mangasini, F., and Ramirez, C. (2013), Helium and carbon isotope systematics of cold "mazuku" CO_2 vents and hydrothermal gases and fluids from Rungwe Volcanic Province, southern Tanzania. *Chemical Geology*, 339, 141-156, doi: 10.1016/j.chemgeo.2012.07.003.

Barry, P. H., Hilton, D. R., Füri, E., Halldórsson, S. A., and Grönvold, K. (2014), Carbon isotope and abundance systematics of Icelandic geothermal gases, fluids and subglacial

basalts with implications for mantle plume-related CO_2 fluxes. *Geochimica et Cosmochimica Acta*, 134, 74-99, doi: 10.1016/j.gca.2014.02.038.

Bastow, I. D., and D. Keir (2011), The protracted development of the continent–ocean transition in Afar. *Nature Geoscience*, *4*(4), 248–250, doi:10.1038/ngeo1095.

Bastow, I. D., G. W. Stuart, J.-M. Kendall, and C. J. Ebinger (2005), Upper-mantle seismic structure in a region of incipient continental breakup: northern Ethiopian rift, *Geophysical Journal International*, *162*, 479–493, doi:10.1111/j.1365-246X.2005.02666.x.

Bastow, I. D., A. A. Nyblade, G. W. Stuart, T. O. Rooney, and M. H. Benoit (2008), Upper mantle seismic structure beneath the Ethiopian hot spot: Rifting at the edge of the African low-velocity anomaly. *Geochemistry, Geophysics, Geosystems*, *9*(12), 1–25, doi:10.1029/2008GC002107.

Bekele, B., T. Mamo, A. Teclu, and Y. Kebede (2007), Compilation of the Geoscientific Study of the Dofan-Fantale Geothermal Prospect, Ethiopia, *[Internal Report:] Geological Survey of Ethiopia, Addis Ababa, Ethiopia*, 140 pp.

Bellier, O., and M. Sébrier (1994), Relationship between tectonism and volcanism along the Great Sumatran Fault Zone deduced by spot image analyses. *Tectonophysics*, *233*(3–4), 215–231, doi:10.1016/0040-1951(94)90242-9.

Bemis, K. G., and M. Ferencz (2017), Morphometric analysis of scoria cones: the potential for inferring process from shape. *Geological Society, London, Special Publications*, *446*(1), 61–100, doi:10.1144/SP446.9.

Benvenuti, M., S. Carnicelli, G. Belluomini, N. Dainelli, S. Di Grazia, G. A. Ferrari, C. Iasio, M. Sagri, D. Ventra, B. Atnafu, and S. Kebede (2002), The Ziway–Shala lake basin (main Ethiopian rift, Ethiopia): a revision of basin evolution with special reference to the Late Quaternary. *Journal of African Earth Sciences*, *35*(2), 247–269, doi:10.1016/S0899-5362(02)00036-2.

Benvenuti, M., M. Bonini, F. Tassi, G. Corti, F. Sani, A. Agostini, P. Manetti, and O. Vaselli (2013), Holocene lacustrine fluctuations and deep CO_2 degassing in the northeastern Lake Langano Basin (Main Ethiopian Rift). *Journal of African Earth Sciences*, *77*, 1–10, doi:10.1016/j.jafrearsci.2012.09.001.

Berner, R. A., A. C. Lasaga, and R. M. Garrels (1983), The carbonate-silicate geochemical cycle and its effect on atmospheric carbon dioxide over the past 100 million years., *American Journal of Science*, *283*(7), 641–683, doi:10.2475/ajs.283.7.641.

Beyene, K., (2000). Preliminary geochemical report on Tulumoye-Gedemsa and the surrounding areas, *[Internal Report:] Geological Survey of Ethiopia, Addis Ababa, Ethiopia*, 8 pp.

Bialas, R. W., W. R. Buck, and R. Qin (2010), How much magma is required to rift a continent? *Earth and Planetary Science Letters*, *292*(1–2), 68–78, doi:10.1016/j.epsl.2010.01.021.

Bigazzi, G., F. Bonadonna, G. M. Di Paola, and O. Giuliani (1993), K-Ar and fission track ages of the last volcano tectonic phase in the Ethiopian Rift Valley (Tullu Moye Area). In *Geology and Mineral Resources of Somalia and Surrounding Regions, Relazioni e monografie agrarie subtropicali e tropicali* (Vol. 113, pp. 311–322). Firenze: Instituto Agronomico per l'Oltremare.

Biggs, J., F. Amelung, N. Gourmelen, T. H. Dixon, and S. W. Kim (2009), InSAR observations of 2007 Tanzania rifting episode reveal mixed fault and dyke extension in an immature continental rift, *Geophysical Journal International*, *179*(1), 549–558, doi:10.1111/j.1365-246X.2009.04262.x.

Biggs, J., I. D. Bastow, D. Keir, and E. Lewi (2011), Pulses of deformation reveal frequently recurring shallow magmatic activity beneath the Main Ethiopian Rift. *Geochemistry, Geophysics, Geosystems*, *12*(9), 1–11, doi:10.1029/2011GC003662.

Braddock, M., J. Biggs, I. M. Watson, W. Hutchison, D.M. Pyle and T. A. Mather (2017), Satellite observations of fumarole activity at Aluto volcano, Ethiopia: implications for geothermal monitoring and volcanic hazard, *Journal of Volcanology and Geothermal Research, 341,* 70-83, doi:10.1016/j.jvolgeores.2017.05.006.

Bretzler, A., K. Osenbrück, R. Gloaguen, J. S. Ruprecht, S. Kebede, and S. Stadler (2011), Groundwater origin and flow dynamics in active rift systems - A multi-isotope approach in the Main Ethiopian Rift. *Journal of Hydrology*, *402*(3–4), 274–289, doi:10.1016/j.jhydrol.2011.03.022.

Buck, W. R. (2004), Consequences of Asthenospheric Variability on Continental Rifting, in *Rheology and Deformation of the Lithosphere at Continental Margins*, pp. 1–30.

Burton, M. R., G. M. Sawyer, and D. Granieri (2013), Deep Carbon Emissions from Volcanoes, *Reviews in Mineralogy and Geochemistry*, *75*(1), 323–354, doi:10.2138/rmg.2013.75.11.

Camarda, M., S. Gurrieri, and M. Valenza (2006), CO_2 flux measurements in volcanic areas using the dynamic concentration method: Influence of soil permeability, *Journal of Geophysical Research: Solid Earth*, *111*(5), 1–14, doi:10.1029/2005JB003898.

Camarda, M., S. De Gregorgio, R. M. R. Di Martino, and R. Favara (2016), Temporal and spatial correlations between soil CO_2 flux and crustal stress, *Journal of Geophysical Research: Solid Earth*, *121*, 7071–7085, doi:10.1002/2015JB012689.Received.

Cardellini, C., G. Chiodini, and F. Frondini (2003), Application of stochastic simulation to CO_2 flux from soil: Mapping and quantification of gas release, *Journal of Geophysical Research: Solid Earth*, *108*(B9), 2425–2437, doi:10.1029/2002JB002165.

Cartigny, P., F. Pineau, C. Aubaud, and M. Javoy (2008), Towards a consistent mantle carbon flux estimate: Insights from volatile systematics (H_2O/Ce, δD, CO_2/Nb) in the North Atlantic mantle (14° N and 34° N), *Earth and Planetary Science Letters*, *265*(3–4), 672–685, doi:10.1016/j.epsl.2007.11.011.

Casagli, A., M. L. Frezzotti, A. Peccerill, M. Tiepolo, and De Astis (2017), (Garnet)-spinel peridotite xenoliths from Mega (Ethiopia): Evidence for rejuvenation and dynamic thinning of the lithosphere beneath the southern Main Ethiopian Rift, *Chemical Geology*, *455*, 231–248, doi:10.1016/j.chemgeo.2016.11.001.

Casey, M., C. Ebinger, D. Keir, R. Gloaguen, and F. Mohamed (2006), Strain accommodation in transitional rifts: extension by magma intrusion and faulting in Ethiopian rift magmatic segments. *Geological Society, London, Special Publications*, *259*(1), 143–163, doi:10.1144/GSL.SP.2006.259.01.13.

Cashman, K. V., S. A. Soule, B. H. Mackey, N. I. Deligne, N. D. Deardorff, and H. R. Dietterich (2013), How lava flows: New insights from applications of lidar technologies to lava flow studies. *Geosphere*, *9*(6), 1664–1680, doi:10.1130/GES00706.1.

Castruccio, A., A. C. Rust, and R. S. J. Sparks (2013), Evolution of crust- and core-dominated lava flows using scaling analysis. *Bulletin of Volcanology*, *75*(1), 1–15, doi:10.1007/s00445-012-0681-2.

Chalie, F., and F. Gasse (2002), Late Glacial-Holocene diatom record of water chemistry and lake level change from the tropical East African Rift Lake Abiyata (Ethiopia). *Palaeogeography, Palaeoclimatology, Palaeoecology*, *187*(3-4), 259–283, doi: 10.1016/S0031-0182(02)00480-7.

Chavrit, D., E. Humler, and O. Grasset (2014), Mapping modern CO_2 fluxes and mantle carbon content all along the mid-ocean ridge system, *Earth and Planetary Science Letters*, *387*, 229–239, doi:10.1016/j.epsl.2013.11.036.

Chernet, T., W. K. Hart, J. L. Aronson, and R. C. Walter (1998), New age constraints on the timing of volcanism and tectonism in the northern Main Ethiopian Rift - southern Afar transition zone (Ethiopia). *Journal of Volcanology and Geothermal Research*, *80*(3–4), 267–280, doi:10.1016/S0377-0273(97)00035-8.

Chiodini, G., R. Cioni, M. Guidi, B. Raco, and L. Marini (1998), Soil CO_2 flux measurements in volcanic and geothermal areas, *Applied Geochemistry*, *13*(5), 543–552, doi:10.1016/S0883-2927(97)00076-0.

Chiodini, G., F. Frondini, D. M. Kerrick, J. Rogie, F. Parello, L. Peruzzi, and A. R. Zanzari (1999), Quantification of deep CO_2 fluxes from Central Italy. Examples of carbon balance for regional aquifers and of soil diffuse degassing, *Chemical Geology*, *159*(1), 205–222, doi:10.1016/S0009-2541(99)00030-3.

Chiodini, G., and F. Frondini (2001), Carbon dioxide degassing from the Albani Hills volcanic region, Central Italy, *Chemical Geology*, *177*(1), 67–83, doi:10.1016/S0009-2541(00)00382-X.

Chiodini, G., F. Frondini, C. Cardellini, D. Granieri, L. Marini, and G. Ventura (2001), CO_2 degassing and energy release at Solfatara volcano, Campi Flegrei, Italy, *Journal of Geophysical Research*, *106*(B8), 16,213-16,221, doi:10.1029/2001JB000246.

Chiodini, G., C. Cardellini, A. Amato, E. Boschi, S. Caliro, F. Frondini, and G. Ventura (2004), Carbon dioxide Earth degassing and seismogenesis in central and southern Italy, *Geophysical Research Letters*, *31*(7), 2–5, doi:10.1029/2004GL019480.

Chiodini, G., A. Baldini, F. Barberi, M. L. Carapezza, C. Cardellini, F. Frondini, D. Granieri, and M. Ranaldi (2007), Carbon dioxide degassing at Latera caldera (Italy): Evidence of geothermal reservoir and evaluation of its potential energy, *Journal of Geophysical Research: Solid Earth*, *112*(12), 1–17, doi:10.1029/2006JB004896.

Chiodini, G., S. Caliro, C. Cardellini, R. Avino, D. Granieri, and A. Schmidt (2008), Carbon isotopic composition of soil CO_2 efflux, a powerful method to discriminate different sources feeding soil CO_2 degassing in volcanic-hydrothermal areas, *Earth and Planetary Science Letters*, *274*(3–4), 372–379, doi:10.1016/j.epsl.2008.07.051.

Chiodini, G., D. Granieri, R. Avino, S. Caliro, A. Costa, C. Minopoli, and G. Vilardo (2010), Non-volcanic CO_2 Earth degassing: Case of Mefite d'Ansanto (southern Apennines), Italy, *Geophysical Research Letters*, *37*(11), 2–5, doi:10.1029/2010GL042858.

Condit, C. D., and C. B. Connor (1996), Recurrence rates of volcanism in basaltic volcanic fields: An example from the Springerville volcanic field, Arizona. *Bulletin of the*

Geological Society of America, *108*(10), 1225–1241, doi:10.1130/0016-7606(1996)108<1225:RROVIB>2.3.CO;2.

Connor, C.B., and F. M. Conway (2000), Basaltic volcanic fields, in: Sigurdsson, H., ed., Encyclopedia of Volcanoes: New York, Academic, p. 331–343.

Connor, C. B., C. D. Condit, L. S. Crumpler, and J. C. Aubele (1992), Evidence of structural controls on Vent Distribution: Springerville Volcanic Field Arizona. *Journal of Geophysical Research*, *97*(B9), 12,349-12,359, doi:10.1029/92JB00929.

Corazzato, C., and A. Tibaldi (2006), Fracture control on type, morphology and distribution of parasitic volcanic cones: An example from Mt. Etna, Italy. *Journal of Volcanology and Geothermal Research*, *158*, 177–194, doi:10.1016/j.jvolgeores.2006.04.018.

Córdoba, G., G. Villarosa, M. F. Sheridan, J. G. Viramonte, D. Beigt, and G. Salmuni (2015), Secondary lahar hazard assessment for Villa la Angostura, Argentina, using Two-Phase-Titan modelling code during 2011 Cordón Caulle eruption. *Natural Hazards and Earth System Sciences*, *15*(4), 757–766, doi:10.5194/nhess-15-757-2015.

Corti, G. (2008), Control of rift obliquity on the evolution and segmentation of the main Ethiopian rift. *Nature Geoscience*, *1*(4), 258–262, doi:10.1038/ngeo160.

Corti, G. (2009), Continental rift evolution: From rift initiation to incipient break-up in the Main Ethiopian Rift, East Africa. *Earth-Science Reviews*, *96*(1–2), 1–53, doi:10.1016/j.earscirev.2009.06.005.

Corti, G., M. Bonini, S. Conticelli, F. Innocenti, P. Manetti, and D. Sokoutis (2003), Analogue modelling of continental extension: A review focused on the relations between the patterns of deformation and the presence of magma. *Earth-Science Reviews*, *63*(3–4), 169–247, doi:10.1016/S0012-8252(03)00035-7.

Corti, G., F. Sani, M. Philippon, D. Sokoutis, E. Willingshofer, and P. Molin (2013), Quaternary volcano-tectonic activity in the Soddo region, western margin of the Southern Main Ethiopian Rift. *Tectonics*, *32*(4), 861–879, doi:10.1002/tect.20052.

Corti, G., A. Agostini, D. Keir, J. Van Wijk, I. D. Bastow, and G. Ranalli (2015), Magma-induced axial subsidence during final-stage rifting: Implications for the development of seaward-dipping reflectors. *Geosphere*, *11*(3), 563–571, doi:10.1130/GES01076.1.

Corti, G., F. Sani, S. Agostini, M. Philippon, D. Sokoutis, and E. Willingshofer (2018a), Off-axis volcano-tectonic activity during continental rifting: Insights from the transversal Goba-Bonga lineament, Main Ethiopian Rift (East Africa). *Tectonophysics*, *728–729*(August 2017), 75–91, doi:10.1016/j.tecto.2018.02.011.

Corti, G., P. Molin, A. Sembroni, I. D. Bastow, and D. Keir (2018b), Control of pre-rift lithospheric structure on the architecture and evolution of continental rifts: insights from the Main Ethiopian Rift, East Africa. *Tectonics*, *37*, 477–496, doi:10.1002/2017TC004799.

Csatho, B., T. Schenk, P. Kyle, T. Wilson, and W. B. Krabill (2008), Airborne laser swath mapping of the summit of Erebus volcano, Antarctica: Applications to geological mapping of a volcano. *Journal of Volcanology and Geothermal Research*, *177*(3), 531–548, doi:10.1016/j.jvolgeores.2008.08.016.

D'Alessandro, W., S. Giammanco, F. Parello, and M. Valenza (1997), CO_2 output and $\delta^{13}C(CO_2)$ from Mount Etna as indicators of degassing of shallow asthenosphere, *Bulletin of Volcanology*, *58*(6), 455–458, doi:10.1007/s004450050154.

Daly, E., D. Keir, C. J. Ebinger, G. W. Stuart, I. D. Bastow, and A. Ayele (2008), Crustal tomographic imaging of a transitional continental rift: The Ethiopian rift. *Geophysical Journal International*, *172*(3), 1033–1048, doi:10.1111/j.1365-246X.2007.03682.x.

Daniels, K. A., I. D. Bastow, D. Keir, R. S. J. Sparks, and T. Menand (2014), Thermal models of dyke intrusion during development of continent-ocean transition. *Earth and Planetary Science Letters*, *385*, 145–153, doi:10.1016/j.epsl.2013.09.018.

Darling, W. G., B. Gizaw, and M. K. Arusei (1996), Lake-groundwater relationships and fluid-rock interaction in the East African Rift Valley: isotopic evidence, *Journal of African Earth Sciences*, *22*(4), 423–431, doi:10.1016/0899-5362(96)00026-7.

Dasgupta, R. (2013), Ingassing, Storage, and Outgassing of Terrestrial Carbon through Geologic Time, *Review of Mineralogy and Geochemistry*, *75*, 183–229, doi:10.2138/rmg.2013.75.7.

Dasgupta, R., A. Mallik, K. Tsuno, A. C. Withers, G. Hirth, and M. M. Hirschmann (2013), Carbon-dioxide-rich silicate melt in the Earth's upper mantle, *Nature*, *493*(7431), 211–216, doi:10.1038/nature11731.

Dawson, J.B., D.M. Pyle, and H. Pinkerton (1996), Evolution of natrocarbonatite from a wollastonite nephelenite parent: evidence from the June 1993 eruption of Oldoinyo Lengai, Tanzania, *Journal of Geology, 104*(1), 41-54, doi:10.1086/629800.

De Angelis, D., A.M. Presanis, S Conti and A.E. Ades (2014) Estimation of HIV Burden through Bayesian Evidence Synthesis, *Statistical Science, 29*, 9-17, doi:10.1214/13-STS428.

de Moor, J. M., T. P. Fischer, Z. D. Sharp, D. R. Hilton, P. H. Barry, F. Mangasini, and C. Ramirez (2013), Gas chemistry and nitrogen isotope compositions of cold mantle gases from Rungwe Volcanic Province, southern Tanzania, *Chemical Geology*, *339*, 30–42, doi:10.1016/j.chemgeo.2012.08.004.

Deardorff, N. D., and K. V. Cashman (2012), Emplacement conditions of the c. 1,600-year bp Collier Cone lava flow, Oregon: A LiDAR investigation. *Bulletin of Volcanology*, *74*(9), 2051–2066, doi:10.1007/s00445-012-0650-9.

Delcamp, A., S. Mossoux, H. Belkus, C. Tweheyo, H. B. Mattsson, and M. Kervyn (2019), Control of the stress field and rift structures on the distribution and morphology of explosive volcanic craters in the Manyara and Albertine rifts. *Journal of African Earth Sciences*, *150*, 566–583, doi:10.1016/j.jafrearsci.2018.09.012.

Di Genova, D., C. Romano, K. U. Hess, A. Vona, B. T. Poe, D. Giordano, D. B. Dingwell, and H. Behrens (2013). The rheology of peralkaline rhyolites from Pantelleria Island. *Journal of Volcanology and Geothermal Research*, *249*, 201–216, doi:10.1016/j.jvolgeores.2012.10.017.

Di Paola, G. M. (1970), Geological-geothermal report on the central part of the Ethiopian Rift Valley, *[Internal Report:] Ministry of Mines, Addis Ababa, Ethiopia*.

Di Paola, G. M. (1971), Geology of the Corbetti Caldera Area (Main Ethiopian Rift Valley). *Bulletin Volcanologique*, *35*(2), 497–506, doi:10.1007/BF02596970.

Dingwell, D. B., K. U. Hess, and C. Romano (1998), Extremely fluid behavior of hydrous peralkaline rhyolites. *Earth and Planetary Science Letters*, *158*(1–2), 31–38, doi:10.1016/S0012-821X(98)00046-6.

Dockrill, B., and Z. K. Shipton (2010), Structural controls on leakage from a natural CO_2 geologic storage site: Central Utah, U.S.A., *Journal of Structural Geology*, *32*(11), 1768–1782, doi:10.1016/j.jsg.2010.01.007.

Donovan, A., J. Blundy, C. Oppenheimer, and I. Buisman (2018), The 2011 eruption of Nabro volcano, Eritrea: perspectives on magmatic processes from melt inclusions. *Contributions to Mineralogy and Petrology*, *173*(1), 1, doi:10.1007/s00410-017-1425-2.

Ebinger, C. J., and M. Casey (2001), Continental breakup in magmatic provinces: An Ethiopian example, *Geology*, *29*(6), 527–530, doi:10.1130/0091-7613(2001)029<0527:CBIMPA>2.0.CO;2.

Ernst, G. G. J., M. Kervyn, and R. M. Teeuw (2008), Advances in the remote sensing of volcanic activity and hazards, with special consideration to applications in developing countries. *International Journal of Remote Sensing*, *29*(22), 6687–6723, doi:10.1080/01431160802168459.

Etiope, G., and G. Martinelli (2002), Migration of carrier and trace gases in the geosphere: An overview, *Physics of the Earth and Planetary Interiors*, *129*(3–4), 185–204, doi:10.1016/S0031-9201(01)00292-8.

Etiope, G., P. Beneduce, M. Calcara, P. Favali, F. Frugoni, M. Schiattarella, and G. Smriglio (1999), Structural pattern and CO_2–CH_4 degassing of Ustica Island, Southern Tyrrhenian basin, *Journal of Volcanology and Geothermal Research*, *88*(4), 291–304, doi:10.1016/S0377-0273(99)00010-4.

Euillades, L. D., P. Grosse, and P. A. Euillades (2013), NETVOLC: An algorithm for automatic delimitation of volcano edifice boundaries using DEMs. *Computers and Geosciences*, *56*, 151–160, doi:10.1016/j.cageo.2013.03.011.

Evans, W. C., D. Bergfeld, R. G. McGimsey, and A. G. Hunt (2009), Diffuse gas emissions at the Ukinrek Maars, Alaska: Implications for magmatic degassing and volcanic monitoring, *Applied Geochemistry*, *24*(4), 527–535, doi:10.1016/j.apgeochem.2008.12.007.

Fagents, S. A., and T. Thordarson (2007), Rootless volcanic cones in Iceland and on Mars. In *The Geology of Mars: Evidence from Earth-Based Analogs* (pp. 151–177), Cambridge: Cambridge University Press, doi:10.1017/cbo9780511536014.007.

Faulkner, D. R., C. A. L. Jackson, R. J. Lunn, R. W. Schlische, Z. K. Shipton, C. A. J. Wibberley, and M. O. Withjack (2010), A review of recent developments concerning the structure, mechanics and fluid flow properties of fault zones, *Journal of Structural Geology*, *32*(11), 1557–1575, doi:10.1016/j.jsg.2010.06.009.

Favalli, M., and A. Fornaciai (2017), Visualization and comparison of DEM-derived parameters. Application to volcanic areas. *Geomorphology*, *290*, 69–84, doi:10.1016/j.geomorph.2017.02.029.

Favalli, M., F. Innocenti, M. T. Pareschi, G. Pasquarè, F. Mazzarini, S. Branca, … A. Tibaldi (1999), The DEM of Mount Etna: geomorphological and structural implications. *Geodinamica Acta*, *12*(5), 279–290, doi:10.1080/09853111.1999.11105350.

Favalli, M., M. T. Pareschi, A. Neri, and I. Isola (2005), Forecasting lava flow paths by a stochastic approach. *Geophysical Research Letters*, *32*(3), 1–4, doi:10.1029/2004GL021718.

Favalli, M., D. Karátson, F. Mazzarini, M. T. Pareschi, and E. Boschi (2009), Morphometry of scoria cones located on a volcano flank: A case study from Mt. Etna (Italy), based on

high-resolution LiDAR data. *Journal of Volcanology and Geothermal Research*, *186*(3–4), 320–330, doi:10.1016/j.jvolgeores.2009.07.011.

Favara, R., S. Giammanco, S. Inguaggiato, and G. Pecoraino (2001), Preliminary estimate of CO_2 output from Pantelleria Island volcano (Sicily, Italy): evidence of active mantle degassing, *Applied Geochemistry*, *16*(7), 883–894, doi:10.1016/S0883-2927(00)00055-X.

Ferguson, D. J., T. D. Barnie, D. M. Pyle, C. Oppenheimer, G. Yirgu, E. Lewi, T. Kidane, S. Carn, and I. Hamling (2010), Recent rift-related volcanism in Afar, Ethiopia. *Earth and Planetary Science Letters*, *292*(3–4), 409–418, doi:10.1016/j.epsl.2010.02.010.

Ferguson, D. J., J. Maclennan, I. D. Bastow, D. M. Pyle, S. M. Jones, D. Keir, J. D. Blundy, T. Plank, and G. Yirgu (2013a), Melting during late-stage rifting in Afar is hot and deep. *Nature*, *499*, 70–74, doi:10.1038/nature12292.

Ferguson, D. J., A. T. Calvert, D. M. Pyle, J. D. Blundy, G. Yirgu, and T. J. Wright (2013b), Constraining timescales of focused magmatic accretion and extension in the Afar crust using lava geochronology. *Nature Communications*, *4*(1416), 1–6, doi:10.1038/ncomms2410.

Field, L., J. Blundy, R. A. Brooker, T. Wright, and G. Yirgu (2012), Magma storage conditions beneath Dabbahu Volcano (Ethiopia) constrained by petrology, seismicity and satellite geodesy. *Bulletin of Volcanology*, *74*(5), 981–1004, doi:10.1007/s00445-012-0580-6.

Field, L., J. Blundy, A. Calvert, and G. Yirgu (2013), Magmatic history of Dabbahu, a composite volcano in the Afar Rift, Ethiopia. *Bulletin of the Geological Society of America*, *125*(1–2), 128–147, doi:10.1130/B30560.1.

Fink, J. (1980), Surface folding and viscosity of rhyolite flows. *Geology*, *8*(5), 250–254, doi:10.1130/0091-7613(1980)8<250:SFAVOR>2.0.CO;2.

Fink, J. H., and R. C. Fletcher (1978), Ropy pahoehoe: Surface folding of a viscous fluid. *Journal of Volcanology and Geothermal Research*, *4*(1–2), 151–170, doi:10.1016/0377-0273(78)90034-3.

Fink, J. H., and R. W. Griffiths (1990), Radial Spreading of Viscous Gravity Currents With Solidifying Crust. *Journal of Fluid Mechanics*, *221*, 485–509, doi:10.1017/S0022112090003640.

Fink, J. H., and R. W. Griffiths (1998), Morphology, eruption rates, and rheology of lava domes: Insights from laboratory models. *Journal of Geophysical Research: Solid Earth*, *103*(B1), 527–545, doi:10.1029/97JB02838.

Fischer, T. P., and G. Chiodini (2015), Volcanic, magmatic and hydrothermal gases, in *The Encyclopedia of Volcanoes*, edited by Sigurdsson, H., Houghton, B., McNutt, SR, Rymer, H., Stix, J., Eds, 779-798, Academic Press, New York.

Fischer, T. P., P. Burnard, B. Marty, D. R. Hilton, E. Füri, F. Palhol, Z. D. Sharp, and F. Mangasini (2009), Upper-mantle volatile chemistry at Oldoinyo Lengai volcano and the origin of carbonatites, *Nature*, *459*(7243), 77–80, doi:10.1038/nature07977.

Fontijn, K., G. G. J. Ernst, M. A. Elburg, D. Williamson, E. Abdallah, S. Kwelwa, E. Mbede, and P. Jacobs (2010), Holocene explosive eruptions in the Rungwe Volcanic Province, Tanzania. *Journal of Volcanology and Geothermal Research*, *196*(1–2), 91–110, doi:10.1016/j.jvolgeores.2010.07.021.

Fontijn, K., D. Williamson, E. Mbede, and G. G. J. Ernst (2012), The Rungwe Volcanic Province, Tanzania - A volcanological review. *Journal of African Earth Sciences*, *63*, 12–31, doi:10.1016/j.jafrearsci.2011.11.005.

Fontijn, K., K. McNamara, A. Zafu Tadesse, D. M. Pyle, F. Dessalegn, W. Hutchison, T. A. Mather, and G. Yirgu (2018), Contrasting styles of post-caldera volcanism along the Main Ethiopian Rift: Implications for contemporary volcanic hazards. *Journal of Volcanology and Geothermal Research*, *356*, 90–113, doi:10.1016/j.jvolgeores.2018.02.001.

Fornaciai, A., M. Favalli, D. Karátson, S. Tarquini, and E. Boschi (2012), Morphometry of scoria cones, and their relation to geodynamic setting: A DEM-based analysis. *Journal of Volcanology and Geothermal Research*, *217–218*, 56–72, doi:10.1016/j.jvolgeores.2011.12.012.

Furman, T., J. Bryce, T. Rooney, B. Hanan, G. Yirgu, and D. Ayalew (2006), Heads and tails: 30 million years of the Afar plume. *Geological Society, London, Special Publications*, (259), 95–119, doi:10.1144/GSL.SP.2006.259.01.09.

Gaffney, E. S., B. Damjanac, and G. A. Valentine (2007), Localization of volcanic activity: 2. Effects of pre-existing structure. *Earth and Planetary Science Letters*, *263*(3–4), 323–338, doi:10.1016/j.epsl.2007.09.002.

Gallacher, R.J., D. Keir, N. Harmon, G. Stuart, S. Leroy, J.O.S. Hammond, J-M. Kendall, A. Ayele, B. Goitom, G. Ogubazghi, and A. Ahmed (2016), The initiation of segmented buoyancy-driven melting during continental breakup, *Nature Communications*, *7*, 13110, doi:10.1038/ncomms13110.

Gasse, F., and F. A. Street (1978), Late Quaternary lake-level fluctuations and environments of the northern Rift Valley and Afar region (Ethiopia and Djibouti). *Palaeogeography, Palaeoclimatology, Palaeoecology*, *24*, 279–325, doi: 10.1016/0031-0182(78)90011-1.

Geological Survey of Ethiopia and United Nations (1976), Geological Maps of Fike (0738 A4), Zeway (0738 B1), Chefe Jila (0738 B2), Kersa (0738 B4), Sembete (0738 C2), and Negele Arusi (0738 D1). *United Nations Geothermal Project. Scale 1:50,000*.

Giammanco, S., F. Parello, B. Gambardella, R. Schifano, S. Pizzullo, and G. Galante (2007), Focused and diffuse effluxes of CO_2 from mud volcanoes and mofettes south of Mt. Etna (Italy), *Journal of Volcanology and Geothermal Research*, *165*(1), 46–63, doi:10.1016/j.jvolgeores.2007.04.010.

Gibson, I. L. (1967), Preliminary Account of the Volcanic Geology of Fantale, Shoa. *Bulletin of the Geophysical Observatory of Addis Ababa*, *10*, 59–67.

Gibson, I. L. (1969), The structure and volcanic geology of an axial portion of the Main Ethiopian Rift. *Tectonophysics*, *8*(4–6), 561–565, doi:10.1016/0040-1951(69)90054-7.

Gibson, I. L. (1970), A Pantelleritic Welded Ash-Flow Tuff flow from the Ethiopian Rift Valley. *Contributions to Mineralogy and Petrology*, *28*(2), 89–111, doi:10.1007/BF00404992.

Gibson, I. L. (1972), The Chemistry and Petrogenesis of a Suite of Pantellerites from the Ethiopian Rift. *Journal of Petrology*, *13*(1), 31–44, doi:10.1093/petrology/13.1.31.

Gibson, I. L. (1974), A Review of the Geology, Petrology and Geochemistry of the Volcano Fantale. *Bulletin Volcanologique*, *38*(2), 791–802, doi:10.1007/BF02596908.

Giordano, D., J. K. Russell, and D. B. Dingwell (2008), Viscosity of magmatic liquids: A model. *Earth and Planetary Science Letters*, *271*(1–4), 123–134, doi:10.1016/j.epsl.2008.03.038.

Giordano, F., M. D'Antonio, L. Civetta, S. Tonarini, G. Orsi, D. Ayalew, G. Yirgu, F. Dell'Erba, M. A. Di Vito, and R. Isaia (2014), Genesis and evolution of mafic and felsic magmas at Quaternary volcanoes within the Main Ethiopian Rift: Insights from Gedemsa and Fanta 'Ale complexes. *Lithos*, *188*, 130–144, doi:10.1016/j.lithos.2013.08.008.

Gíslason, G., H. Eysteinsson, G. Björnsson, and V. Harðardóttir (2015), Results of Surface Exploration in the Corbetti Geothermal Area, Ethiopia. In *Proceedings of the World Geothermal Congress, 2015*. Melbourne, Australia.

Gizaw, B. (1996), The origin of high bicarbonate and fluoride concentrations in waters of the Main Ethiopian Rift Valley, East African Rift system, *Journal of African Earth Sciences*, *22*(4), 391–402, doi:10.1016/0899-5362(96)00029-2.

Gleeson, M. L. M., M. J. Stock, D. M. Pyle, T. A. Mather, W. Hutchison, G. Yirgu, and J. Wade (2017), Constraining magma storage conditions at a restless volcano in the Main Ethiopian Rift using phase equilibria models. *Journal of Volcanology and Geothermal Research*, *337*, 44–61, doi:10.1016/j.jvolgeores.2017.02.026.

Gregg, T. K. P. (2017), Patterns and processes: Subaerial lava flow morphologies: A review. *Journal of Volcanology and Geothermal Research*, *342*, 3–12, doi:10.1016/j.jvolgeores.2017.04.022.

Gregg, T. K. P., and J. H. Fink (2000), A laboratory investigation into the effects of slope on lava flow morphology. *Journal of Volcanology and Geothermal Research*, *96*(3–4), 145–159, doi:10.1016/S0377-0273(99)00148-1.

Gregg, T. K. P., J. H. Fink, and R. W. Griffiths (1998), Formation of multiple fold generations on lava flow surfaces: influence of strain rate, cooling rate, and lava composition. *Journal of Volcanology and Geothermal Research*, *80*(3–4), 281–292, doi:10.1016/S0377-0273(97)00048-6.

Grosse, P., P. A. Euillades, L. D. Euillades, and B. van Wyk de Vries (2014), A global database of composite volcano morphometry. *Bulletin of Volcanology*, *76*(1), 1–16, doi:10.1007/s00445-013-0784-4.

Guðmundsson, Á. (1995), Infrastructure and mechanics of volcanic systems in Iceland. *Journal of Volcanology and Geothermal Research*, *64*(1–2), 1–22, doi:10.1016/0377-0273(95)92782-Q.

Haile Selassie, D. (1984), Compiled report on low enthalpy geothermal resources of Ethiopia, *[Internal Report:] Ministry of Mines and Energy, Addis Ababa, Ethiopia*, 48 pp.

Harris, W. C. (1844). *The Highlands of Æthiopia* (2nd ed.). London: Longman, Brown, Green, and Longmans.

Hayward, N. J., and C. J. Ebinger (1996), Variations in the along-axis segmentation of the Afar Rift system. *Tectonics*, *15*(2), 244–257, doi:10.1029/95TC02292.

Helo, C., M.-A. Longpré, N. Shimizu, D. a. Clague, and J. Stix (2011), Explosive eruptions at mid-ocean ridges driven by CO_2-rich magmas, *Nature Geosciences*, *4*(4), 260–263, doi:10.1038/ngeo1104.

Hernández Perez, P., K. Notsu, M. Tsurumi, T. More, M. Ohno, Y. Shimoike, J. Salazar, and N. Perez (2003), Carbon dioxide emissions from soils at Hakkoda, north Japan, *Journal of Geophysical Research*, *108*(B4), 1–10, doi:10.1029/2002JB001847.

Hernández, P. A., N. M. Pérez, T. Fridriksson, J. Egbert, E. Ilyinskaya, A. Thárhallsson, G. Ívarsson, G. Gíslason, I. Gunnarsson, B. Jónsson, E. Padrón, G. Melián, T. Mori, and K. Notsu (2012), Diffuse volcanic degassing and thermal energy release from Hengill volcanic system, Iceland. *Bulletin of Volcanology*, *74*(10), 2435–2448, doi:10.1007/s00445-012-0673-2.

Hess, K. U., D. B. Dingwell, and S. L. Webb (1995), The influence of excess alkalis on the viscosity of a haplogranitic melt. *American Mineralogist*, *80*(3–4), 297–304, doi:10.2138/am-1995-3-411.

Hochstein, M. P., E. P. Temu and C. M. A. Moshy (2000), Geothermal resources of Tanzania, *World Geothermal Congress*, (May-June 2000), pp. 1233—1238.

Hochstein, M. P., B. Oluma, and H. Hole (2017), Early exploration of the Aluto geothermal field, Ethiopia (History of discovery well LA-3), *Geothermics*, *66*, 73–84, doi:10.1016/j.geothermics.2016.11.010.

Hofmann, B. (2013), *How do faults grow in magmatic rifts? LiDAR and InSAR observations of the Dabbahu rift segment, Afar, Ethiopia.* PhD Thesis, University of Leeds.

Hofton, M. A., E. Malavassi, and J. B. Blair (2006), Quantifying recent pyroclastic and lava flows at Arenal Volcano, Costa Rica, using medium-footprint lidar. *Geophysical Research Letters*, *33*(21), 1–5, doi:10.1029/2006GL027822.

Holohan, E. P., V. R. Troll, T. R. Walter, S. Münn, S. McDonnell, and Z. K. Shipton (2005), Elliptical calderas in active tectonic settings: An experimental approach. *Journal of Volcanology and Geothermal Research*, *144*, 119–136, doi:10.1016/j.jvolgeores.2004.11.020.

Hübert, J., K. Whaler, and S. Fisseha (2018), The Electrical Structure of the Central Main Ethiopian Rift as Imaged by Magnetotellurics: Implications for Magma Storage and Pathways. *Journal of Geophysical Research: Solid Earth*, *123*(7), 6019–6032, doi:10.1029/2017JB015160.

Hughes, S. S., P. H. Wetmore, and J. L. Casper (2002), Evolution of Quaternary Tholeiitic Basalt Eruptive Centers on the Eastern Snake River Plain, Idaho. *Idaho Geological Survey Bulletin*, *30*, 1–23.

Hughes, E. C., D. A. Neave, K. J. Dobson, P. J. Withers, and M. Edmonds (2017), How to fragment peralkaline rhyolites: Observations on pumice using combined multi-scale 2D and 3D imaging. *Journal of Volcanology and Geothermal Research*, *336*, 179–191, doi:10.1016/j.jvolgeores.2017.02.020.

Hulme, G. (1974), The interpretation of lava flow morphology. *Geophysical Journal International*, *39*(2), 361–383, doi:10.1111/j.1365-246X.1974.tb05460.x.

Hutchison, W., T. A. Mather, D. M. Pyle, J. Biggs, and G. Yirgu (2015), Structural controls on fluid pathways in an active rift system: A case study of the Aluto volcanic complex, *Geosphere*, *11*(3), 542–562, doi:10.1130/GES01119.1.

Hutchison, W., R. Fusillo, D. M. Pyle, T. A. Mather, J. D. Blundy, J. Biggs, G. Yirgu, B. E. Cohen, R. A. Brooker, D. N. Barfod, and T. A. Calvert (2016a), A pulse of mid-

Pleistocene rift volcanism in Ethiopia at the dawn of modern humans. *Nature Communications*, *7*, 13192, doi:10.1038/ncomms13192.

Hutchison, W., D. M. Pyle, T. A. Mather, G. Yirgu, J. Biggs, B. E. Cohen, D. N. Barfod, and E. Lewi (2016b), The eruptive history and magmatic evolution of Aluto volcano: new insights into silicic peralkaline volcanism in the Ethiopian rift. *Journal of Volcanology and Geothermal Research*, *328*, 9–33, doi:10.1016/j.jvolgeores.2016.09.010.

Hutchison, W., J. Biggs, T. A. Mather, D. M. Pyle, E. Lewi, G. Yirgu, S. Caliro, G. Chiodini, L. E. Clor, and T. P. Fischer (2016c), Causes of unrest at silicic calderas in the East African Rift: new constraints from InSAR and soil-gas chemistry at Aluto volcano, Ethiopia. *Geochemistry, Geophysics, Geosystems*, *17*, 3008–3030, doi:10.1002/2016GC006395.

Hutchison, W., T. A. Mather, D. M. Pyle, A. J. Boyce, M. L. M. Gleeson, G. Yirgu, J. D. Blundy, D. J. Ferguson, C. Vye-Brown, I. L. Miller, K. W. W. Sims, and A. A. Finch (2018), The evolution of magma during continental rifting: New constraints from the isotopic and trace element signatures of silicic magmas from Ethiopian volcanoes. *Earth and Planetary Science Letters*, *489*, 203–218, doi:10.1016/j.epsl.2018.02.027.

Ibs-von Seht, M., S. Blumenstein, R. Wagner, D. Hollnack, and J. Wohlenberg (2001), Seismicity, seismotectonics and crustal structure of the southern Kenya Rift - new data from the Lake Magadi area, *Geophysical Journal International*, *146*, 439–453, doi:10.1046/j.1365-246X.2001.01464.x.

Italiano, F., M. Martelli, G. Martinelli, and P. M. Nuccio (2000), Geochemical evidence of melt intrusions along lithospheric faults of the Southern Apennines, Italy' Geodynamic and seismogenic implications, *Journal of Geophysical Research*, *105*(B6), 13,569–13,578, doi:10.1029/2000JB900047.

Jeffery, A. J., R. Gertisser, B. O'Driscoll, J. M. Pacheco, S. Whitley, A. Pimentel, and S. Self (2016), Temporal evolution of a post-caldera, mildly peralkaline magmatic system: Furnas volcano, São Miguel, Azores. *Contributions to Mineralogy and Petrology*, *171*(5), 1–24, doi:10.1007/s00410-016-1235-y.

Kagoshima, T., Y. Sano, N. Takahata, T. Maruoka, T. P. Fischer, and K. Hattori (2015), Sulphur geodynamic cycle, *Scientific Reports*, *5*, 8330, doi:10.1038/srep08330.

Kebede, S. (2012), Geothermal exploration and development in Ethiopia: Status and future plan, *Exploration for Geothermal Resources, Short Course VII, Kenya*, 16 pp.

Kebede, S., T. Mamo, and T. Abebe (1985), Geological report and explanation to the geological map of Aluto-Langano geothermal area: Addis Ababa, *Ethiopian Institute of Geological Surveys, Addis Ababa, Ethiopia*, 60 pp.

Kebede, S., Y. Travi, A. Asrat, T. Alemayehu, T. Ayenew, and Z. Tessema (2008), Groundwater origin and flow along selected transects in Ethiopian rift volcanic aquifers. *Hydrogeology Journal*, *16*, 55–73, doi:10.1007/s10040-007-0210-0.

Keir, D., C. J. Ebinger, G. W. Stuart, E. Daly, and A. Ayele (2006), Strain accommodation by magmatism and faulting as rifting proceeds to breakup: Seismicity of the northern Ethiopian rift. *Journal of Geophysical Research: Solid Earth*, *111*(5), 1–17, doi:10.1029/2005JB003748.

Keir, D., I. D. Bastow, K. A. Whaler, E. Daly, D. G. Cornwell, and S. Hautot (2009a), Lower crustal earthquakes near the Ethiopian rift induced by magmatic processes. *Geochemistry, Geophysics, Geosystems*, *10*(6), 1–10, doi:10.1029/2009GC002382.

Keir, D., I. J. Hamling, A. Ayele, E. Calais, C. Ebinger, T. J. Wright, E. Jacques, K. Mohamed, J. O. S. Hammond, M. Belachew, E. Baker, J. V. Rowland, E. Lewi, and L. Bennati (2009b), Evidence for focused magmatic accretion at segment centers from lateral dike injections captured beneath the Red Sea rift in Afar. *Geology*, *37*(1), 59–62, doi:10.1130/G25147A.1.

Keir, D., M. Belachew, C. J. Ebinger, J.-M. Kendall, J. O. S. Hammond, G. W. Stuart, A. Ayele, and J. V. Rowland (2011a), Mapping the evolving strain field during continental breakup from crustal anisotropy in the Afar Depression. *Nature Communications*, *2*, 285, doi:28510.1038/ncomms1287.

Keir, D., C. Pagli, I. D. Bastow, and A. Ayele (2011b), The magma-assisted removal of Arabia in Afar: Evidence from dike injection in the Ethiopian rift captured using InSAR and seismicity. *Tectonics*, *30*(2), 1–13, doi:10.1029/2010TC002785.

Keir, D., I. D. Bastow, C. Pagli, and E. L. Chambers (2013), The development of extension and magmatism in the Red Sea rift of Afar. *Tectonophysics*, *607*, 98–114, doi:10.1016/j.tecto.2012.10.015.

Keir, D., I. D. Bastow, G. Corti, F. Mazzarini, and T. O. Rooney (2015), The origin of along-rift variations in faulting and magmatism in the Ethiopian Rift. *Tectonics*, *34*(3), 464–477, doi:10.1002/2014TC003698..

Kelemen, P. B., and C. E. Manning (2015), Reevaluating carbon fluxes in subduction zones, what goes down, mostly comes up, *Proceedings of the National Academy of Sciences*, *112*(30), 3997–4006, doi:10.1073/pnas.1507889112.

Kendall, J. M., G. W. Stuart, C. J. Ebinger, I. D. Bastow, and D. Keir (2005), Magma-assisted rifting in Ethiopia. *Nature*, *433*(7022), 146–148, doi:10.1038/nature03161.

Keranen, K., and S. L. Klemperer (2008), Discontinuous and diachronous evolution of the Main Ethiopian Rift: Implications for development of continental rifts, *Earth and Planetary Science Letters*, *265*(1–2), 96–111, doi:10.1016/j.epsl.2007.09.038.

Keranen, K., S. L. Klemperer, R. Gloaguen, L. Asfaw, A. Ayele, C. Ebinger, T. Furman, S. Harder, G.R. Keller, G.D. Mackenzie, P.K.H. Maguire, and G. W. Stuart (2004), Three-dimensional seismic imaging of a protoridge axis in the Main Ethiopian rift, *Geology*, *32*(11), 949–952, doi:10.1130/G20737.1.

Kereszturi, G., K. Németh, G. Csillag, K. Balogh, and J. Kovács (2011), The role of external environmental factors in changing eruption styles of monogenetic volcanoes in a Mio/Pleistocene continental volcanic field in western Hungary. *Journal of Volcanology and Geothermal Research*, *201*(1–4), 227–240, doi:10.1016/j.jvolgeores.2010.08.018.

Kerr, R. C., R. W. Griffiths, and K. V. Cashman (2006), Formation of channelized lava flows on an unconfined slope. *Journal of Geophysical Research: Solid Earth*, *111*(10), 1–13, doi:10.1029/2005JB004225.

Kervyn, M., F. Kervyn, R. Goossens, S. K. Rowland, and G. G. J. Ernst (2007), Mapping volcanic terrain using high-resolution and 3D satellite remote sensing. *Geological Society, London, Special Publications*, *283*(1), 5–30, doi:10.1144/SP283.2.

Kervyn, M., G. G. J. Ernst, J. C. Carracedo, and P. Jacobs (2012), Geomorphometric variability of "monogenetic" volcanic cones: Evidence from Mauna Kea, Lanzarote and

experimental cones. *Geomorphology*, *136*(1), 59–75, doi:10.1016/j.geomorph.2011.04.009.

Kim, S., A. A. Nyblade, J. Rhie, C. E. Baag, and T. S. Kang (2012), Crustal S-wave velocity structure of the Main Ethiopian Rift from ambient noise tomography. *Geophysical Journal International*, *191*(2), 865–878, doi:10.1111/j.1365-246X.2012.05664.x.

Koepenick, K. W., S. L. Brantley, J. M. Thompson, G. L. Rowe, A. A. Nyblade, and C. Moshy (1996), Volatile emissions from the crater and flank of Oldoinyo Lengai volcano, Tanzania, *Journal of Geophysical Research*, *101*(B6), 13819–13830, doi:10.1029/96JB00173.

Korme, T., J. Chorowicz, B. Collet, and F. F. Bonavia (1997), Volcanic vents rooted on extension fractures and their geodynamic implications in the Ethiopian Rift. *Journal of Volcanology and Geothermal Research*, *79*(3–4), 205–222, doi:10.1016/S0377-0273(97)00034-6.

Korme, T., V. Acocella, and B. Abebe (2004), The Role of Pre-existing Structures in the Origin, Propagation and Architecture of Faults in the Main Ethiopian Rift. *Gondwana Research*, *7*(2), 467–479, doi:10.1016/S1342-937X(05)70798-X.

Latutrie, B., A. Harris, E. Médard, and L. Gurioli (2017), Eruption and emplacement dynamics of a thick trachytic lava flow of the Sancy volcano (France). *Bulletin of Volcanology*, *79*(1), 1–21, doi:10.1007/s00445-016-1084-6.

Le Corvec, N., K. B. Spörli, J. Rowland, and J. Lindsay (2013a), Spatial distribution and alignments of volcanic centers: Clues to the formation of monogenetic volcanic fields. *Earth-Science Reviews*, *124*, 96–114, doi:10.1016/j.earscirev.2013.05.005.

Le Corvec, N., T. Menand, and J. Lindsay (2013b), Interaction of ascending magma with pre-existing crustal fractures in monogenetic basaltic volcanism: An experimental approach. *Journal of Geophysical Research: Solid Earth*, *118*(3), 968–984, doi:10.1002/jgrb.50142.

Le Corvec, N., M. S. Bebbington, J. M. Lindsay, and L. E. McGee (2013c), Age, distance, and geochemical evolution within a monogenetic volcanic field: Analyzing patterns in the Auckland Volcanic Field eruption sequence. *Geochemistry, Geophysics, Geosystems*, *14*(9), 3648–3665, doi:10.1002/ggge.20223.

Le Turdu, C., J.-J. Tiercelin, E. Gibert, Y. Travi, K.-E. Lezzar, J.-P. Richert, M. Massault, F. Gasse, R. Bonnefille, M. Decobert, B. Gensous, V. Jeudy, E. Tamrat, M. U. Mohammed, K. Martens, B. Atnafu, T. Chernet, D. Williamson, and M. Taieb (1999), The Ziway–Shala lake basin system, Main Ethiopian Rift: Influence of volcanism, tectonics, and climatic forcing on basin formation and sedimentation. *Palaeogeography, Palaeoclimatology, Palaeoecology*, *150*, 135–177, doi:10.1016/S0031-0182(98)00220-X.

Le Voyer, M., K. A. Kelley, E. Cottrell, and E. H. Hauri (2017), Heterogeneity in mantle carbon content from CO2-undersaturated basalts, *Nature Communications*, *8*, 14062, doi:10.1038/ncomms14062.

Lee, H., J. D. Muirhead, T. P. Fischer, C. J. Ebinger, S. A. Kattenhorn, Z. D. Sharp, and G. Kianji (2016), Massive and prolonged deep carbon emissions associated with continental rifting, *Nature Geosciences*, *9*, 145–149, doi:10.1038/NGEO2622.

Lee, H., T. P. Fischer, J. D. Muirhead, C. J. Ebinger, S. A. Kattenhorn, Z. D. Sharp, G. Kianji, N. Takahata, and Y. Sano (2017), Incipient rifting accompanied by the release of subcontinental lithospheric mantle volatiles in the Magadi and Natron basin, East Africa, *Journal of Volcanology and Geothermal Research*, *346*, 118–133, doi:10.1016/j.jvolgeores.2017.03.017.

Lescinsky, D. T., S. V. Skoblenick, and L. Mansinha (2007), Automated identification of lava flow structures using local Fourier spectrum of digital elevation data. *Journal of Geophysical Research*, *112*, B05212, doi:10.1029/2006JB004263.

Lloyd, R., J. Biggs, M. Wilks, A. Nowacki, J. M. Kendall, A. Ayele, E. Lewi, and H. Eysteinsson (2018a), Evidence for cross rift structural controls on deformation and seismicity at a continental rift caldera. *Earth and Planetary Science Letters*, *487*, 190–200, doi:10.1016/j.epsl.2018.01.037.

Lloyd, R., J. Biggs, Y. Birhanu, M. Wilks, J. Kendall, A. Ayele, and E. Lewi (2018b), Sustained Uplift at a Continental Rift Caldera. *Journal of Geophysical Research B: Solid Earth*, *123*(6), 5209–5226, doi:10.1029/2018JB015711.

Lucic, G., J. Stix, and B. Wing (2015), Structural controls on the emission of magmatic carbon dioxide gas, Long Valley Caldera, USA, *Journal of Geophysical Research: Solid Earth*, *120*, 2262–2278, doi:10.1002/2014JB011760.Received.

Maccaferri, F., E. Rivalta, D. Keir, and V. Acocella (2014), Off-rift volcanism in rift zones determined by crustal unloading. *Nature Geoscience*, *7*(4), 297–300, doi:10.1038/ngeo2110.

Maccaferri, F., V. Acocella, and E. Rivalta (2015), How the differential load induced by normal fault scarps controls the distribution of monogenic volcanism. *Geophysical Research Letters*, *42*(18), 7507–7512, doi:10.1002/2015GL065638.

Macdonald, R., and I. L. Gibson (1969), Pantelleritic obsidians from the volcano Chabbi (Ethiopia). *Contributions to Mineralogy and Petrology*, *24*(3), 239–244, doi:10.1007/BF00376050.

Magee, C., J. D. Muirhead, A. Karvelas, S. P. Holford, C. A. L. Jackson, I. D. Bastow, N. Schofield, C. T. E. Stevenson, C. McLean, W. McCarthy, and O. Shtukert (2016), Lateral magma flow in mafic sill complexes, *Geosphere*, *12*(3), 809–841, doi:10.1130/GES01256.1.

Maguire, P. K. H., C. J. Ebinger, G. W. Stuart, G. D. Mackenzie, K. A. Whaler, J.-M. Kendall, M. A. Khan, C. M. R. Fowler, S. L. Klemperer, G. R. Keller, S. Harder, T. Furman, K. Mickus, L. Asfaw, A. Ayele, and Abebe, B. (2003), Geophysical Project in Ethiopia Studies Continental Breakup. *EOS, Transactions American Geophysical Union*, *84*(35), 337, 342–343, doi:10.1029/2003EO350002.

Maguire, P. K. H., G. R. Keller, S. L. Klemperer, G. D. Mackenzie, K. Keranen, S. Harder, B. O'Reilly, H. Thybo, L. Asfaw, M. A. Khan, and M. Amha (2006), Crustal structure of the northern Main Ethiopian Rift from the EAGLE controlled-source survey; a snapshot of incipient lithospheric break-up. *Geological Society, London, Special Publications*, *259*(1), 269–292, doi:10.1144/GSL.SP.2006.259.01.21.

Mahood, G. A. (1984), Pyroclastic rocks and calderas associated with strongly peralkaline magmatism. *Journal of Geophysical Research*, *89*(B10), 8540–8552, doi:10.1029/JB089iB10p08540.

Mahood, G. A., and W. Hildreth (1986), Geology of the peralkaline volcano at Pantelleria, Strait of Sicily. *Bulletin of Volcanology*, *48*(2–3), 143–172, doi:10.1007/BF01046548.

Manning, C. E., and S. E. Ingebritsen (1999), Permeability of the Continental Crust: Implications of Geothermal Data and Metamorphic Systems, *Reviews of Geophysics*, *37*(1), 127–150, doi:10.1029/1998RG900002.

Martin-Jones, C. M., C. S. Lane, N. J. G. Pearce, V. C. Smith, H. F. Lamb, F. Schaebitz, F. Viehberg, M. C. Brown, U. Frank, and A. Asrat (2017), Recurrent explosive eruptions from a high-risk Main Ethiopian Rift volcano throughout the Holocene. *Geology*, *45*(12), 1127–1130, doi:10.1130/G39594.1.

Marty, B., and I. N. Tolstikhin (1998), CO_2 fluxes from mid-ocean ridges, arcs and plumes, *Chemical Geology*, *145*(3–4), 233–248, doi:10.1016/S0009-2541(97)00145-9.

Mazzarini, F., and I. Isola (2010), Monogenetic vent self-similar clustering in extending continental crust: Examples from the East African Rift System. *Geosphere*, *6*(5), 567–582, doi:10.1130/GES00569.1.

Mazzarini, F., T. Abebe, F. Innocenti, P. Manetti, and M. T. Pareschi, (1999), Geology of the Debre Zeyt area (Ethiopia) (with a geologic map at scale 1:100,000). *Acta Vulcanology*, *11*, 131–141.

Mazzarini, F., M. T. Pareschi, M. Favalli, I. Isola, S. Tarquini, and E. Boschi (2005), Morphology of basaltic lava channels during the Mt. Etna September 2004 eruption from airborne laser altimeter data. *Geophysical Research Letters*, *32*(4), 1–4, doi:10.1029/2004GL021815.

Mazzarini, F., D. Keir, and I. Isola (2013a), Spatial relationship between earthquakes and volcanic vents in the central-northern Main Ethiopian Rift. *Journal of Volcanology and Geothermal Research*, *262*, 123–133, doi:10.1016/j.jvolgeores.2013.05.007.

Mazzarini, F., T. O. Rooney, and I. Isola (2013b), The intimate relationship between strain and magmatism: A numerical treatment of clustered monogenetic fields in the Main Ethiopian Rift. *Tectonics*, *32*(1), 49–64, doi:10.1029/2012TC003146.

Mazzarini, F., N. Le Corvec, I. Isola, and M. Favalli (2016), Volcanic field elongation, vent distribution, and tectonic evolution of a continental rift: The Main Ethiopian Rift example. *Geosphere*, *12*(3), 706–720, doi:10.1130/GES01193.1.

McNamara, K., K. V. Cashman, A. C. Rust, K. Fontijn, F. Chalié, E. L. Tomlinson, and G. Yirgu (2018), Using Lake Sediment Cores to Improve Records of Volcanism at Aluto Volcano in the Main Ethiopian Rift. *Geochemistry, Geophysics, Geosystems*, *19*(9), 3164–3188, doi:10.1029/2018GC007686.

Medynski, S., R. Pik, P. Burnard, A. Williams, C. Vye-Brown, D. Ferguson, P.-H. Blard, L. France, G. Yirgu, J. I. Seid, D. Ayalew, and A. Calvert (2013), Controls on magmatic cycles and development of rift topography of the Manda Hararo segment (Afar, Ethiopia): Insights from cosmogenic ^{3}He investigation of landscape evolution. *Earth and Planetary Science Letters*, *367*, 133–145, doi:10.1016/j.epsl.2013.02.006.

Mengistu, Y. (2016), Detection of geothermal anomalies using Landsat 8 thermal infrared data in Tulu Moye geothermal prospect, Main Ethiopia Rift, *[M.Sc. thesis]: Addis Ababa, Ethiopia, Addis Ababa University*, 98 pp.

Michon, L., and O. Merle (2001), The evolution of the Massif Central rift: spatio-temporal distribution of the volcanism. *Bulletin de La Société Géologique de France*, *172*(2), 201–211, doi:10.2113/172.2.201.

Ministry of Water Resources (MOWR) (2008), Butajira – Ziway Areas Development Study: Hydrogeology and Growndwater Modeling, *[Internal Report:] Ethiopian Water Technology Centre, Addis Ababa, Ethiopia*, 102 pp.

Mohr, P. A. (1966), Chabbi Volcano (Ethiopia). *Bulletin Volcanologique*, *29*(1), 797–815, doi:10.1007/BF02597195.

Mohr, P., J. G. Mitchell, and R. G. H. Raynolds (1980), Quaternary Volcanism and Faulting at O'A Caldera, Central Ethiopian Rift, *Bulletin of Volcanology, 43*(1), 173–189, doi:10.1007/BF02597619.

Moore, H. J., D. W. G. Arthur, and G. G. Schaber (1978), Yield strengths of flows on the Earth, Mars, and Moon. In *Proceedings of the Ninth Lunar and Planetary Scientific Conference (Vol. 3)* (pp. 3351–3378). Houston, Texas.

Mörner, N.-A., and G. Etiope (2002), Carbon degassing from the lithosphere, *Glob. Planet. Change*, *33*(1), 185–203, doi:10.1016/S0921-8181(02)00070-X.

Muirhead, J. D., S. A. Kattenhorn, and N. Le Corvec (2015), Varying styles of magmatic strain accomodation across the East African Rift. *Geochemistry, Geophysics, Geosystems*, *16*, 2775–2795, doi: 10.1002/2015GC005918.

Muirhead, J. D., S. A. Kattenhorn, H. Lee, S. Mana, B. D. Turrin, T. P. Fischer, G. Kianji, E. Dindi, and D. S. Stamps (2016a), Evolution of upper crustal faulting assisted by magmatic volatile release during early-stage continental rift development in the East African Rift, *Geosphere*, *12*(6), GES01375.1, doi:10.1130/GES01375.1.

Muirhead, J. D., A. R. Van Eaton, G. Re, J. D. L. White, and M. H. Ort (2016b), Monogenetic volcanoes fed by interconnected dikes and sills in the Hopi Buttes volcanic field, Navajo Nation, USA. *Bulletin of Volcanology*, *78*(2), 11, doi:10.1007/s00445-016-1005-8.

Nakamura, K. (1977), Volcanoes as possible indicators of tectonic stress orientation - principle and proposal. *Journal of Volcanology and Geothermal Research*, *2*, 1–16, doi:10.1007/BF02199968.

Nomikou, P., M. M. Parks, D. Papanikolaou, D. M. Pyle, T. A. Mather, S. Carey, A. B. Watts, M. Paulatto, M. L. Kalnins, I. Livanos, K. Bejelou, E. Simou, and I. Perros (2014), The emergence and growth of a submarine volcano: The Kameni islands, Santorini (Greece). *GeoResJ*, *1–2*, 8–18, doi:10.1016/j.grj.2014.02.002.

Nowacki, A., M. Wilks, J. M. Kendall, J. Biggs, and A. Ayele (2018), Characterising hydrothermal fluid pathways beneath Aluto volcano, Main Ethiopian Rift, using shear wave splitting. *Journal of Volcanology and Geothermal Research*, *356*, 331–341, doi:10.1016/j.jvolgeores.2018.03.023.

Oppenheimer, C., M.R. Burton, J. Durieux, and D.M. Pyle (2002), Open-path Fourier transform spectroscopy of gas emissions from Oldoinyo Lengai volcano, Tanzania, *Optics Lasers Eng., 37*, 203-214.

Parks, M. M., S. Caliro, G. Chiodini, D. M. Pyle, T. A. Mather, K. Berlo, M. Edmonds, J. Biggs, P. Nomikou, and C. Raptakis (2013), Distinguishing contributions to diffuse CO_2 emissions in volcanic areas from magmatic degassing and thermal decarbonation using soil gas ^{222}Rn- $\delta^{13}C$ systematics: Application to Santorini volcano, Greece, *Earth and Planetary Science Letters*, *377–378*, 180–190, doi:10.1016/j.epsl.2013.06.046.

Peccerillo, A., M. R. Barberio, G. Yirgu, D. Ayalew, M. Barbieri, and T. W. Wu (2003), Relationships between Mafic and Peralkaline Silicic Magmatism in Continental Rift

Settings: a Petrological, Geochemical and Isotopic Study of the Gedemsa Volcano, Central Ethiopian Rift. *Journal of Petrology*, *44*(11), 2003–2032, doi:10.1093/petrology/egg068.

Peccerillo, A., C. Donati, A. P. Santo, A. Orlando, G. Yirgu, and D. Ayalew (2007), Petrogenesis of silicic peralkaline rocks in the Ethiopian rift: Geochemical evidence and volcanological implications. *Journal of African Earth Sciences*, *48*(2–3), 161–173, doi:10.1016/j.jafrearsci.2006.06.010.

Pedersen, G. B. M., and P. Grosse (2014), Morphometry of subaerial shield volcanoes and glaciovolcanoes from Reykjanes Peninsula, Iceland: Effects of eruption environment. *Journal of Volcanology and Geothermal Research*, *282*, 115–133, doi:10.1016/j.jvolgeores.2014.06.008.

Peitersen, M. N., and D. A. Crown (1999), Downflow width behavior of Martian and terrestrial lava flows. *Journal of Geophysical Research*, *104*(E4), 8473–8488, doi:10.1029/1999JE900003.

Pérez, N. M., P. A. Hernández, G. Padilla, D. Nolasco, J. Barrancos, G. Melían, E. Padrón, S. Dionis, D. Calvo, F. Rodríguez, K. Notsu, T. Mori, M. Kusakabe, M. Carmencita Arpa, P. Reniva, and M. Ibarra (2011), Global CO_2 emission from volcanic lakes, *Geology*, *39*(3), 235–238, doi:10.1130/G31586.1.

Plasman, M. C. Tiberi, C. Ebinger, S. Gautier, J. Albaric, S. Peyrat, J. Déverchère, B. Le Gall, P. Tarits, S. Roecker, F. Wambura, A. Muzuka, G. Mulibo, K. Mtelela, M. Msabi, G. Kianji, S. Hautot, J. Perrot and R. Gama (2017), Lithospheric low-velocity zones associated with a magmatic segment of the Tanzanian Rift, East Africa, *Geophysical Journal International*, *210*, 465–481, doi:10.1093/gji/ggx177.

Porter, S. C. (1972), Distribution, Morphology, and Size Frequency of Cinder Cones on Mauna Kea Volcano, Hawaii. *Geological Society of America Bulletin*, *83*(12), 3607–3612, doi: 10.1130/0016-7606(1972)83[3607:DMASFO]2.0.CO;2.

Prima, O. D. A., and T. Yoshida (2010), Characterization of volcanic geomorphology and geology by slope and topographic openness. *Geomorphology*, *118*(1–2), 22–32, doi:10.1016/j.geomorph.2009.12.005.

Pürschel, M., R. Gloaguen, and S. Stadler (2013), Geothermal activities in the Main Ethiopian Rift: Hydrogeochemical characterization of geothermal waters and geothermometry applications (Dofan-Fantale, Gergede-Sodere, Aluto-Langano), *Geothermics*, *47*, 1–12, doi:10.1016/j.geothermics.2013.01.001.

Pyle, D. M., and J. R. Elliott (2006), Quantitative morphology, recent evolution, and future activity of the Kameni Islands volcano, Santorini, Greece. *Geosphere*, *2*(5), 253–268, doi:10.1130/GES00028.1.

Rampey, M. L., C. Oppenheimer, D. M. Pyle, and G. Yirgu (2010), Caldera-forming eruptions of the Quaternary Kone Volcanic Complex, Ethiopia. *Journal of African Earth Sciences*, *58*(1), 51–66, doi:10.1016/j.jafrearsci.2010.01.008.

Rapprich, V., V. Žáček, K. Verner, V. Erban, T. Goslar, Y. Bekele, F. Legesa, T. Hroch, and P. Hejtmánková (2016), Wendo Koshe Pumice: The latest Holocene silicic explosive eruption product of the Corbetti Volcanic System (Southern Ethiopia). *Journal of Volcanology and Geothermal Research*, *310*, 159–171, doi:10.1016/j.jvolgeores.2015.12.008.

Reyners, M., D. Eberhart-Phillips, and G. Stuart (2007), The role of fluids in lower-crustal earthquakes near continental rifts, *Nature*, *446*, 1075–1078, doi:10.1038/nature05743.

Riedel, C., G. G. J. Ernst, and M. Riley (2003), Controls on the growth and geometry of pyroclastic constructs. *Journal of Volcanology and Geothermal Research*, *127*, 121–152, doi:10.1016/S0377-0273(03)00196-3.

Risso, C., K. Németh, A. María, F. Nullo, and M. Drosina (2008), The role of phreatomagmatism in a Plio-Pleistocene high-density scoria cone field: Llancanelo Volcanic Field (Mendoza), Argentina. *Journal of Volcanology and Geothermal Research*, *169*, 61–86, doi:10.1016/j.jvolgeores.2007.08.007.

Robertson, E. A. M., J. Biggs, K. V. Cashman, M. A. Floyd, and C. Vye-Brown (2015), Influence of regional tectonics and pre-existing structures on the formation of elliptical calderas in the Kenyan Rift. *Geological Society, London, Special Publications*, *420*(1), 43–67, doi:10.1144/SP420.12.

Robertson, E., J. Biggs, M. Edmonds, L. Clor, T. P. Fischer, C. Vye-Brown, G. Kianji, W. Koros, and R. Kandie (2016), Diffuse degassing at Longonot volcano, Kenya: Implications for CO_2 flux in continental rifts, *Journal of Volcanology and Geothermal Research*, *327*, 208–222, doi:10.1016/j.jvolgeores.2016.06.016.

Roecker, S., C. Ebinger, C. Tiberi, G. Mulibo, R. Ferdinand-Wambura, K. Mtelela, G. Kianji, A. Muzuka, S. Gautier, J. Albaric, and S. Peyrat (2017), Subsurface images of the Eastern Rift, Africa, from the joint inversion of body waves, surface waves and gravity: investigating the role of fluids in early-stage continental rifting, *Geophysical Journal International*, *210*, 931–950, doi:10.1093/gji/ggx220.

Rogers, P. G., M. T. Zuber, and B. A. Campbell (1996), Crossflow topographic effects on the emplacement of leveed lava flows: Implications for Venusian lava flows. In *Lunar and Planetary Science Conference* (Vol. XXVII, pp. 1095–1096).

Rogie, J. D., D. M. Kerrick, G. Chiodini, and F. Frondini (2000), Flux measurements of nonvolcanic CO_2 emission from some vents in central Italy, *Journal of Geophysical Research*, *105*, 8435–8445, doi: 10.1029/1999JB900430.

Romine, W. L., A. G. Whittington, P. I. Nabelek, and A. M. Hofmeister (2012), Thermal diffusivity of rhyolitic glasses and melts: Effects of temperature, crystals and dissolved water. *Bulletin of Volcanology*, *74*(10), 2273–2287, doi:10.1007/s00445-012-0661-6.

Rooney, T. O., T. Furman, G. Yirgu, and D. Ayalew (2005), Structure of the Ethiopian lithosphere: Xenolith evidence in the Main Ethiopian Rift. *Geochimica et Cosmochimica Acta*, *69*(15), 3889–3910, doi:10.1016/j.gca.2005.03.043.

Rooney, T., T. Furman, I. Bastow, D. Ayalew, and G. Yirgu (2007), Lithospheric modification during crustal extension in the Main Ethiopian Rift. *Journal of Geophysical Research*, *112*(B10201), doi:10.1029/2006JB004916.

Rooney, T. O., I. D. Bastow, and D. Keir (2011), Insights into extensional processes during magma assisted rifting: Evidence from aligned scoria cones. *Journal of Volcanology and Geothermal Research*, *201*(1–4), 83–96, doi:10.1016/j.jvolgeores.2010.07.019.

Rooney, T. O., C. Herzberg, and I. D. Bastow (2012), Elevated mantle temperature beneath East Africa. *Geology*, *40*(1), 27–30, doi:10.1130/G32382.1.

Rooney, T. O., W. R. Nelson, L. Dosso, T. Furman, and B. Hanan (2014a), The role of continental lithosphere metasomes in the production of HIMU-like magmatism on the northeast African and Arabian plates, *Geology*, *42*(5), 419–422, doi:10.1130/G35216.1.

Rooney, T. O., I. D. Bastow, D. Keir, F. Mazzarini, E. Movsesian, E. B. Grosfils, J. R. Zimbelman, M. S. Ramsey, D. Ayalew, and G. Yirgu (2014b), The protracted development of focused magmatic intrusion during continental rifting. *Tectonics*, *33*, 875–897, doi:10.1002/2013TC003514.Received.

Rooney, T. O., W. R. Nelson, D. Ayalew, B. Hanan, G. Yirgu, and J. Kappelman (2017), Melting the lithosphere: Metasomes as a source for mantle-derived magmas, *Earth and Planetary Science Letters*, *461*, 105–118, doi:10.1016/j.epsl.2016.12.010.

Rychert, C. A., J. O. S. Hammond, N. Harmon, J.-M. Kendall, D. Keir, C. Ebinger, I. D. Bastow, A. Ayele, M. Belachew, and G. Stuart (2012), Volcanism in the Afar Rift sustained by decompression melting with minimal plume influence. *Nature Geoscience*, *5*(6), 1–4, doi:10.1038/ngeo1455.

Saal, A. E., E. H. Hauri, C. H. Langmuir, and M. R. Perfit (2002), Vapour undersaturation in primitive mid-ocean-ridge basalt and the volatile content of Earth's upper mantle., *Nature*, *419*(6906), 451–455, doi:10.1038/nature01073.

Samrock, F., A. Kuvshinov, J. Bakker, A. Jackson, and S. Fisseha (2015), 3-D analysis and interpretation of magnetotelluric data from the Aluto-Langano geothermal field, Ethiopia. *Geophysical Journal International*, *202*(3), 1923–1948, doi:10.1093/gji/ggv270.

Sano, Y., and Marty, B. (1995), Origin of carbon in fumarolic gas from island arcs. *Chemical Geology*, *119*(1), 265-274, doi: 10.1016/0009-2541(94)00097-R.

Saria, E., E. Calais, D. S. Stamps, D. Delvaux, and C. J. H. Hartnady (2014), Present-day kinematics of the East African Rift, *Journal of Geophysical Research: Solid Earth*, *119*, 3584–3600, doi:10.1002/2013JB010901.

Self, S., M. Widdowson, T. Thordarson, and A. E. Jay (2006), Volatile fluxes during flood basalt eruptions and potential effects on the global environment: A Deccan perspective, *Earth and Planetary Science Letters*, *248*(1–2), 517–531, doi:10.1016/j.epsl.2006.05.041.

Settle, M. (1979), The structure and emplacement of cinder cone fields. *American Journal of Science*, *279*, 1089–1107, doi:10.2475/ajs.279.10.1089.

Seward, T. M., and D. M. Kerrick (1996), Hydrothermal CO_2 emission from the Taupo Volcanic Zone, New Zealand, *Earth and Planetary Science Letters*, *139*(1–2), 105–113, doi:10.1016/0012-821X(96)00011-8.

Sibson, R. H. (2000), Fluid involvement in normal faulting, *Journal of Geodynamics*, *29*, 469–499, doi:10.1016/S0264-3707(99)00042-3.

Siegburg, M., T. M. Gernon, J. M. Bull, D. Keir, D. N. Barfod, R. N. Taylor, B. Abebe, and A. Ayele (2017), Geological evolution of the Boset-Bericha Volcanic Complex, Main Ethiopian Rift: $^{40}Ar/^{39}Ar$ evidence for episodic Pleistocene to Holocene volcanism. *Journal of Volcanology and Geothermal Research*, *351*, 115–133, doi:10.1016/j.jvolgeores.2017.12.014.

Smets, B., D. Tedesco, F. Kervyn, A. Kies, O. Vaselli, and M. M. Yalire (2010), Dry gas vents ("mazuku") in Goma region (North-Kivu, Democratic Republic of Congo):

Formation and risk assessment, *Journal of African Earth Sciences*, *58*(5), 787–798, doi:10.1016/j.jafrearsci.2010.04.008.

Smith, I. E. M., and K. Németh (2017), Source to surface model of monogenetic volcanism: a critical review. *Geological Society, London, Special Publications*, *446*(1), 1–28, doi:10.1144/SP446.14.

Sorey, M. L., W. C. Evans, B. M. Kennedy, C. D. Farrar, and B. Hausback (1998), Carbon dioxide and helium emissions from a reservoir of magmatic gas beneath Mammoth Mountain, California, *Journal of Geophysical Research*, *103*, 303–323.

Sparks, R. S. J., H. Pinkerton, and G. Hulme (1976), Classification and formation of lava levees on Mount Etna, Sicily. *Geology*, *4*(5), 269–271, doi:10.1130/0091-7613(1976)4<269:CAFOLL>2.0.CO;2.Spinks, K. D., V. Acocella, J. W. Cole, and K. N. Bassett (2005), Structural control of volcanism and caldera development in the transtensional Taupo Volcanic Zone, New Zealand. *Journal of Volcanology and Geothermal Research*, *144*, 7–22, doi:10.1016/j.jvolgeores.2004.11.014.

Stadler, S., K. Adem, and R. Gloaguen (2007), Isotopes as a marker for potential impact of rift tectonics on the groundwater system of the Awash Basin in the East African Rift, in: *Proc. 7th International Symposium on Applied Isotope Geochemistry, Stellenbosch, Cape Town, South Africa, September 10–14*.

Stefanescu, E. R., M. Bursik, and A. K. Patra (2012), Effect of digital elevation model on Mohr-Coulomb geophysical flow model output. *Natural Hazards*, *62*(2), 635–656, doi:10.1007/s11069-012-0103-y.

Stevenson, R. J., A. P. W. Hodder, and R. M. Briggs (1994), Rheological estimates of rhyolite lava flows from the okataina volcanic centre, New Zealand. *New Zealand Journal of Geology and Geophysics*, *37*(2), 211–221, doi:10.1080/00288306.1994.9514616.

Tadesse, A. Z., D. Ayalew, R. Pik, G. Yirgu, and K. Fontijn (2018), Magmatic evolution of the Boku Volcanic Complex, Main Ethiopian Rift. *Journal of African Earth Sciences*, *149*, 109–130, doi:10.1016/j.jafrearsci.2018.08.003.

Tarquini, S., M. Favalli, F. Mazzarini, I. Isola, and A. Fornaciai (2012), Morphometric analysis of lava flow units: Case study over LIDAR-derived topography at Mount Etna, Italy. *Journal of Volcanology and Geothermal Research*, *235–236*, 11–22, doi:10.1016/j.jvolgeores.2012.04.026.

Teclu, A. (2002), Geochemistry of Dofan-Fentale geothermal prospect. *[Internal Report:] Geological Survey of Ethiopia, Addis Ababa, Ethiopia, 31 pp.*

Thouret, J. C. (1999), Volcanic geomorphology – an overview. *Earth Science Reviews*, *47*(1–2), 95–131, doi:10.1016/S0012-8252(99)00014-8.

Thrall, R. (1973). *Gadamsa Caldera, Ethiopia*. Center for Astrophysics, Harvard College Observatory and Smithsonian Astrophysical Observatory (Preprint Series No. 280).

Tibaldi, A. (1995), Morphology of pyroclastic cones and tectonics. *Journal of Geophysical Research*, *100*(B12), 24521–24535, doi:10.1029/95JB02250.

Trestrail, K. R., T. O. Rooney, G. Girard, C. Svoboda, G. Yirgu, D. Ayalew, and J. Keppelman (2017), Sub-continental lithospheric mantle deformation in the Yerer-Tullu Wellel Volcanotectonic Lineament: A study of peridotite xenoliths, *Chemical Geology*, *455*, 249–263, doi:10.1016/j.chemgeo.2016.10.013.

United Nations Development Programme (UNDP) (1973), Geology, Geochemistry and Hydrology of Hot Springs of the East African Rift System within Ethiopia, *in: Investigation of geothermal resources for power development (DP/SF/UN 116-technical report), United Nations, New York*, 275 pp.

Ventura, G., and G. Vilardo (2007), Emplacement mechanism of gravity flows inferred from high resolution Lidar data: The 1944 Somma–Vesuvius lava flow (Italy). *Geomorphology*, *95*, 223–235, doi:10.1016/j.geomorph.2007.06.005.

Vye-Brown, C., R. S. J. Sparks, E. Lewi, G. Mewa, A. Asrat, S. C. Loughlin, K. Mee, and T. J. Wright (2016), Ethiopian volcanic hazards: a changing research landscape. *Geological Society, London, Special Publications*, *420*, 355–365, doi:10.1144/SP420.16.

Wadge, G., and R. M. C. Lopes (1991), The lobes of lava flows on Earth and Olympus Mons, Mars. *Bulletin of Volcanology*, *54*(1), 10–24, doi:10.1007/BF00278203.

Wadge, G., J. Biggs, R. Lloyd, and J.-M. Kendall (2016), Historical Volcanism and the State of Stress in the East African Rift System. *Frontiers in Earth Science*, *4*(September), doi:10.3389/feart.2016.00086.

Wantim, M. N., M. Kervyn, G. G. J. Ernst, M. A. Marmol, C. E. Suh, and P. Jacobs (2013), Numerical experiments on the dynamics of channelised lava flows at Mount Cameroon volcano with the FLOWGO thermo-rheological model. *Journal of Volcanology and Geothermal Research*, *253*, 35–53, doi:10.1016/j.jvolgeores.2012.12.003.

Warner, N. H., and T. K. P. Gregg (2003), Evolved lavas on Mars? Observations from southwest Arsia Mons and Sabancaya volcano, Peru. *Journal of Geophysical Research*, *108*(E10), 5112, doi:10.1029/2002JE001969.

Webster, J. D., R. P. Taylor, and C. Bean (1993), Pre-eruptive melt composition and constraints on degassing of a water-rich pantellerite magma, Fantale volcano, Ethiopia. *Contributions to Mineralogy and Petrology*, *114*(1), 53–62, doi:10.1007/BF00307865.

Werner, C., and S. Brantley (2003), CO_2 emissions from the Yellowstone volcanic system, *Geochemistry, Geophysics, Geosystems*, *4*(7), doi:10.1029/2002GC000473.

Whaler, K. A., and S. Hautot (2006), The electrical resistivity structure of the crust beneath the northern Main Ethiopian Rift. *Geological Society, London, Special Publications*, *259*(1), 293–305, doi:10.1144/GSL.SP.2006.259.01.22.

White, R., and D. McKenzie (1989), Magmatism at Rift Zones: The Generation of Volcanic Continental Margins and Flood Basalts. *Journal of Geophysical Research*, *94*, 7685–7729, doi:10.1029/JB094iB06p07685.

Wignall, P. B. (2001), Large igneous provinces and mass extinctions, *Earth-Science Reiews*, *53*(1–2), 1–33, doi:10.1016/S0012-8252(00)00037-4.

Wilks, M., A. Ayele, J.-M. Kendall, and J. Wookey (2017a), The 24th January 2016 Hawassa earthquake: Implications for seismic hazard in the Main Ethiopian Rift. *Journal of African Earth Sciences*, *125*, 118–125, doi:10.1016/j.jafrearsci.2016.11.007.

Wilks, M., J-M. Kendall, A. Nowacki, J. Biggs, J. Wookey, Y. Birhanu, A. Ayele, and E. Lewi (2017b), Seismicity associated with magmatism, faulting and geothermal circulation at Aluto Volcano, Main Ethiopian Rift. *Journal of Volcanology and Geothermal Research*, *340*, 52–67, doi:10.1016/j.jvolgeores.2017.04.003.

Williams, F. M., M. A. J. Williams, and F. Aumento (2004), Tensional fissures and crustal extension rates in the northern part of the Main Ethiopian Rift. *Journal of African Earth Sciences*, *38*(2), 183–197, doi:10.1016/j.jafrearsci.2003.10.007.

Wilson, L., and P. J. Mouginis-Mark (2014), Dynamics of a fluid flow on Mars: Lava or mud? *Icarus*, *233*, 268–280, doi:10.1016/j.icarus.2014.01.041.

WoldeGabriel, G., J. L. Aronson, and R. C. Walter (1990), Geochronology and rift basin development in the central sector of the Main Ethiopian Rift. *Geological Society of America Bulletin*, *102*(4), 439–485, doi:10.1130/0016-7606(1990)102<0439.

Wolfenden, E., C. Ebinger, G. Yirgu, A. Deino, and D. Ayalew (2004), Evolution of the northern Main Ethiopian rift: Birth of a triple junction. *Earth and Planetary Science Letters*, *224*(1–2), 213–228, doi:10.1016/j.epsl.2004.04.022.

Wolfenden, E., C. Ebinger, G. Yirgu, P. R. Renne, and S. P. Kelley (2005), Evolution of a volcanic rifted margin: Southern Red Sea, Ethiopia. *Bulletin of the Geological Society of America*, *117*(7–8), 846–864, doi:10.1130/B25516.1.

Wood, C. A. (1980a), Morphometric evolution of cinder cones. *Journal of Volcanology and Geothermal Research*, *7*, 387–413, doi:10.1016/0377-0273(80)90040-2.

Wood, C. A. (1980b), Morphometric analysis of cinder cone degradation. *Journal of Volcanology and Geothermal Research*, *8*, 137–160, doi:10.1016/0377-0273(80)90101-8.

Wright, T. J., C. Ebinger, J. Biggs, A. Ayele, G. Yirgu, D. Keir, and A. Stork (2006), Magma-maintained rift segmentation at continental rupture in the 2005 Afar dyking episode, *Nature*, *442*(7100), 291–294, doi:10.1038/nature04978.

Wright, T. J., F. Sigmundsson, C. Pagli, M. Belachew, I. J. Hamling, B. Brandsdóttir, ... P. Einarsson (2012), Geophysical constraints on the dynamics of spreading centres from rifting episodes on land. *Nature Geoscience*, *5*(4), 242–250, doi: 10.1038/NGEO1428.

Younger, P. L. (2014), Missing a trick in geothermal exploration. *Nature Geoscience*, *7*(7), 479–480, doi:10.1038/ngeo2193.

Žáček, V., V. Rapprich, Y. Aman, B. Berhanu, D. Čížek, K. Dereje, V. Erban, T. Ezra, L. Firdawok, M. Habtamu, T. Hroch, V. Kopačková, P. Kycl, J. Málek, J. Mišurec, A. Orgoň, Z. Pécskay, J. Šíma, D. Tarekegu, and K. Verner (2014). *Explanation booklet to the set of geoscience maps of Ethiopia at scale 1:50,000, subsheet 0738-C4 Hawasa*. Prague/Addis Ababa, Czech Republic/Ethiopia: Czech Geological Survey/Aquatest/Geological Survey of Ethiopia.

Žáček, V., V. Rapprich, J. Šíma, R. Škoda, F. Laufek, and F. Legesa (2015), Kogarkoite, $Na_3(SO_4)F$, from the shalo hot spring, Main Ethiopian Rift: Implications for F-enrichment of thermal groundwater related to alkaline silicic volcanic rocks. *Journal of Geosciences (Czech Republic)*, *60*(3), 171–179, doi:10.3190/jgeosci.195.

Zhou, Y., B. Parsons, J. R. Elliott, I. Barisin, and R. T. Walker (2015), Assessing the ability of Pleiades stereo imagery to determine height changes in earthquakes: A case study for the El Mayor-Cucapah epicentral area. *Journal of Geophysical Research: Solid Earth*, *120*(12), 8793–8808, doi:10.1002/2015JB012358.

Zouzias, D., G. C. Miliaresis, and K. S. Seymour (2011), Interpretation of Nisyros volcanic terrain using land surface parameters generated from the ASTER Global Digital Elevation Model. *Journal of Volcanology and Geothermal Research*, *200*(3–4), 159–170, doi:10.1016/j.jvolgeores.2010.12.012.

Appendix 1

A1 Supporting Information for Chapter 2: Spatially variable CO_2 degassing and its implications

A1.1. Introduction

This supplementary information includes details concerning the methodology employed in the soil gas surveys, as well as specific results from each survey area. This may be useful for future reference by those interested in local geothermal activity and gas/fluid flow. Tables A1.1-A1.2 document the sources and regional results of the compilation work concerning geothermal manifestations. Breakdown of CO_2 survey results by fault/profile line are found in Table A1.3.

A1.2. Accumulation chamber method

Measurements were made by the accumulation chamber method [*Chiodini et al.*, 1998], with a PP Systems EGM-4 Environmental Gas Analyzer for CO_2 and an SRC-1 Soil Respiration Chamber and soil collar. In this method, the soil collar is inserted into the ground, ensuring close coupling between the soil and chamber. The chamber then circulates a known volume of gas through the analyzer. The concentration of CO_2 is monitored and the rate of increase/decrease gives the flux (Equation A1.1) which is typically positive (i.e., increasing). The final calculation depends on the volume (V) of the cylinder (including the soil collar) and its area

(A). The analyzer outputs flux values directly given values of V and A - results can be corrected for different values (Equation A2.2).

$$\Phi^{CO_2} = \frac{d(V \times [CO_2])}{dt} \div A = \frac{d[CO_2]}{dt} \times \frac{V}{A} \quad \text{(A1.1)}$$

$$\Phi_2 = \frac{V_2}{V_1} \times \frac{A_1}{A_2} \times \Phi_1 \quad \text{(A1.2)}$$

A1.3. Survey results by area

A1.3.1. Butajira

The mean flux of all measurements in the Butajira area is 28.7 g m^{-2} d^{-1}, and the mean flux for each fault in the area also exceeds the mean flux of the highest such value in the Aluto-Wonji area (Table 2.2, see also Table A1.3). Fault-controlled degassing is observed, most notably along fault SDFZ5 (see Figure 2.7a). Other faults show little signs of significant degassing, although it is possible that the width of signal is lower than the measurement spacing in some cases. In their survey in the Kenyan Rift Valley, *Lee et al.* [2016] find elevated degassing within fault zones with a width equal to the maximum throw of each fault – this can be dismissed for most faults in the Butajira area.

The highest measurement is 226 g m^{-2} d^{-1} with all but two measurements less than 120 g m^{-2} d^{-1}. The largest flux is observed along the trace of SDFZ5 which has no clear scarp in the field and is the fault furthest east of those surveyed. The extent of the active area is therefore not clear. The high fluxes measured east of SDFZ1 (up to 120 g m^{-2} d^{-1}) are close to the extension of a fault scarp, a linear feature in the ASTER GDEM and the Kuntane swamp, associated with hot springs [*MOWR*,

2008; Figure 2.5]. The Butajira area is therefore considered a degassing region in which faults are concentrating gas flow. Elevated values away from faults (Figure 2.7, upper left panel) and a high mean and standard deviation hints at diffuse degassing across the region. This distributed degassing may also be the reason for a nearly elevated mean flux across the possibly analogous Sodere area (see Figure 2.4, bottom panels).

A1.3.2. Aluto-Wonji

In contrast to the Butajira area, the Aluto-Wonji region is typified by very low mean flux and no results greater than 30 g m^{-2} d^{-1} (Table A1.3). The CMER is therefore asymmetric in its CO_2 degassing, as Figure 2.8 shows. Despite its close proximity to Aluto volcano and the Aluto-Langano geothermal field, the Wonji faults seem not to be mediating any magmatic degassing, implying that the Aluto CO_2 flux [*Hutchison et al*., 2015] is spatially restricted. The number of measurements taken across the Aluto-Wonji area is lower than other areas but three faults were surveyed adequately (< 50 m spacing), with no elevated values (Figure 2.7, lower left panel).

A1.3.3. Habilo-Fentale

The targeted survey in Habilo allows us to make a concentrated study of the signal given by degassing faults. The smaller and more regular spacing between measurements enables more confidence in capturing the signal in a more complete manner. Four of the six profiles we completed show clear degassing signals, absent in the remaining two (see Figure 2.7, right panel). HF1–3 are taken across two E-dipping faults on the western side of the basin, along which lie a number of

fumaroles; HF5 is taken across a W-dipping fault on the eastern side of the basin. HF4 and HF6 are each taken across the floor of the basin, with HF6 exhibiting major degassing.

Figure 2.7 (right panel) shows that the main body of the degassing signal lies within ~200–500 g m^{-2} d^{-1}, implying that the survey in the Butajira area lacks the higher range of elevated values. The signal ranges from ~40–200 m wide. Within the signal, flux values are highly variable on a very small spatial scale—in the HF6 profile the flux can vary from ~40–400 g m^{-2} d^{-1} over < 10 m.

Table A1.1. List of sources used for the database of hot springs and fumaroles. Theses, reports and published papers covering a variety of study areas were compiled. Table entries are ordered by area, entire rift followed by area-specific studies (south to north), and by year within area. GSE: Geological Survey of Ethiopia.

Source	Literature format	Study area	Notes
***United Nations Development Programme* [1973]**	Government report	Entire rift	Pioneering study using fieldwork and infra-red imagery across the MER, Afar and the Danakil Depression. Not all locations have been reproduced for database – many areas have been subsequently studied more thoroughly, but locations for other areas have been included. Relocation from maps and field descriptions necessary.
***Haile Selassie* [1984]**	Government report	Entire rift	Preliminary report of hot springs, fumaroles and associated hot ground areas, including descriptions of structural relationships, confirming many features from UNDP (1973).
***Purschel et al.* [2013]**	Published paper	Entire rift	Characterisation of geothermal waters from three regions (Dofan-Fentale, Gargadi-Sodere, Aluto-Langano).
***Kebede* [pers. comm.]**	Unpublished database	Entire rift	Working database of hot springs along the Main Ethiopian Rift, including grid reference locations of varying accuracy (estimated 20—2000 m).
***Gislason et al.* [2015]**	Industry report (Reykjavik Geothermal)	Corbetti	Surface exploration of the Corbetti geothermal area including a magnetotelluric survey. Relocation from maps necessary.
***GSE and the United Nations* [1976]**	Geological maps	Lake Shalla-Aluto-Langano	Set of maps produced by a variety of authors from the GSE. Relocation from maps necessary.
***Hutchison et al.* [2015]**	Published paper	Aluto-Langano	Comprehensive study of Aluto volcano's structure from field work and remote sensing. Fumarole and hot spring locations included and confirmed in Braddock *et al.* (2017).
***Braddock et al.* [2017]**	Paper in prep	Aluto-Langano	Confirmed locations from Hutchison *et al.* (2015) and Kebede *et al.* (1985) using ASTER infra-red satellite imagery.
***Ministry of Water and Resources* [2008]**	Government report	Butajira	A series of government reports on the hydrology and geology of the Butajira-Ziway area, targeting development and research concerning local groundwater. Grid references for three thermal springs are given but more may exist.

Table A1.1. Continued.

Source	Literature format	Study area	Notes
***Beyene* [2000]**	GSE report	Tulu Moye-Gedemsa	Included in the data used by *Purschel et al.* (2013).
***Ayele et al.* [2002]**	GSE report	Tulu Moye-Gedemsa	Preliminary exploration of the Tulu Moye-Gedemsa geothermal prospect, including geological and hydrothermal maps. Hydrothermal fields are described, including fumaroles, altered ground and fossil manifestations. Further investigated by Mengistu (2016).
***Bahiru* [2007]**	Master's thesis	Tulu Moye-Gedemsa	Structural study of the Tulu Moye-Gedemsa area, including the compilation of an inventory of thermal vents and relationships with fault systems.
***Mengistu* [2016]**	Master's thesis	Tulu Moye	Assessment of hydrothermal fields from Ayele *et al.* (2002) using Landsat 8 infra-red imagery. Relocation from maps necessary, with significant uncertainties concerning the location and nature of geothermal manifestations.
***Alula et al.* [1992]**	Geological maps	Gedemsa-Sodere	Relocation from maps necessary.
***Abera et al.* [2014]**	GSE report	Gedemsa-Sodere	Geophysical survey of the Gedemsa geothermal prospect area. A map of relevant features identifies hot springs to the north and hydrothermalised areas south of Lake Koka.
***Abiye and Haile* [2008]**	Published paper	Sodere	Geophysical survey of Boku/Sodere caldera, investigating flow of heat and fluids. Areas of current geothermal manifestations are given. Relocation from maps necessary.
***Stadler et al.* [2007]**	Conference abstract	Awash basin (Hubicha)	Included in the data used by *Purschel et al.* (2013).
***Ayenew et al.* [2008]**	Published paper	Awash basin	Hydrogeological study investigating groundwater regimes.
***Rampey et al.* [2010]**	Published paper	Kone	Geological assessment of the Kone volcanic complex.
***Williams et al.* [2004]**	Published paper	Kone-Fentale	Relocation from maps necessary.
***Teclu* [2002]**	GSE report	Fentale-Dofan	Included in the data used by *Purschel et al.* (2013).
***Bekele et al.* [2007]**	GSE report	Fentale-Dofan	A geological, geochemical and geophysical study of the Dofan-Fentale geothermal prospect, including identification of hot springs and fumaroles with field descriptions and photos. Relocation from maps necessary.
This study	n/a	Habilo-Fentale	Fumaroles observed along fault in Habilo region.

Table A1.2. Regional assessment of geothermal activity along the Main Ethiopian Rift detailing notable sites of hot springs and fumaroles including their structural associations. The study area is limited by Lake Abaya in the south and the Fentale region in the north. Notable sites excluded by these boundaries include (but are not limited to) the Nech Saar and Belbo Springs to the south, the highland springs (e.g., Ambo, Filwoha, Wolliso) and an abundance of features across the Afar and Danakil regions.

Region	Notable sites	Structural associations	Comments	Key references
Abaya	Chokore	NW shore of Lake Abaya, along western margin faults.	Ongoing interest for geothermal energy production.	*UNDP* [1973], *Haile Selassie* [1984]
	Bilate valley	Isolated hot springs along Bilate river and at the base of Ashire volcano (pre-Holocene).	Distributed features, structure and source unclear.	
	Bodicho	Along a fault through ignimbrite at the SE base of Data volcano (pre-Holocene).	Possible site of off-edifice magma storage? Off-axis from other geothermal features.	
Awassa	Corbetti volcanic complex	Solely fumarolic activity along WNW-ESE belt, near the summits of Mts Urji and Danshe, and near vents on Mt Chabbi.	Geothermal energy plant in construction.	*Gislason et al.* [2015]
	Wondo Genet	Caldera plain and E-W fault (possibly Awassa caldera rim).	Numerous springs, and tourist resort.	*UNDP* [1973], *Haile Selassie* [1984]
	Graha Quhe	Base of small rhyolite dome (SE of Awassa swamp).		
	Doredimtu	Weak fumaroles along base of major NE-trending regional fault.	Additional warm ground and weak fumaroles to the NE.	*Gislason et al.* [2015], *UNDP* [1973]
Lake Shalla	Eastern, southern, western shores	Numerous hot springs along O'a caldera rim (eastern half of lake) and western boundary fault.	Unknown present activity, strongly alkaline waters.	*UNDP* [1973], *GSE and UN* [1976]
	Lake Chitu	Southern lake shore, basaltic tuff ring.	Along strike from Doredimtu?	
Aluto-Langano	Aluto volcano	Western base (e.g. Auto, Hulo). Southern base (e.g. Gebiba, Kore). Within caldera (e.g. Bobesa, Finkilo).	Geothermal production ongoing. Fault-concentrated flow, particularly along Artu Jawe.	*Kebede et al.* [1985], *Hutchison et al.* [2015], *Braddock et al.* [2017]
	Lake Langano	Geyser Island, activity along regional faults (Bole, Oitu).	Previous geyser activity.	
	Lake Ziway	Debre Tseyon – hot springs along shore of volcanic island.	North of Aluto heat source?	*UNDP* [1973]

Table A1.2. Continued.

Region	Notable sites	Structural associations	Comments	Key references
Butajira	Kuntane	Multiple thermal springs in graben.	Off-edifice magma storage.	*MOWR* [2008], *Haile Selassie* [1984]
Bora-Tulu Moye	Bora	7 hydrothermal fields identified in the west (near Bora), aligned mostly NNW on transverse structures.	Area of current geothermal exploration (Reykjavik Geothermal).	*Ayele et al.* [2002], *Mengistu* [2016]
	Tulu caldera	Fumaroles aligned NNE with regional structures, and are commonly located at the bases of fault scarps.		*Bahiru* [2007]
Gedemsa-Sodere	Gedemsa caldera	No manifestations of current volcanic activity.	Geological map of Nazret-Dera area identifies zero active sites.	*Abera et al.* [2014], *Alula et al.* [1992], *Thrall* [1973]
	Gecha Island?	Unknown location.	Sole report of activity at Lake Koka.	*UNDP* [1973]
	Hippo Pool, Gargadi Springs		Well known, commonly reported.	*Alula et al.* [1992], *Purschel et al.* [2013], *UNDP* [1973]
	Boku	Amongst faults between Wonji and Nazret.	Locations unclear.	*Abiye and Haile* [2008]
	Sodere Springs	Near Boku ridge, possibly associated with Boku/Sodere caldera.	Popular tourist resort.	*Alula et al.* [1992], *Purschel et al.* [2013], *UNDP* [1973]
Boset		Fumarole on NW plain – off edifice? Reported fumaroles – Gudda and Bariccia volcanoes	Field descriptions only	*Di Paola* [1970], *UNDP* [1973], *Haile Selassie* [1984]
Kone		Single mention of small fumarole in southern Birenti Caldera (location unclear)	Field description only	*Rampey et al.* [2010]
Fentale	Fentale caldera	Many fumaroles from central obsidian flow and pit.	Popular tourist resort.	*Bekele et al.* [2007], *UNDP* [1973], *Williams et al.* [2004], this study
	Filoa	Regional fault (strike ~NNE).		
	Hubicha	SW of Lake Beseka along regional fault.		
	Habilo	High-temperature hot spring and line of fumaroles along E-dipping regional fault.		
	Others	Possible flank fumaroles. Additional off-edifice areas, e.g. Kessem River, Western Fentale?		

Table A1.3. Results from the three campaigns (summarised by numbers in bold), with breakdowns by fault. Fault/profile numbers are shown in Figure 2.5, names are derived from appending a regional code (SDFZ – Silti-Debre Zeyit Fault Zone, WFB – Wonji Fault Belt, HF – Habilo-Fentale).

Area Fault*	Number of measurements	Mean flux, g m^{-2} d^{-1}	Standard deviation
Sodere	**90**	**21.9**	**9.3**
Butajira	**88**	**28.7**	**34.7**
Guraghe	15	24.8	17.3
SDFZ1	20	25.3	27.4
SDFZ2	10	15.4	15.8
SDFZ3	12	16.1	6.1
SDFZ5	11	75.8	71.9
Koshe	15	25.0	13.5
Aluto-Wonji	**44**	**10.6**	**6.4**
WFB1	10	11.8	8.1
WFB4	10	14.3	7.2
WFB5	13	7.5	4.4
Habilo	**247**	**157.3†**	**401.3†**
HF1	22	158.5	147.4
HF2	60	273.6†	592.6†
HF3	38	294.9†	638.7†
HF4	60	20.3	10.1
HF5	12	20.4	15.7
HF6	57	112.9	103.2

*Only faults with number of measurements, $n \geq 10$ shown.
†Represents an underestimate – some values exceed measurement limit (2400 g m^{-2} d^{-1}).

Appendix 2

A2 Supporting Information for Chapter 3: Geomorphology and structure of peralkaline rift volcanoes

A2.1. Introduction

This supplementary information includes further details concerning observations of deposits and features at Fentale (see Section 3.3.1.3), calculation of levee slopes and widths (see Figure 3.14), and locations of features for which volumes have been calculated (see Table 3.2).

A2.2. Additional observations from Fentale

Further to the two nested craters in the centre of Fentale caldera, there is evidence for at least two small craters to the south and a low, broad crater to the east, though they are less clearly defined by topography.

Two small cones and a ridge border the western side of the obsidian coulee, likely to be pumice or scoria. In the south-west of the caldera there is a dissected dome and an area of hummocky, elevated topography projecting towards the north-west. This may be a lava dome and associated coulee. A similar area of elevated topography lies to the east and may also represent a silicic lava deposit, although this remains a hypothesis to be tested by further future field observations.

Field observations from the top of the caldera suggest that the southern half of the caldera is covered by a surficial pumice deposit, possibly relating to the explosive eruption(s) that formed the central craters.

A collection of small cones is found on the northern rim of Tinish Sabober, with a larger cone within the crater (Figure 3.2a). To the north, a series of cones have been emplaced on the footwall of an east-dipping fault, with a larger cone on the lower plain to the west (Figure 3.2a). A cone to the west is onlapped by the ignimbrite, indicating that some cones may predate the caldera-forming eruption.

The blister structures hosted by the ignimbrite on the flat plain around the edifice are not clearly visible on the DEM. In the field we mapped an area of 1.5 km^2 in which we located 24 blisters. They occur in a range of forms (collapsed, circular, elliptical, crescent-shaped), from near-flat to 2 m high and from 4 to 90 m wide (Figure A2.3). The surface of the blisters hosts polygonal fractures, creating a skin covering a smoother surface exposed in some locations. The brittle crust is on the order of 0.4 m thick (Figure A2.3).

The size and long axes of the blisters in the area we mapped did not vary systematically with location (Figure A2.4). The low, broad blisters are similar in form to ridges in topography formed by the ignimbrite deposited on pre-existing topography – it is likely that the blisters' shape, size and location depends strongly on the pre-deposit surface.

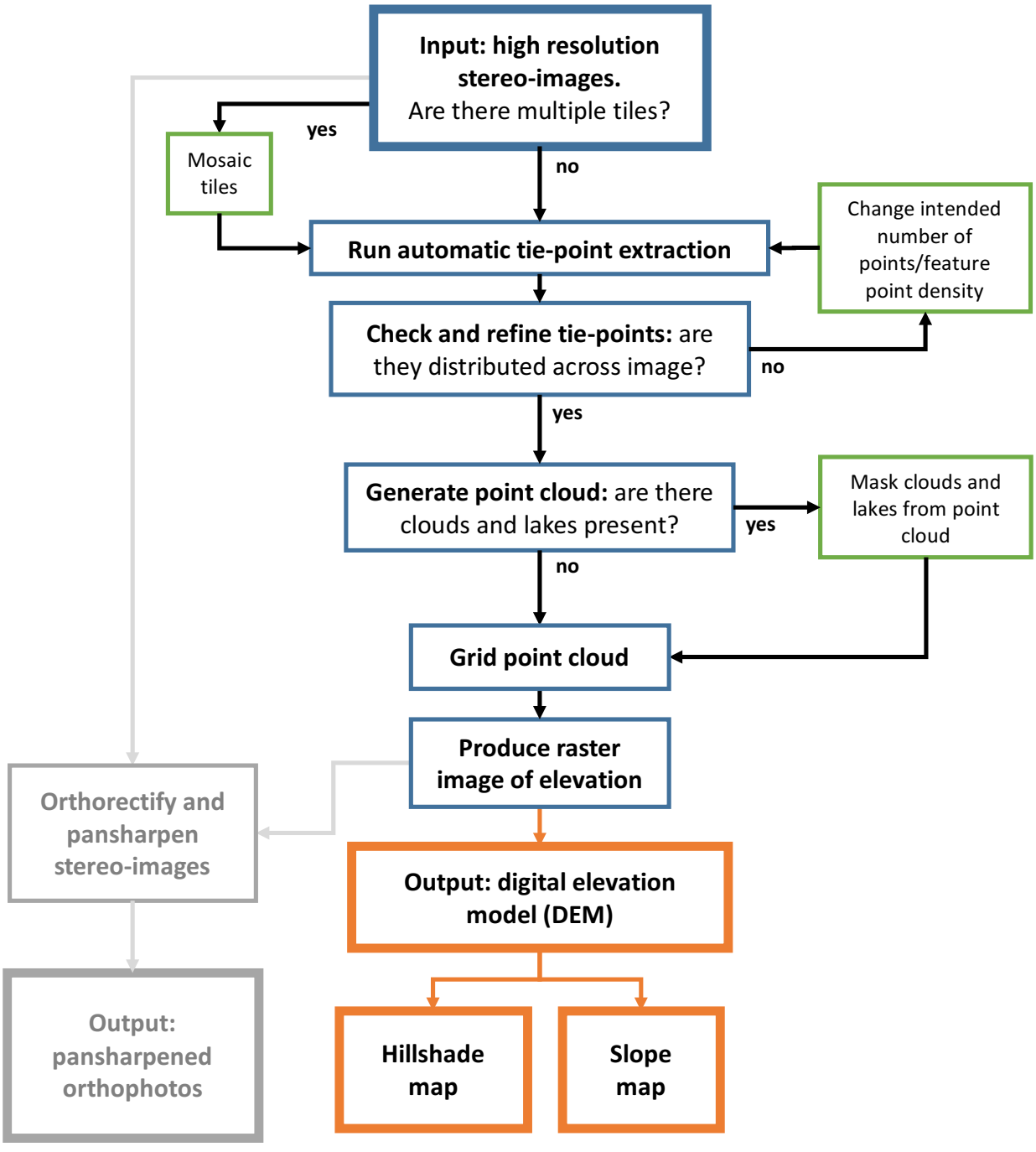

Figure A2.1. Flow chart outlining the methodology for generating high-resolution digital elevation models from Pleiades optical imagery.

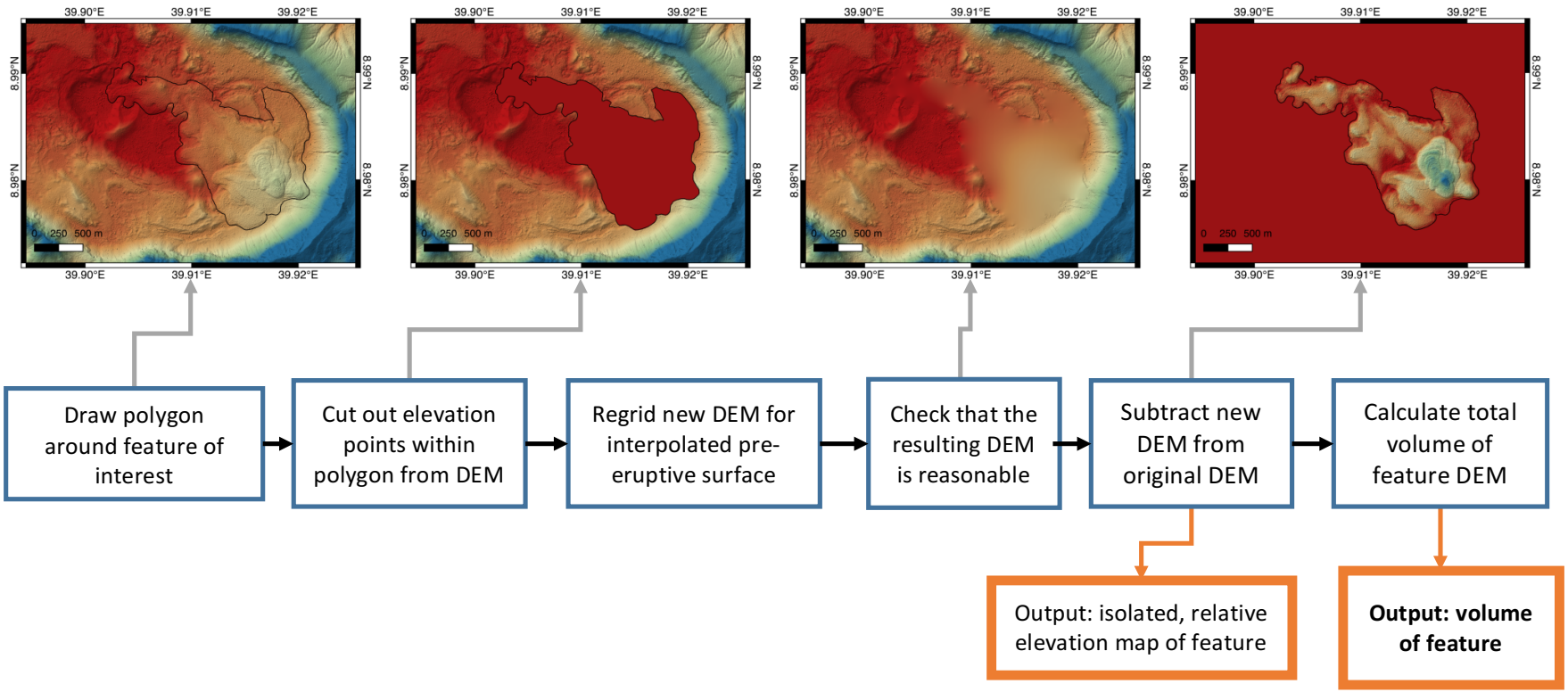

Figure A2.2. Flow chart outlining the DEM-differencing methodology for calculating volumes for features, using the example of the central lava coulee at Fentale.

Figure A2.3. Photos of blister structures, photo credit Fiona Iddon. *Top left:* A broad, collapsed blister, in which a circle of fractured and weathered ignimbrite remains. *Top right:* A low, uncollapsed blister. *Bottom:* A large, uncollapsed blister comprising a brittle crust with polygonal fractures overlaying a smoother raised surface.

Figure A2.4. Map of blisters observed in the field. Black ellipses delineate approximate bounds of each blister, red lines show the orientation of ellipses and blue arrows indicate breach directions where applicable. Red shaded area to the north east of the map was not covered by our field observations. Inset shows the location of the mapped area (red rectangle) and nearby Lake Metahara.

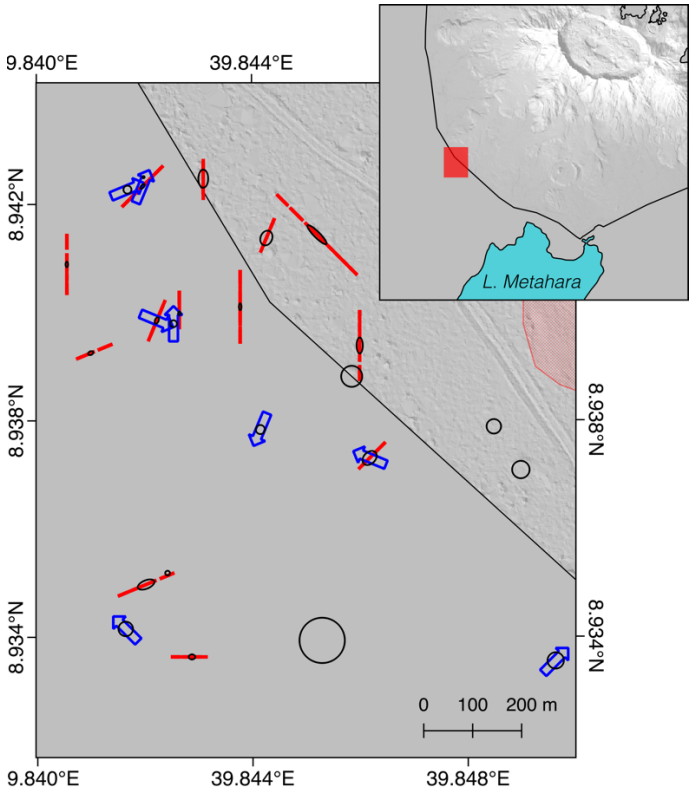

Figure A2.5. *Left:* Maps of features with volumes (in km^3). *Right:* Map of levee features on Fentale used in analysis (see Figure 3.14; red shows L1 and L2, blue shows L4a and b).

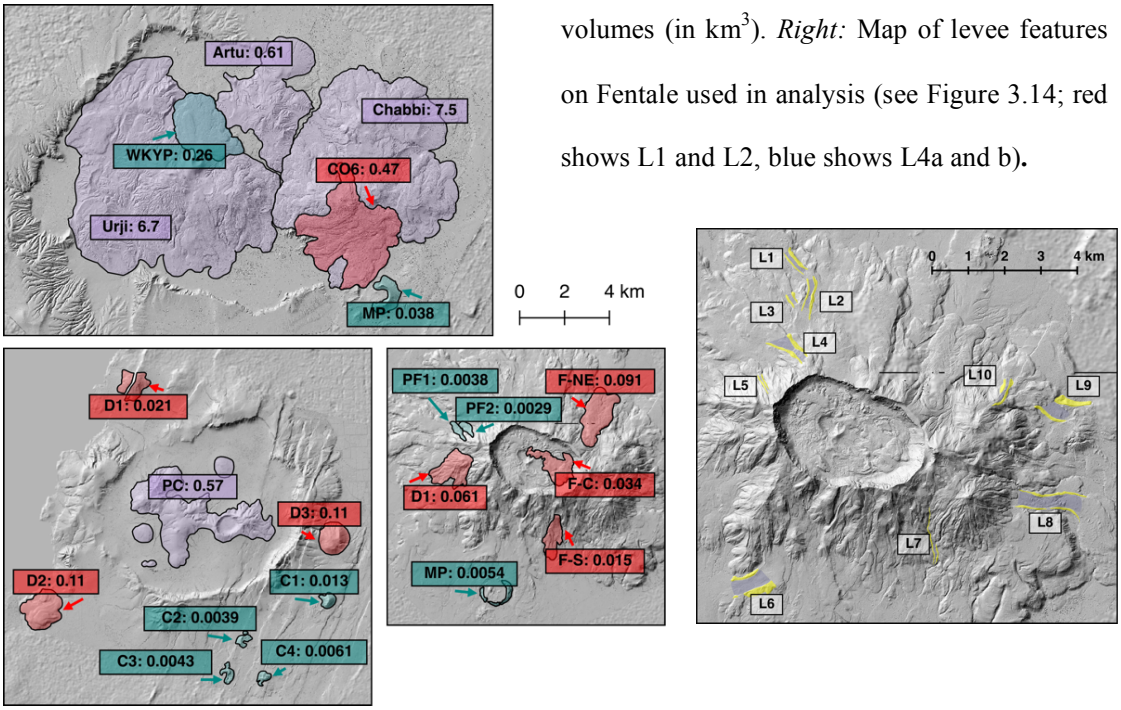

Table A2.1. Details of levee dimensions. Mean slope is calculated using the slope map, computing the mean within a polygon of the channel. Slope difference is calculated using the minimum and maximum elevation divided by the distance between the two. Slope difference is used, as mean slope is affected by irregularities in the data.

Name	L1	L2	L3	L4a	L4b	L5	L6	L7	L8	L9	L10
Mean slope	13.2	12.8	13.1	21.9	11.3	26.4	9.2	15.9	11.9	11.3	20.1
Max. elevation	1210	1340	1330	1570	1440	1660	1110	1210	1240	1220	1500
Min. elevation	1140	1240	1270	1460	1390	1450	1040	1100	1090	1200	1320
Distance	740	810	330	360	510	440	1000	520	170	660	650
Slope difference	5.4	7.0	10.3	17.0	5.6	25.5	4.0	11.9	4.8	1.7	15.5
Min. width	60	60	90	110	100	20	300	30	270	320	60
Max. width	100	140	120	180	370	50	380	70	370	400	90

Appendix 3

A3 Supporting Information for Chapter 4: Morphological comparison of distributed volcanic fields

A3.1. Introduction

This supplementary information includes further details concerning the methodology of calculating volumes from an ideal cone (see section 4.2.1, Table 4.1), maps showing the categorization of cones and mapping of features in the Pleiades analysis (see section 4.2.1, Table 4.1), and graphs showing results from all cone fields in the Aster analysis (see section 4.3.3).

A3.2. Methodology of calculating volumes from an ideal cone

Figure A3.3 shows a diagram of an ideal cone. The volume of an ideal cone of known height (**h**), basal width ($\mathbf{x_1}$), crater width ($\mathbf{x_2}$) and crater depth (**d**) can be calculated using similar triangles to find h_1 and h_2:

$$\frac{h_1}{\boldsymbol{x_1}} = \frac{h_2}{\boldsymbol{x_2}}$$

and,

$$h_1 - h_2 = \boldsymbol{h}$$

which gives

$$h_1 = \frac{\boldsymbol{x_1}}{(\boldsymbol{x_1} - \boldsymbol{x_2})}\boldsymbol{h}$$

$$h_2 = \frac{\boldsymbol{x_2}}{(\boldsymbol{x_1} - \boldsymbol{x_2})}\boldsymbol{h}$$

The volume of the ideal cone is then calculated using the conical volumes of the large cone, the missing peak and the crater:

$$V_{cone}(W = \boldsymbol{x_1}, H = h_1) - V_{cone}(W = \boldsymbol{x_2}, H = h_2) - V_{cone}(W = \boldsymbol{x_2}, H = \boldsymbol{d})$$

where

$$V_{cone}(W, H) = \pi \left(\frac{W}{2}\right)^2 \frac{H}{3}$$

A3.3. Comparing idealized volumes to DEM volumes

Figure A3.7 shows a comparison of volumes calculated from DEMs and volumes estimated using the geometry of an ideal cone. The idealized cone volumes are within 10% of the volumes calculated from DEMs, except for cones EZ40 (14%) and EZ45 (21%).

Cone EZ40 has missing data on its northern flank – the volume calculated from the DEM is likely to be an underestimate and the higher value of the idealized cone volume for this cone is likely more accurate. Cone EZ45 is highly asymmetric – the calculation of idealized cone volume assumes axisymmetric form, so it is likely to overestimate the actual cone volume.

The idealized cone volumes reproduce the volumes calculated from the DEM for all other cones, and are therefore a useful comparison for cones for which volumes cannot be calculated using the DEM (i.e., BU19e and BU23a).

Figure A3.1. Slope maps of each cone/maar in the Butajira cone field by category. Red lines mark the outer area of each cone/maar used for estimating base topography and associated volumes. Blue lines mark crater rims, used for calculating Wcr for regular cones. Green lines mark regular cone bases used for calculating Wco.

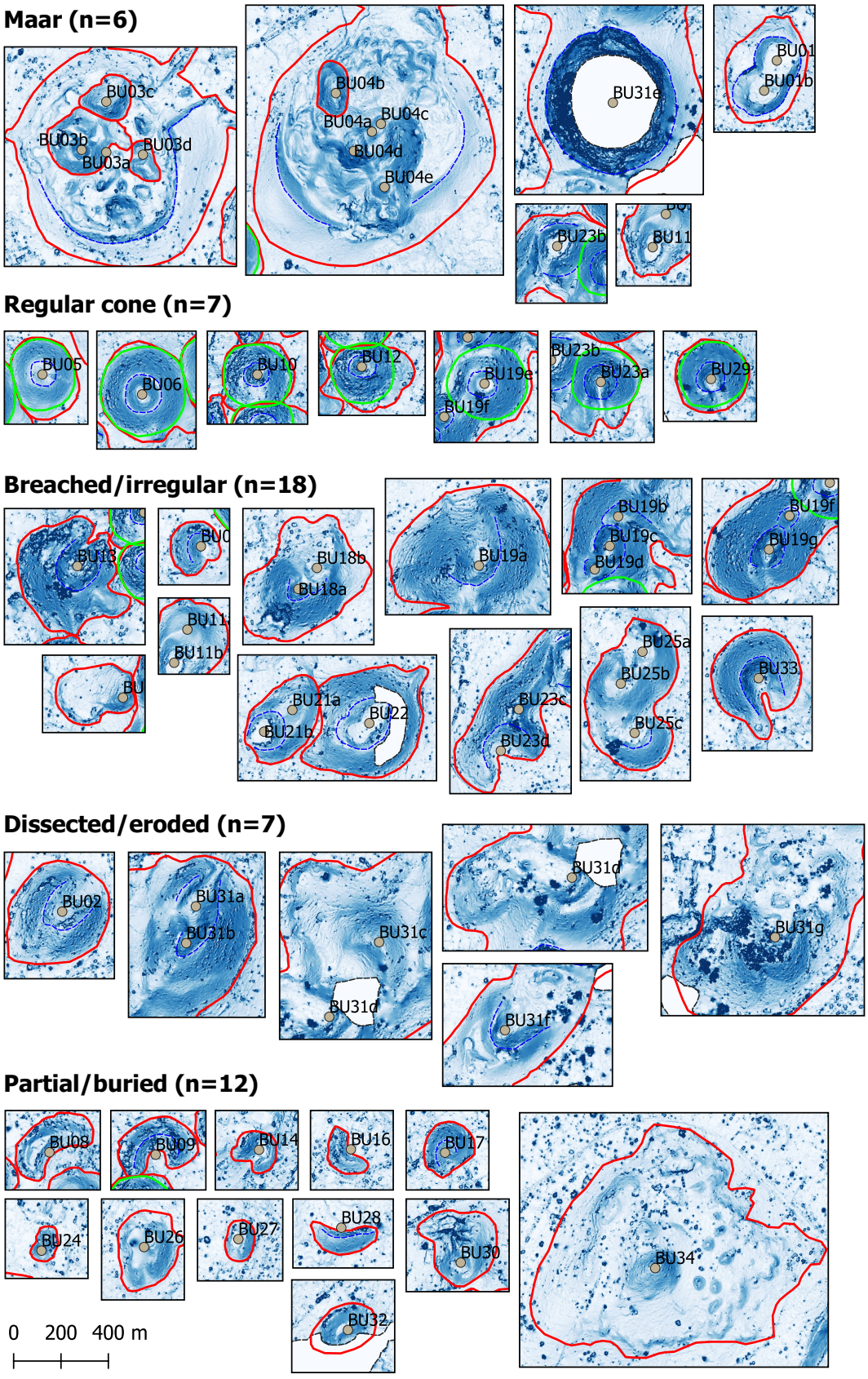
Maar (n=6)
BU03c
BU03b
BU03d
BU03a
BU04b
BU04a
BU04c
BU04d
BU04e
BU31e
BU01
BU01b
BU23b
BU11
Regular cone (n=7)
BU05
BU06
BU10
BU12
BU19e
BU19f
BU23b
BU23a
BU29
Breached/irregular (n=18)
BU18
BU18b
BU18a
BU19a
BU19b
BU19c
BU19d
BU19f
BU19g
BU11b
BU21a
BU21b
BU22
BU23c
BU23d
BU25a
BU25b
BU25c
BU33
Dissected/eroded (n=7)
BU02
BU31a
BU31b
BU31c
BU31d
BU31d
BU31f
BU31g
Partial/buried (n=12)
BU08
BU09
BU14
BU16
BU17
BU24
BU26
BU27
BU28
BU30
BU34
BU32
0 200 400 m

Regular cone (n=8)

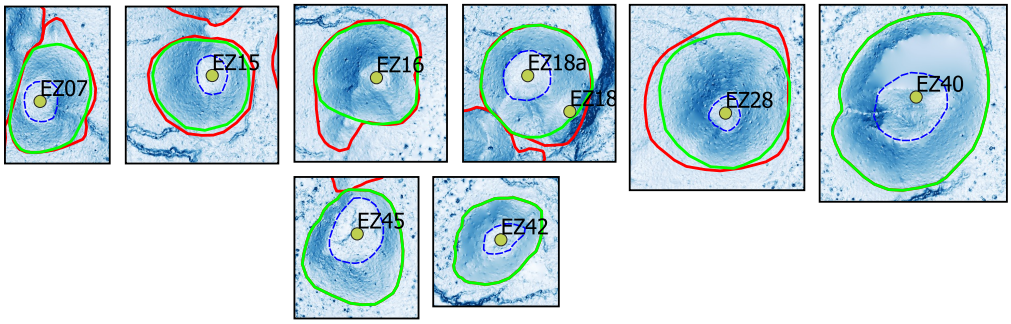

Breached/irregular (n=15)

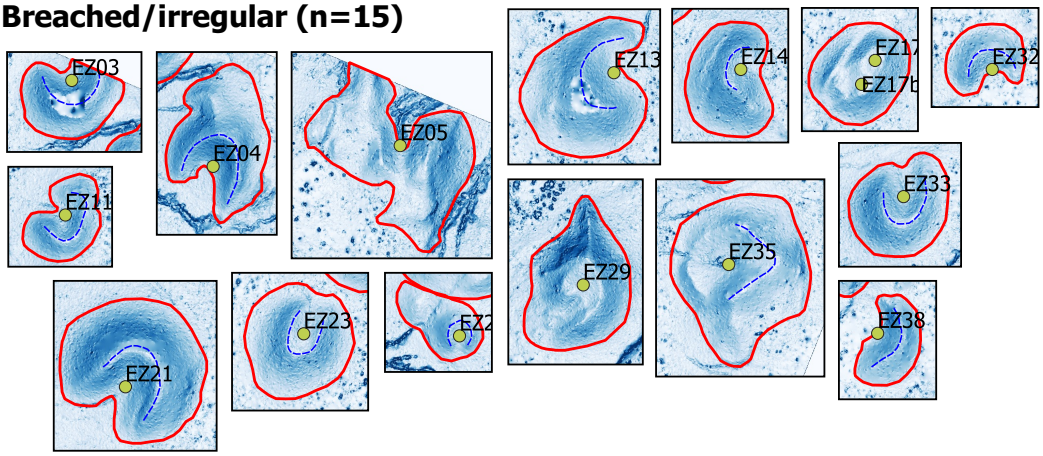

Dissected/eroded (n=9)

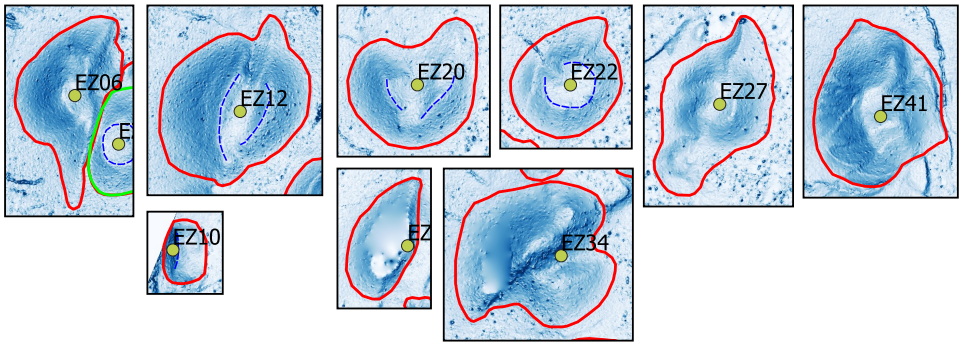

Partial/buried (n=14)

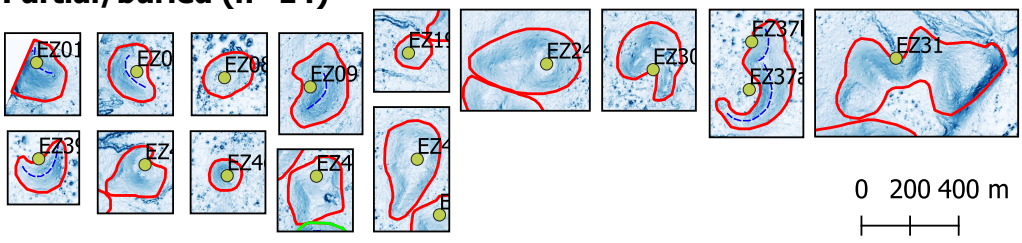

Figure A3.2. Slope maps of each cone/maar in the East Ziway cone field by category. Red lines mark the outer area of each cone/maar used for estimating base topography and associated volumes. Blue lines mark crater rims, used for calculating Wcr for regular cones. Green lines mark regular cone bases used for calculating Wco.

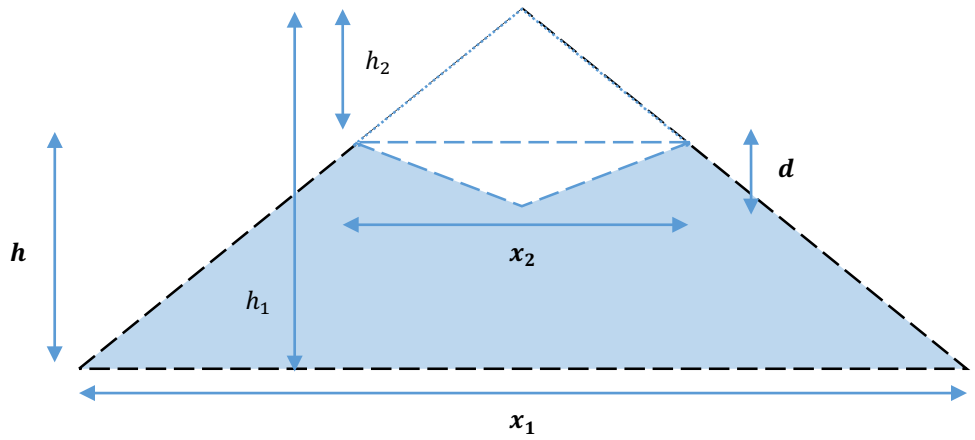

Figure A3.3. Diagram of an ideal cone, for use in calculating idealized volumes on the basis of known cone width and height, and crater width and depth.

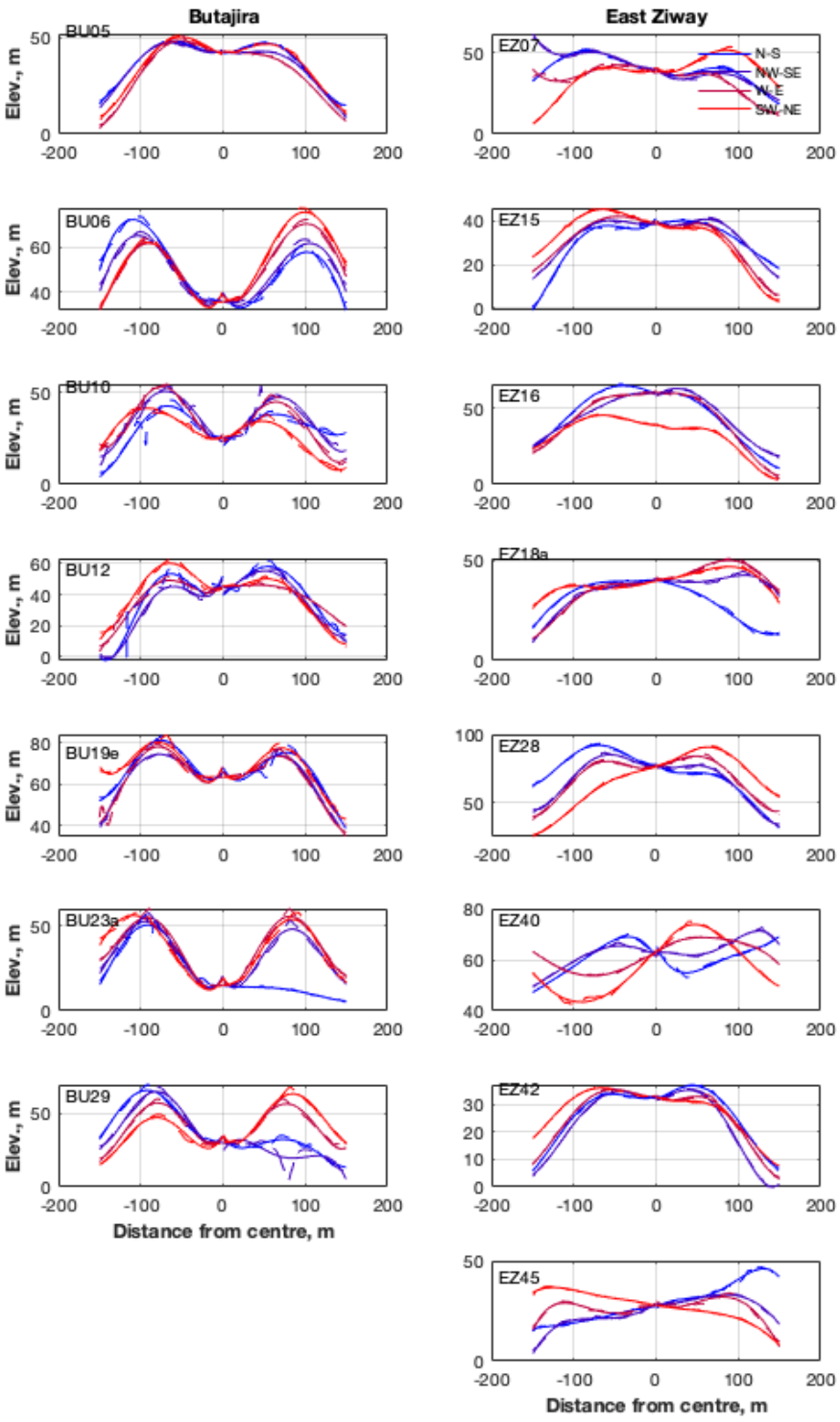

Figure A3.4. Best-fitting polynomials (4th-degree) for sections of each regular cone profile.

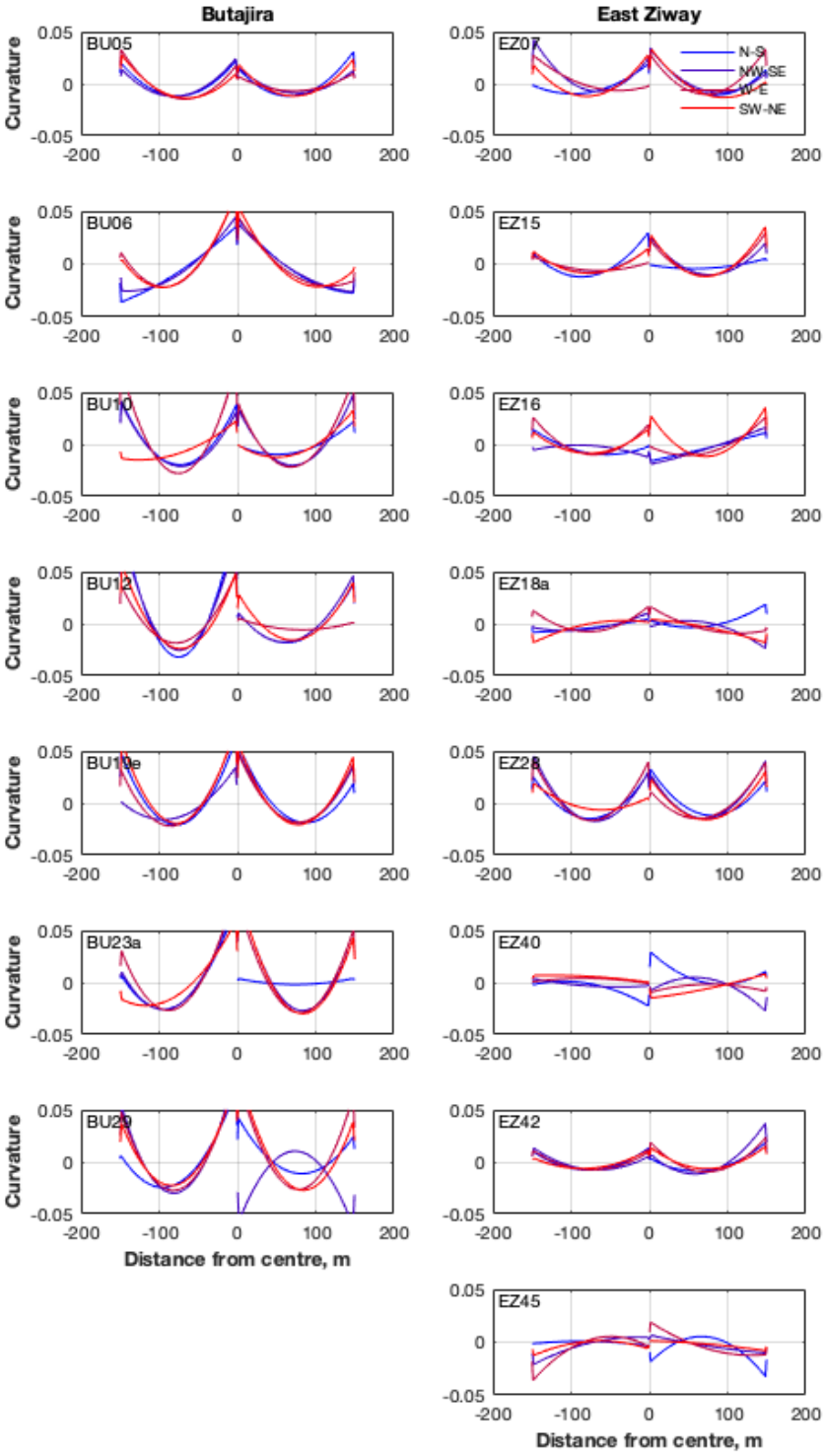

Figure A3.5. Curvature (second derivative of elevation profile) for sections of each regular cone profile. The greatest negative values for each profile in which the cone rim is represented by the greatest negative curvature cone are plotted in Figure 4.4b.

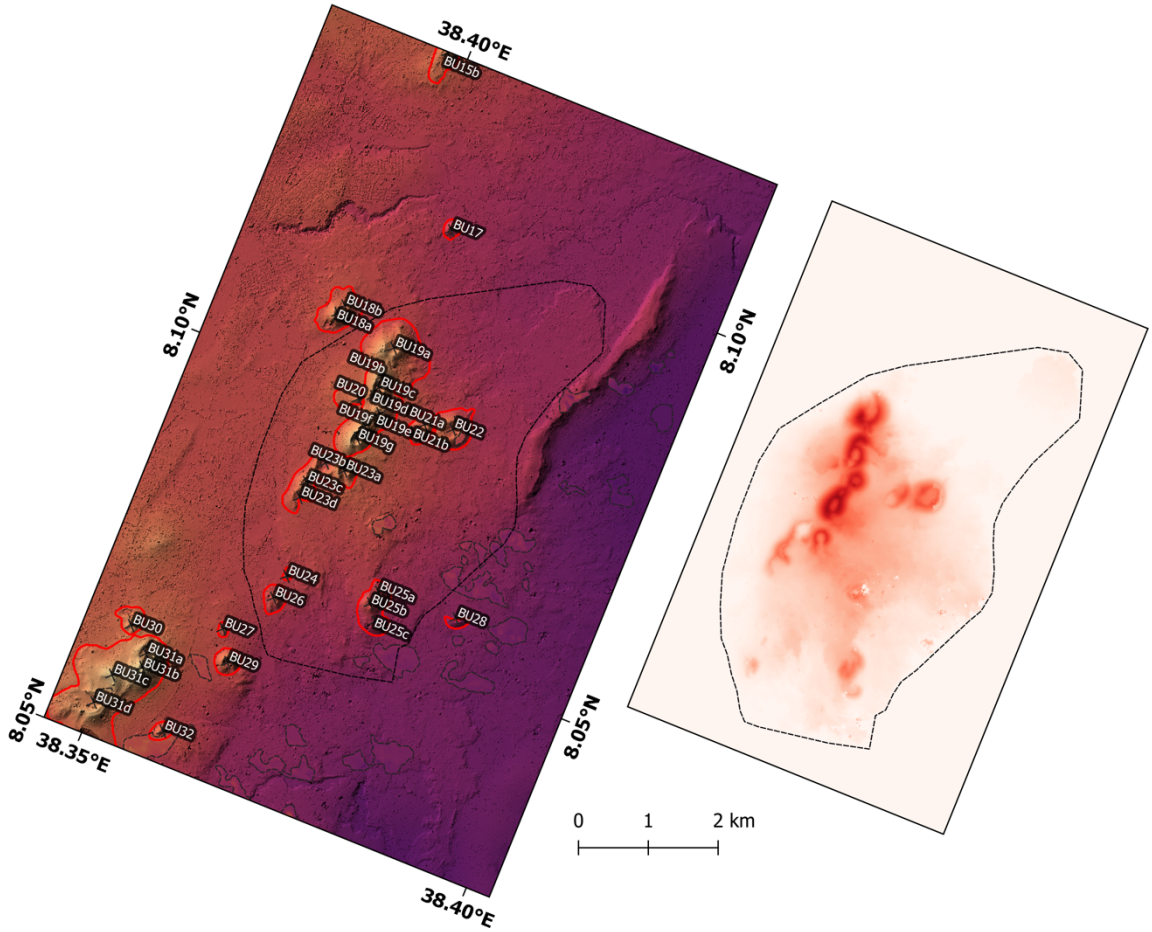

Figure A3.6. *Left:* Combined hillshade and elevation map of the Butajira field showing the extent of the broad high associated with lava flows around the central cluster of scoria cones. *Right:* Isolated digital elevation model of the broad high after removing an estimated baseline topography. The volume of the broad high excluding the scoria cones (bounds in thick red lines) is 0.46 km^3.

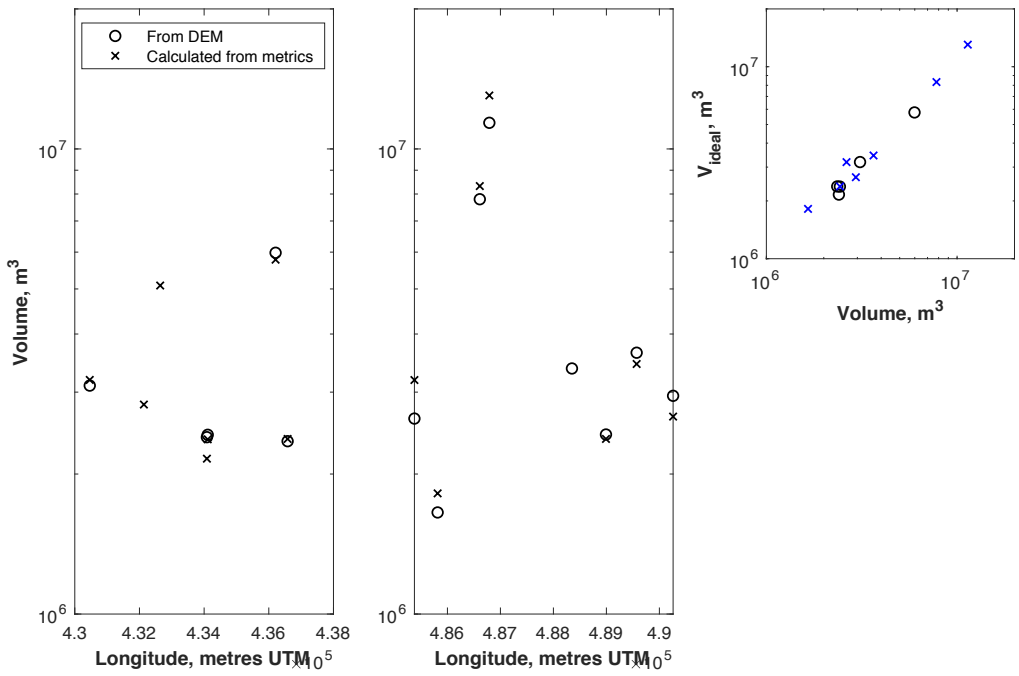

Figure A3.7. Graphs from Butajira (left) and East Ziway (center) comparing volumes calculated from the DEMs and estimated from the geometry of an ideal cone. In the right panel, volumes and ideal volumes are plotted against each other on a log-log plot: black circles = Butajira, blue crosses = East Ziway.

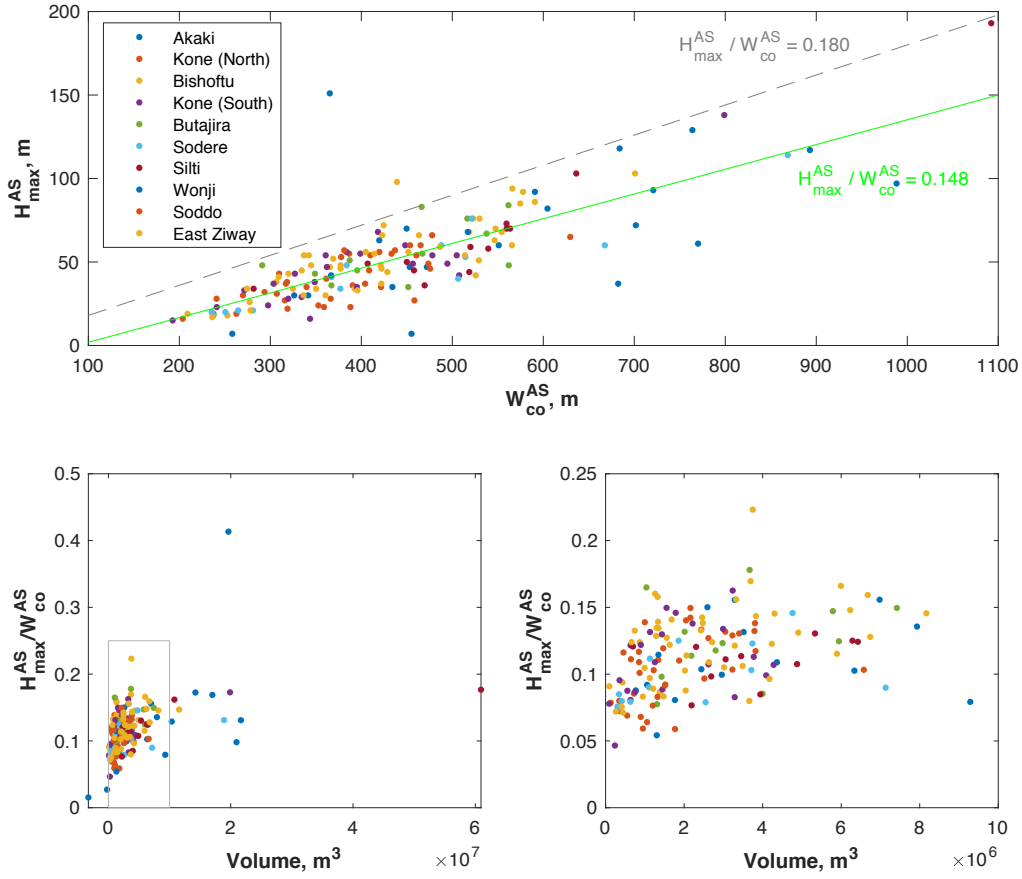

Figure A3.8. Graphs of metrics calculated using the ASTER GDEM for ten cone fields in the Main Ethiopian Rift, which are also presented as the grey background fields in Figure 4.7. *Upper panel:* H^{AS}_{max}–W^{AS}_{co} plot with the global average of 0.18 shown, alongside the average for this data, 0.148. *Bottom left:* H^{AS}_{max}/W^{AS}_{co}–volume plot, enlarged in bottom right.